

**Applications of Magnetic
Resonance in Materials Science
and
Solid State Physics**

**A Thesis Submitted for the Degree of
Doctor of Philosophy**

By

Christopher John Noble

B. Sc. (Hons), Monash University, Australia.

Department of Physics

Monash University

Australia

November 2001

Contents

Abstract	v
Declaration	vi
Acknowledgments	vii
1. Introduction.	1
1.1 General	1
1.2 Summary	2
1.3 References	5
2. Methodologies in EPR	6
2.1 Basic Principles of EPR	6
2.2 The Spin Hamiltonian	8
2.3 Multiple Resonance Techniques	14
2.3.1 ENDOR	14
2.3.2 ODMR	16
2.4 Pulsed EPR Techniques	18
2.4.1 Nutation spectroscopy	22
2.4.2 ESEEM	24
2.4.3 Relaxation Experiments	27
2.4.4 Echo Detected EPR.	28
2.5 Choice of Technique	31
2.6 References	32
3. Paramagnetic Defects in Coloured Argyle Diamonds.	33
3.1 Introduction	33
3.2 Experimental	38
3.3 Results	42
3.4 Discussion	49
3.5 Conclusion	53
3.6 References	53
4. Photo/Thermochromic Effects in Argyle Pink Diamonds	55
4.1 Introduction	55
4.2 Experimental	59
4.3 Results	59
4.4 Discussion	65
4.5 Conclusion	72

4.6 References	72
5. ENDOR Spectra of Natural Blue Argyle Diamonds[†]	74
5.1 Introduction	74
5.2 Experimental	79
5.3 Results	81
5.4 Discussion	89
5.5 Conclusion	98
5.6 Acknowledgments	98
5.7 References	99
6. ODMR of Nickel Centres in Synthetic HTHP Diamonds[†]	100
6.1 Introduction	100
6.2 Experimental	100
6.3 Results	103
6.4 Discussion	113
6.5 Conclusion	121
6.6 Acknowledgements	121
6.7 References	122
7. Characterisation of Ion-implantation Damage in Type IIa Diamond Using EPR	123
7.1 Introduction	123
7.2 Experimental	125
7.3 Results	126
7.4 Discussion	130
7.5 Conclusion	134
7.6 Acknowledgments	135
7.7 References	135
8. Interaction Between Localised And Conduction Electron Spins In The High T_c Superconductor Gd:EuBa₂Cu₃O_{6+x}[†]	136
8.1 Introduction	136
8.2 Experimental	141
8.3 Results	144
8.4 Discussion	151
8.5 Conclusion	154
8.6 Acknowledgments	155
8.7 References	155

9. Nutation spectroscopy of Ti:CsAl(SO₄)₂·12H₂O.	157
9.1 Introduction	157
9.2 Experimental	161
9.3 Results	162
9.4 Discussion	165
9.5 Conclusion	167
9.6 References	167
10. EPR of Natural Rutile Powder	169
10.1 Introduction	169
10.2 Experimental	170
10.3 Results	170
10.4 Discussion	172
10.5 Conclusions	174
10.6 References	174
Appendix: Supporting Publications	175

Abstract

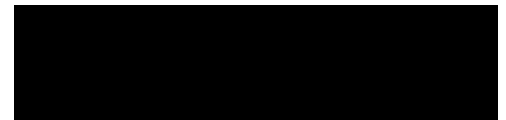
This thesis describe several, largely independent, studies where electron paramagnetic resonance (EPR) and related techniques have been applied to a number of problems in materials science and solid state physics. The diversity has resulted from appropriate opportunities that arose during this work. Each of these studies involved different materials and a different set of questions. The unifying theme throughout this thesis is the use of magnetic resonance techniques to characterise materials.

The majority of the work presented in this thesis has involved diamonds. Initially the focus was on natural diamonds and in particular the nature and origin of coloured Argyle diamonds. This work was a survey that attempted to correlate EPR spectra with the colour of the diamonds. This was followed by a photo-EPR investigation of the photochromic behaviour of EPR centres in pink Argyle diamonds. Electron nuclear double resonance (ENDOR) was then used to establish a structural model for a defect in the blue Argyle diamonds. These investigations were extended to synthetic diamonds where similar defects were studied with optically detected magnetic resonance (ODMR). The ion-implantation damage in synthetic diamonds was also investigated with conventional EPR and a relationship between the EPR linewidth and the electrical conductivity was established.

Other materials that were investigated include the high T_c superconductor $\text{EuBa}_2\text{Cu}_3\text{O}_{6+x}$ where the EPR spectra of gadolinium was used as a probe of the conduction system, caesium titanium alum, where pulsed techniques provided insight into the Jahn-Teller effect and natural rutile where paramagnetic impurities were identified.

Declaration

This thesis contains no material accepted for the award of any other degree or diploma in any university. To the best of my knowledge, it contains no material published or written by another person, except where due reference is made in the text.



Christopher John Noble

Acknowledgments

I would like to thank my supervisors Prof. John Pilbrow and Dr. Don Hutton for their faith in my abilities and the constant support they gave during my PhD.

I would also like to thank other colleagues, past and present, in the EPR group at Monash University, including Dr. R. Song and Dr. Yong Zhong and in particular Dr. Gordon Troup, whose acumen and lively interest in both gemstones and EPR provided the initial impetus for a large part of this thesis.

The technical staff in the physics department deserve thanks for the many jobs that have assisted me in completing my project including above all the constant supply of liquid helium and nitrogen.

Further acknowledgments are made in each of the chapters in this thesis.

1. Introduction.

1.1 General

Electron paramagnetic resonance (EPR) refers to the resonant absorption of microwave radiation by paramagnetic ions in a magnetic field. EPR is also referred to as electron spin resonance (ESR) or perhaps more generally as electron magnetic resonance (EMR). The phenomenon was discovered by Zavoiskii in 1945, two years before the corresponding nuclear technique, nuclear magnetic resonance (NMR).¹

The EPR spectrum can provide information about the identity and valency of the paramagnetic centre, its local symmetry and environment, the overall concentration of the defect and its local concentration or distribution. The technique has a high sensitivity and only low concentrations of paramagnetic centres are needed in contrast to NMR where concentrated samples are necessary.

It is a powerful technique that is used in wide range of fields including physics, chemistry, materials science, and the biological sciences. Examples of applications in physics and materials science include the structural determination of defects in insulators and semiconductors, probing disorder in materials, monitoring phase changes and probing the conduction systems of metals and superconductors.

Electron nuclear double resonance (ENDOR) was subsequently developed in 1956.² This technique detects the nuclear magnetic resonances by measuring the EPR signal with an additional radio-frequency radiation.. It has the advantage of the sensitivity of EPR but accesses the nuclear transitions directly. It can also resolve much smaller interactions of the electron spin with neighbouring nuclei than conventional EPR.

Optically detected magnetic resonance (ODMR) is another multiple resonance technique³ where EPR is detected through optical transitions. Optical detection often has

a sensitivity advantage over conventionally detected EPR and also selectivity so that overlapping spectra can be separated.

Pulsed EPR experiments were performed as early as 1958^{4,5} but have only recently become routinely used in research. This is primarily due to the demands on the hardware in pulsed EPR. Microwave pulses with nanosecond resolution for example, have only been achieved in the last two decades. Pulsed EPR has not totally replaced continuous wave (cw) methods whereas basically all NMR is currently time domain. This is partly due to the technical constraints that have already been mentioned but also because there are differences between the experimental parameters in the two types of magnetic resonance experiments. Typically electron spin relaxation times are much shorter than those for nuclear transitions. Fourier transform EPR (FTEPR) also does not have the sensitivity and resolution advantages of the NMR technique.

The value of pulsed EPR lies instead in its ability to give information that is not available in cw EPR. Electron spin echo envelope modulation (ESEEM) experiments provide access to small interactions that are not resolved in cw EPR. Different pulse sequences can also be used that effectively look at only a subset of the interactions of the electron spin in a manner that is not possible in cw EPR.

1.2 Summary

This thesis contains ten chapters including this introduction. In the second chapter of this thesis a brief summary of the theory and experimental techniques that are used in EPR is given. Special emphasis is given to the techniques that are used in later chapters although it is attempted to provide the reader with an overall perspective of magnetic resonance techniques and how they are used in physics and materials science.

The remaining chapters in this thesis describe several studies where EPR and related techniques have been applied to a number of problems in materials science and solid state physics. The diversity has resulted from appropriate opportunities that arose during this work. Each of these studies involved different materials and a different set of questions. The unifying theme throughout these chapters is the use of magnetic resonance techniques to characterise materials

The initial study, chapter 3, was on natural diamonds from the Argyle mine in Western Australia. The interest was in the origin of the pink and brown colouration in some of these diamonds. An EPR survey was made of a set of diamonds in an attempt to find an EPR centre that correlated with these colours. EPR spectra can provide much more structural information than optical techniques and if the defects responsible for the colour were EPR active it would be possible to shed more light on the origin of these colours.

In the next chapter the photochromic behaviour of some of the EPR centres in the pink Argyle diamonds is reported. It was found that several EPR centres in these diamonds were affected when exposed to UV irradiation. It was also evident that several different processes were active under different conditions of illumination. One of these processes was investigated using photo-EPR and an activation energy was obtained.

In chapter 5 a previously unreported EPR centre is described that is present in natural blue Argyle diamonds. It was not possible to unequivocally determine the nature of this defect but it was found likely to be due to a nickel impurity, partly because other identified nickel centres were also present in these diamonds, and also because the spectrum was characteristic of a transition metal ion. No hyperfine splittings were

resolved in the cw spectrum but ENDOR spectra revealed an interaction with one or more nitrogen nuclei. A tentative model of the defect is proposed.

Synthetic diamonds containing nickel centres were then obtained and research into these centres was continued. In chapter 6 the results of EPR and ODMR studies of these diamonds are presented. Several new EPR centres were observed and characterised. ODMR was extremely effective, firstly due to the sensitivity of the techniques, and secondly because EPR centres are unequivocally correlated with optical spectra.

In chapter 7 an EPR study of ion implantation damage in synthetic diamonds is presented. These diamonds had previously been investigated with electron microscopy and conductivity measurements. It was found that the temperature dependent linewidth of the EPR spectrum was determined largely by the conductivity in these samples which followed a variable range hopping model.

Conduction mechanisms are again investigated in chapter 8 where Gd^{3+} ions are used to probe the conduction electron system in the high T_c superconductor $EuBa_2Cu_3O_{6+x}$. The EPR spectra of the gadolinium ion in this material was found to be affected by an exchange interaction with the conduction electrons. The temperature dependence of the linewidth of the gadolinium spectrum was linear above T_c indicating metallic type conduction.

In chapter 9 nutation spectroscopy is used to characterise a classic Jahn Teller system, Ti^{3+} in $CsAl(SO_4)_2 \cdot 12H_2O$. The nutation experiment helped to provide an interpretation of the complex cw EPR spectrum. More importantly, it showed, in a two dimensional experiment, the importance of treating the inhomogeneously broadened spectrum as a true distribution of parameters.

In the final chapter, an EPR study of transition metal ions in a natural polycrystalline rutile sample is presented. The chemical state of iron in these samples was previously investigated with Mössbauer spectroscopy. Iron, chromium and manganese were found to be present in these samples. The results are not extremely notable but serve to illustrate some of the capabilities of EPR in characterising materials, namely the identification of paramagnetic impurities and the determination of their charge state.

1.3 References

-
- ¹ Zavoiskii, E., *Fyz. Zh.* **9**, (1945) 211.
 - ² Feher, G., *Phys. Rev.*, **103**, (1956) 834.
 - ³ Karlov, N.V., Margerie, J. and Merle d'Aubigné, Y., *J. Physique*, **24**, (1963) 717.
 - ⁴ Gordon, J.P., and Bowers, K.D., *Phys. Rev. Lett.*, **1**, (1958) 368.
 - ⁵ Blume, R.J., *Phys. Rev.*, **109**, (1958) 1867.

2. Methodologies in EPR

2.1 Basic Principles of EPR

A free electron, with an electron spin $S = 1/2$, has a magnetic moment, μ , given by

$$\mu = g\beta S \quad [2.1]$$

where g is the electron g factor, β is the electron Bohr magneton and S is the spin operator. The energy of interaction between the electron spin and a static magnetic field, B , is then given by

$$H = g\beta S \cdot B \quad [2.2]$$

For a free electron with an electron spin, $S = 1/2$, there are two possible states with quantum numbers, $m_s = +1/2$ and $m_s = -1/2$, and corresponding energies,

$$E_{\pm} = \pm \frac{1}{2} g\beta B \quad [2.3]$$

When the microwave energy, $h\nu$, is equal to the difference in energy between the two levels resonant absorption of microwaves will occur. This resonant condition is described by the equation.

$$E_{+} - E_{-} = h\nu = g\beta B \quad [2.4]$$

where h is Planck's constant.

Figure 2.1a shows the splitting of the two energy levels in the presence of a magnetic field and a transition at B_0 where equation 2.4 is satisfied. Figure 2.1c shows the microwave absorption centred at B_0 . EPR is usually recorded with magnetic field modulation and phase sensitive detection and the signal is normally shown as a first derivative with respect to field.

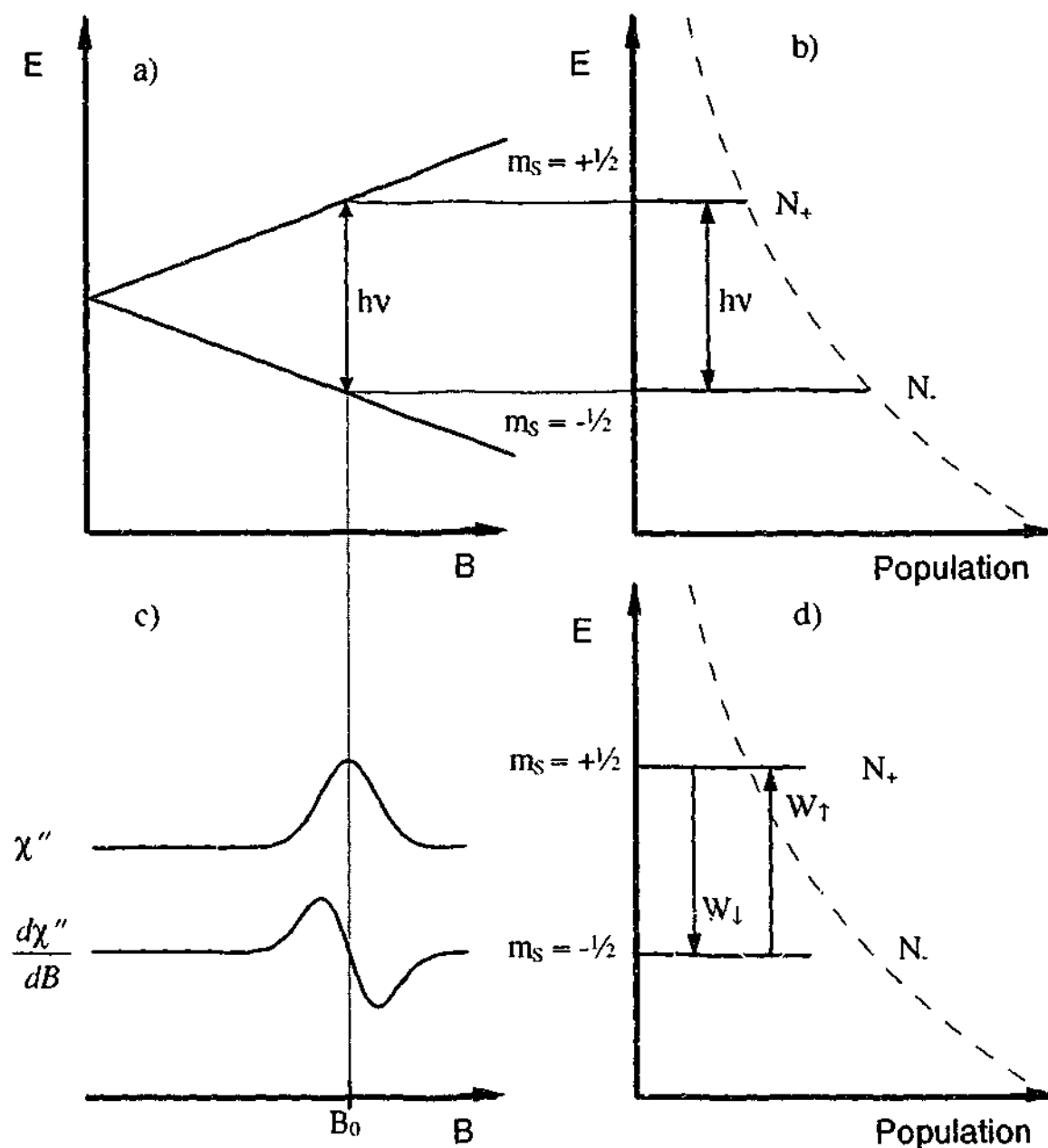


Figure 2.1 Schematic explanation of EPR with an example of a $S=1/2$ Kramers ion. a) The two energy levels are split in the presence of a magnetic field according to equation 2.4. b) The population of the two energy levels are indicated by the lengths of the horizontal lines and are governed by a Boltzmann distribution. c) Absorption and first derivative spectra centred at B_0 . χ'' is the imaginary component of the microwave absorption. d) The populations of the two energy levels are determined by the two process rates W_\uparrow and W_\downarrow , where it has been assumed that these processes dominate relaxation

The probability of a transition from the $m_s = -1/2$ level to the $m_s = +1/2$ level, W_\uparrow , will be the same as the reverse transition probability, W_\downarrow , and the absorption will be determined by the population difference, $N_- - N_+$, between the two levels. The population of the two energy levels at equilibrium will be determined by the Boltzmann distribution as shown in Figure 2.1b. The lower state will have a slightly higher population than the

higher state. This difference will depend on the temperature. At lower temperatures the difference will be greater and hence the absorption stronger.

In the absence of any other processes the population of the two levels will therefore rapidly become equivalent. At this point the transition is said to be saturated and no further absorption can occur. This is shown in Figure 2.1d. In reality there are relaxation processes which restore the populations of the energy levels to the equilibrium values. These processes involve the interaction of the electron spins and lattice phonons, and are termed spin lattice relaxation. It is characterised by a spin lattice relaxation time, T_1 . The magnitude of T_1 will determine how easy it is to saturate a given transition. In cases where T_1 is short the transition will not be saturated unless a high microwave power is used. T_1 also determines the linewidth of the transition. Transitions with a short T_1 will have a large homogeneous linewidth. In practise the linewidth is normally dominated by other processes.

2.2 The Spin Hamiltonian

EPR spectra are generally more complicated than the simple example given above. The electron spin is often greater than $1/2$ and there are also interactions with the magnetic moment due to neighbouring nuclei. This is fortunate in that the spectra can be interpreted, through models, and yield information about the interaction of the electron spins with their environment. In the environment of the electron is the influence of the electric fields from nearby ions, and the magnetic moments due to the central atom nucleus, neighbouring nuclei, and other paramagnetic species.

These interactions are interpreted in terms of a spin Hamiltonian. The spin Hamiltonian can then be written as a series of these interactions in order of decreasing importance for EPR as

$$H = H_{EZ} + H_{FS} + H_{HF} + H_{NZ} + H_Q \quad [2.5]$$

H_{EZ} is the electron Zeeman term and describes the interaction of the electrons with the applied field. In most cases only terms linear with \mathbf{B} are necessary although in some cases higher order terms are needed.

$$H_{EZ} = \beta \cdot \mathbf{S} \cdot \mathbf{g} \cdot \mathbf{B} \quad [2.6]$$

where \mathbf{g} is a 3×3 matrix, \mathbf{B} the magnetic field vector. The \mathbf{g} matrix can be transformed to a representation where it is diagonal and expressed in terms of its principal components and principal directions. The principal directions of the \mathbf{g} matrix may or may not correspond to crystallographic axes or the principal directions of other interactions.

$$\mathbf{g} = \begin{bmatrix} g_1 & & \\ & g_2 & \\ & & g_3 \end{bmatrix} \quad [2.7]$$

When this interaction is axial then two parameters $g_{||}$ and g_{\perp} are sufficient.

$$g_{||} = g_3 \quad [2.8]$$

$$g_{\perp} = g_1 = g_2 \quad [2.9]$$

H_{FS} is the fine structure or zero field splitting term and describes the interaction between the electric field and the electron spin \mathbf{S} . It can be written as a series of spin operators, O_n^m , corresponding to terms in different orders of \mathbf{S} which are tabulated in Abragam and Bleaney.¹

$$H_{FS} = \frac{1}{3} \sum_m b_2^m O_2^m + \frac{1}{60} \sum_m b_4^m O_4^m + \frac{1}{1260} \sum_m b_6^m O_6^m \quad [2.10]$$

and b_n^m are the associated parameters. The parameters in this equation refer to a specific set of cartesian axes which may be different again from the principal directions of any of the other matrices. If only second order terms are included then the fine structure interaction can be written in the form

$$H_{FS} = \mathbf{S} \cdot \mathbf{D} \cdot \mathbf{S} \quad [2.11]$$

where \mathbf{D} is a 3×3 matrix. In a representation where \mathbf{D} is diagonal it can be written in terms of two parameters, D and E .

$$\mathbf{D} = \begin{bmatrix} -\frac{1}{3}D + E & & \\ & -\frac{1}{3}D - E & \\ & & \frac{2}{3}D \end{bmatrix} \quad [2.12]$$

so that

$$H_{FS} = D(S_z^2 - \frac{1}{3}S(S+1)) + E(S_x^2 - S_y^2) \quad [2.13]$$

The inclusion of additional fourth order terms for tetragonal symmetry, a and F , then give

$$\begin{aligned} H_{FS} = & D(S_z^2 - \frac{1}{3}S(S+1)) + E(S_x^2 - S_y^2) \\ & + \frac{a}{6}[S_x^4 + S_y^4 + S_z^4 - \frac{1}{5}(S(S+1)(3S^2 + 3S - 1))] \\ & + \frac{F}{180}[35S_z^4 - 30S(S+1)S_z^2 + 25S_z^2 - 6S(S+1) + 3S^2(S+1)^2] \end{aligned} \quad [2.14]$$

The terms D , E , a and F can be related to the parameters b_n^m by

$$D = b_2^0 \quad [2.15]$$

$$E = \frac{1}{3}b_2^2 \quad [2.16]$$

$$a = 2(b_4^0 + 5b_4^4) \quad [2.17]$$

$$F = 3b_4^0 \quad [2.18]$$

H_{HF} is the hyperfine term and describes the interaction between the electron spin, \mathbf{S} , and the nuclear spin, \mathbf{I} , of the ion. It can be written in the form

$$H_{HF} = \mathbf{S} \cdot \mathbf{A} \cdot \mathbf{I} \quad [2.19]$$

where \mathbf{A} is the hyperfine interaction matrix and \mathbf{I} is the nuclear spin vector. The \mathbf{A} matrix is usually given in terms of its principal components, A_1 , A_2 and A_3 .

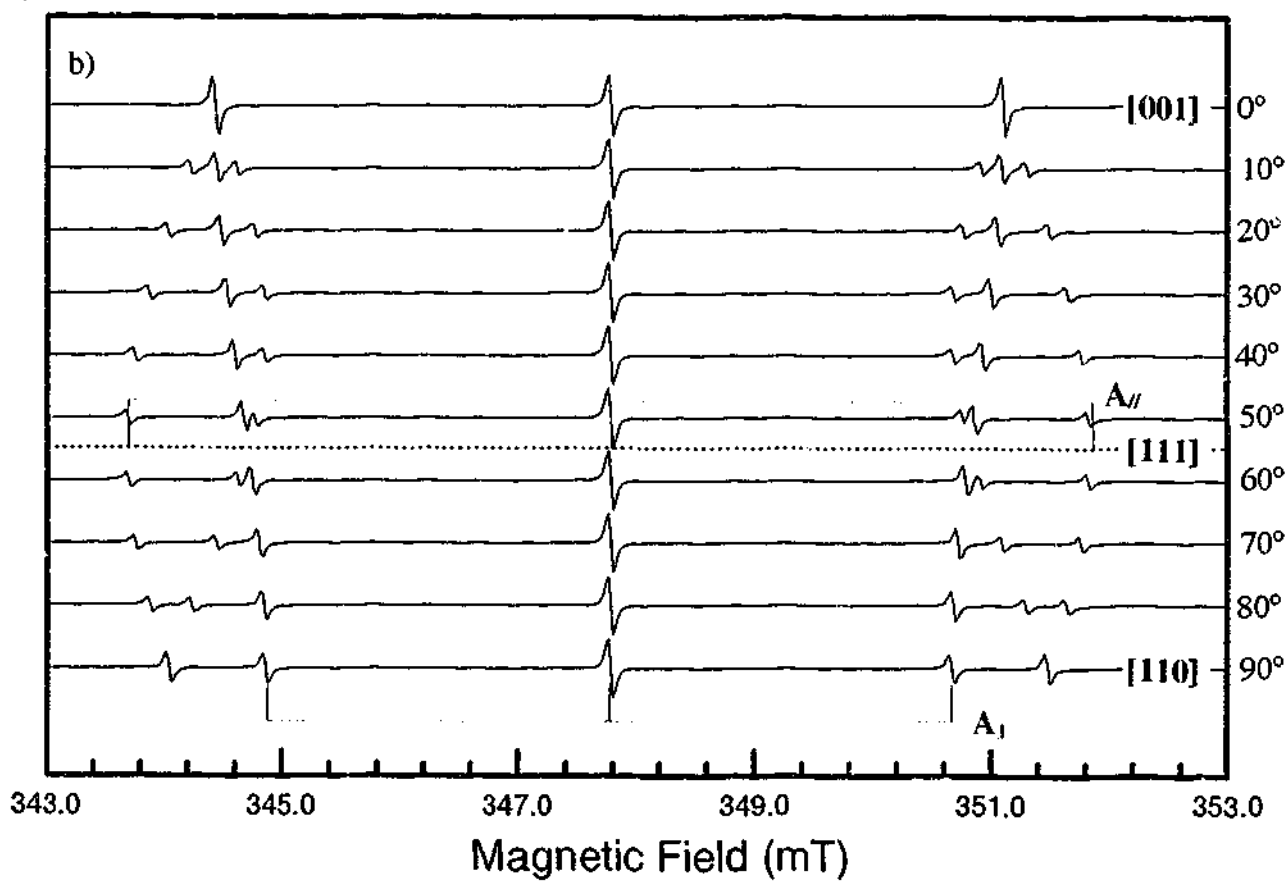
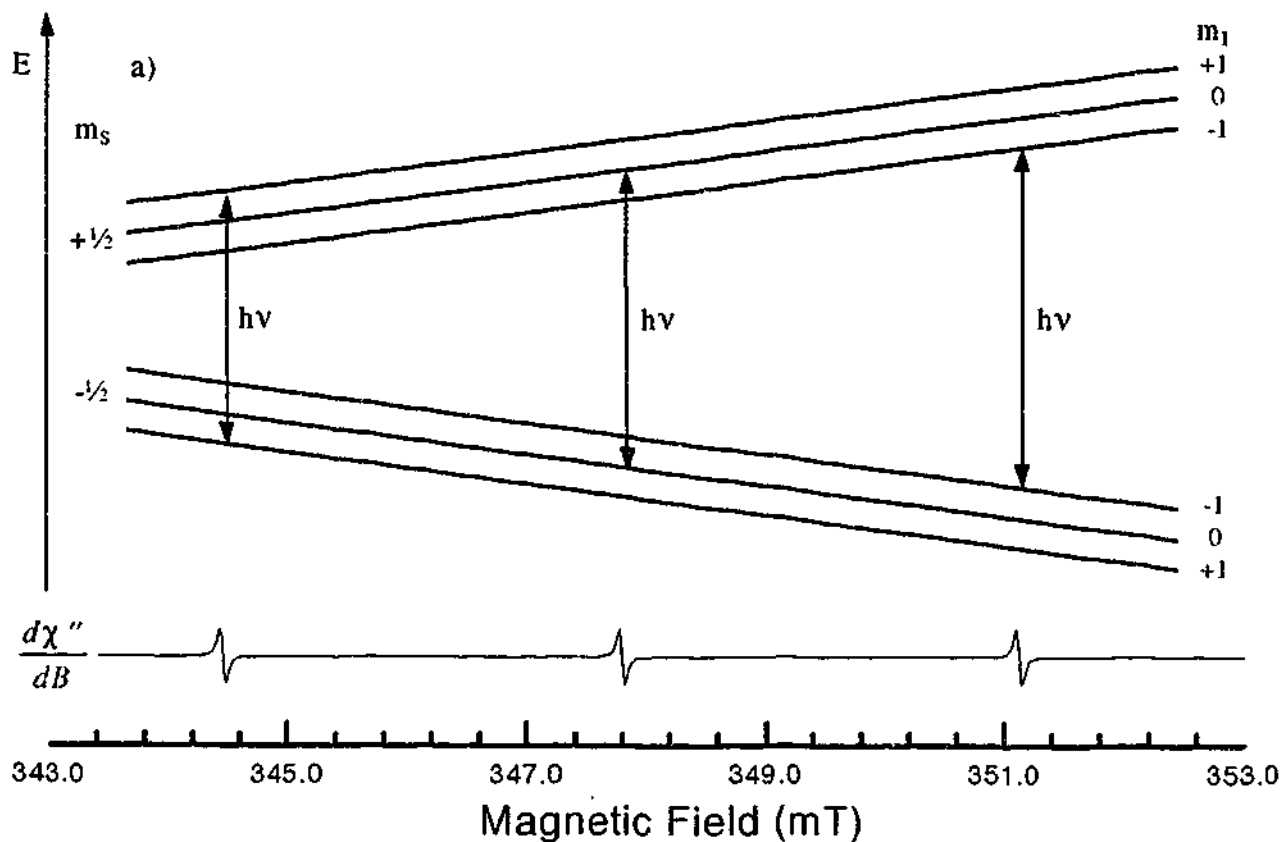


Figure 2.2 Schematic explanation of the EPR spectrum arising from a $S = 1/2, l = 1$ system. Three allowed transitions ($\Delta m_s = 1, \Delta m_l = 0$) occur at fields where the difference between the energy levels is equal to the microwave energy. b) The angular dependence of the EPR spectrum of the P1 centre in diamond. Spectra with the applied magnetic field from 0 - 90 degrees from a $\langle 100 \rangle$ axis in a $\{110\}$ plane. The splittings corresponding to the magnetic field parallel and perpendicular to the principal direction of the hyperfine interaction are marked.

$$\mathbf{A} = \begin{bmatrix} A_1 & & \\ & A_2 & \\ & & A_3 \end{bmatrix} \quad [2.20]$$

When this interaction is axial then it can be expressed in terms of parallel and perpendicular components; A_{\parallel} and A_{\perp} .

$$A_{\parallel} = A_3 \quad [2.21]$$

$$A_{\perp} = A_1 = A_2 \quad [2.22]$$

The hyperfine interaction is also often written in terms of isotropic and anisotropic components, a and b

$$A_{\parallel} = a + 2b \quad [2.23]$$

$$A_{\perp} = a - b \quad [2.24]$$

H_{NZ} is the nuclear Zeeman term and describes the interaction of the nuclear spin, \mathbf{I} , with the static magnetic field, \mathbf{B} . It can be written in the form

$$H_{NZ} = g_n \beta_n \mathbf{I} \cdot \mathbf{B} \quad [2.25]$$

where g_n is the nuclear g factor and β_n is the nuclear Bohr magneton

H_Q is the quadrupole term and describes the interaction of the nuclear spin, \mathbf{I} , with the electric field. It can be written in the form

$$H_Q = \mathbf{I} \cdot \mathbf{P} \cdot \mathbf{I} \quad [2.26]$$

where \mathbf{P} is the quadrupole interaction matrix and \mathbf{I} is the nuclear spin vector. The \mathbf{P} matrix is usually given in terms of its principal components, P_1 , P_2 and P_3 .

$$\mathbf{P} = \begin{bmatrix} P_1 & & \\ & P_2 & \\ & & P_3 \end{bmatrix} \quad [2.27]$$

The quadrupole interaction is often small in comparison with the other interactions and is poorly resolved in EPR spectra. It is often assumed to be adequately described by a single parameter, q .

$$P_{11} = P_{33} = 2q \quad [2.28]$$

$$P_{12} = P_{13} = P_{23} = -q \quad [2.29]$$

A simple example of a spin system with an electron spin $S = 1/2$ and a nuclear spin $I = 1$ is used as an example to show the relationship between the spin Hamiltonian and the EPR spectrum. The spin Hamiltonian for this system, if we neglect the nuclear Zeeman and quadrupole terms is then given by

$$H = \beta \cdot \mathbf{S} \cdot \mathbf{g} \cdot \mathbf{B} + \mathbf{S} \cdot \mathbf{A} \cdot \mathbf{I} \quad [2.30]$$

Figure 2.2a shows the energy levels of such a system as a function of applied field. The electron Zeeman interaction results in two energy levels, $m_S = +1/2$ and $m_S = -1/2$, which are then split by the hyperfine interaction into three levels, $m_I = 1$, $m_I = 0$ and $m_I = -1$. Transitions occur at magnetic field values where the difference in energy between these levels is equivalent to the microwave energy. For this system there are three allowed transitions which satisfy the selection rule, $\Delta m_S = 1$, $\Delta m_I = 0$.

The P1 EPR centre in diamond has been shown to be a substitutional nitrogen defect.² The main features of the EPR spectrum of this defect can be explained with equation 2.30. The electron Zeeman interaction has little anisotropy and can be described with an isotropic g value of 2.0024, close to the free electron value. The hyperfine interaction is axial about a $\langle 111 \rangle$ direction in the crystal. The hyperfine parameters are $A_{\parallel} = 114.034$ MHz and $A_{\perp} = 81.325$ MHz. The nuclear Zeeman interaction is much smaller than the hyperfine interaction and can be ignored in this treatment. There are also four distinct, magnetically inequivalent sites, for this defect in the lattice aligned along

the four possible $\langle 111 \rangle$ axes. For a given orientation of the magnetic field there will then be four different EPR spectra. When the magnetic field is aligned with a $\langle 100 \rangle$ axis each of the sites will be equivalent. The EPR spectrum of the P1 centre in Figure 2.2b with the magnetic field in different orientations in a $\{110\}$ plane. In this plane two of the sites are equivalent and therefore three different spectra with three lines are seen.

The information that is obtained from the EPR spectrum of this centre can be summarised. The electron spin of the centre is $1/2$, and the nuclear spin is 1 , which indicates the involvement of a ^{14}N nucleus, one of the few nuclei with this spin number. The defect has symmetry about a $\langle 111 \rangle$ axis and the hyperfine interaction is axial. This information can be used to provide the structural model of the defect although details of the nitrogen quadrupole interactions and superhyperfine interactions with neighbouring ^{13}C nuclei are needed for more accuracy.

2.3 Multiple Resonance Techniques

2.3.1 ENDOR

A schematic explanation of ENDOR spectroscopy is shown in Figure 2.3. The four energy levels in an $S = 1/2, I = 1/2$ system with equilibrium populations determined by Boltzmann statistics are shown in Figure 2.3a. The population of two of the levels is driven away from equilibrium when an EPR transition is induced. If the microwave power is sufficiently strong the transition will be saturated and the population of the two levels will become equal. If an NMR transition in one of the electron spin manifolds is induced then the EPR transition can be desaturated with a subsequent increase in the EPR absorption.

In ENDOR experiments the magnetic field is set so that one of the EPR transitions is on resonance and the frequency of the second radiation is then scanned.

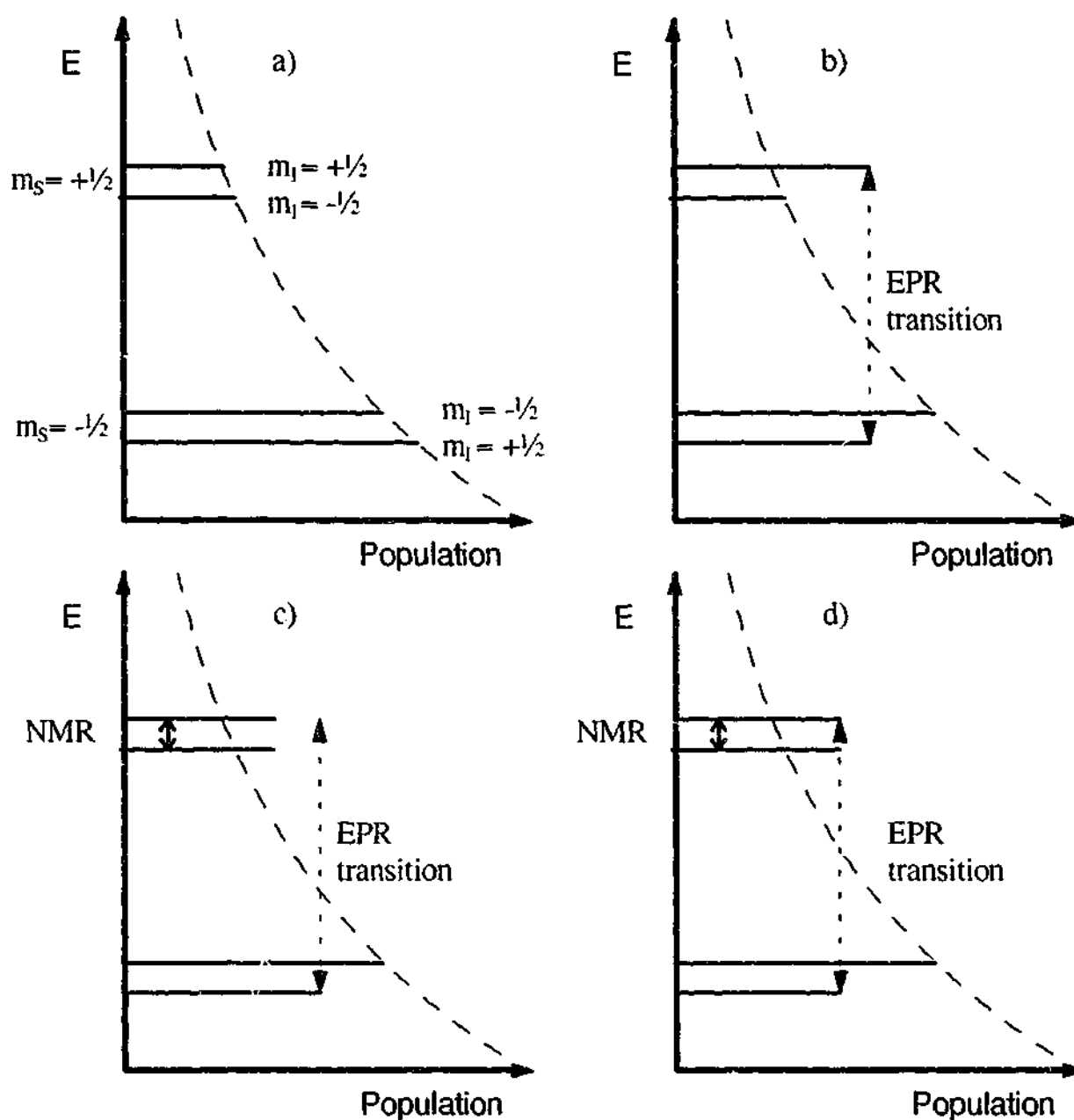


Figure 2.3 Schematic representation of ENDOR after Spach (1992).³ a) Energy level scheme for a $S = 1/2$, $I = 1/2$ system. The dashed line shows the Boltzmann distribution governing the equilibrium population of the energy levels. b) Populations of the energy levels under a saturating EPR transition between energy levels from different electron spin manifolds. c) The initial effect of an additional NMR transition between levels in the same electron spin manifold. d) The population of the three energy levels connected by the EPR and NMR transitions are almost equalised.

When this frequency is equal to that of an NMR transitions there will be a change in the EPR signal.

Particularly in cases where a number of nuclei are interacting with the electron spin the ENDOR spectra are easier to interpret than the EPR spectra. ENDOR can also measure small hyperfine, nuclear Zeeman and quadrupole interactions that are unresolved in EPR. A first order approximation for axial symmetry gives the ENDOR frequencies.

$$f_{ENDOR} = \frac{1}{h} m_s \left\{ a + b \left[3 \cos^2(\theta_A) - 1 \right] \right\} - g_n \beta_n B_0 + m_q 3q \left[3 \cos^2(\theta_Q) - 1 \right] \quad [2.31]$$

where m_s is the electron quantum number, a and b are the isotropic and anisotropic parts of the hyperfine interaction, m_q is the average of the two nuclear quantum states, m_I and m_I' , involved in the transition, q is the quadrupole parameter and θ_A and θ_Q are the angle between the static magnetic field and the principal axes of the hyperfine and quadrupole interactions respectively.

It is also possible to simplify EPR spectra using a technique termed ENDOR induced EPR (EI-EPR). In this technique the radio frequency is kept on resonance with one of the nuclear transitions and the magnetic field is swept. Only the EPR transitions that are connected with the levels in the nuclear transition will appear in this spectrum. In this way overlapping EPR spectra can be separated and complicated spectra with several electron and nuclear transitions can be simplified.

2.3.2 ODMR

Optically detected EPR is another multiple resonance technique. The EPR spectrum is measured from an optical transition that is connected with the energy levels in the EPR transitions. One of the major advantages of ODMR is the greater sensitivity associated with the optical transitions. ODMR also allows a high degree of selectivity in that only EPR transitions that share energy levels with the optical transition will be detected. In this way different EPR centres that have the same field range can be separated. It also allows the direct correlation between optical and EPR spectra. Optical spectroscopy is often more sensitive than EPR but cannot provide the same amount of structural information. It is therefore useful to be able to correlate the two.

The particular experimental method that will be discussed here and used in the experimental part of the thesis is magnetic circular dichroism absorption (MCDA)

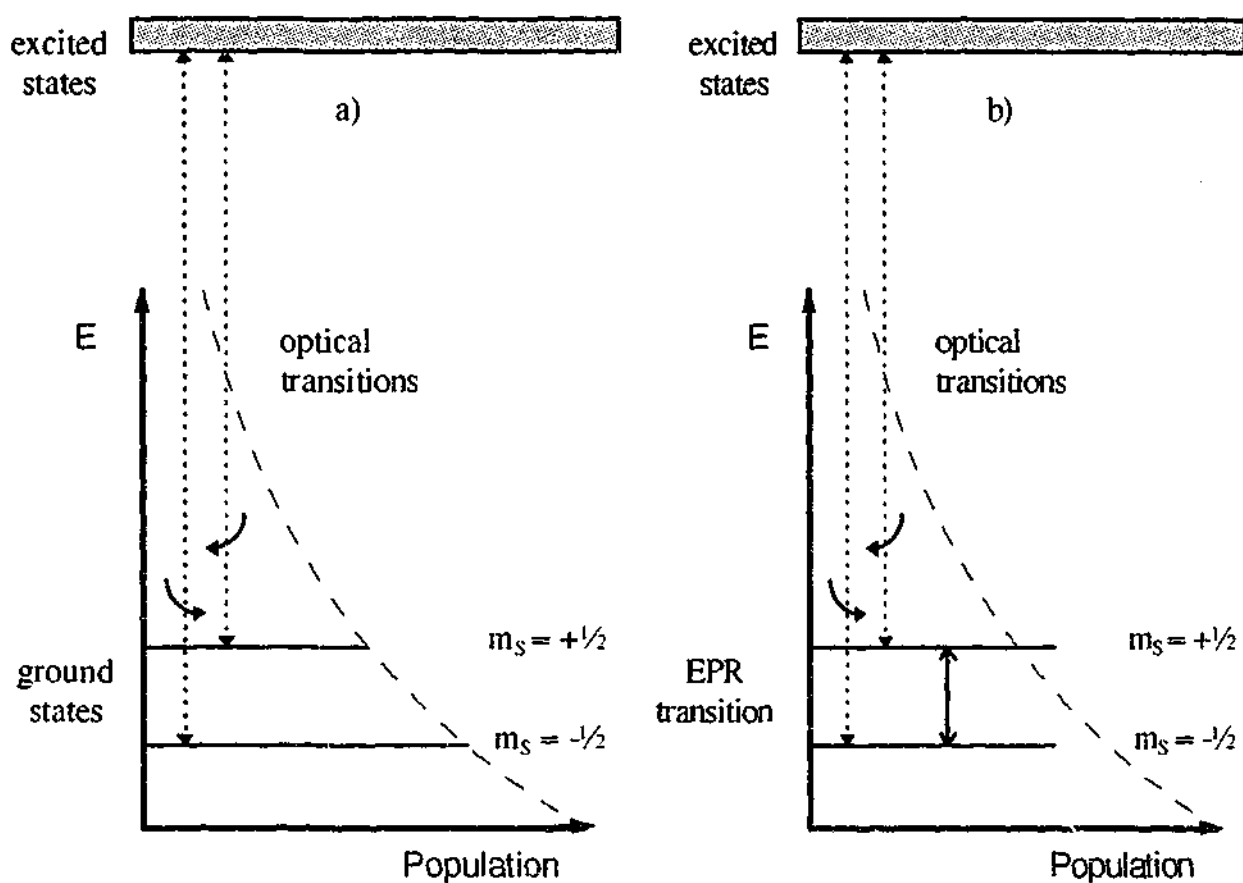


Figure 2.4 Schematic explanation of ODMR. a) Energy level diagram for a system with a ground state Kramers doublet. Two optical transitions from each of the $m_s = \pm 1/2$ states to excited states are shown with opposite circular polarisation. b) The effect of an EPR transition on the population of the $m_s = \pm 1/2$ states.

detected EPR. MCDA is the preferential absorption of right and left polarised light, where the light is propagating along the direction of an applied magnetic field. The measure of MCDA can be defined as

$$\epsilon = \frac{I_r - I_l}{2(I_r + I_l)} \quad [2.32]$$

where I_r and I_l are the transmitted intensities of light passing through the sample with right and left polarisations.

The MCDA arises from the electron Zeeman splitting of the ground state. This is shown in Figure 2.4 for a system with an $S = 1/2$ ground state. The optical absorption from the two different m_s levels can have different polarisations and the proportion of each will depend on the population of the energy levels. The population difference between these levels is determined by the magnetic field and temperature. If an EPR

transition between the two energy levels is induced then the population difference and the MCDA signal will be reduced. In MCDA detected EPR experiments, the MCDA of an optical transition is monitored as the magnetic field is swept through the EPR resonances.

2.4 Pulsed EPR Techniques

Pulsed EPR opens up a new range of experiments that, under certain conditions, offer better resolution, sensitivity and selectivity than continuous wave methods. In contrast to NMR where pulsed techniques focus on the free induction decay (FID), pulsed EPR generally uses the refocussed FID or echo.

The echo phenomenon can best be conceptualised by considering an inhomogeneously broadened line as consisting of a series of non-interacting spin packets. When a static magnetic field is applied each of these spin packets will experience a slightly different magnetic field. The motion of the magnetisation of each of these independent spin packets can then be described by the well known Bloch equations.

$$\frac{d\mathbf{M}}{dt} = -\gamma \mathbf{B} \times \mathbf{M} \quad [2.33]$$

The solution of this equation describes a precession of the magnetisation about the direction of the field vector. The frequency of this precession, the Larmor frequency, for each spin packet is then given by the equation.

$$\omega_j = \gamma B_j \quad [2.34]$$

where B_j is the local field experienced by the spin packet. For a given distribution in the magnetic field there is therefore a corresponding distribution in the Larmor frequencies of the spin packets.

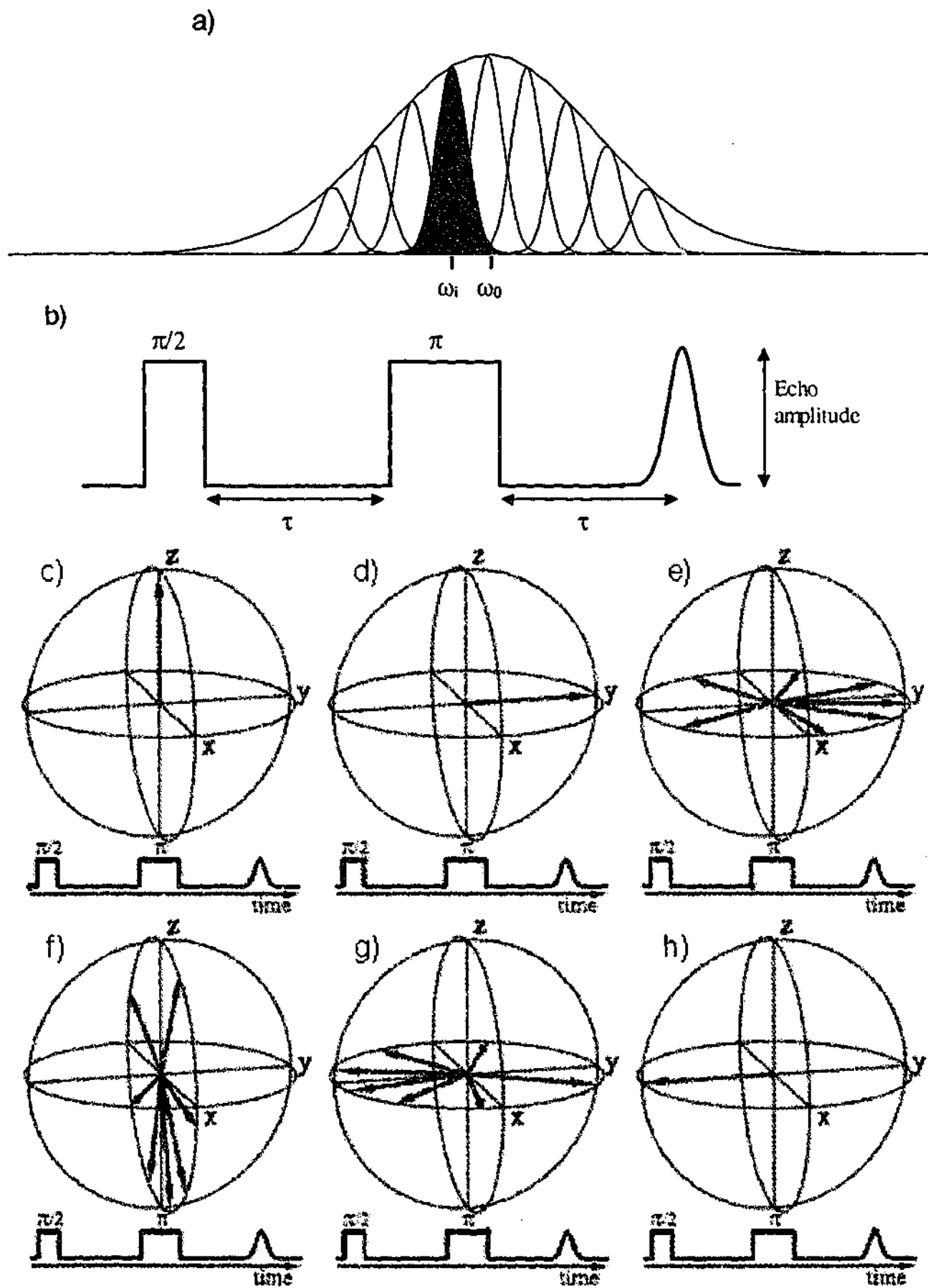


Figure 2.5 Explanation of echo phenomena. a) Initial net magnetisation in the z direction. b) First $\pi/2$ pulse flips magnetisation into the x-y plane. c-d) magnetisation dephases in the first free evolution period τ . e-f) π pulse flips magnetisation through 180 degrees about the x axis. g-h) magnetisation refocusses in the -y direction at time τ after the second pulse.⁴

Each of the spin packets in the inhomogeneously broadened line will precess about the axis of the field vector at different frequencies. The relative phases of the spin packets in the plane perpendicular to the magnetic field in the steady state will be random and hence only a resultant magnetisation in the direction of the magnetic field will be seen.

The interaction with the microwave radiation is most simply described in the rotating frame. If we consider the static field as defined along the z direction and the oscillating magnetic field of the microwave polarised in the x-y plane then in the rotating frame we now rotate about the z direction at the microwave frequency.

In this rotating frame the precession frequency of the spin packets is reduced by the microwave frequency. The precession of the j^{th} spin packet in the rotating frame is then $\omega'_j = \gamma B_j - \omega_{mv}$, where ω_{mv} is the microwave frequency. The magnetic field due to the microwave radiation is now seen to be constant in direction in the rotating frame and for convenience we can define this direction as the x' direction.

If a microwave pulse is applied then the magnetisation of the spin packets will be seen to precess about an 'effective' field vector in the rotating frame. If the microwave pulse is sufficiently strong then we can take this precession to occur about the x' direction with a frequency $\omega_1 = \gamma B_1$, where B_1 is the strength of the microwave magnetic field. If a pulse of the correct duration is applied it is possible to rotate the steady state magnetisation, originally along the z direction, 90° so that it now lies in the y' direction. The spin packets then precess at their individual Larmor frequencies about the z direction. As a result of the spread in these frequencies the spin packets quickly become out of phase with each other and the observable magnetisation disappears. This decay is termed the free induction decay.

The beauty of the echo phenomenon can be seen when a second pulse is applied. This pulse is of twice the duration of the first and rotates the spin packets 180° about the x' axis. After this pulse the position of the spin packets is such that after another period of free precession the spin packets will again come back into phase. This will be seen as an echo of the original magnetisation immediately after the first pulse. This is shown graphically in Figure 2.5.

This can also be expressed in equations for the magnetisation of the spin system during and after the pulse sequence. The transverse magnetisation after this pulse sequence of a $\pi/2$ pulse followed by a π pulse can then be described by the equation.⁴

$$M_+ = -\sum_j M_{o,j} \exp(i\omega_j t) \quad [2.35]$$

where $M_{o,j}$ is the steady state magnetisation of the j^{th} spin packet. It can be seen from this equation that the transverse magnetisation after the second pulse is the Fourier transform of the line shape defined by the $M_{o,j}$ distribution.

The refocussed magnetisation is also reduced by relaxation processes. These can be spin-lattice relaxation and also spin-spin relaxation between the electron spin and other spins. The spin-spin relaxation is characterised by a time, T_2 . T_2 is generally much shorter than T_1 in solids and determines the decay for a two pulse echo.

The electron spin echo can be used in Fourier transform EPR to obtain similar information to that from cw EPR. In practice, however, the linewidths in EPR are often large and the bandwidths of the microwave pulses small and hence only parts of the EPR spectrum are involved in the electron spin echo at a given magnetic field. Instead, the spectra in pulsed EPR are measured by monitoring the amplitude of the echo as a function of parameters in the pulse sequence.

Four examples of different types of pulsed EPR experiments are now described. Each of them offers different information and is applicable in a different range of investigations.

2.4.1 Nutation spectroscopy

In the previous treatment of the electron spin echo idealised microwave pulses were assumed that instantaneously flipped all spins through exactly 90° or 180° . The motion of the magnetisation during the microwave pulses is of course more complicated. This motion, or nutation, can be used in a different type of spectroscopy to obtain information about the spin system.

The simplest case to deal with is an $S = 1/2$ system with an isotropic g -matrix. The spin Hamiltonian in the laboratory frame during the microwave pulse can then be written as⁵

$$H(t) = \omega_s S_z + 2 \cos(\omega_{mw} t) \omega_1 S_x \quad [2.36]$$

$$\omega_s = g\beta B_0 / \hbar \quad [2.37]$$

$$\omega_1 = g\beta B_1 / \hbar \quad [2.38]$$

The linearly polarised oscillating magnetic field can be thought of as two counter-rotating circularly polarised oscillating fields.

$$H(t) = \omega_s S_z + \cos(\omega_{mw} t) \omega_1 S_x + \sin(\omega_{mw} t) \omega_1 S_y + \cos(\omega_{mw} t) \omega_1 S_x - \sin(\omega_{mw} t) \omega_1 S_y \quad [2.39]$$

Transformation to the rotating frame, and ignoring one of the circularly polarised components, gives a time independent spin Hamiltonian.

$$H' = \Omega_s S_z + \omega_1 S_x \quad [2.40]$$

$$\Omega_s = \omega_s - \omega_{mw} \quad [2.41]$$

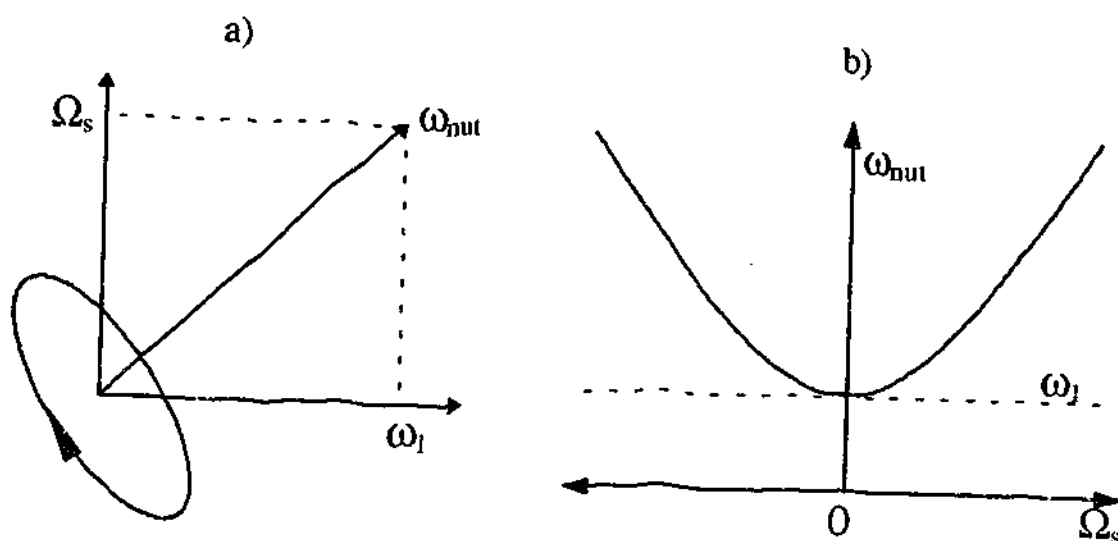


Figure 2.6 a) The nutation frequency is determined by the vector sum of the resonance offset frequency, Ω_s , and ω_1 . b) The nutation frequency is a minimum when the transition is on-resonance.

The nutation frequency of the spin about a direction θ from the x direction in the rotating frame is given by the equation.

$$\omega_{nut} = \sqrt{\Omega_s^2 + \omega_1^2} \quad [2.42]$$

$$\tan(\theta) = \frac{\omega_1}{\Omega_s} \quad [2.43]$$

In this trivial example little information is obtained from the nutation spectrum. We can generalise the treatment to a spin system with axial g values by replacing equation 2.38 with

$$\omega_1 = 2\pi g_1 \beta B_1 / h \quad [2.44]$$

where

$$g_1 = \sqrt{\left(\frac{g_{\perp} g_{\parallel}}{g}\right)^2 \cos^2 \alpha + g_{\perp}^2 \sin^2 \alpha} \quad [2.45]$$

$$g = \sqrt{g_{\parallel}^2 \cos^2 \theta + g_{\perp}^2 \sin^2 \theta} \quad [2.46]$$

and θ is the orientation of the magnetic field with respect to the principal direction of the g matrix and α is the orientation of the B_1 field in the plane perpendicular to the static

magnetic field. It can be seen that g value information can be obtained at a single field orientation.

In high spin systems with $S > 1/2$, a large zero field splitting, and isotropic g matrix the nutation frequencies are determined by the equation.

$$\omega_1 = \frac{2\pi g\beta B_1}{h} \sqrt{S(S+1) - m_s(m_s + 1)} \quad [2.47]$$

The nutation frequency will therefore depend on both the individual transition and the electron spin, S. Overlapping transitions from different m_s levels can be separated and the electron spin can be determined.⁶

In general, the nutation frequency is proportional to the square root of the transition probability. In the case where there are "allowed" and "forbidden" transitions nutation spectra therefore provide an ability to separate overlapping transitions.

2.4.2 ESEEM

If the echo amplitude in a primary echo sequence is measured as a function of the interpulse spacing, τ , then in addition to a decay function determined by T_2 there can also be a sinusoidal modulation. The electron spin echo envelope modulation (ESEEM) results from the hyperfine interaction of the electron spin with neighbouring nuclei. It can occur when both the excited and allowed transitions are excited by the pulses. The different transitions lead to terms in the density matrix that evolve during the free evolution period in the pulse sequence and interfere with each other. The modulation frequencies are related to the NMR frequencies and can therefore be used to obtain this information. Like ENDOR, ESEEM can also resolve smaller interactions that are unresolved in cw EPR. It also has the advantage that different pulse sequences can be used that selectively monitor different interactions in the Hamiltonian.

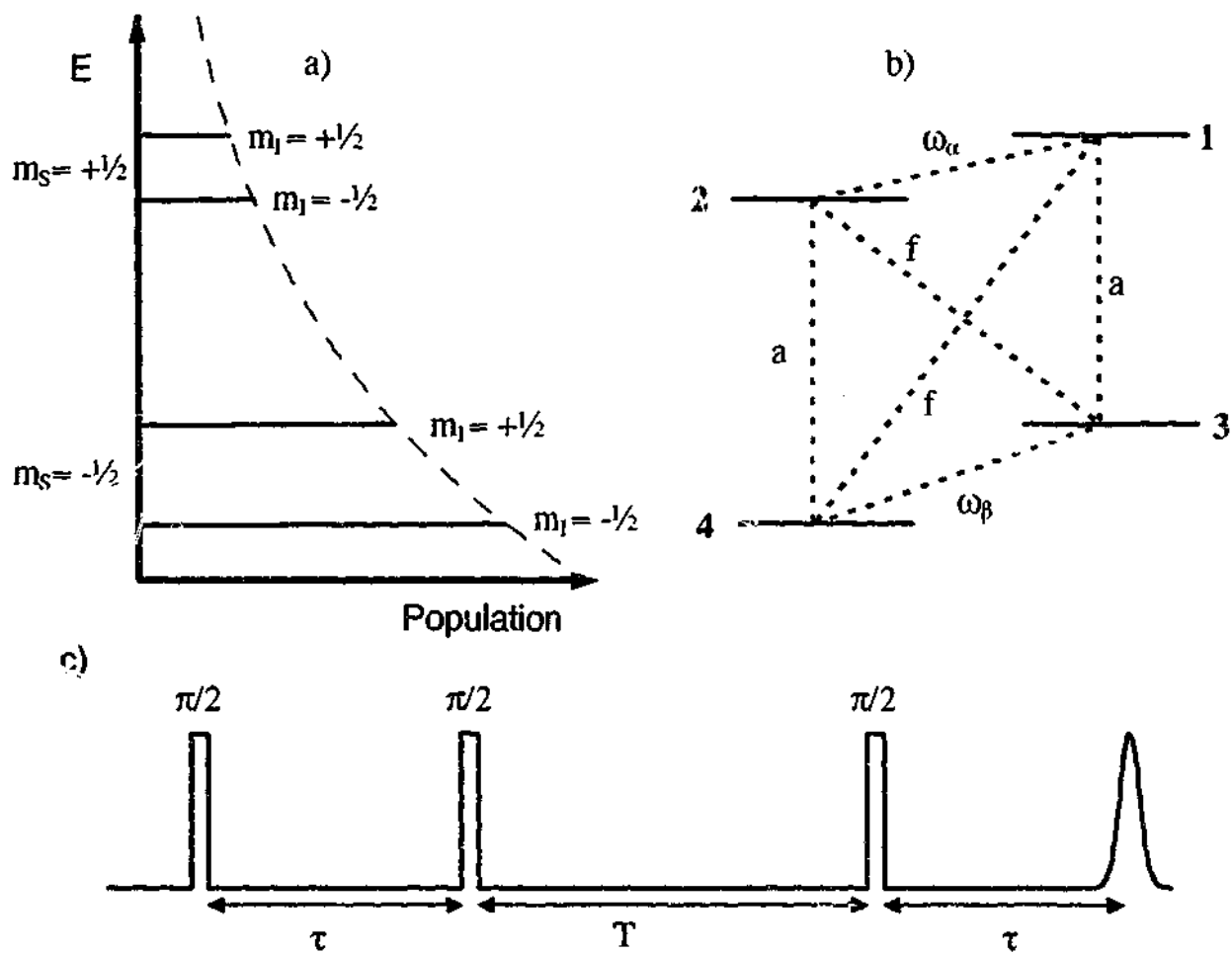


Figure 2.7 a) Energy levels in an ESEEM experiment. b) Transitions between the four energy levels. c) The three pulse stimulated echo sequence.

ESEEM experiments, although general for all spin systems, are normally explained in terms of a simple spin system, $S = 1/2$, $I = 1/2$, with an isotropic g matrix and an axial hyperfine interaction. After transformation to the rotating frame the Hamiltonian is given by the equation⁷

$$H = \Omega_s S_z - \omega_I I_z + A S_z I_z + B S_z I_x \quad [2.48]$$

where Ω_s is the offset of the electron Zeeman frequency ω_s from the microwave frequency ω_{mw} , and ω_I is the nuclear Zeeman frequency.

$$\Omega_s = \omega_s - \omega_{mw} \quad [2.49]$$

$$\omega_s = g\beta B_0/\hbar \quad [2.50]$$

$$\omega_I = g_n \beta_n B_0/\hbar \quad [2.51]$$

A and B are related to the parallel and perpendicular hyperfine parameters, $A_{||}$ and A_{\perp} by

$$A = A_{//} \cos^2 \theta + A_{\perp} \sin^2 \theta \quad [2.52]$$

$$B = (A_{//} - A_{\perp}) \sin \theta \cos \theta \quad [2.53]$$

where θ is the angle between the static magnetic field and the principal axis of the hyperfine interaction. The energy levels in such a spin system are shown in Figure 2.7.

The echo amplitude in a two pulse echo sequence as a function of the pulse separation, τ , has been evaluated with density matrix formalism.⁷

$$V_2(\tau) = 1 - \frac{k}{2} [2 - 2\cos(\omega_{\alpha}\tau) - 2\cos(\omega_{\beta}\tau) + \cos(\omega_{+}\tau) + \cos(\omega_{-}\tau)] \quad [2.54]$$

where ω_{α} and ω_{β} are the nuclear transitions in the $m_s = +1/2$ and $m_s = -1/2$ electron spin manifolds and ω_{+} and ω_{-} are the sum and difference of these two frequencies.

$$\omega_{\alpha} = \sqrt{(A/2 - \omega_I)^2 - (B/2)^2} \quad [2.55]$$

$$\omega_{\beta} = \sqrt{(A/2 + \omega_I)^2 - (B/2)^2} \quad [2.56]$$

$$\omega^{+} = \omega_{\alpha} + \omega_{\beta} \quad [2.57]$$

$$\omega^{-} = \omega_{\alpha} - \omega_{\beta} \quad [2.58]$$

$$k = \left(\frac{\omega_I B}{\omega_{\alpha} \omega_{\beta}} \right)^2 \quad [2.59]$$

and k is the modulation depth parameter. It can be seen from equations 2.53 and 2.59 that if the hyperfine interaction is isotropic, $A_{//} = A_{\perp}$, or the magnetic field is along a principal direction of the hyperfine interaction, $\theta = 0^\circ$ or $\theta = 90^\circ$, then the modulation depth will be zero.

A similar expression, equation 2.60, is obtained for three pulse ESEEM.⁷ The echo modulation in this experiment contains only the nuclear frequencies, ω_{α} and ω_{β} , without the sum and difference frequencies, ω_{+} and ω_{-} , which means that these spectra are normally easier to interpret than two pulse ESEEM spectra. The echo modulation is also

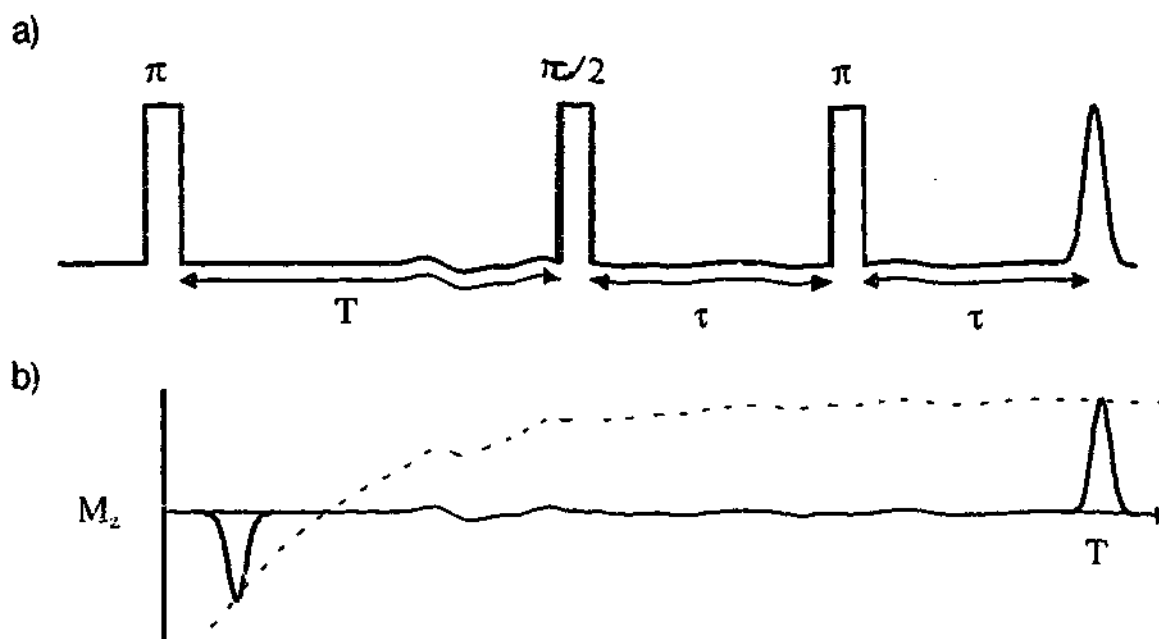


Figure 2.8 The inversion recovery experiment. a) The pulse sequence consists of a π "inversion" pulse followed by a time T by a primary echo sequence. b) The primary echo amplitude plotted as a function of T , the separation between the inversion pulse and the second pulse in the sequence.

generally longer in the three pulse experiment, leading to better resolution. However, the factors, $\cos(\omega_a \tau)$ and $\cos(\omega_p \tau)$ can lead to "blind spots" in the spectrum where the amplitude of the modulation is zero for certain τ values.

$$V_s(\tau) = 1 - \frac{k}{4} \{ [1 - \cos(\omega_a \tau)] [1 - \cos(\omega_p(\tau + T))] + [1 - \cos(\omega_p \tau)] [1 - \cos(\omega_a(\tau + T))] \} \quad [2.60]$$

2.4.3 Relaxation Experiments

There are also a set of experiments whereby relaxation times can be determined. T_1 can be measured in an inversion recovery sequence. In this sequence, Figure 2.8, an initial π pulse flips the magnetisation to the $-x$ direction. The magnetisation then returns to the equilibrium value with an exponential recovery. A primary echo sequence then measures the magnetisation at different time intervals after the inversion pulse. If the echo amplitude is measured as a function of T , the separation between the inversion pulse and the second pulse, then a curve is obtained that can be fitted with an exponential recovery determined by T_1 .

2.4.4 Echo Detected EPR.

Each of the pulsed experiments described above, nutation, ESEEM and relaxation experiments, provide an extra dimension that is not available in the classic cw experiment. Information about the transition probabilities, unresolved hyperfine splittings and relaxation times can then be obtained. Another option is to record field swept spectra using the echo as a detection mechanism.

Echo detected EPR (EDEPR) can provide the same information as cw EPR and in some cases can have better resolution and sensitivity. However, it is often stated that EDEPR gives a spectrum that is equivalent to the cw-EPR spectrum. Whilst this may be true for simple spin systems it is not the case for many experimental systems.

Firstly, for EDEPR experiments the bandwidth of the excitation pulses should be much smaller than the linewidth of the observed transition. Otherwise the features in the EDEPR spectrum are broadened by the bandwidth of the pulses. It is not always possible to achieve this condition but the problem can be overcome by either using an integrating detector or Fourier transforming the time domain signal.⁸

In addition, a variety of effects can on the one hand lend themselves to experiments that selectively isolate overlapping transitions or totally distort the spectra. Each of the three pulsed EPR techniques that has been described above will affect the intensity of the echo-detected EPR spectrum.

If relaxation times vary across an EPR spectrum then the echo-detected spectrum will be distorted and can be very different from the cw EPR spectrum. This is because the echo amplitude for a given pulse separation, τ , is strongly dependent on the relaxation times. This can be used to advantage if spectra from two species with different relaxation times overlap and cannot be resolved in cw EPR spectra.⁹ The EDEPR spectra

recorded with different τ values will then have different proportions of the two signals, and, with some processing, the spectra of the two species can be isolated.

Nutation frequencies can also dramatically affect EDEPR spectra. This is particularly true in highly anisotropic spectra. If either large zero field splittings or g-value anisotropy are present then the nutation frequencies will vary across the spectrum. The turn angle experienced by one part of the spectrum will be different from that at another and hence the echo amplitude will vary. This can be used to advantage when overlapping transitions have different nutation frequencies.⁵ EDEPR spectra recorded with different pulse lengths, optimised for each of the transitions, can then separate the different signals.

It can also be seen that the nuclear modulation frequencies can also vary throughout a spectrum. If the modulation depth is sufficiently deep then the EDEPR spectra can be distorted.¹⁰ A particularly extreme example of this effect is shown in Figure 2.9. The cw EPR spectrum of Ce^{3+} doped in a fluoride glass shows a broad featureless line starting at approximately 200 mT and going up to high fields, beyond the range of the spectrometer. The EDEPR spectrum of the same sample shows an apparent series of peaks in the same magnetic field region which are in fact due to nuclear modulation. The modulation arises from weak hyperfine coupling to the ^{19}F nuclei in the glass. In the case of weak coupling the modulation frequencies reduce to

$$\omega_a \approx \omega_b \approx \omega_l \quad [2.61]$$

$$\omega^+ \approx 2\omega_l \quad [2.62]$$

$$\omega^- \approx 0 \quad [2.63]$$

As the Larmor frequency is directly proportional to the applied field we can see from equation 2.54 that for a constant τ value the field-swept echo-detected EPR

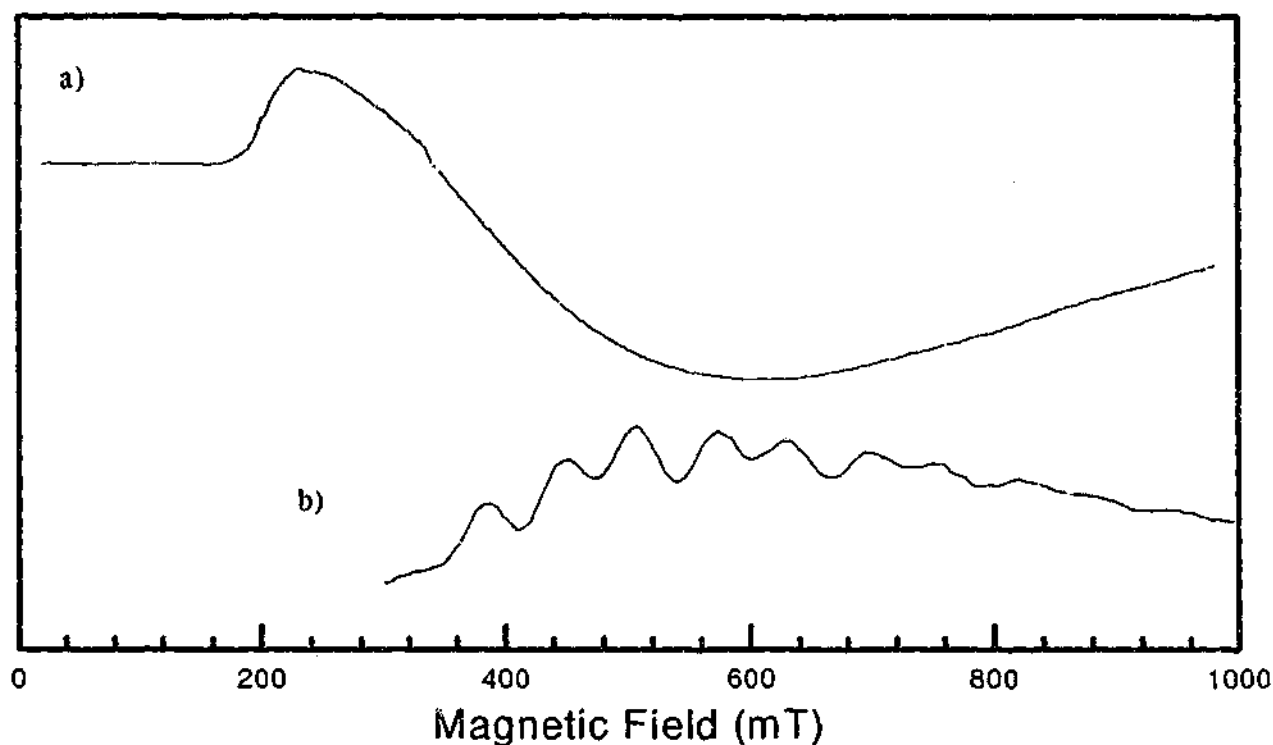


Figure 2.9 The effects of nuclear modulation on echo detected EPR. a) Cw EPR spectrum of Ce^{3+} in a fluoride glass. b) Two pulse echo detected EPR of the same sample with τ value of 400 ns. The modulation in the echo detected spectrum that is not in the cw spectrum is caused by the nuclear modulation from the $I = 1/2$, ^{19}F nuclei in the glass. c) Two pulse ESEEM recorded as a function of magnetic field. The dominant frequency is that of the ^{19}F Larmor frequency. d) When the echo detected spectrum is Fourier transformed a time domain spectrum is obtained containing the delay times of the pulse sequence.

spectrum will be modulated. This modulation will change when the τ value in the pulse sequence is altered and in fact if the field domain spectrum is transformed to the Larmor frequency of the ^{19}F nuclei and then Fourier transformed, a time domain spectrum with a peak at τ is obtained.

It is apparent then, that pulsed EPR spectra can have more information content than cw EPR spectra. This is an advantage in studying many systems where cw-EPR cannot resolve features or where many transitions overlap. It is also apparent that many difficulties are present in obtaining an EDEPR spectrum such that spectra are distorted or unobtainable. In general, it is most beneficial to record a two dimensional spectrum with field as one axis and nutation, relaxation or ESEEM as the other.

2.5 Choice of Technique

With EPR, as with any other spectroscopic technique, the ultimate goal is the acquisition of useful information about the material. In comparison with other forms of spectroscopy there is a large scope for modifying EPR experiments to investigate different interactions of the electron spins and reveal a wide range of information about the material. This is especially true of pulsed techniques, where the pulse sequence can be modified to selectively monitor specific interactions in the spin Hamiltonian.

The pulsed methods outlined in this chapter have been little used in the following experimental chapters. In most cases this has been due to the fact that no echo or FID was observed from either too short relaxation times, low spin concentration or a combination of both. In several cases pulsed techniques could have yielded useful information. In chapter 5 ESEEM would have been applicable to the characterisation of the newly observed EPR centre but as the relaxation times of this centre were too short no echo was observed. In chapters 7 and 8 the use of pulsed techniques would have allowed the direct measurement of relaxation times. However, the relaxation times of these systems was much shorter than the deadtime of pulsed EPR spectrometers and therefore the investigations were restricted to the analysis of the cw lineshape. In other cases the EPR centres had been well characterised by cw EPR and ENDOR and little was to be gained. The exception in this thesis is the investigation of the Jahn-Teller system in caesium titanium alum. This study highlighted the ability of pulsed EPR techniques to yield information that is not obtainable with cw methods

In the work that is presented in this thesis the techniques used were determined by the samples and the information that was needed. In many cases cw EPR was the most useful or the only technique that was used. In other cases ENDOR and ODMR

were successfully used. EPR was also most useful when used in conjunction with other methods such as optical absorption and FTIR spectroscopies.

2.6 References

-
- ¹ Abragam, and Bleaney, B. *Electron Paramagnetic Resonance of Transition Ions*, Clarendon, (1970).
 - ² Smith, W.V., Sorokin, P.P., Gelles, I.L. and Lasher, G.J., *Physical Review*, **115**, (1959), 1546
 - ³ Spaeth, J.-M., Niklas, J.R. and Bartram, R.H., *Structural Analysis of Point Defects in Solids*, Spinger-Verlag, (1992).
 - ⁴ Mims, W.B., *Electron Spin Echoes*, in *Electron Paramagnetic Resonance*, ed S. Geschwind, Bell Telephone Laboratories, Murray Hill, New Jersey.
 - ⁵ Astashkin, A., and Schweiger, A., *Chem. Phys. Lett.*, **174**, (1990) 595.
 - ⁶ Astashkin, A., Kodera, Y. and Kawamori, A., *J. Magn. Reson. B*, **105**, (1994) 113.
 - ⁷ Mims, W., *Phys. Rev. B*, **5**, (1972) 2409.
 - ⁸ Noble, C.J., Zhong, Y.C., Pilbrow, J.R. and Hutton, D.R., *J. Magn. Reson. Series A*, **105**, (1993) 323.
 - ⁹ Mehring, M., Seidel, H., Müller, W. and Wegner, G., *Solid State Commun.*, **45**, (1983) 1075.
 - ¹⁰ Goldfarb, D. and Kevan, L., *J. Magn. Reson.*, **76**, (1988) 276.

3. Paramagnetic Defects in Coloured Argyle Diamonds.

3.1 Introduction

Far from being a perfect material, both synthetic and natural diamonds invariably contain defects of one sort or another. These can be structural such as dislocations or vacancies or they can be due to substitutional and interstitial impurities such as nitrogen and boron. These defects modify the properties of the diamond in many ways, not all of them detrimental.

The value of natural diamonds is determined to a large extent by their colour. Traditionally clear diamonds with no colour have been highly prized. Any increase in colouration decreases the value of the stone. However, diamonds with intense colouration are also highly valued. So called "Fancy" diamonds can be blue, yellow, green, red and pink.¹ The colour of a diamond is in turn determined by the defects that it contains. For example the incorporation of boron impurities produce a diamond with a blue colour. Other defects and colours can be produced by irradiation and heat treatment. The market value of artificially coloured diamonds, however, is far less than that of natural diamonds. Much of the research on defects in diamond has therefore been focussed on means of distinguishing synthetically coloured diamonds from natural diamonds.

The most common impurity in diamond is nitrogen. The number of defect centres that involve nitrogen is quite large. These defects have been well studied using optical and magnetic resonance techniques. The study of nitrogen centres in diamond has been recently reviewed by Newton and Baker². A brief introduction will be given here.

In natural diamond the nitrogen is generally present in four different forms. Two of these, labelled P1 and P2, are paramagnetic and have been studied using EPR and

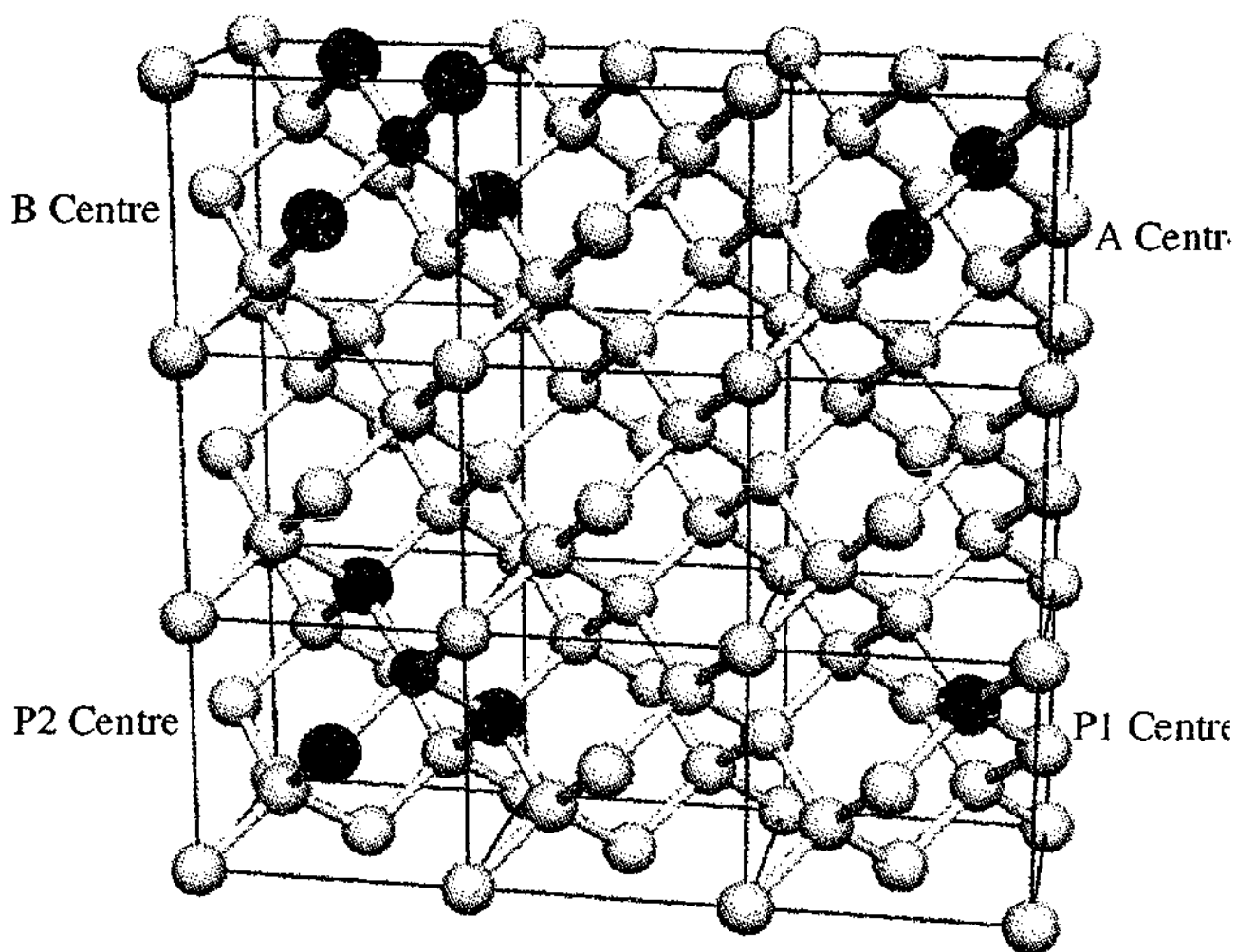


Figure 3.1 Common nitrogen centres in diamond. Four different defects are shown. The B centre consists of four nitrogens tetrahedrally arranged about a vacancy. The A centre consists of two nitrogens in nearest neighbour positions. The P2 centre consists of three nitrogens in a $\{111\}$ plane adjacent to a vacancy. The P1 centre is a single nitrogen in the substitutional position. (Carbon = \circ , Nitrogen = \bullet , Vacancy = \circ)

ENDOR. The structure of these defects is well established with the P1 defect believed to be a single substitutional nitrogen³ and the P2 defect believed to be three nitrogens forming a triangle in a $\{111\}$ plane together with an adjacent vacancy.⁴ The ionised state of P1(N⁻) has also been studied by IR spectroscopy.⁵ The N3 optical spectrum has been correlated with the P2 EPR defect.⁶

The A and B defects are diamagnetic and the structure of these defects have not been established with as much certainty. The defects are observed as characteristic absorptions in the infra-red region below 1332 cm^{-1} . The A centre gives rise to a characteristic FTIR spectrum with a dominant peak at 1282 cm^{-1} .⁷ The A centre is believed to be a pair of nearest neighbour nitrogens. Although the A centre is

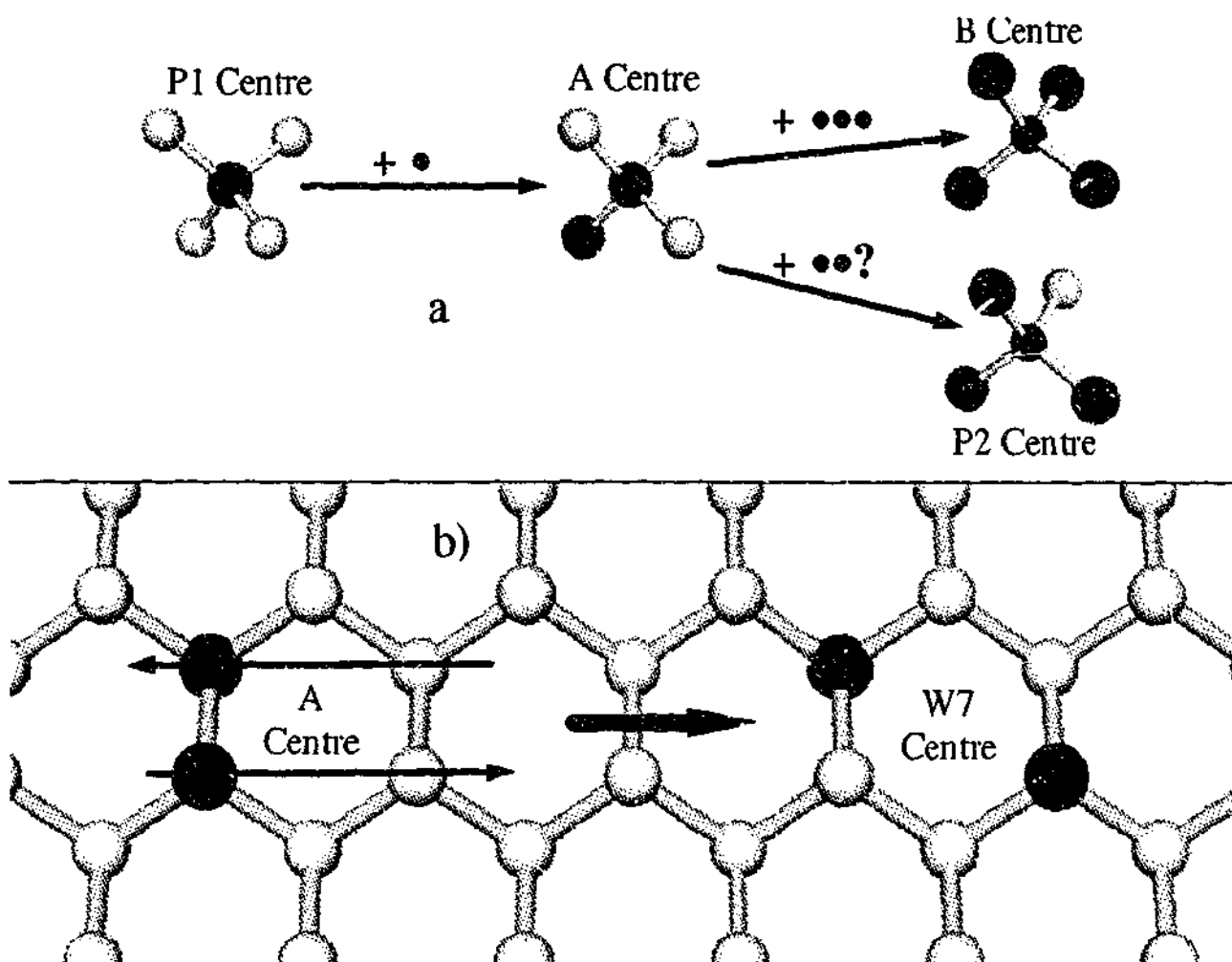


Figure 3.2 Formation of nitrogen centres in diamond. a) aggregation of nitrogen to form A, P2 and B centres. b) plastic deformation converting A centre to W27 centre. (Carbon = \bullet , Nitrogen = \bullet , Vacancy = \bullet)

diamagnetic, and hence no EPR measurements are possible, this assignment is supported by EPR spectra of the W24 centre.^{8,9} The W24 centre is produced by UV irradiation of diamonds containing the A centre and has been shown to be a singly ionised pair of nearest neighbour nitrogens. The W24 centre is not produced by UV irradiation in diamonds that do not contain A centres and is therefore believed to be an ionised A centre.

The B centre gives rise to a characteristic FTIR spectrum with a dominant peak at 1172 cm^{-1} .⁷ The currently accepted model for the B centre is four nitrogens in a tetrahedral arrangement about a vacancy. The assignment of this structure to the B centre has been supported by the EPR spectra of the paramagnetic H4 centre which is produced after electron irradiation and annealing of diamonds that contain the B centre.¹⁰

The structure of the H4 centre has been determined from the EPR spectrum to be a vacancy at a B centre (N₃-V-V-N). Likewise, a similar defect, the H3 centre is thought to be a vacancy trapped at an A centre (N-V-N). A strong correlation exists between the concentration of the H4 centres that is produced and the original concentration of the B centre. Importantly the ratio of H4 to H3 centres produced by irradiation and annealing is found to match the ratio of B to A centres in the untreated diamond. The current models for the P1, P2, A and B defects are shown in Figure 3.1.

Diamonds are categorised into several main types according to the amount and type of nitrogen centres present.¹¹ The first division is into type I, which contains measurable amounts of nitrogen defects, and type II, which has no detectable nitrogen. Type I is then divided into type Ia, which contains nitrogen predominantly in the A and B form, and type Ib where the nitrogen is in the isolated P1 defects. Type Ia can be further divided into type IaA, with more A centres, and type IaB, with more B defects. Diamonds of type II can also be separated into categories on the basis of boron concentration. Type IIa contains no boron and is insulating and colourless. Type IIb which contains boron is semiconducting and blue.

The form of the nitrogen defects has been related to the geological history of the diamonds.¹² The nitrogen aggregates are believed to form with the migration and aggregation of nitrogen in the diamonds under geological conditions of high temperature (~1000 °C) and pressure (~5 GPa) over periods of the order of 1×10^8 years. This is supported by annealing studies in synthetic diamonds. In diamonds immediately after synthesis the nitrogen is present as randomly dispersed isolated P1 impurities. Annealing at high temperatures and pressures leads to the formation of A centres when two P1 centres combine. Further annealing leads to production of B centres. The P2 centre appears to be a by product of the annealing process.

Larger defects are also produced in the aggregation process although it is not known how much nitrogen, if any, they contain. The various models that have been proposed for these defects have been recently reviewed.¹³ The larger defects were first observed in X-ray diffraction studies.¹⁴ and have been termed platelets due to their extended plate like structure in {100} planes. Platelets are also seen in FTIR as a local mode vibration at $\sim 1365 \text{ cm}^{-1}$.¹⁵ The exact wavenumber of the peak absorption was found to depend on the size of the platelet.

The presence of some defects in diamond has been associated with the occurrence of plastic deformation. The N2 centre occurs only in diamonds that also show microstructural evidence of plastic deformation. The EPR spectrum of the N2 centre consists of a single broad line at $g = 2$ with no visible hyperfine structure. ENDOR spectroscopy reveals that the centre does in fact involve nitrogen.¹⁶ The model that has been proposed for this defect is a nitrogen trapped at a dislocation.

The W7 centre is also seen exclusively in plastically deformed diamonds. The structure of this defect, determined from EPR spectra, is two nitrogens on third nearest neighbour substitutional sites. Importantly, not all of the possible 24 orientations of this defect occur in a particular diamond. Shcherbakova et al have proposed a model to explain this observation and connect the formation of this defect with plastic deformation.¹⁷ In this model existing A centres are transformed into a W7 centre by slip in a {111} plane. This is shown in Figure 3.2. The concentration of these defects has been found to correlate with a brown colouration in these plastically deformed diamonds.^{17,18}

The Argyle mine in Western Australia is renowned for the number and quality of coloured diamonds extracted each year. These include browns and pinks and the rarer blues. The cause of these colours is to a large extent still a mystery. The brown Argyle

diamonds and to a lesser degree the pink Argyle diamonds have been found to contain EPR centres related to plastic deformation. The relationship of these EPR centres to the colour is not known. No centres that correlate with the pink colouration have so far been found, although an association with manganese was proposed at one stage¹⁹

The work in this chapter was essentially a survey of these pink and brown Argyle diamonds to identify any defect centres that correlated with their colour and follows an earlier study by Hutton and Troup.²⁰ The major interest was in the pink diamonds which are the rarest and the most valuable of the Argyle diamonds. The brown 'champagne' diamonds are also successfully marketed by Argyle and are of interest. The extremely rare blue Argyle diamonds are described in more detail in a later chapter of this thesis.

3.2 Experimental

The samples used in this investigation were all supplied by Argyle diamonds, courtesy of Mr John Chapman. In all 42 were provided all with an approximate weight of 1-2 carats (0.2-0.4 g), Figure 3.3. These consisted of 10 whites (relatively colourless), 10 browns of various intensities, 7 browns of roughly equal intensity, 7 pinks of various intensities, 6 pinks of roughly equal intensity and two blue diamonds. All diamonds had easily recognisable {111} faces except for the two blue diamonds.

The colour of these diamonds had been graded by eye under standard conditions of lighting. In this system the diamonds labelled P1 - P7 had a pink colour with an intensity ranging from light pink to a deep mauve. The diamonds labelled P5a - P5g had a pink colouration of approximately equal intensity.

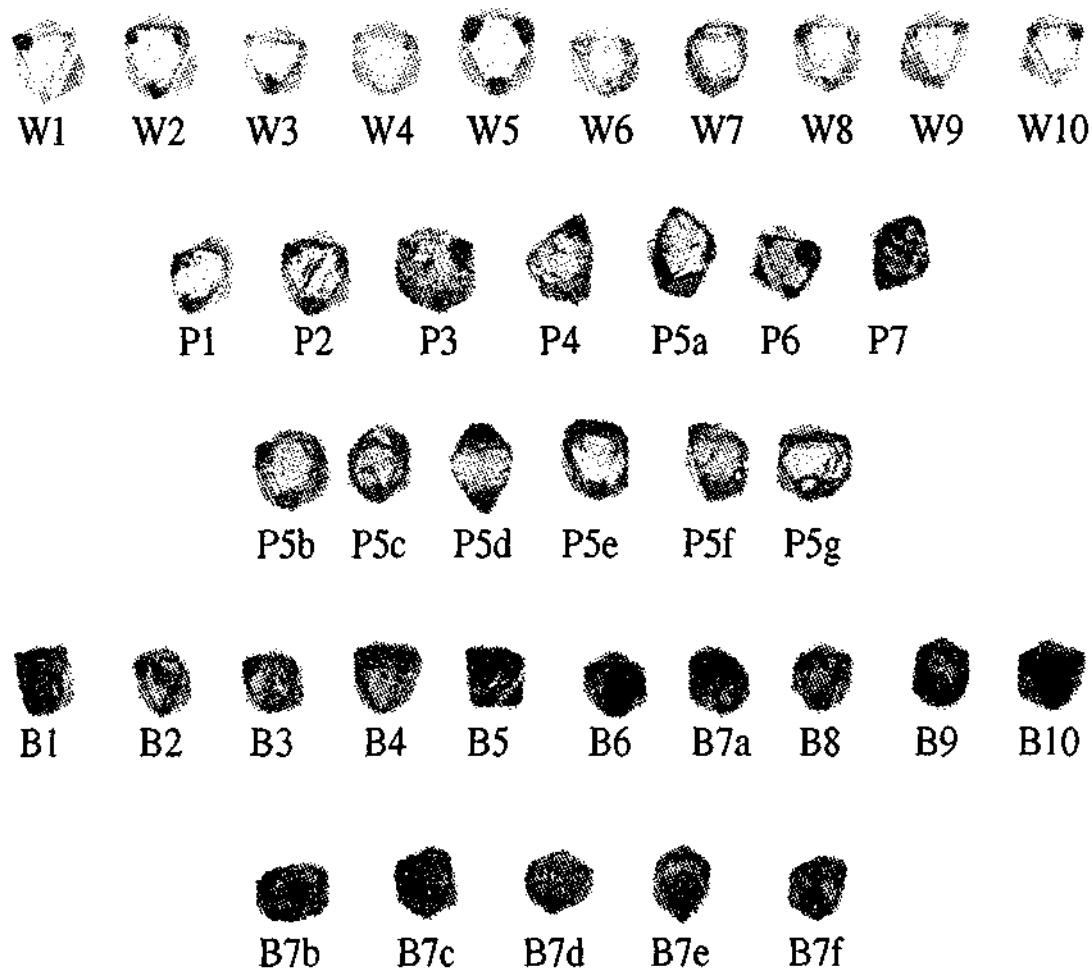


Figure 3.3 Samples used in the thesis. W1-10, clear 'white' diamonds. P1-7, p5a-p5g, graded pink diamonds. B1-10, B7a-b7f, graded brown diamonds. Approximate scale 1.5:1

Although optical absorption spectra of these diamonds were measured it was not possible to directly quantify the colouration for a number of reasons. All stones used in the study were uncut and did not have polished optical faces. The path length through the sample could not be accurately determined due to the irregular shape of the stones and complications of scattering and multiple internal reflections. These stones were on short term loan from Argyle Diamonds and could not be modified for more accurate measurements. After the return of the samples to Argyle Diamonds semi-quantitative estimates of the colouration of the pink diamonds were made based on recorded photographs under standard lighting conditions. These photographs were scanned into digital format and the pink colour was estimated from the red, green and blue values in the image using the equation $p = r/(r+g+b)$.

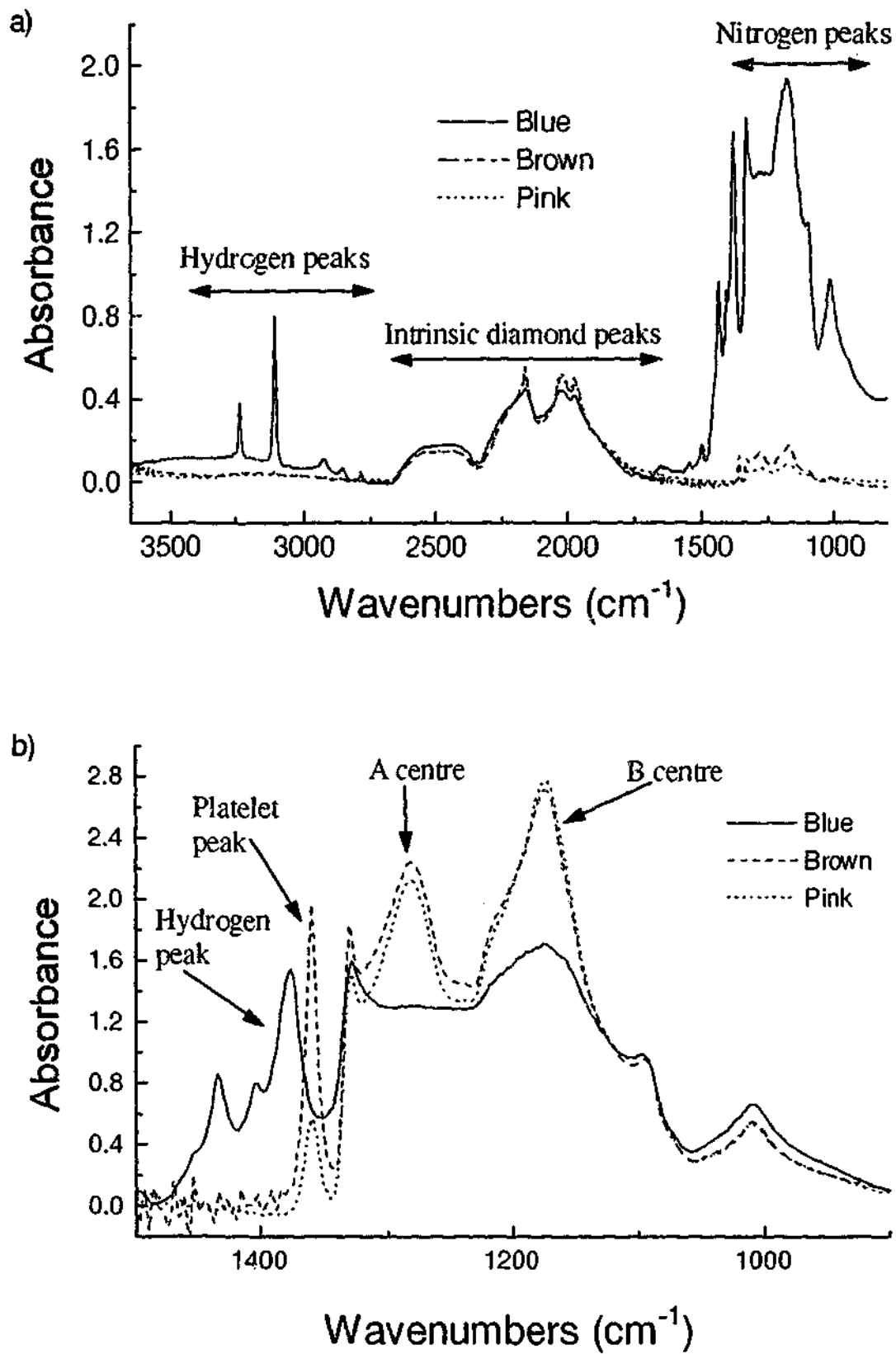


Figure 3.4 FTIR spectra of typical examples of blue, brown and pink Argyle diamonds. a) The spectra have been normalised on the intrinsic diamond absorption in the two phonon region. Notice the large difference in the one phonon region between the blue diamonds and the pink and brown diamonds. b) One phonon region of the FTIR spectra of coloured Argyle diamonds. The spectra have been arbitrarily normalised.

Likewise, the diamonds labelled B1 - B10 had a brown colouration ranging from light brown to almost opaque and the diamonds labelled B7a - B7f were all of approximately the same colour. Estimates of the brown colouration were made by visual inspection of the recorded photographs.

The EPR measurements were obtained using a Bruker ESP380e pulsed/cw EPR spectrometer. The cw spectra were taken with a standard rectangular TEM_{102} cavity and the pulsed experiments were performed using a Bruker dielectric ring resonator. Measurement of the angular dependence of the EPR spectra was achieved with a simple one axis goniometer. The crystals were mounted on perspex rods using the visible faces to align them with a $\langle 110 \rangle$ direction along the axis of the rod.

Rotation of the sample in the cavity could then be achieved with the applied magnetic field in any direction in the $\{110\}$ plane. In this manner spectra could be obtained with the field parallel to the $\langle 100 \rangle$, $\langle 110 \rangle$ and $\langle 111 \rangle$ directions. The alignment was checked by observing the angular variation of the P1 spectrum which was present in all the diamonds to varying degrees. If a significant deviation from the $\{110\}$ plane was detected the crystal was remounted and the experiment repeated. In this way the error associated with the orientation of the sample was limited to less than 2 degrees. A more accurate two angle goniometer is currently under development for use with this spectrometer but was not available at the time of these measurements.

The experimental parameters used in the cw spectra depended on the properties of the EPR centre being observed. The EPR centres fell into two categories; those with extremely long relaxation times which saturated easily, and those with shorter relaxation times that did not saturate until relatively higher microwave power was used. The centres with long relaxation times, such as P1 and P2, were best observed under adiabatic rapid passage conditions,²¹ with the microwave reference phase adjusted to 90° and with small

modulation amplitude (0.005 mT). Using these conditions the power could be increased to 1 mW without saturation and with other centres minimised. Centres with shorter relaxation times, such as N2 and W7 were best observed with normal reference phase and with larger modulation amplitude (>0.1 mT). With a microwave power of more than 1 mW these centres were easily observed while the intensity of the EPR signal due to the centres with long relaxation times was greatly reduced.

The optical absorption spectra were recorded at Monash University, Department of Physics, with a Varian DMS 100 UV-vis spectrophotometer fitted with a diffuse reflectivity attachment. The spectra were recorded in transmission mode but the diffuse reflectivity attachment was used as it contained an integrating sphere. In this way reasonable spectra could be obtained with samples that had no polished faces.

IR spectra were obtained using a Perkin Elmer FTIR Microscope attached to a PE 1600 series FTIR in the Department of Chemistry, Monash University. The samples were manipulated on the stage until sufficient transmission and relatively undistorted spectra were obtained. It was not possible to measure the path length due to the irregular shape of the diamonds.

3.3 Results

FTIR spectra of the coloured diamonds showed that the diamonds are all type Ia. Typical FTIR spectra of pink, brown and blue Argyle diamonds are shown in Figure 3.4. Within each type of stone there was some scatter in the type and quantity of nitrogen centres, as can be seen in Figure 3.5. Nevertheless, there were some noticeable trends in the FTIR spectra between the different colours. As the samples were uncut and did not have polished faces it was not possible to systematically investigate the spatial variation

of the defect centre concentrations in the stones and in particular any variation with growth sector.

The most notable distinction is between the blue diamonds and the other colours. The blue diamonds showed a much higher concentration of nitrogen which was present predominantly in the B form. The concentration of nitrogen in the B form was estimated to be 500 atomic ppm.²² A large platelet peak was also seen. A number of hydrogen related peaks were also seen, the largest of these at 3107 cm^{-1} .²³

The pinks and the browns showed lower concentrations of nitrogen which was present in both the A and B form. The concentration of nitrogen in the pink and brown diamonds was estimated to be approximately 50 atomic ppm. The FTIR spectra varied within the same sample indicating inhomogeneity in the concentration of these defects.

There were some apparent differences between the pink and brown diamonds. The browns typically had a large number of platelets and B features present in the spectra and a higher overall concentration of nitrogen. The pinks on the other hand had a smaller overall nitrogen concentration, with few or no platelets present and a higher proportion of A features relative to B features.

Although the FTIR spectra showed differences between the pinks and browns no obvious trends were seen when pinks of different intensities were studied, Figure 3.5. There was a small apparent trend towards a smaller platelet peak with increasing colour in the samples P1-P7. However, a larger variation in the platelet peak intensity was seen in pinks of roughly the same colour, samples P5a-P5g. Overall there was more variation in the FTIR spectra of the diamonds of equivalent colour than those with different colour.

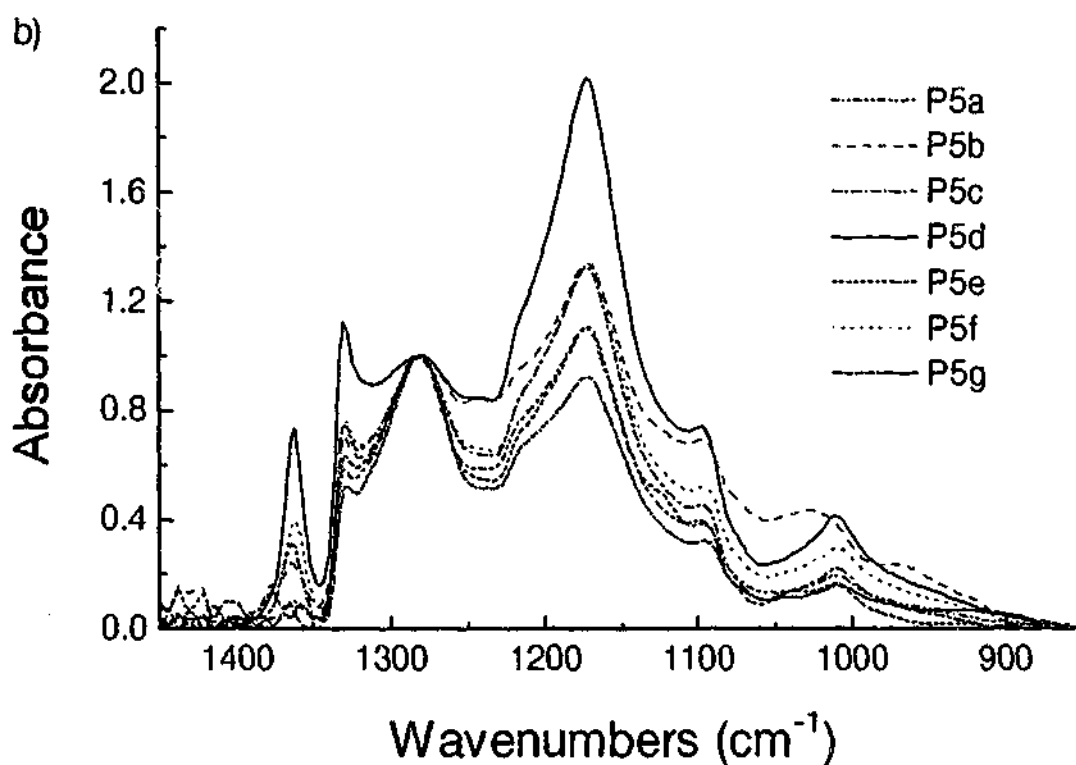
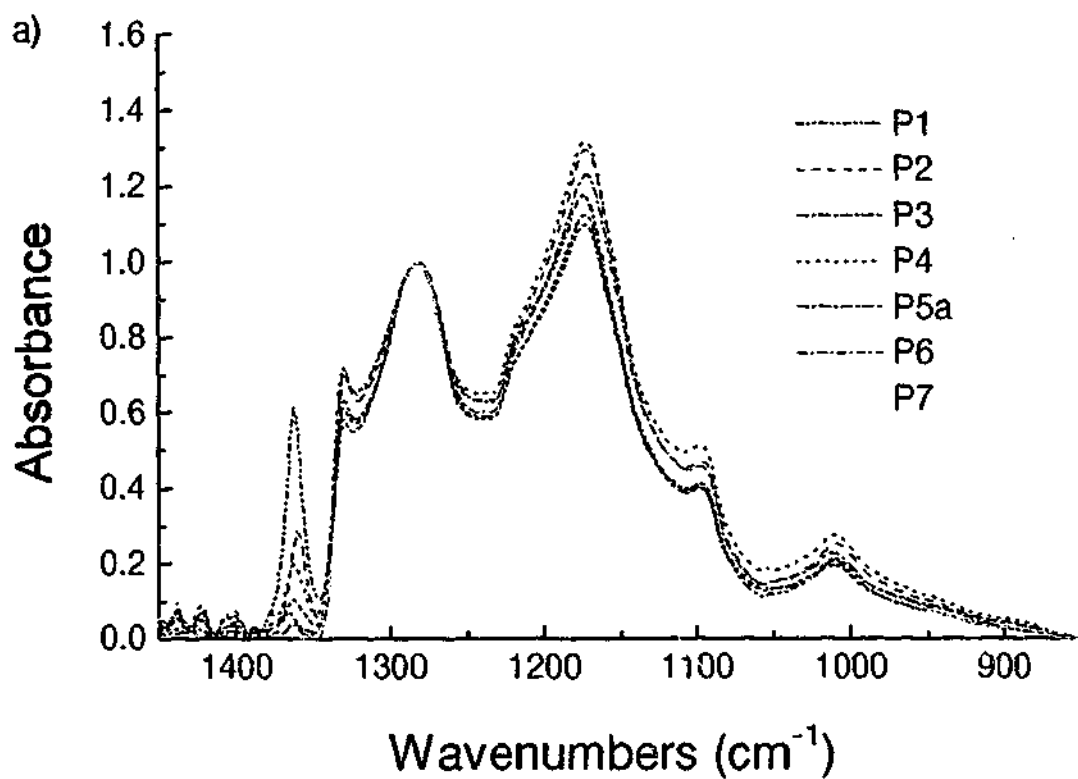


Figure 3.5 FTIR spectra of pink diamonds. a) graded pink diamonds. The colour of the diamonds ranges from light pink, P1, to dark pink, P7. b) pink diamonds with similar colour. The FTIR spectra show no obvious trend with colour. The spread of results in the set of similar pinks was greater than in the set of graded pinks

The lack of any obvious correlations can be partly explained by the small number of samples. The largest factor however is the inhomogeneity of the diamonds. The beam path through the diamond only sampled a small volume and spectra taken through different parts of the diamond gave very different spectra. It is apparent that the concentration of the various nitrogen defects varies significantly throughout the diamond.

A large number of EPR centres were observed in the coloured diamonds. The common P1 and P2 centres were observed in all diamonds to varying degrees. The EPR spectra of the P1 and P2 centres are shown in Figure 3.6a. Also visible in this spectrum is the W24 centre. The P1 centre is easily recognised by the $I = 1$ hyperfine splitting due to the single nitrogen. The angular dependence of the P1 centre is shown in Figure 3.7a. The P2 centre gives rise to a large number of lines with a complicated angular dependence close to $g = 2$ and is also seen in this spectrum.

In the coloured diamonds a broad peak at $g=2$ was observed. This was present in all the coloured diamonds to some degree but was particularly strong in the brown diamonds. This centre was identified as the N2 centre. The brown diamonds also show the W7 centre. This centre was observed by Troup and Hutton²⁰ but was not correctly identified due to the motional averaging that occurs at room temperature. The W7 and N2 spectra are shown in Figure 3.6b. At room temperature the hyperfine structure from the two nitrogen nuclei in the W7 centre collapses to a three line spectrum.²⁴ Figure 3.7b shows the angular dependence of the W7 centre with weaker transitions present due to incomplete motional averaging

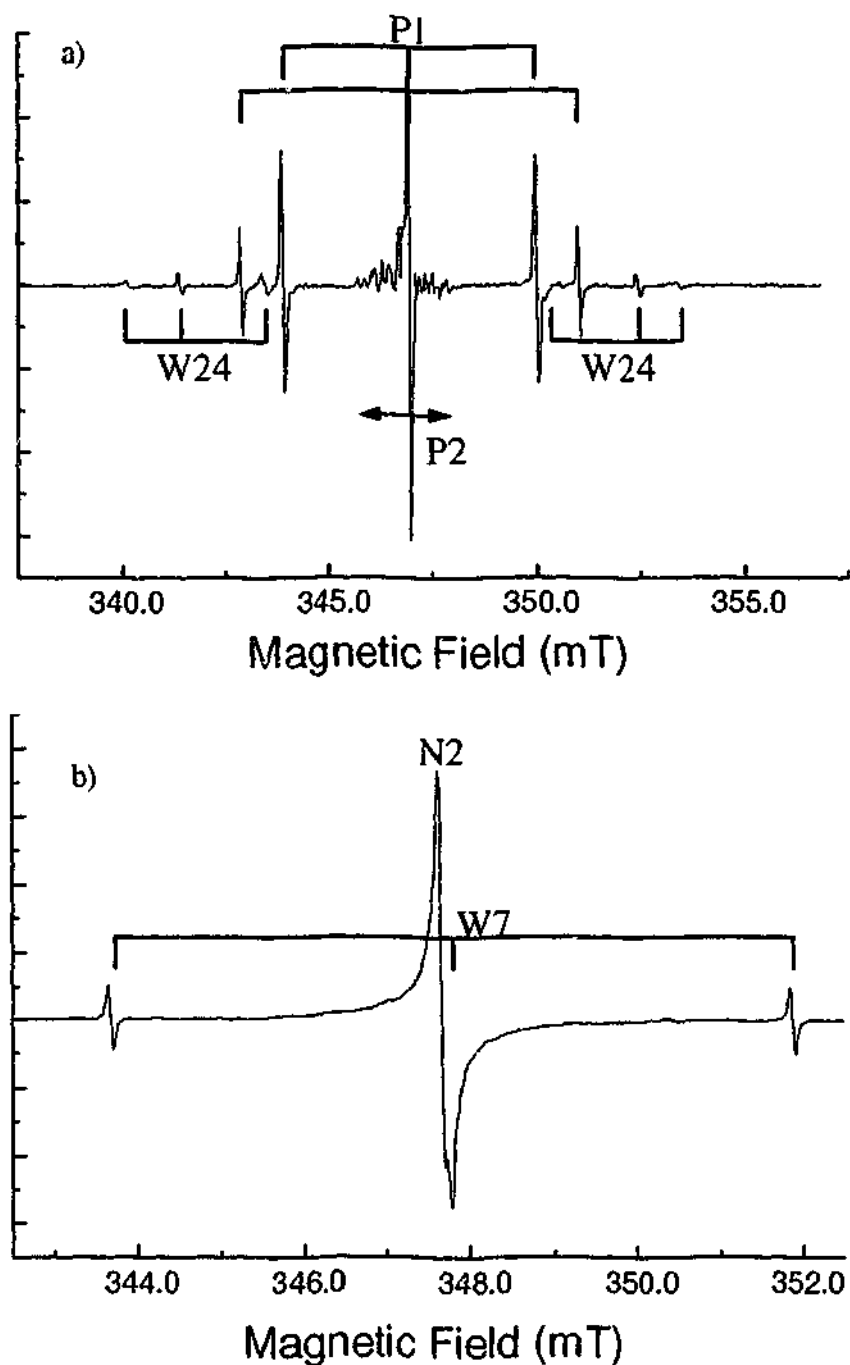


Figure 3.6 EPR spectra showing centres in pink and brown diamonds. a) room temperature EPR spectrum of large pink after UV irradiation. The magnetic field is aligned to a $\langle 111 \rangle$ direction. The P1, P2 and W24 centres are indicated. b) room temperature EPR spectrum of diamond B10. The magnetic field is aligned to a $\langle 100 \rangle$ axis. The N2 and W7 lines are marked.

In one of the 'whites' that had a faint yellow tinge, another spectrum was seen that overlapped with the P1 and P2 spectra. Once the angular dependence and the number of lines was resolved the centre was easily identified as the W21 centre. This centre is believed to be another three nitrogen centre and commonly occurs in 'Cape Yellow' diamonds.²⁵ The angular dependence of the W21 centre is shown in the stack plots of Figure 3.7a

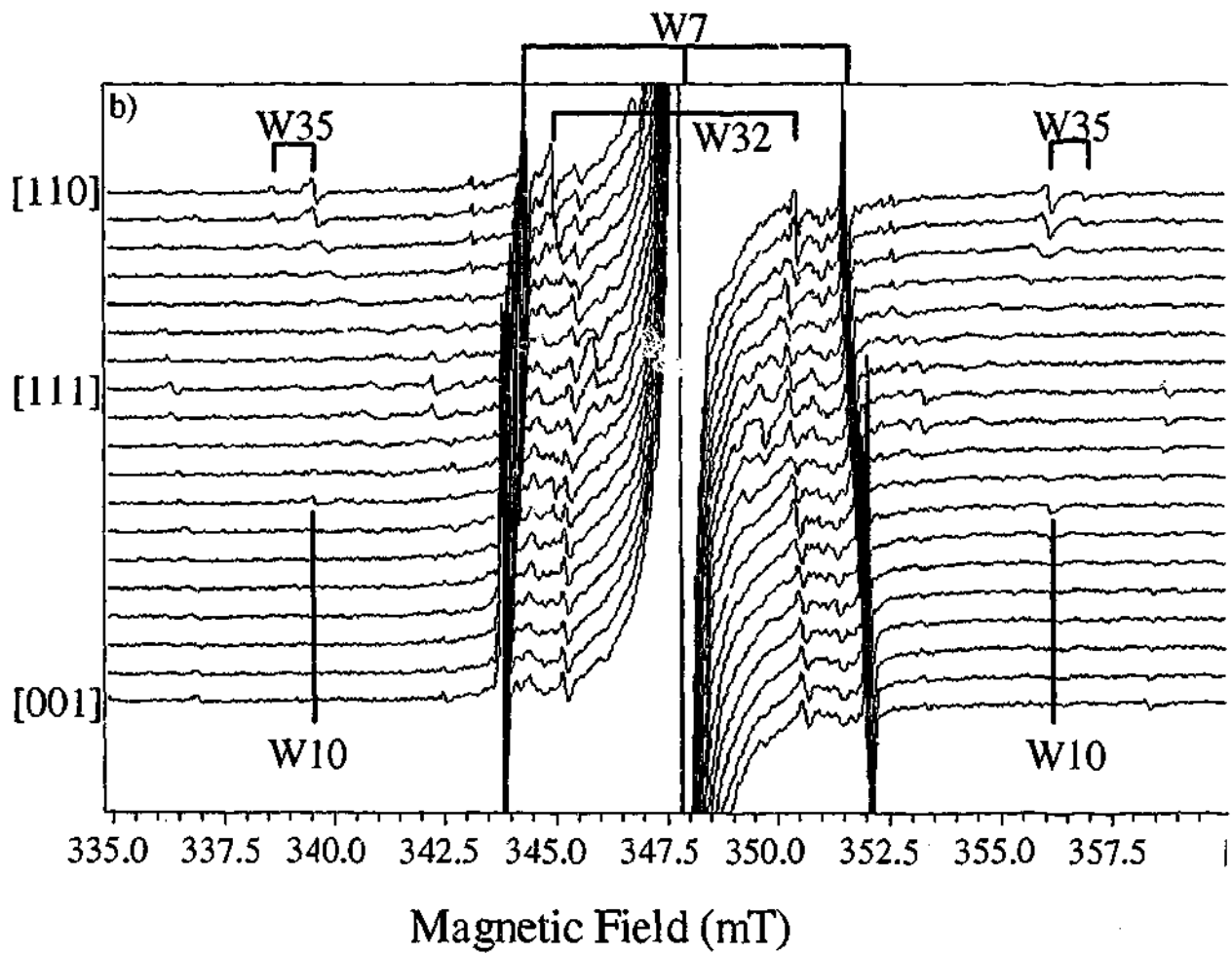
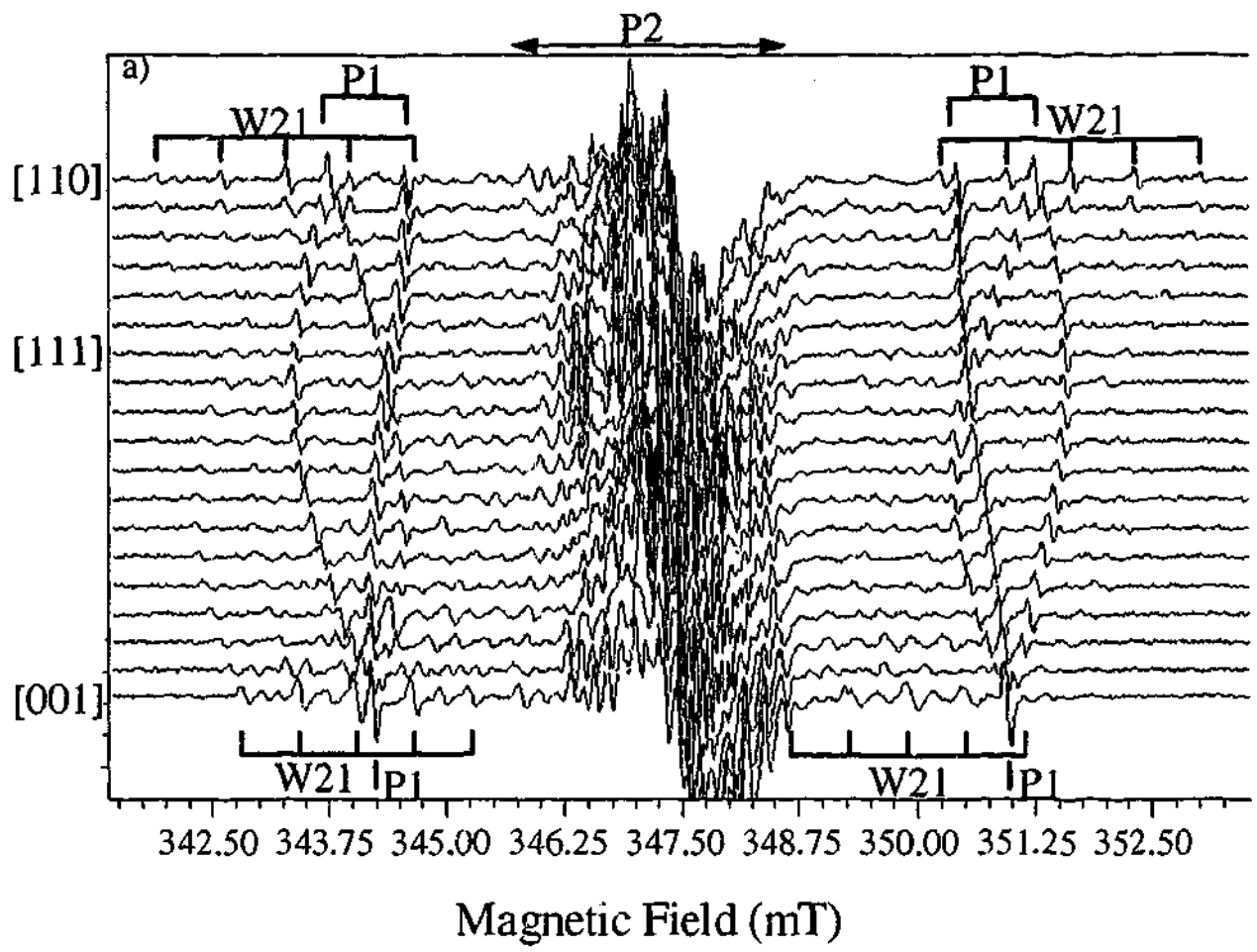


Figure 3.7 Angular dependence of EPR spectra with rotation about a $\langle 112 \rangle$ axis a) Diamond W5 showing P1, P2 and W21 centres. b) diamond B10 showing W7, W10, W32 and W35 centres.

When some of the samples were illuminated with UV light another centre was seen that was identified as the W24 centre⁸. This centre was quickly bleached by ambient white light and hence was only observed if the sample was placed immediately in the cavity without any exposure. In the cavity the centre was stable for several hours. However if the specimen was illuminated with white light in the cavity the signal from the W24 centre could be seen to disappear in seconds. The W24 centre is seen in Figure 3.6a

A number of other centres were also seen in the darkest of the browns (b10). These have been identified as the W10, W32 and W35. All of these have previously been seen in brown diamonds²⁶. Some of these can be seen in Figure 3.7b

No EPR centres were found that were unique to the pink diamonds. All centres observed in the pinks have also been observed in other diamonds without the pink colouration. The blue Argyle diamonds, however, all show a different complex characteristic EPR spectrum. This spectrum is observed in all the Argyle blue diamonds that have been analysed and has not been reported in any type of diamonds. The Argyle blue diamonds are discussed in more detail in a later chapter of this thesis.²⁷

Although no new EPR centres were found in the Argyle pink diamonds a rough correlation was found between the P1 EPR centre intensity and the pink colouration. This is shown in Figure 3.8a. The intensity of the P1 centre increases with the stronger pink colour. The pinks that are the same shade have approximately the same P1 intensity. This is obviously not a direct correlation as the P1 centre is present in non-pink diamonds.

The W7 and N2 centres were found to correlate roughly with the intensity of colouration in the brown diamonds. This is shown in Figure 3.8b. The darkest diamond

B10 is much darker than B9 and the intensity of the W7 and N2 peaks are an order of magnitude greater. Newton and Baker reported that not all the possible orientations of the W7 centre are populated in the plastically deformed diamonds²⁸. This was not actively investigated here but could account for some variability in the data. Nevertheless, a consistent trend was still seen.

3.4 Discussion

The survey of the Argyle diamonds focussed on two techniques, FTIR and EPR. The FTIR spectra were useful in the categorisation of the diamonds into types Ia, Ib and IIa ,Iib. These categories have previously been shown to relate to the geological history of the diamond particularly the length of time that the stone has been subject to high temperature and pressure.¹² These same conditions obviously play a role in determining the other defects that are produced including the colour centres.

The pink and brown diamonds were found to have quite low nitrogen concentrations, less than 50 ppm. The amount of nitrogen was found to vary between diamonds but there was no observed trend with colouration. There was also a large amount of variation within each diamond which indicates significant inhomogeneity of the nitrogen concentration in these stones. It has also been recently observed that the regions of the diamonds which have the pink colouration, which is also typically non-uniformly distributed, are actually type IIa with no observable nitrogen.²⁹ The measurement of the bulk nitrogen, however, placed the coloured diamonds in the type Ia category, with the pink diamonds tending towards type IaA and the brown diamonds tending towards type IaB. The Argyle blue diamonds were found to be type IaB with high N and high H content. No boron was detected in the blue Argyle diamonds.

A number of previously described centres were observed. All diamonds were found to contain detectable levels of P1 and P2 centres in different concentrations. The W21 centre was observed in one diamond with a yellowish colour. The W24 centre was seen in some diamonds after UV irradiation. The N2 and W7 centres were seen in the brown Argyle diamonds and to a lesser degree in the pink Argyle diamonds. These pink diamonds also had a noticeably brown background hue. The W10, W32 and W36 centres were also seen in darkest brown diamond.

Surprisingly a correlation between the intensity of the P1 EPR centre signal and the intensity of the pink colouration was observed. The low number of samples in the survey makes it difficult to make strong conclusions regarding this correlation. It is also difficult to make absolute quantitative measurements using the adiabatic rapid passage technique due to the complicated effect of sweep rate, detection phase and other experimental parameters on the detected signal. However, relative measurements of defect centre concentration between diamonds using the same experimental parameters are still valid.

It is difficult to establish a causal relationship between the P1 centre concentration and the pink colouration. There are a number of possible explanations for this observation. If we assume that the pink colour centre exists in more than one charge state then only one of these will give rise to the pink colour. The P1 centre is a deep donor and will affect the Fermi level in the diamond. This will in turn determine the population of the charge state of the pink colour centre depending on its energy level. It would also appear to be important that the level of other centres such as A centres, which are believed to be acceptors, are low as these would also affect the Fermi level.²⁵ A second possibility is that it is the concentration of the pink colour centre that determines the Fermi level and this then determines the charge state of the isolated

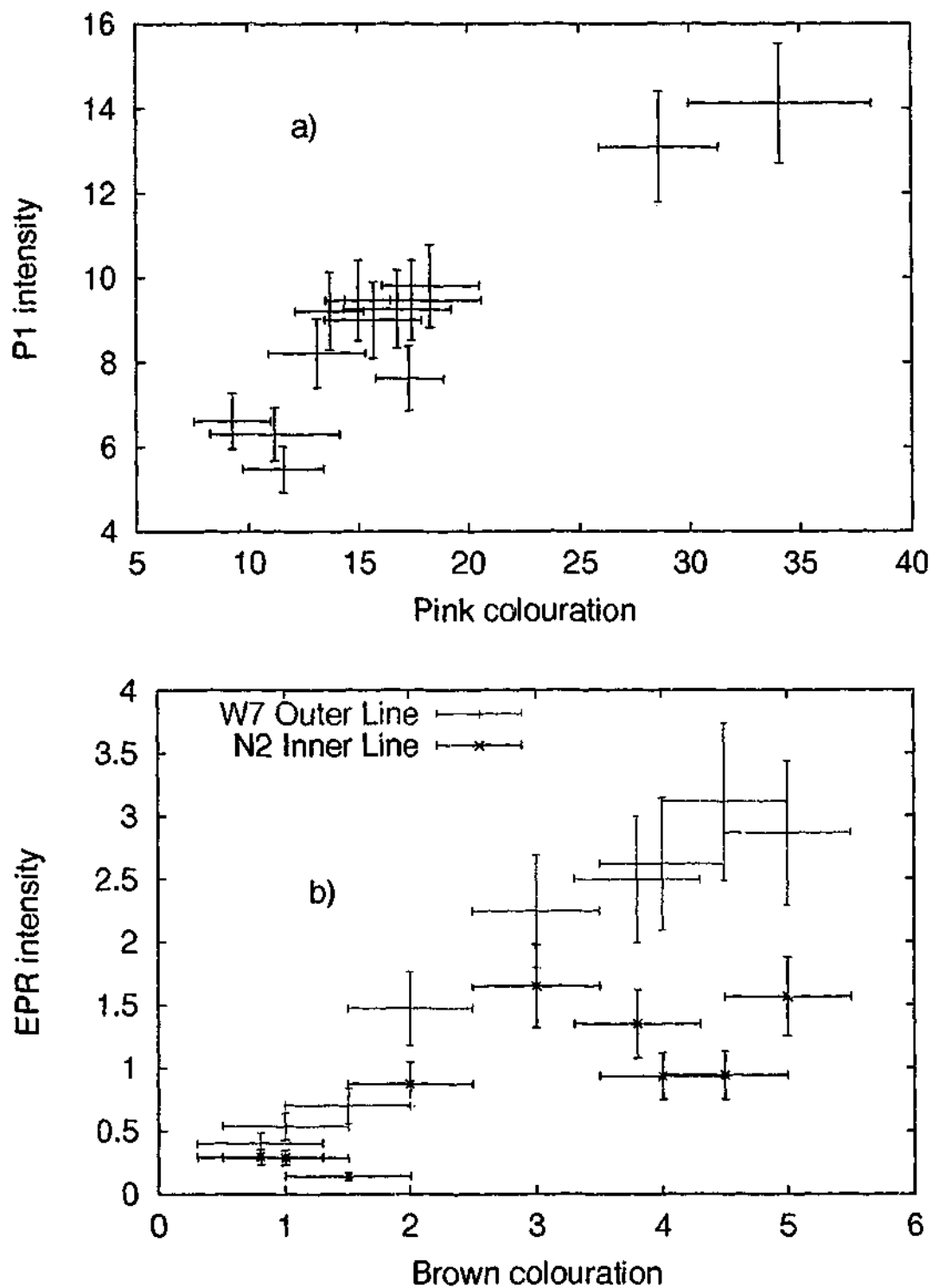


Figure 3.8 Intensity of EPR centres in pink and brown Argyle diamonds. a) P1 intensity in pink diamonds of different shades ranging from light pink to dark pink. The numerical value of the pink colouration was achieved by taking the ratio $r/(r+g+b)$ from the rgb values in digital images. b) N2 and W7 intensity in ten brown diamonds of varying shades of brown.

nitrogen and hence the intensity of the P1 EPR centre. These possibilities are explored in more detail in the next chapter.

Alternatively the relationship between the P1 centre and the pink colouration may be much less direct. The presence of the pink colour centre and the concentration of the

P1 centre could both relate to the geological history of the diamonds. Both the pink and brown diamonds have been subject to plastic deformation as evidenced by the presence of visible slip planes and complicated birefringence patterns. The features that distinguish between the pink and brown diamonds appear to be that the brown diamonds have more B centres and platelets than the pink diamonds. The P1 centre concentration also appears to be important for the pink diamonds. It is possible that the differences in the form of the nitrogen centres in the pink and brown diamonds reflect the different temperature and pressure conditions they have been subject to after the plastic deformation. The brown diamonds appear to have been subject to longer high temperature and pressure annealing to produce the B centres and platelets. It is possible that this annealing also destroys the pink colour centre and the presence of the P1 centres simply reflects this.

The defect centre responsible for the pink colour of Argyle diamonds does not appear to be EPR active or if it is paramagnetic it is not observable for other reasons such as short relaxation times. Another possibility that was not thoroughly investigated was that the pink colour centre has an EPR spectrum that is obscured in the $g = 2$ region that contains the N2 and, most likely, other centres. It was not possible to separate different components in this region based on their saturation behaviour in cw EPR. Pulsed EPR experiments, which might be able to differentiate between different centres, only showed the P1 and P2 centres and not other centres including N2. Optically detected EPR on the pink diamonds was attempted but was not successful in finding an EPR signal that was connected with the absorption band centred at 2.25 eV (550 nm) that has been associated with the pink colouration.¹ The optical quality of the diamonds was low, with no polished faces. This meant that the signal-to-noise ratio of these measurements were quite low for these samples. It was possible to observe optically detected EPR spectra of the P2 EPR centre on the N3 optical absorption band.

3.5 Conclusion

The EPR survey of the Argyle coloured diamonds uncovered no new centres, with the exception of the blue diamonds which will be described in more detail in chapter 5. The W7 and N2 centres were found in the Argyle brown diamonds and were found to correlate with the depth of colouration. These centres were also found to a lesser extent in the pink Argyle diamonds but no centres unique to the pink diamonds were found. However, an apparent correlation was observed between the P1 EPR centre and the pink colouration.

3.6 References

- ¹ Collins, A.T., *J. Gemm.*, **18**, (1982), 37.
- ² Newton, M.E. and Baker, J.M., *Appl. Magn. Reson.* **8**, (1995), 207-228.
- ³ Smith, W.V., Sorokin, P.P., Gelles, I.L. and Lasher, G.J., *Physical Review*, **115**, (1959), 1546.
- ⁴ Van Wyk, J.A. and Loubser, J.H.N., *J. Phys. Condensed Matter*, **5**, (1993), 3019.
- ⁵ Lawson, S.C., Fisher, D., Hunt, D.C., and Newton, M.E., *J. Phys.: Condens. Matter* **10**, (1998), 6167.
- ⁶ Davies, G., Welbourn, C.M. and Loubser, J.H.N., *Diamond Research*, (1978), 23.
- ⁷ Davies, G., *J. Phys. C: Solid State Phys.*, **9**, (1976), L357.
- ⁸ Van Wyk, J.A. and Loubser, J.H.N., *J. Phys. C: Solid State Phys.*, **16**, (1983), 1501
- ⁹ Tucker, O.D., Newton, M.E., and Baker, J.M., *Phys. Rev. B*, **50**, (1994), 15586.
- ¹⁰ Mainwood A., *Phys. Rev. B*, **49**, (1994), 7934.
- ¹¹ Davies, G., *Chemistry and Physics of Carbon*, **13**, (1977), 1.
- ¹² Evans, T., in *The Properties of Natural and Synthetic Diamond*, Field, J.E., ed., Academic Press, London, (1992), 259.
- ¹³ Baker, J.M., *Diamond and Related Materials*, **7**, (1998), 1282.
- ¹⁴ Lonsdale, K., *Proc. R. Soc. Lond. A*, **179**, (1942), 315.
- ¹⁵ Sumida, N. and Lang, A.R., *Proc. R. Soc. Lond. A*, **419**, (1988), 235.
- ¹⁶ Newton, M.E. and Baker, J.M., *J. Phys.: Condensed Matter*, **1**, (1989), 9801.
- ¹⁷ Shcherbakova, M.Ya., Sobolev, E.V., Nadolinnyi, V.A., Aksenov, V.K. *Sov. Phys. Dokl.*, **20**, (1976), 725.
- ¹⁸ Samsonenko, N.D., Shul'ga, V.G., and Litvin, Yu.A., *Sinteticheskie Almazы*, **3**, (1970), 22.
- ¹⁹ Raal., F.A., *Proc. Phys. Soc.*, **71**, (1958), 846.
- ²⁰ Hutton, D.R., and Troup, G.J., *Aust. J. Phys.*, **46**, (1993), 663.
- ²¹ Campbell, I.D., *J. Magn. Reson.*, **74**, (1987), 155.
- ²² Clark, C.D., Collins, A.T. and Woods, G.S., in *The Properties of Natural and Synthetic Diamond*, Field, J.E., ed., Academic Press, London, (1992), 39.
- ²³ Fritsch, E., Scarrat, K., Collins, A.T., in *New Diamond Science and Technology*, *MRS Int. Conf. Proc.*, (1991), 671-676.
- ²⁴ Loubser, J.H.N. and Wright, A.C.J., *J. Phys. D: Appl. Phys.*, **6**, (1973), 1129

-
- ²⁵ Loubser, J.H.N., Van Wyk, J.A., and Welbourn, C.M., *J.Phys.C:Solid State Phys.*, **15**, (1982), 6031.
- ²⁶ Loubser, J.H.N., Van Wyk, J.A., *S. Afr. J. Phys.*, **10**, (1987), 165.
- ²⁷ Noble, C.J., Pawlik, Th. and Spaeth, J-M., *J. Phys.: Condens. Matter*, **10**, (1998) 11781.
- ²⁸ Newton, M.E. and Baker, J.M., *J.Phys.:Condensed Matter*. **3**, (1991), 3605.
- ²⁹ Chapman, J., *Personal Communication*, (1998).

4. Photo/Thermochromic Effects in Argyle Pink Diamonds

4.1 Introduction

Natural and synthetic diamonds can contain many colour centres that display photochromic and thermochromic behaviour. In many cases the mechanism relates to the ionisation state of the colour centre. In these cases the different charge states of the defect have different energy levels in the band-gap and have different absorption bands. Consequently, two optical centres exist that correspond to the two charge states of the same defect. Typically illumination with short wavelength light will destroy one centre and create another by photo-ionisation. Illumination with longer wavelength light or heat treatment will reverse the process.

Examples of this type of system include the H2/H3 centres,¹ and the GR1/ND1 centres.² The H3 optical centre has been mentioned in the previous chapter and is believed to be a vacancy trapped at an A centre. Both the H2 and H3 centres were observed in irradiated and annealed type Ib diamonds. Illumination with light of energy higher than 2.07 eV (600 nm) reduced the absorption due to the H2 centre and increased that due to the H3 centre. In the dark the process is reversed. The GR1 and ND1 centres are produced in electron irradiated type Ia diamonds and are believed to be the neutral vacancy and the negative vacancy respectively. Illumination with UV light increases the absorption due to the GR1 centre and decreases that due to the ND1 centre. Heat treatment at 500 °C increased the GR1 absorption and decreased the ND1 absorption.

In both of these cases the free charge carrier produced by the photoionisation of the defect is trapped at a trapping centre some distance from the colour centre. The charge carrier can be released from the trap by light of a different wavelength or by heat treatment. The depth of this trapping centre determines whether the photochromic

effects are stable at room temperature or are reversed by thermal ionisation such as with the H2/H3 centres.

The free charge carriers obviously allow the diamond to conduct electricity. Photoconductivity experiments show that these photochromic effects are due to photo-ionisation of the colour centres. In these experiments the conductivity is measured as a function of the light wavelength. The photoconductivity spectra of the GR1 and ND1 centres show the same features as the optical absorption spectra showing the connection between the conductivity and optical centres.³ The thermoelectric effect and the Hall effect can be used to determine the nature of the charge carrier and the photo-ionisation process.⁴

In these cases at least one charge state of the defect is assured to be EPR active. The photochromic behaviour is then seen when the EPR spectra of the colour centre is monitored under illumination. For example, an excited state of the H3 optical centre is seen in EPR as the W26 centre⁵ and the S1 EPR centre has been associated with the ND1 optical centre.⁶

In other systems the photochromic change corresponds not to a change in the charge state of the defect but to a change in its geometrical configuration. A pair of optical centres observed in irradiated type Ib diamonds are believed to be of this type.⁷ The two optical absorptions have zero phonon lines at 2.367 eV and 1.979 eV. No photoconductivity was detected that was associated with these bands. It was therefore proposed that the two absorption bands correspond to the same defect in different symmetry configurations, rather than in different charges states.

The P1 EPR centre is a donor at a depth of approximately 1.7 eV below the conduction band.⁸ It has a photoconduction band starting at 1.7 eV and increasing with

higher photon energies. The P1 centre has been shown to take part in a number of photochromic mechanisms in synthetic diamonds that contain nickel. The P1 centre firstly changes the Fermi level in the diamond and hence affects the charge state of the nickel defects and, secondly, with light of higher photon energies than 1.7 eV provides more electrons which are trapped at the nickel defects. The nickel centres that are affected are substitutional nickel,⁹ interstitial nickel,¹⁰ and a series of nickel nitrogen complexes.^{11,12}

The changes in the optical absorption spectra in diamonds with photochromic defects can give rise to an observable change in colour. These diamonds have been termed chameleon diamonds for their ability to change colour.¹³ These diamonds have an "equilibrium" or "stable" green colour but if heated to 200 °C- 300 °C or, if left in the dark for a period of several hours to days, will turn a bright yellow colour. The colour change is reversed under normal illumination conditions in a few minutes. The absorption bands that are responsible for these colours are believed to be related to hydrogen.¹⁴

Argyle pink diamonds are another type of diamond that show marked photochromic changes. These diamonds range from pink to mauve in colour and often have a brown background hue. When these diamonds are exposed to UV light from a mercury lamp the pink colour is bleached from the diamond and they are noticeably brown. This process is reversed by exposure to sunlight or artificial white light. When the diamonds are heated to temperatures over 800 °C the colouration intensifies to a darker mauve. This effect is also reversed by white light.

This chapter describes a series of experiments to investigate the photochromic behaviour of Argyle pink diamonds using optical absorption, EPR and photo-EPR spectroscopies.

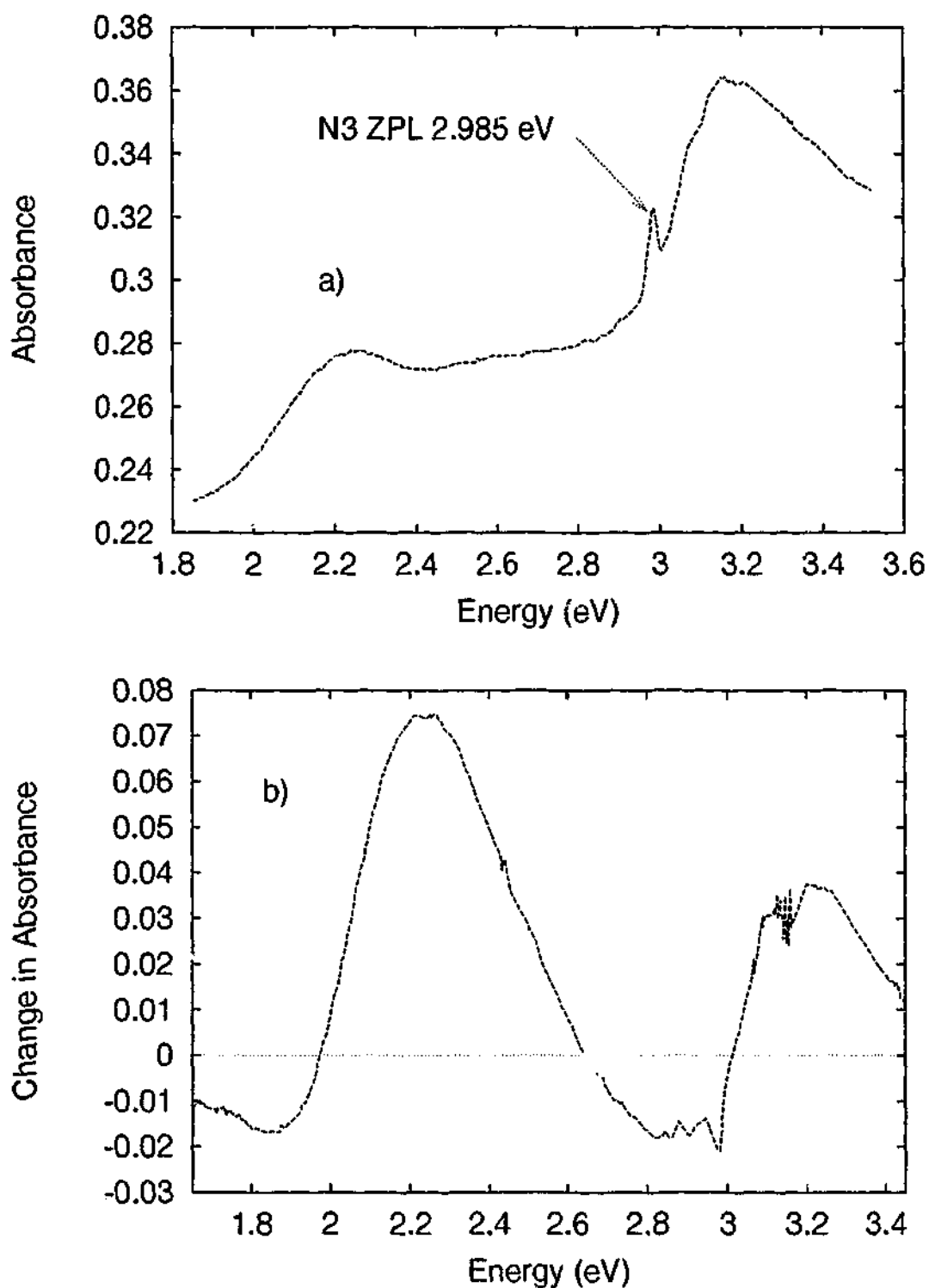


Figure 4-1 Photochromic effects in pink diamonds. a) room temperature optical absorption spectrum of pink Argyle diamond. The spectrum shows a broad band centred at 2.25 eV (550 nm) and an associated band at approximately 3.15 eV (394 nm). It is the broad band at 2.25 eV that is responsible for the colour. The vibronic band of the N3 defect also overlaps with the absorption at 3.15 eV. b) Change in optical absorption in pink diamonds after optical irradiation. The spectrum represents the difference between the optical absorption of a pink diamond after bleaching with UV and the "equilibrium" state produced by illumination with white light.

4.2 Experimental

The photochromic effects were investigated by exposing the diamonds to UV irradiation. Two sources were used for this purpose; a small 6 W mercury lamp with a UV pass filter ($h\nu > 3.1$ eV), and a large 500W xenon lamp in a Schoeffel 151N lamp housing. The small lamp took several minutes to produce noticeable changes in the colour of the pinks. The xenon lamp did not appear to produce as much of a colour change compared to the small lamp. The output of the xenon lamp, although stronger, was predominantly in the visible region with a broad peak at approximately 2.25 eV. The mercury lamp, by contrast, has intense lines with photon energies greater than 4.1 eV and it is presumably these lines that are necessary for the bleaching process.

A selected number of the diamonds were also heated to 850° C in an electric furnace for approximately 10 minutes to assess the thermochromic behaviour of the pinks. The samples were also illuminated with strong white light whilst in the EPR cavity using a standard 500 W projector lamp. The EPR spectra could then be taken whilst the effects of the UV and heat treatment were being bleached by the white light. A 100 W Hg/Xe lamp and a prism monochromator were also used.

4.3 Results

The pink diamonds displayed large photochromic and thermochromic effects. The diamonds appeared paler after UV irradiation and darker after heat treatment. It should also be noted that a very pale yellow-brown colour was visible after most of the pink colour had been bleached out by UV and the colour after heat treatment appeared to be more of a mauve colour than dark pink. The UV and heat modified colours were reversed under illumination with strong white light.

The optical absorption spectrum of a pink Argyle diamond is shown in Figure 4-1a. The broad band at 2.25 eV (550 nm) is responsible for the pink colour. An absorption at approximately 3.15 eV (392 nm) is also associated with this absorption.¹⁵ The absorption from the N3 centre overlaps with this band. Also evident is a continuum absorption increasing monotonically with higher energy.

The photochromic effects can be seen in Figure 4-1b. This spectrum shows the difference between the optical absorption spectrum after 1) bleaching with UV and 2) illumination with white light. Bleaching with UV decreases the intensity of the broad absorption at 2.25 eV associated with the pink colouration and the related absorption at 3.15 eV. Illumination with white light has the reverse effect producing an increase in the intensity of the 2.25 eV band and also in the 3.15 eV band. In addition there is also a decrease in the optical absorption in some wavelengths suggesting that the continuum absorption mentioned previously is reduced by the white light.

It was also possible to observe these effects directly in a spectrophotometer by recording the optical absorption at a fixed wavelength as a function of time. This can be seen in Figure 4-2a where the optical absorption at 3.15 eV decreases exponentially as a function of time indicating that the diamond is being bleached.

The effect of white light was determined by the prior treatment of the diamond. If the diamond has previously been bleached with UV irradiation then the colour darkens in white light. If the colour has been darkened by heating then white light restores the colour to the original level.

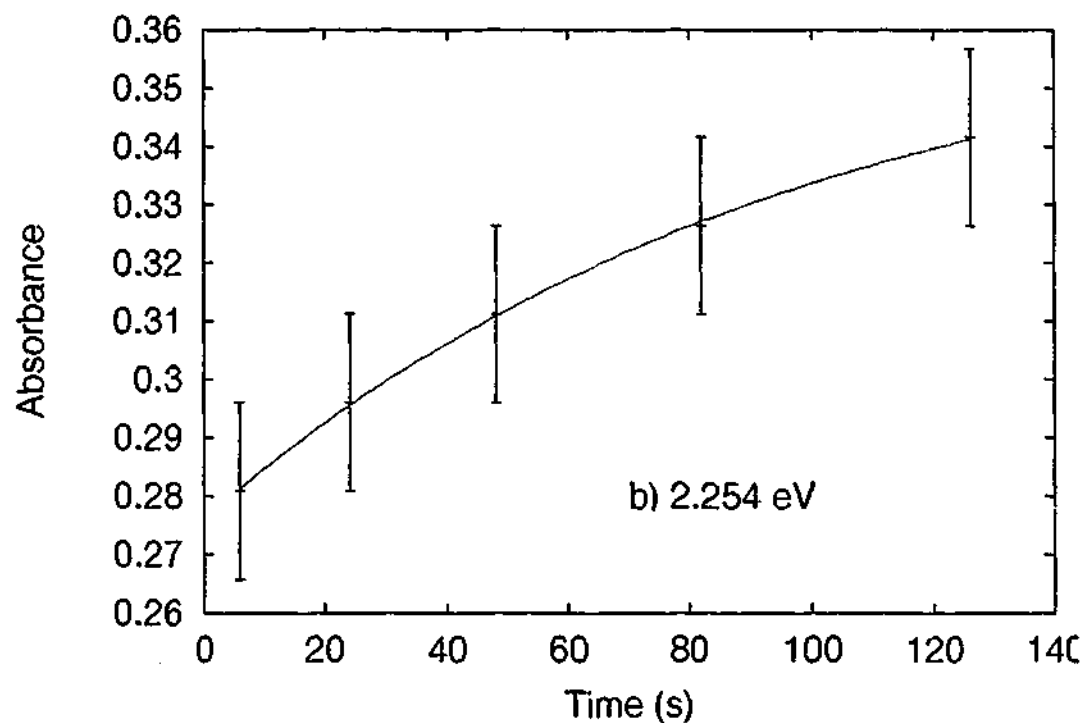
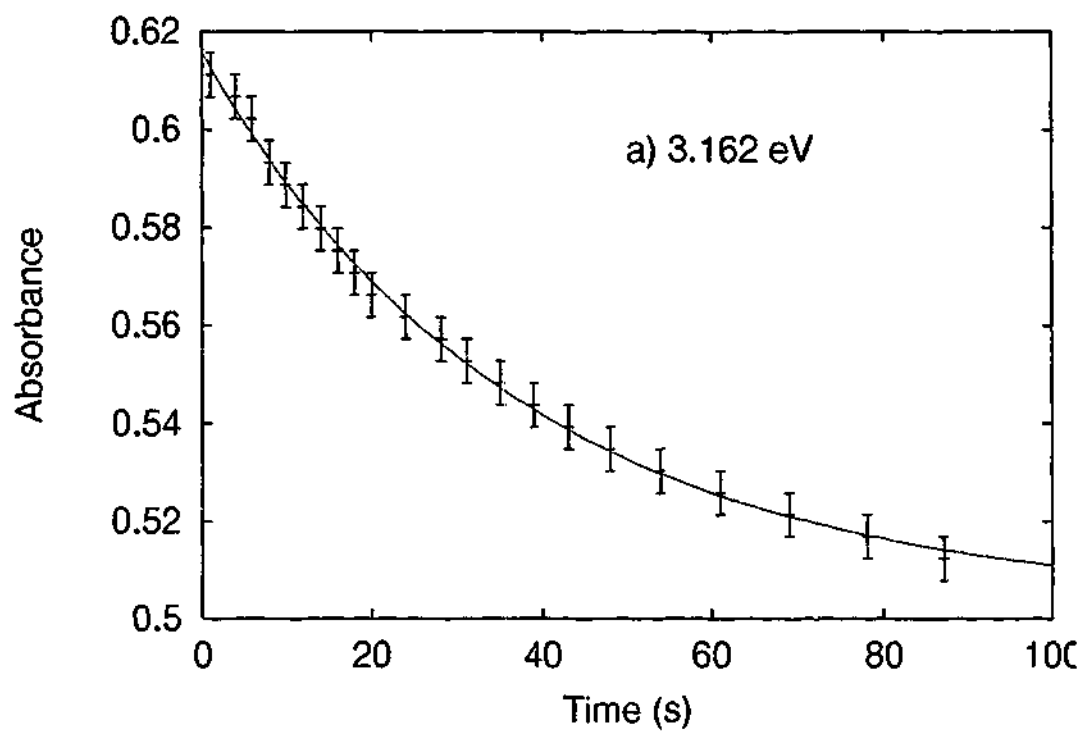


Figure 4-2 Optical absorption measured as a function of time. a) The diamond has previously been illuminated with white light to reverse any bleaching of 2.25 eV and 3.15 eV bands. The optical absorption at 3.15 eV is measured as a function of time. The intensity of the incident beam is sufficient to bleach this band over a long period of time. b) The sample has previously been bleached with UV to reduce the intensity of the 2.25 eV and 3.15 eV bands. The optical absorption at 2.25 eV is measured as a function of time. The intensity of the incident beam is sufficient to reverse the bleaching and the absorption at this energy increases over time. The error bars in the plot represent the resolution of the instrument

The same effects can be seen with time resolved absorption at 2.25 eV. If the sample is heated then the optical absorption at 2.25 eV decreases with time. If the sample is first bleached with UV then the optical absorption at 2.25 eV actually increases. This is seen in Figure 4-2b

Significant changes in the EPR spectra were seen with these colour changes. Firstly a new centre, identified as the W24 centre, was seen after UV irradiation.¹⁶ This centre was rapidly bleached by even low level illumination and was not seen if the irradiated diamond was exposed to light for only a very short time. In the dark it was stable for a period of hours.

By monitoring the intensity of the W24 EPR signal during illumination with UV it was possible to observe the production of this centre. This is shown in Figure 4-3. The W24 signal increases exponentially when illuminated with a mercury arc lamp filtered by a UG11 UV pass filter. The intensity decreases upon exposure with light from a Hg/Xe lamp with the same filter. The Hg/Xe lamp has more output in the visible which causes the destruction of the W24 centre. Removal of the filter leads to a complete bleaching of the W24 centre. Importantly illumination again with the filter restores the W24 centre intensity to an equilibrium level balancing the two processes creating and destroying the W24 centre.

The P1 centre was also affected by the UV irradiation. After this treatment the P1 lines had increased in intensity by approximately 30 percent. The change in the P1 intensity was reversed with exposure to white light. In addition the P1 line intensity is reduced to almost zero after the heat treatment and fully recovers during white light illumination. These two processes are shown in Figure 4-4. The change in spin concentration of the P1 and W24 centres during these photochromic processes was not quantified. However, the changes in the P1 concentration occurred on a much longer

time scale than that of the W24 centre and so there was not a direct correlation between the two.

An attempt to record photo-EPR on the P1 centre after UV irradiation was made. The diamond was first irradiated with UV from a Hg lamp to increase the population of the P1 centre. The intensity of the P1 EPR signal was then monitored as a function of time with illumination with different wavelengths of light using a Xenon arc lamp and a monochromator.

The initial slope of the decay is proportional to the optical cross section for the ionisation process. The energy dependence of the optical cross section can then be determined.¹⁷ The calculated optical cross section is shown in Figure 4-5b. From this spectrum an activation energy of approximately 2.4 ± 0.1 eV is estimated.

No correction has been made for the spectral output of the lamp or for the transmission properties of the monochromator although both are fairly flat around 2.5 eV. The last point at 3.55 eV is not reliable for a number of reasons. Firstly the P1 concentration was low in this measurement. Secondly the photon flux was low at these wavelengths. It is also evident from other measurements that there is more than one process that is active in changing the valency of the defect centres. Different processes will either raise or lower the population of a given defect centre charge state.

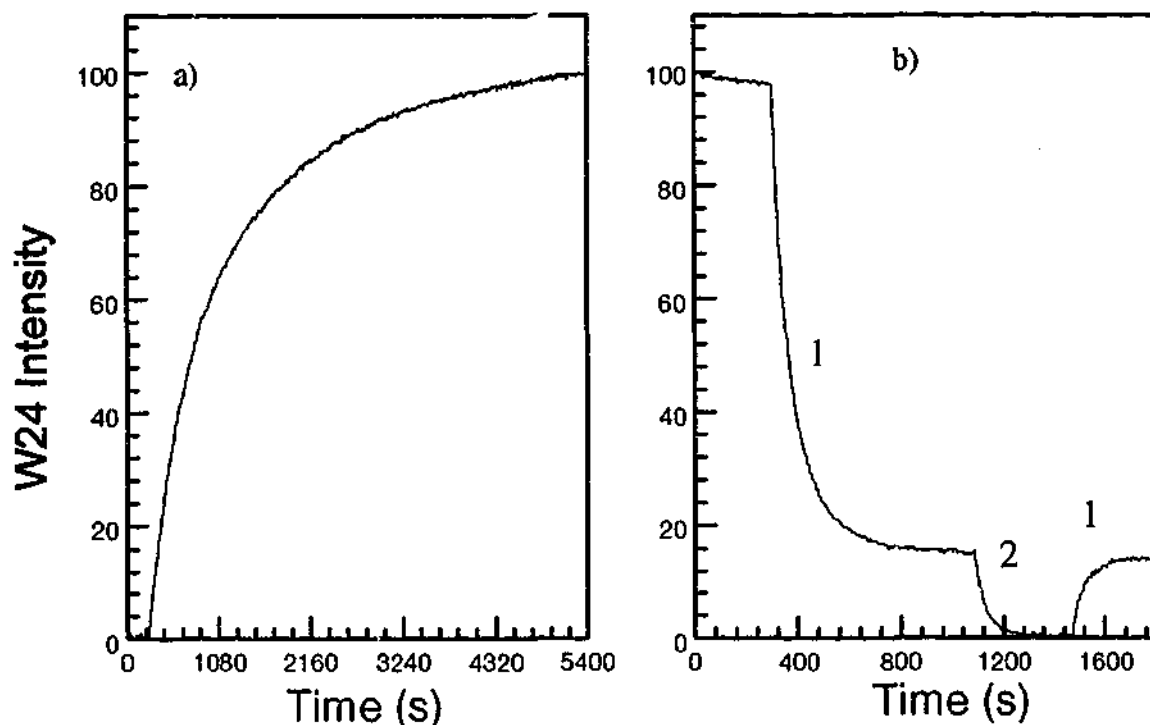


Figure 4-3 Intensity of the W24 EPR centre under illumination with different combinations of lamps and filters. a) production of W24 centre with illumination with 6W Hg lamp and a UG11 filter. b) effect on W24 centre with illumination with 100 W Hg/Xe lamp with a UG11 filter (1) and with no filter (2).

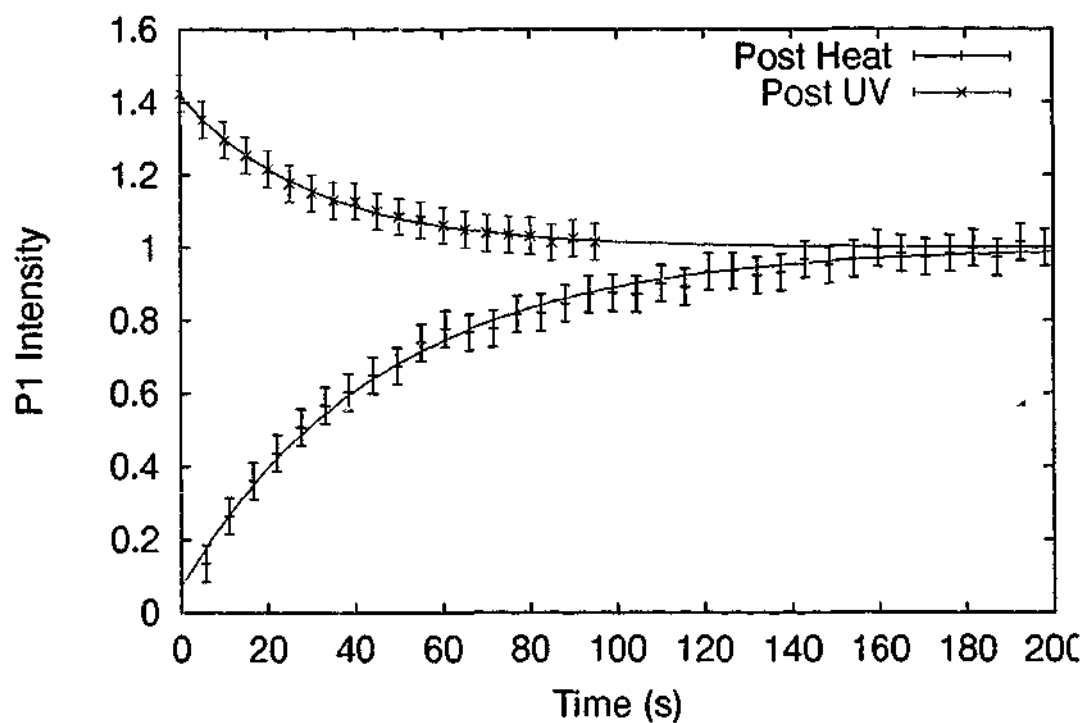


Figure 4-4 The change in the intensity of the EPR P1 spectrum in pink Argyle diamonds during illumination with white light. The two curves represent the response after heat treatment with an initial raised P1 level and after UV irradiation with an initial lowered P1 level. During illumination with white light the intensity of the P1 line was restored to an "equilibrium" level.

4.4 Discussion

In the previous chapter a relationship between the P1 centre concentration and the pink colouration was shown. To explain this apparent correlation it was hypothesised that the pink colour centre could exist in more than one charge state and that only one of these charge states gave rise to the characteristic optical absorption of the pink diamonds. The proportion of this centre in a particular charge state would then be determined by the Fermi level, which is in turn determined by the proportion of acceptors and donors in the diamond. The presence of the P1 EPR centre, a deep donor, in higher concentrations than the nitrogen acceptor centres, raises the Fermi level and changes the proportion of the pink colour centres in the optically active charge state. Alternatively the presence of the pink colour centre could lower the Fermi level and the population of the EPR active charge state, the P1 EPR centre, of the isolated nitrogen centre. The photo/thermochromic behaviour of the pink diamonds more directly relates to the charge states of the pink colour centre and the nitrogen centres, especially the P1 EPR centre.

The colour of the pink diamonds can be changed by either exposure to UV or heat treatment. UV irradiation bleaches the pink colouration and heat treatment at 800 °C intensifies the colour. Both of these effects can be reversed by exposure to artificial lighting or sunlight. The effect of broad band white light is therefore to restore the colour to an "equilibrium" level.

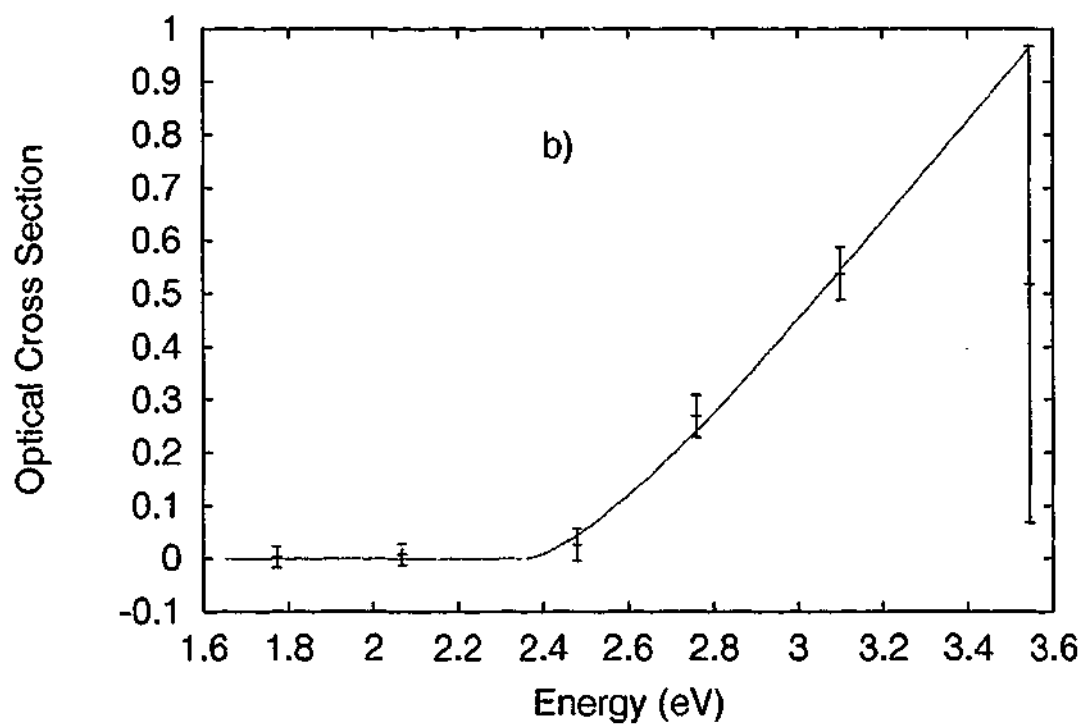
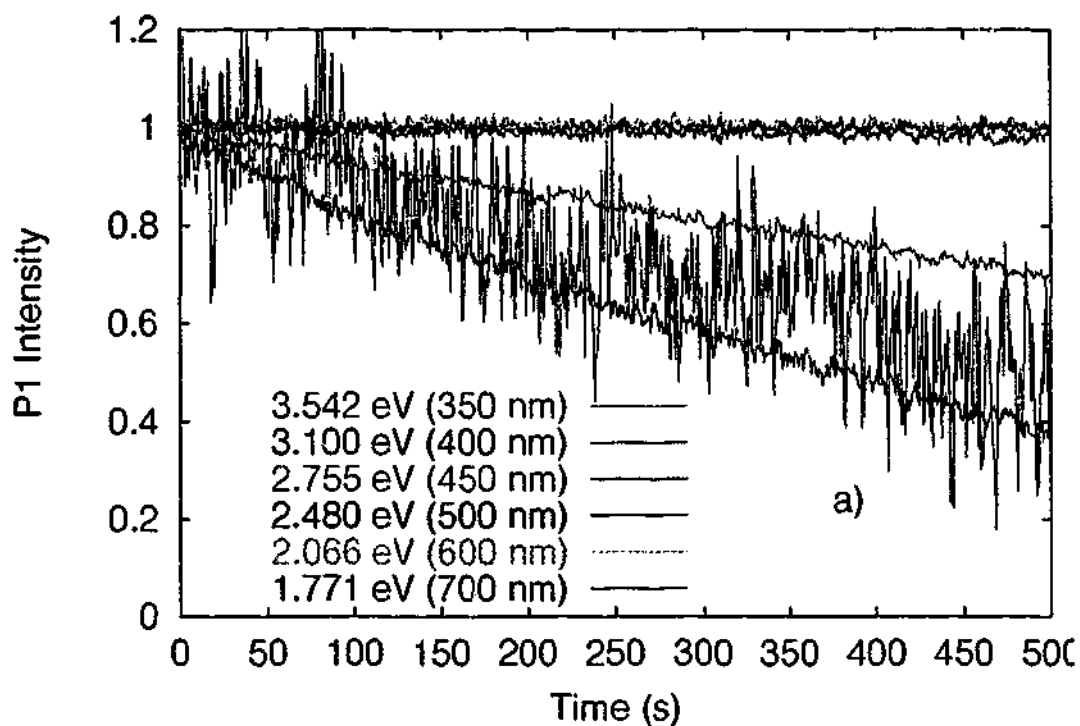


Figure 4-5 Photo EPR of the P1 centre. a) Percentage change in P1 EPR signal under illumination with different wavelengths of light. b) Optical cross section for the ionisation process calculated from the initial slope in a). No correction has been made for the spectral dependence of the lamp or the monochromator. The continuous line is a fit to the equation $\sigma_n \sim (x-1)^{3/2}/x$, $x = h\nu/E_T$, $E_T = 2.4 \pm 0.1$ eV.

The colour of the Argyle pink diamonds can be seen in optical absorption spectroscopy as a broad absorption band at 2.25 eV. Associated with this absorption is a related band at ~3.15 eV. The visible change in the colour of the pink diamonds can also be seen as changes in the optical absorption spectrum before and after bleaching. The bands at 2.25 eV and 3.15 eV become stronger with an increase in the pink intensity. The broad continuum absorption that is also seen in the pink and brown diamonds also decreases at the same time.

The photochromic effects are large enough such that they can influence the absorption spectrum recorded in a spectrophotometer as can be seen in Figure 4-1 where the optical absorption is recorded at a fixed wavelength as a function of time. Measuring on the band at 3.16 eV the absorption decreases exponentially, as a function of time, indicating bleaching. The reverse effect is seen if the optical absorption of a bleached pink diamond is measured at 2.25 eV in the centre of the broad band. In this case the optical absorption actually increases but only very weakly. This indicates that there are two absorption processes that occur with light of 2.25 eV. One of these is a photo ionisation process which will decrease with time but will populate another centre which also absorbs at this energy and will actually increase the optical absorption. The magnitude of this effect depended on how well the diamond had been previously bleached. Eventually an equilibrium will be reached where the two processes will balance each other.

With the available apparatus it was not possible to perform more sophisticated experiments to shed more light on these effects. It was not possible, for instance, to irradiate with different wavelengths of light whilst monitoring one peak in the optical absorption spectrum. It was established that at least two processes were occurring, light whose quantum energy is greater than 3.0 eV bleaches the pink colour, heat darkens the

diamond and light with a quantum energy less than 3.0 eV both bleaches and darkens depending on prior history.

The photochromic effects were also seen in the EPR spectra. As described in chapter 3 the W24 EPR centre is produced by UV irradiation in some of the pink Argyle diamonds. In contrast to previous reports, the W24 centre in the pink diamonds was found to be stable in the dark for hours or days.¹⁶ This indicates that in these diamonds there exist trapping levels not thermally activated at room temperature.

Tucker *et al* performed detailed measurements of the lifetime of the W24 centre in Cape Yellow diamonds after UV irradiation.¹⁸ At room temperature the W24 centre disappeared instantaneously when the UV irradiation was turned off. Above 50 K the lifetime was less than 30 minutes and showed a temperature dependence indicating thermally activated hopping. Below 25K the lifetime of the W24 centre in these Cape Yellow diamonds was found to be temperature independent and hence it was proposed that tunnelling between the trapping centre and the W24 centre dominated in this temperature range. A distribution of lifetimes was also observed and hence a distribution of the separation between the W24 centre and the electron traps was inferred.

The behaviour of the W24 centre in the Argyle pink diamonds is quite different and it is apparent that different electron trapping centres are involved. The nature of these trapping levels are not known but it is likely they are related to the plastic deformation in these diamonds. It was not possible to measure the activation energy of these centres as a high temperature EPR cavity was not available, but it must be significantly greater than kT at room temperature.

It was also found that photons with energies higher than 4.1 eV are needed to produce the W24 centre in detectable amounts rather than the photon energies of more

than 3.1 eV as reported previously.^{16,18} This is evident when the ability of three different light sources to produce the W24 centre are compared. In all cases a UG11 filter with a cut out at ~ 3.1 is used. The best production of the W24 centre was achieved with a Hg arc lamp. A Xe arc lamp, in contrast, produced no measurable quantities of the W24 centre. A Hg/Xe lamp produced $\sim 15\%$ of the level of W24 centres as the Hg lamp. It was apparent that although the Xe lamp has a large spectral output between 3.1 and 4.1 eV the strong mercury lines > 4.1 eV are needed to produce the W24 centre in these diamonds. This could be explained by the absorption at 3.15 eV that is seen in the Argyle pink diamonds. This absorption band may be due to another ionisation process that destroys W24 centres.

The intensity of the P1 EPR centre is also seen to change with illumination. The P1 centre intensity increases with exposure to UV light and decreases with heat. This is apparently the opposite trend to that observed in chapter 3 where the P1 centre was found to correlate to the pink colour. The changes in the P1 population are quite stable at room temperature in the dark and are reversed with exposure to white light.

Again, as with the changes in the optical absorption spectra, at least two processes can occur depending on the wavelength of light. White light which has a peak at approximately 2.25 eV can either increase or decrease the population of the P1 centre depending on the prior history of the diamond. If the population of the P1 centre is low then white light will increase the population of the centre whilst the reverse will occur if the P1 centre population is high. The "equilibrium" level of the P1 centre (N_s^0) and the ionised defect (N_s^+) is determined by the balance of shorter and longer wavelengths present in the light.

In fact, the populations never really come to equilibrium at room temperature as deep levels are involved which are not thermally activated. Hence the concept of a Fermi

level should be used with caution as the population of the different charge states of the defects are not simply determined by the temperature, but are affected by the previous radiation history of the diamond.

Although there were a number of different processes occurring, involving a large number of defects, an attempt to ascertain the wavelength dependencies of the photochromic effects using photo-EPR was made. The intensity of the P1 EPR centre was increased by UV irradiation the decrease of this signal with different wavelengths of light was measured. The results were not conclusive for a variety of reasons. Firstly, it was not possible to determine the incident photon flux on the sample across the spectral range of the lamp. The lamp itself had a broad spectral output with a maximum at approximately 2.25 eV but it was not possible to allow for the spectral dependence of the monochromator and other optics used in this setup. Secondly, and more importantly, the percentage change in the EPR spectrum was very small if a small slit width on the monochromator was used. It was then a trade off between the resolution and the signal-to-noise ratio. In the final results only six wavelengths were chosen and there was still a low signal-to-noise ratio.

However, the experiment appeared to show the onset of this process at photon energies greater than ~2.5 eV which is in a region where the output of the lamp is relatively constant. It is also a value that was obtained in a photoconductivity experiment which is not described here. This is also the same activation energy that is reported for a process involving a nickel defect Ni_5^- and the P1 centre.⁹ This can, of course, be a coincidence but the behaviour is quite similar and is consistent with other optical and EPR observations of Ni_5^- . The Ni_5^- centre is observed only in type Ib or low nitrogen diamonds. This is presumably because the type of nitrogen centres in the diamond determine the Fermi level and the charge state of other impurities. The P1 centre is a

donor and hence favours the negatively charged nickel defect. Charge transfer reactions between the Ni and N then alter the charge state of both.

The evidence for the involvement of nickel has been supported by a recent observation of Ni_s^- luminescence in pink Argyle diamonds by Chapman.¹⁹ This luminescence was only observed in pink Argyle diamonds and not other diamonds from the Argyle mine. The luminescence was not observed uniformly throughout each pink diamond. This matches observations that the nitrogen centres are not homogeneously distributed. In regions with more A and B centres the Ni is present in the neutral charge state and Ni_s^- luminescence will not be observed.

The possible presence of the Ni_s^- centre in the pink Argyle diamonds does not explain the 2.25 eV optical absorption which is not seen in other diamonds that contain both Ni and N. It also does not explain the role of plastic deformation in producing the pink diamonds. The Ni_s^- centre has also been observed in powdered natural diamonds which do not previously show the centre.²⁰ The substitutional nickel was presumably present beforehand but was in a different charge state. The grinding of the diamond produced defects that could charge compensate the Ni to produce the negative charge state. Another EPR spectrum, labelled O1, was also observed in these powdered diamonds which has been reinterpreted by Tucker *et al* as the W24 centre.¹⁸ The role of plastic deformation in the pinks might be similar and produce defects that change the Fermi level.

Cathodoluminescence studies of Argyle pink and brown diamonds show a characteristic cross hatch pattern indicating slip in $\{100\}$ planes due to plastic deformation.²¹ The emission is from N3 and H3 centres that decorate these slip planes.

This indicates that vacancies in these plastically deformed diamonds could also affect the nitrogen aggregation and hence the nickel charge state.

4.5 Conclusion

Pronounced photochromic effects were seen in the W24 and P1 EPR centres in pink Argyle diamonds. The W24 centre was formed with exposure to UV light with photon energies greater than 4.1 eV. The W24 centre was stable in the dark for indefinite periods of time but was removed rapidly by exposure to light or heat. The population of the neutral charge state of the substitutional nitrogen defect, the P1 EPR centre, was found to vary upon illumination with UV or visible light. The effect of illumination depended on the wavelength of light and the prior radiation history of the diamond. One of the photochromic processes was investigated with photo-EPR and an activation energy of approximately 2.4 ± 0.1 eV is obtained. The defect responsible for the pink colouration in these diamonds was not revealed in these studies but it is suggested that a substitutional nickel defect may be involved. It is also apparent that defects produced by the plastic deformation in these diamonds play a role in providing electron traps and altering the charge state of other defects.

4.6 References

-
- ¹ Mita, Y., Nisida, Y., Suito, K., Onodera, A., and Yazu, S., *J. Phys.: Condens. Matter*, **2**, (1990), 8567.
 - ² Dyer, H.B. and du Preez, L., *J. Chem. Phys.*, **42**, (1965), 1898.
 - ³ Farrer, R.G., Vermeulen, L.A., *J. Phys. C: Solid State Phys.*, **5**, (1972), 2762.
 - ⁴ Vermeulen, L.A., and Farrer, R.G., *Diamond Research*, (1975), 18.
 - ⁵ Davies, G., *Chem. Phys. Carbon*, **13**, (1977), 1.
 - ⁶ Isoya, J., Kanda, H., Uchida, Y., Lawson, S.C., Yamasaki, S., Itoh, H., and Morita, Y., *Phys. Rev. B*, **45**, (1992), 1436.
 - ⁷ Collins, A.T. and Rafique, S., *Proc. R. Soc. A*, **367**, (1979), 81.
 - ⁸ Farrer, G., *Solid State Communications*, **7**, (1969), 685.
 - ⁹ Hofmann, D.M., Ludwig, M., Christmann, P., Volm, D., Meyer, B.K., Pereira, L., Santos, L., and Pereira, E., *Phys. Rev. B*, **50**, (1994), 17618.
 - ¹⁰ Lawson, S.C., and Kanda, H., *J. Appl. Phys.*, **73**, (1993), 3967.

-
- ¹¹ Nadolinny, V., Yelisseyev, A., Yurjeva, O., Hofstaetter, A., Meyer, B., and Feigelson, B., *Diamond and Related Materials*, **7**, (1998), 1558.
- ¹² Nadolinny, V.A., Yelisseyev, A.P., Yurjeva, O.P., and Feigelson, B.N., *Appl. Magn. Reson.*, **12**, (1997), 543.
- ¹³ Fritsch, E., Scarrat, K., Collins, A.T., in *New Diamond Science and Technology*, *MRS Int. Conf. Proc.*, (1991), 671-676.
- ¹⁴ Fritsch, E., in *The Nature of Diamonds*, ed. Harlow, G.E., Cambridge University Press, Cambridge, (1998), 23-47.
- ¹⁵ Collins, A.T., *J. Gemm.*, **18**, (1982), 37.
- ¹⁶ van Wyk, J.A. and Loubser, J.H.N., *J. Phys. C: Solid State Phys.*, **16**, (1983), 1501.
- ¹⁷ Godlewski, M., *phys. stat. sol.*, **90**, (1985), 11.
- ¹⁸ Tucker, O.D., Newton, M.E., and Baker, J.M., *Phys. Rev. B*, **50**, (1994) 15586.
- ¹⁹ Chapman, J., personal communication (1998).
- ²⁰ Loubser, J.H.N., *Solid State Commun.*, **22**, (1977) 767.
- ²¹ Kaneko, K., personal communication (1996).

5. ENDOR Spectra of Natural Blue Argyle Diamonds[†]

5.1 Introduction

In previous chapters research has been presented from studies of pink and brown diamonds from the Argyle mine in Western Australia. Another type of diamond which has a greyish blue colour is also found at the Argyle mine. It is extremely rare with only a few found each year and is not related to the semiconducting blue diamonds which contain boron.¹

The greyish-blue diamonds have not previously been extensively investigated. One optical spectroscopy study has been published to date.² It was found that these diamonds contain an unusually high concentration of hydrogen. The blue colour of these diamonds was believed to be related to these hydrogen defects.

This chapter reports on the first paramagnetic resonance study of these diamonds. In contrast to other diamonds from the Argyle mine these diamonds were found to contain nickel defects which have previously been observed in synthetic diamonds. More importantly a previously unreported EPR centre was also observed and it is proposed that this defect also contains nickel. This defect is found only in these diamonds and it is suggested that the blue colour may result from the incorporation of nickel.

A number of defects involving isolated nickel, and nickel associated with nitrogen have been observed previously in synthetic diamonds. To provide some background to discuss the investigation of nickel defects in natural blue diamonds a brief review of the known centres is presented.

[†] Parts of this chapter have previously been published in an article, Noble, C.J., Pawlik, Th. Spaeth, J-M., *J. Phys. Condens. Matter*, 10, (1998) 11781.

Of all the defects observed in natural diamond, by far the majority are nitrogen and vacancy related. Some of these centres have been discussed in the previous chapter on natural diamonds from the Argyle mine.

Nickel defect centres in diamond were first observed in synthetic polycrystalline diamonds grown at high temperature and pressure from a nickel-containing solvent.³ The defect centre was labelled the W8 EPR centre and was reported to give a single line at $g = 2.031$. It was present only in diamond grown from a nickel containing solvent and hence was attributed to nickel. It was later confirmed to be a nickel centre from the resolved hyperfine splitting of ^{61}Ni in a synthetic diamond containing nickel isotopically enriched to 10% ^{61}Ni .⁴ This is the only confirmed centre due to nickel to date.

Since then optical transitions that have been correlated with nickel have been observed at 1.4, 1.883, 2.51, 2.56 and 3.1 eV.⁵ Again these features were present in diamonds grown from a nickel catalyst but absent from those grown without, and hence were ascribed to nickel. The relative strength of these bands was determined by the concentration of nitrogen in the diamond.⁵ Diamonds grown with a nitrogen getter, and therefore low nitrogen content, show a dominant 1.4 eV ZPL. Diamonds grown without a nitrogen getter by contrast show stronger 1.883 and 2.51 eV lines. The effects of nitrogen on these lines is thought to be due to changes in the Fermi level, isolated nitrogen being a deep donor.⁵

The 1.4 eV ZPL has been proposed to be associated with an $S = 1/2$ interstitial Ni^+ ion.^{6,7} An EPR centre labelled NIRIM 2 having a spin of $1/2$, $g_{\parallel} = 2.3285$ and $g_{\perp} \cong 0$ has also been proposed to be an interstitial Ni^+ ion perturbed by a neighbouring charge compensator, probably a vacancy.⁸ This EPR centre is observed in diamonds showing a dominant 1.4 eV line which gives support for the model applying to both although no

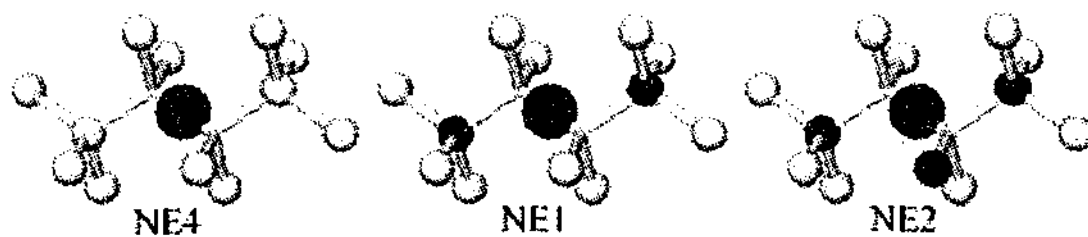


Figure 5.1 Models for the NE4, NE1 and NE2 centres as proposed by Nadolinny and Yelisseyev¹¹ and more recently modified in Nadolinny et al.¹² The NE4 defect is proposed to be a nickel accommodated in a di-vacancy position. The NE1 shows hyperfine splittings from two nitrogens and is proposed to be the nickel in the di-vacancy position with two nitrogens in first nearest neighbour positions, the two nitrogens being opposite each other in a $\langle 110 \rangle$ plane. The NE2 defect has an extra nitrogen in the first shell surrounding the di-vacancy defect. (● = nickel, ○ = nitrogen, □ = carbon)

direct correlation between the optical and EPR centres has previously been established.

The NIRIM1 centre, $S=1/2$, $g=2.0112$, is also believed to be an interstitial Ni^+ defect.⁸

An EPR centre with a line at $g=2.0319$ has been found in synthetic single crystal diamond.⁹ Although there is some ambiguity in the literature it is apparent that this is the same defect that had been observed in powdered diamond and originally labelled the W8 centre. In various papers the g value for this centre had been given as 2.031 or 2.032. This defect was found to be $S=3/2$ by a nutation experiment. This centre is found in diamonds showing dominant 1.883 and 2.51 eV lines and is attributed to a substitutional Ni^{2+} ion with configuration $3d^7$ in site of T_d symmetry, because ^{13}C hyperfine structure showed that the site had four nearest neighbouring carbon sites and twelve next nearest neighbour carbon sites.

More recently, studies involving the annealing of synthetic diamonds containing nickel have provided evidence that complex defects involving both nickel and nitrogen are formed in this process.^{10,11,12,13} Nadolinny and Yelisseyev discovered three EPR centres that formed during the heat treatment at 2100 K and 5.5 GPa in diamonds containing both nickel and nitrogen.¹¹ These centres were labelled NE1-NE3. All had anisotropic g values with magnitudes between 2.00 and 2.14 and had characteristic

hyperfine splittings indicating interactions with two, three and three nitrogens respectively for NE1, NE2 and NE3. The EPR centres were also correlated statistically with optical features labelled the S2 and S3 bands and a line at 2.3692 eV (523.2 nm), but no direct correlation was made.

Further investigations by the same authors uncovered another four EPR centres. One, the NE4 centre, was present in as grown diamonds and had $\langle 111 \rangle$ symmetry, $g_{\parallel} = 2.0227$, $g_{\perp} = 2.0988$ and no observed hyperfine splittings. The NE5, NE6 and NE7 centres were seen in the heat treated diamonds but only during optical illumination. They all had anisotropic g values greater than 2 and had interactions with two, zero and one nitrogen respectively. The centres NE1-NE5 were found to be a nickel in a di-vacancy position associated with zero to three nitrogens.

A series of optical absorption lines have also been observed in synthetic diamonds after heat treatment.¹² When diamonds which initially showed the 1.883 and 2.51 eV lines were annealed, these lines decayed in strength and a new series of absorptions appeared. The most prominent of these was a vibronic band with a zero phonon line (ZPL) at 1.693 eV and a dominant 51 meV phonon energy. Associated with this band was a complicated series of lines between 2.2 and 2.6 eV. The 1.693 eV structure annealed out at temperatures over 1700 °C showing that it was a transient species. The maximum in the intensity of the 1.693 eV line was found to correlate well with the initial 1.883 eV line intensity. Some of the lines in the range 2.2 to 2.6 eV annealed out at this temperature and some remained, indicating that several separate defect species were being produced during the annealing. Again complex defects involving nickel and nitrogen are proposed to account for these features.

These optical and EPR features have all been observed in synthetic diamonds. These defects would appear to be extremely rare in natural diamonds which have quite different origins. The NE1 and NE2 EPR centres have however been reported in natural diamonds from the Jakutii and Ural mines.¹⁴ Also reported in this article was a new EPR centre with $S=1/2$, $\langle 100 \rangle$ symmetry and the parameters $g_{\parallel}=2.0151$, $g_{\perp}=2.2113$ and no hyperfine structure.

Theoretical analyses of the electronic configuration of nickel centres in diamond have been attempted by several authors.^{9,15,16} A model by Ludwig and Woodbury¹⁷ has been used to provide a simple picture of how the various spin states arise. In this model transition metal ions, that have a free-ion configuration $3d^n4s^2$, when in interstitial positions in silicon and germanium lead to an electronic configuration of $3d^{n+2}$ as the two 4s-shell electrons are transferred to the 3d shell. When the ion is on a substitutional site four electrons are transferred from the 4s and 3d shells to the valence shell to complete tetrahedral bonds with the nearest neighbours. Thus a transition metal ion with the free ion configuration $3d^n4s^2$ results in a $3d^{n-2}$ configuration. Therefore a Ni^+ ion on an interstitial site gives rise to the configuration $3d^9$ and a spin state $S=1/2$ and a Ni^- ion on a substitutional site would be expected to have the electronic configuration $3d^7$ and a spin state $S=3/2$. The expected configurations for these defects in diamond are shown in Figure 5.2

Lowther¹⁵, however, provided a different view. In this model the substitutional nickel defect is seen as a vacancy with the nickel weakly bonded, only altering the occupancy of the dangling bond orbitals. In the negative charge state the nickel is weakly bonded to the surrounding carbons via the 4s electron. The d and s shells of the nickel are then full and three out of four electrons are left in the dangling bond orbitals,

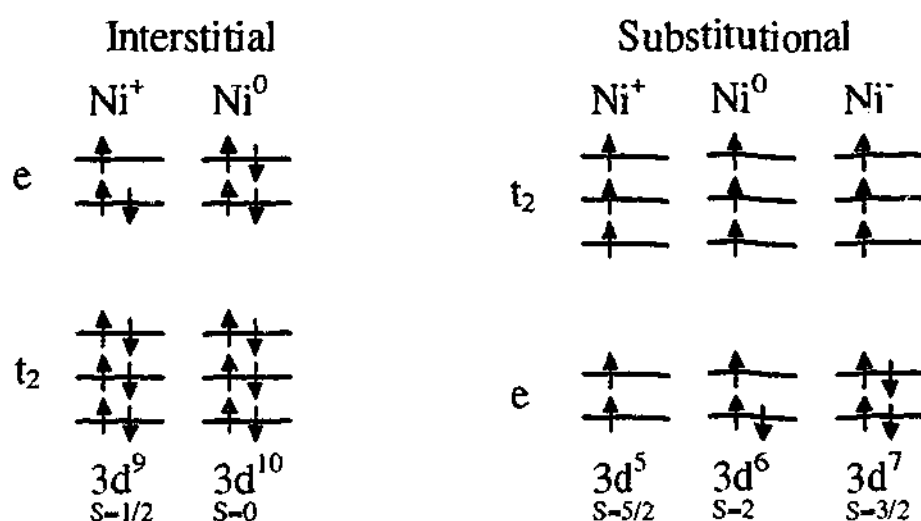


Figure 5.2 Electronic configuration for various charge states of a Nickel ion in substitutional and interstitial positions in a diamond lattice according to the Ludwig and Woodbury model¹⁷ after Isoya *et al*⁹

resulting in a S=3/2 spin state. The defect then appears similar to the positively charged vacancy. Other qualitative evidence to support this model is given in this paper.

A more recent paper on the electronic states of nickel in diamond, calculated by a discrete-variational X α (DV-X α) method¹⁶, also finds that the negatively charged substitutional nickel defect gives rise to an S=3/2 state and that the positively charged interstitial nickel defect gives rise to an S=1/2 state. Despite the differing theories put forward by various authors, there is a general agreement on the charge state and position of the nickel ions that give rise to the S=1/2 and S=3/2 spin states.

5.2 Experimental

The natural blue diamonds were of a grey-blue colour and generally of a rough shape with no discernible crystallographic faces. The largest stone was approximately 8mm along its longest axis. In total, six stones of this type were found at the Argyle mine and made available for study over a period of four years. This small number reflects the rarity of this variety of diamond.

The cw EPR was performed on a Bruker ESP380e EPR spectrometer at Monash University in the Department of Physics. Most of the cw spectra were recorded at room

temperature using a standard rectangular cavity. The pulsed EPR and some cw spectra were recorded using a cylindrical dielectric resonator. In this case an Oxford Instruments helium flow cryostat was used and temperatures down to 2 K could be reached. The sample could be rotated in the resonator using a simple one axis-goniometer.

The optical absorption spectra were recorded at Monash University, Department of Physics, with a Cary13 UV-vis spectrophotometer fitted with a diffuse reflectivity attachment. The spectra were recorded in transmission mode but the diffuse reflectivity attachment was used as it contained an integrating sphere. In this way reasonable spectra could be obtained with samples that had no polished faces. All optical absorption spectra were recorded at room temperature.

Fourier transform Infra-Red (FTIR) spectra were obtained in the Department of Chemistry, Monash University, using a Perkin Elmer FTIR microscope attached to a PE 1600 series FTIR spectrometer. The samples were manipulated on the stage of the microscope until sufficient transmission and relatively undistorted spectra were obtained.

Electron Nuclear Double Resonance (ENDOR) measurements were performed on a home-built X-band spectrometer in the Physics Department at the University of Paderborn in Germany. The microwave source was a 120 mW YIG oscillator and double balanced mixers were used for detection. One mixer provides the absorptive signal while the other provides the dispersive signal which is used for the AFC of the source. The RF is generated with a computer controlled synthesiser and a broad band amplifier. A frequency range of up to 30 MHz could be achieved with this amplifier. The cavity was a TE_{011} cavity with an integrated helium flow cryostat and the rf field was produced by 4 silver rods in a Helmholtz arrangement in the cavity. For more details about the ENDOR spectrometer refer to Spaeth et al¹⁸.

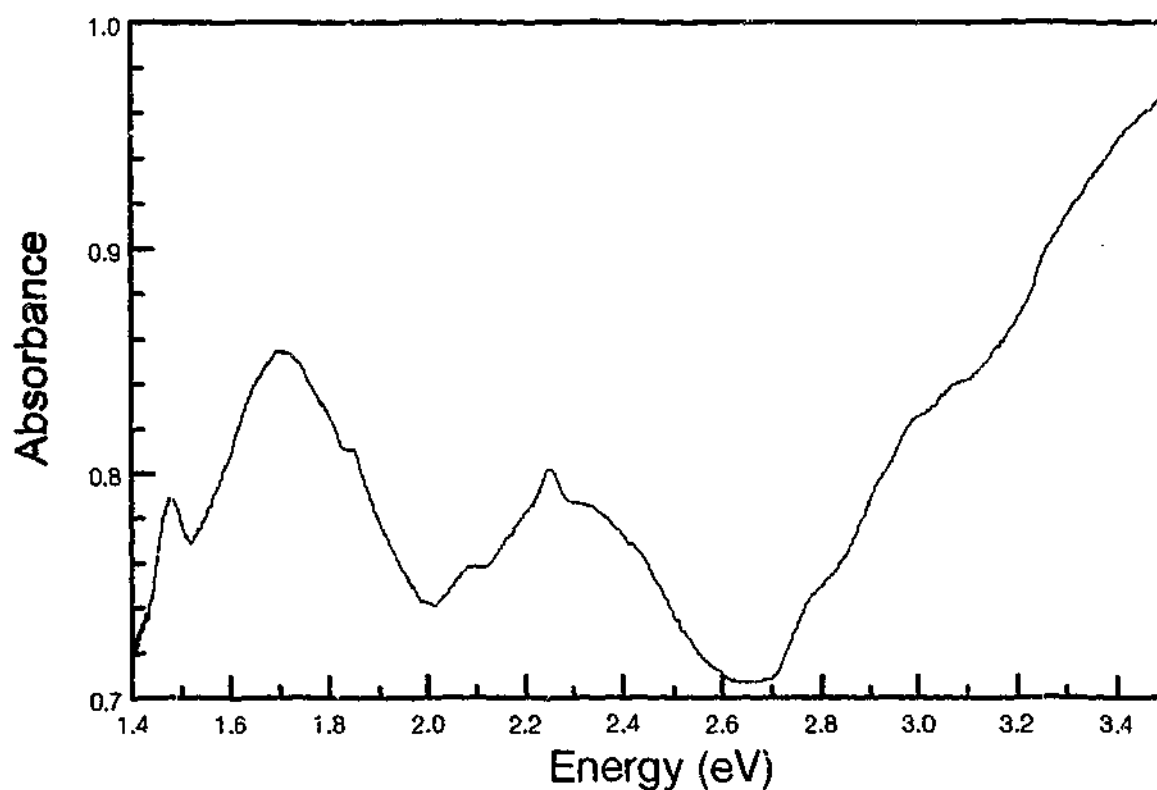


Figure 5.3 Optical absorption spectrum of Argyle blue diamond

5.3 Results

The room temperature optical absorption spectra, Figure 5.3, of the natural blue diamonds had two dominant broad absorption bands, one centred at 1.71 eV (725 nm) and another at 2.25 eV (550 nm). It is presumably the peak at 2.25 eV which is responsible for the blue colouration. The peak at 2.25 eV is also of interest because of its similarity to the absorption in the pink diamonds from the same mine. It has the same position and line width as the absorption band in the pinks and it is possible that the same defect is responsible in each case. However, as the absorptions are broad and there were no sharp features to indicate zero phonon lines, it is not possible to draw any firm conclusions. The smaller bumps at approximately 2.25 and 1.48 eV are also reproducible but it is not possible to identify them at this stage.

The FTIR spectra of the natural blue diamonds, Figure 5.4, indicate a relatively high nitrogen content, at least an order of magnitude greater than the pink diamonds, with the nitrogen predominantly in the form of B aggregates. The concentration of

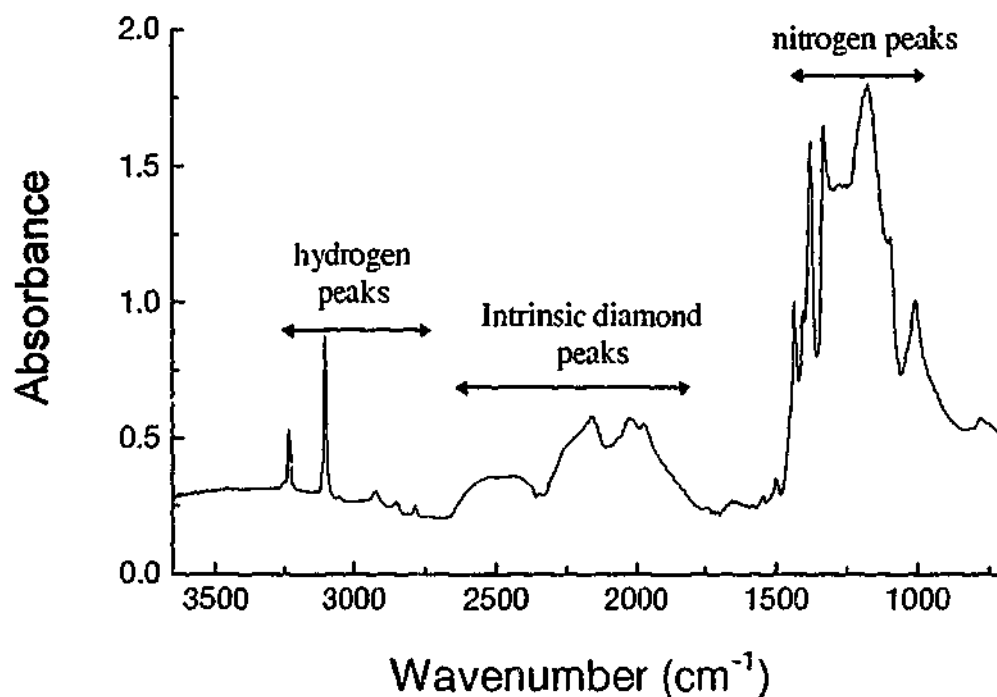


Figure 5.4 FTIR spectrum of Argyle blue diamond

nitrogen in the form of B aggregates is estimated to be 600 atomic ppm using the relation given by Woods et al.¹⁹ Also present is a large platelet peak at 1376 cm^{-1} . This places some lower limits on the geological history of these diamonds, as long times at high temperatures are needed to achieve this state of aggregation. Several other hydrogen related peaks are also present which have been previously reported by Fritsch et al.² The most prominent of these are the 3107 cm^{-1} and 3235 cm^{-1} peaks. The concentration of hydrogen in similar diamonds has been estimated to be 500 ppm.² Other lines are observed at 1404 cm^{-1} , 1434 cm^{-1} , 1498 cm^{-1} , 1546 cm^{-1} , 2784 cm^{-1} , 2852 cm^{-1} and 2924 cm^{-1} .

In the room temperature EPR spectra of the natural blue diamonds, Figure 5.5a, the common centres P1 and P2 were present as well other partially resolved and unidentified centres, possibly OK1, which have g values almost at the free electron value of 2.0023. In addition two other features at higher g values are also present in all of the blue diamonds. These are a broad isotropic line at $g = 2.02$ and a complicated series of

lines centred at $g=2.07$. The complicated spectrum was thought to be the result of superhyperfine splitting from at least three nitrogens. A centre involving three nitrogens had previously been described in nickel containing synthetic diamonds.¹⁰ This centre labelled NE2 was proposed to contain a nickel and three nitrogens. Simulations of the EPR spectrum for the NE2 centre using the literature spin Hamiltonian parameters gave a good fit to the experimental spectrum. This is shown for a spectrum with the field applied along a $\langle 100 \rangle$ axis (Figure 5.5b). A complete angular dependence of this EPR centre was not recorded as the poor signal to noise ratio necessitated long accumulation times to be able to resolve the complicated superhyperfine splittings. It was only with the field along a $\langle 100 \rangle$ axis that a clear spectrum could be obtained. Away from the $\langle 100 \rangle$ axis the spectrum becomes somewhat more complicated with lines moving to higher and lower fields

The broad line has not been previously reported. It shows no structure and the lineshape does not appear to vary with orientation. It is difficult to verify this because the NE2 spectrum overlaps with this line and obscures the lineshape at orientations of the applied field away from a $\langle 100 \rangle$ axis. The lineshape also showed no dependence on temperature or microwave power. This observation rules out some possible explanations for the large linewidth such as a highly spin coupled or ferromagnetic system. This leaves only inhomogeneous broadening to explain the large linewidth.

Pulsed EPR at a variety of temperatures was attempted on this line and the NE2 centre but an echo was seen only for the P1 centre. Thus no ESEEM or other pulsed EPR experiments were performed on these centres. It is not known whether the reason for the failure to observe an echo was due to there being too few spins or fast relaxation times or possibly a combination of both. The broad line would be expected to be inhomogeneously broadened and to give an echo.

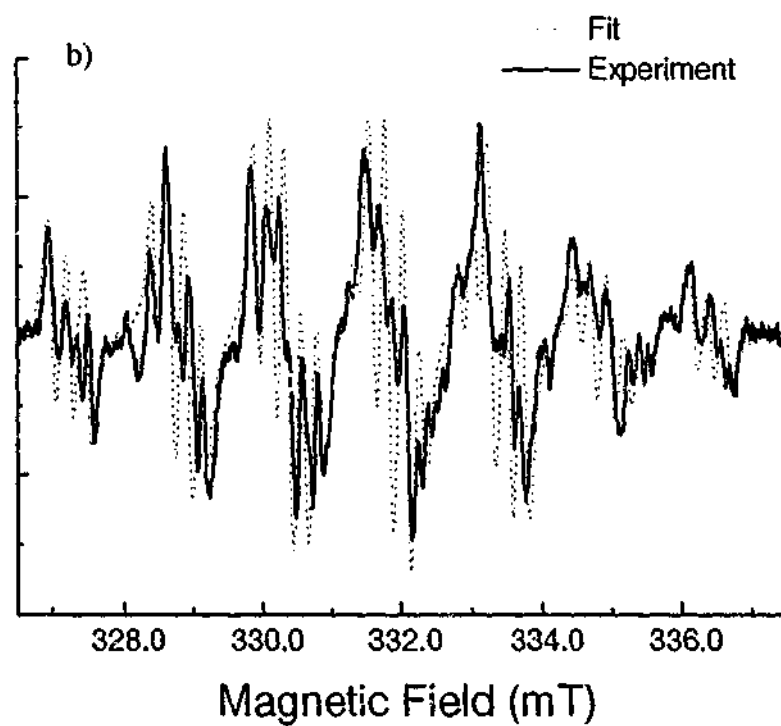
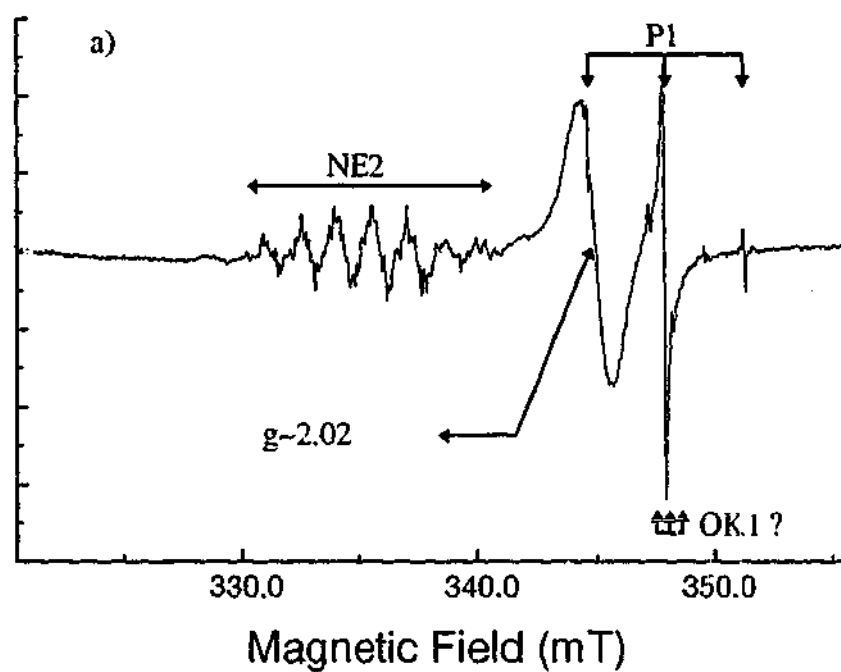


Figure 5.5 a) Room temperature EPR spectrum of Argyle blue diamond. The magnetic field is parallel to a $\langle 100 \rangle$ axis. At this orientation the P1 centre gives rise to three lines centred at $g = 2$. The other features are a broad isotropic line at 344.0 mT ($g \sim 2.02$) and a complicated set of lines at higher g values. b) Simulation of the EPR spectrum of Argyle blue diamond. The simulation was obtained by numerical diagonalisation of the spin Hamiltonian using the parameters for the NE2 centre given by Yelisseyev and Nadolinny.¹⁰

ENDOR spectra recorded on the broad $g=2.02$ line are shown in Figure 5.6. The spectra were recorded at 80 K with a microwave power of $12 \mu\text{W}$. Long accumulation times were needed to achieve a satisfactory signal to noise ratio. The dominant feature in the ENDOR spectra was a peak at the ^{13}C Larmor frequency indicating an interaction with matrix carbons. With the applied field close to a $\langle 100 \rangle$ axis another four lines were observed. These were arranged in two pairs with roughly equal spacing between them, centred at $1.711 \pm 0.005 \text{ MHz}$ and $3.020 \pm 0.005 \text{ MHz}$. These lines decreased dramatically in intensity as the applied field was rotated away from the $\langle 100 \rangle$ axis. There appeared to be some small variation in the line position, of the order of 10 kHz, but as the lines were only observed over a range of a few degrees it was not possible to determine the anisotropic part of the hf interaction with precision.

With these observations it was not possible to unambiguously assign the lines in the spectrum. However, an analysis of equation 5.1¹⁸, which shows the ENDOR frequencies to first order, does narrow the possibilities.

$$\nu_{\text{ENDOR}} = |m_s A - \nu_L + m_q P| \quad [5.1]$$

where

$$A = \frac{a + b[3\cos^2(\theta_A) - 1]}{h} \quad [5.2]$$

$$\nu_L = \frac{g_n \beta_n B_0}{h} \quad [5.3]$$

$$P = \frac{3q[3\cos^2(\theta_Q) - 1]}{h} \quad [5.4]$$

$$m_q = \frac{m_l + m_{l+1}}{2} \quad [5.5]$$

Equation 5.2 describes the superhyperfine (shf) interaction with a and b , the isotropic and anisotropic contributions. These quantities are related to the shf interaction tensor in the principal axis system, in the case of axial symmetry by

$$A_x = A_y = A_{\perp} = a - b \quad [5.6]$$

$$A_z = A_{\parallel} = a + 2b \quad [5.7]$$

θ_A is the angle between the applied field and z direction in this representation and h is the Planck constant. Equation 5.3 describes the nuclear Zeeman interaction with ν_L the Larmor frequency, g_n the nuclear g factor, β_n the nuclear magneton and B_0 the applied magnetic field Equation 5.4 describes the nuclear quadrupole interaction. The quadrupole coupling constant, q , is related to the quadrupole interaction tensor in the principal axis system, in the case of axial symmetry by

$$P_x = P_y = P_{\perp} = -q \quad [5.8]$$

$$P_z = P_{\parallel} = 2q \quad [5.9]$$

θ_Q is the angle between the applied field and z direction in this representation. In these equations m_s and m_I refer to the electron and nuclear spin states respectively and m_q is used to denote the two m_I states involved in the ENDOR transition where the quadrupole interaction is observed.

The most noteworthy feature of the experimental spectrum is the equal spacing between the two pairs labelled a-b and c-d in Figure 5.6. We can see that this splitting could, in principle, be due to any of the terms in equation 5.1. If we neglect the last term and assume $S=1/2$, the splitting can be either equal to $2A$ or $2\nu_L$. In the first case each pair would be centred at ν_L . The experimental values do not correspond to the Larmor frequency of any nucleus at this field so we can discount this possibility. Likewise, a nucleus with a Larmor frequency corresponding to the second case with a splitting of $2\nu_L$

cannot be found. We can then assume that the splitting is due to the last term in equation 5.1 and involves a quadrupole interaction with a nucleus with $I=1$.

To explain the position of the two pairs, a-b and c-d, we can look at three possibilities. If we assume $S=1/2$ then the two pairs could correspond either to the $m_s=1/2$ and $m_s=-1/2$ manifolds or to two different sites with different orientations to the magnetic field. In the first case the separation between the centre of each pair would be equal to $2\nu_L$ and again we find that a nucleus with this Larmor frequency does not exist. If the two pairs correspond to different sites with their principal axes at different angles to the magnetic field, then the quadrupole splitting would not be identical for the two pairs. Therefore, both of these possibilities can be discounted. In the third possibility, $S=3/2$, and the two pairs correspond to the $m_s=1/2$ and $m_s=3/2$ manifolds. In this case the position of the centres of the pairs would occur at $|A/2+\nu_L|$ and $|3A/2+\nu_L|$. The Larmor frequency of ^{14}N at this field is 1.0227 MHz and if we assume $A=1.336$ MHz good agreement is found with the experimental line positions. The calculated positions for the centres of the pairs a-b and c-d are then 1.691 and 3.026 MHz which correspond well with the experimental values of 1.711 ± 0.005 and 3.020 ± 0.005 MHz. Two more pairs of lines corresponding to the $m_s=-1/2$ and $m_s=-3/2$ manifolds would also be expected at 0.3547 and 0.9813 MHz. These lines were not resolved presumably due to a large non-resonant absorption occurring below 1.2 MHz.

Using equation 5.1, for the ENDOR frequencies to first order, we find that the model that best explains the number and position of the peaks in the ENDOR spectrum involves a defect with $S=3/2$ and $I=1$. We assume that both the shf and quadrupole interactions have the same principal axes along a $\langle 100 \rangle$ direction. The parameters that are calculated from the fitting are then, $A_{//}=1.336\pm 0.005$ MHz and $P_{//}=92\pm 5$ kHz if we take $\theta_A=\theta_Q=0^\circ$. As there will be sites with their principal axes along all six of the $\langle 100 \rangle$

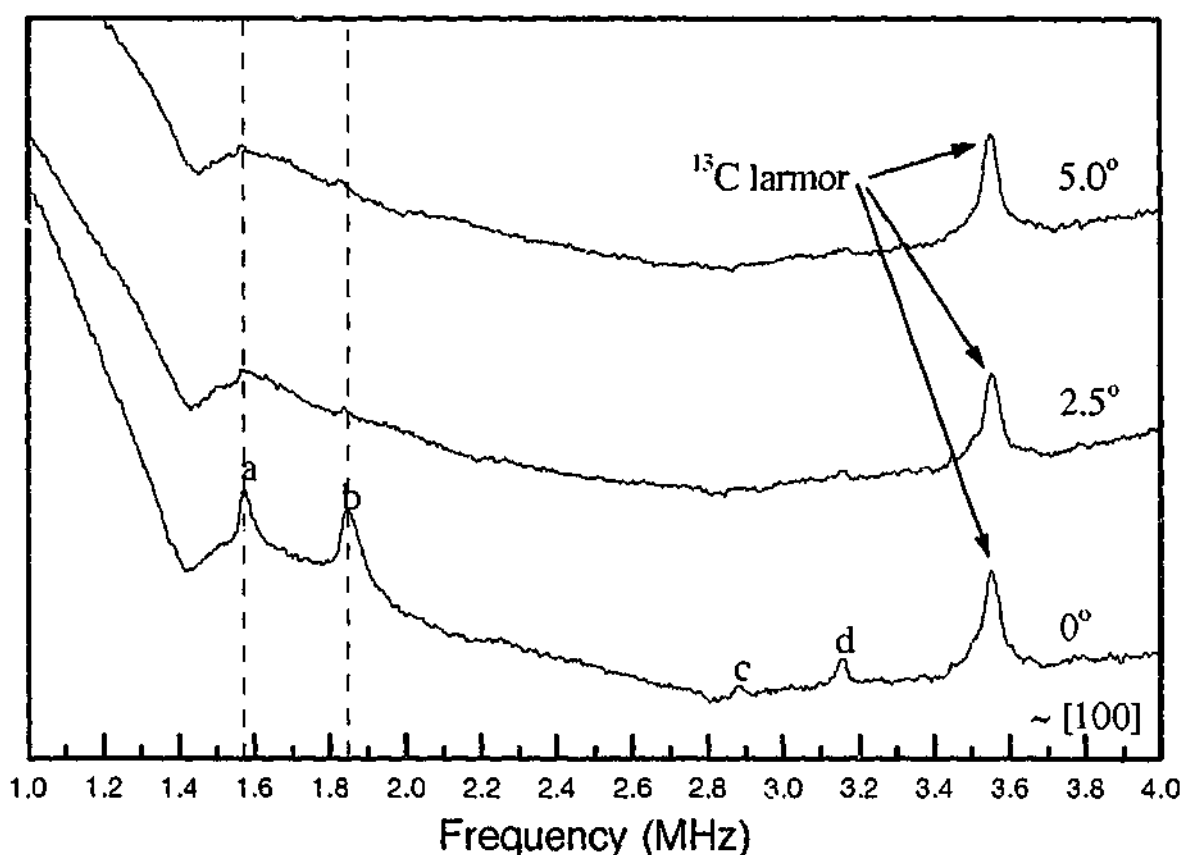


Figure 5.6 ENDOR spectra of Argyle blue diamond with the static magnetic field set at the centre of the broad resonance at $g=2.02$ seen in Figure 5.5. Magnetic field = 332.28 mT, microwave frequency = 9.3665 GHz, microwave power = 12 μ W, temperature = 80 K. ENDOR detected EPR was measured on the ^{13}C larmor frequency and matched the EPR lineshape of the broad resonance indicating that the ENDOR lines were related to this EPR resonance. For the lower trace the magnetic field was oriented parallel to a $\langle 100 \rangle$ axis. The middle and upper traces correspond to crystal rotations of 2.5 degrees and 5.0 degrees away from the $\langle 100 \rangle$ axis. A peak at 3.6 MHz, the ^{13}C Larmor frequency, is seen at all orientations of the magnetic field. It is only with the applied magnetic field close to a $\langle 100 \rangle$ axis that a set of lines labelled a-d are observed.

directions we would expect to see lines corresponding to both A_{\parallel} and A_{\perp} . We therefore assume that the set of the lines corresponding to the perpendicular orientation occur below 1 MHz and are not resolved in the experimental spectra. The situation could, of course, be the reverse with the perpendicular component being resolved rather than the parallel component. Without evidence to the contrary we will assume the former in the following discussion.

As these peaks in the ENDOR spectrum could only be well resolved with the field parallel to a $\langle 100 \rangle$ axis, the anisotropy of the shf interaction could not be determined with precision. The fact that a quadrupole interaction is observed implies that

b in equation 5.1 is non-zero and hence there is some anisotropy in the shf interaction. The ENDOR frequencies for the $m_s=1/2$ manifold appear to shift by a small amount of the order of 10 kHz within the 5 degrees in which the spectrum could be observed. If we neglect the quadrupole interaction, then over 5 degrees we would expect a shift in the ENDOR frequencies of approximately 1 percent of b . Therefore for a shift of 10 kHz we obtain an upper estimate for b of 1 MHz. If b were significantly larger than 1 MHz, then this would produce a more noticeable angular dependence of the ENDOR frequencies.

5.4 Discussion

Observations of Argyle blue diamonds show that the colour is caused by a characteristic absorption band at approximately 1.675 eV (740 nm). The absorption spectrum shows no sharp lines or structure indicating vibronic bands and it is not possible to speculate on the defect responsible for the absorption from these spectra. A broad absorption band is also seen at 2.25 eV (550 nm) and it is possible that it is due to the same defect that is present in the Argyle pink diamonds.

A set of hydrogen related lines in the infra-red as observed by Fritsch et al² are also seen in the blue diamonds. These hydrogen defects had been related to the colour but no direct correlation has been established. The diamonds also contain high concentrations of nitrogen >500 ppm predominantly in the B form. A statistical correlation between the nitrogen concentration and the hydrogen lines has also been observed.²⁰

The EPR spectra show P1 and P2 defects and other unresolved defects at $g=2.00$. Of more interest are other lines at $g>2.00$ which have also been observed. One of these has been identified as the NE2 centre which is believed to be a complex defect involving a nickel atom and three nitrogens.¹⁰ The other feature, a broad isotropic line at

$g \approx 2.02$, has not previously been reported. Out of all these features only the last is observed exclusively in Argyle blue diamonds. So far all Argyle blue diamonds that have been available for study, six, have had this feature. It is possible therefore that the defect responsible for this EPR feature is also responsible for the blue colour. Attempts to determine a direct correlation using ODMR were not successful due to the poor optical quality of the samples used. Future experiments with specimens with polished faces might resolve this issue but the rarity of these diamonds presents some problems.

The broad EPR line has no structure even at 4 K and no apparent angular variation. It is therefore impossible to obtain any structural information directly from the EPR spectra. It is possible to make a number of inferences. Firstly the line has a g value greater than 2. This is unusual in diamond where the strong covalent bonding quenches the spin-orbit coupling. Out of all the EPR centres observed, by far the majority have g values close to the free electron value.²¹ A g value greater than 2 is indicative of a more than half filled d-shell. The centres associated with nickel all have g values greater than 2. The fact that another nickel related centre, the NE2 centre, is found in the blue diamonds also implicates nickel in the new EPR centre.

Synthetic diamonds have been produced that contain nickel in a wide variety of defects but none show this broad line. What then is different in the natural blue diamonds? One feature of the blue diamonds is the high concentration of hydrogen. The EPR spectrum does not show a hyperfine splitting characteristic of hydrogen $I=1/2$ that would be expected if hydrogen were directly involved in the defect. The involvement of hydrogen could only be indirect such as a distant charge compensator.

The second major difference between the synthetic diamonds and the natural blue diamonds is the concentration and form of nitrogen defects. The natural blue diamonds

show a higher concentration of nitrogen, and probably more importantly it is present predominantly in the B form. A large platelet peak was also observed. The nitrogen in the natural blue diamonds is much more aggregated than in the synthetic diamonds where the nitrogen is in the A form. This indicates the extensive annealing that the natural diamonds have experienced over geological time scales. It is reasonable to expect that other defects containing nickel and a number of nitrogens may have been produced in this process.

The ENDOR spectrum was consistent with an $S = 3/2$ and $I = 1$ defect where ^{14}N is the nucleus involved. This could be consistent with nickel in an $S = 3/2$ spin state, Ni_s^+ , with shf from a neighbouring ^{14}N nucleus or, alternatively, the nitrogen itself could be in an $S = 3/2$ spin state. Nitrogen has recently been observed in nitrogen implanted C_{60} in an $S=3/2$ spin state.²² No EPR spectrum associated with interstitial nitrogen has so far been observed although it would be expected to be paramagnetic and theoretical calculations predict that a nitrogen interstitial in the tetrahedral site in diamond would give rise to an $S=3/2$ state with a hf interaction of the same order of magnitude as that observed in our spectra.²³ This defect would be expected to have a g value close to the free electron value in contrast to the experimental value of 2.02 and no quadrupole splitting, also in contrast to the experimental results.

The experimental results are therefore not consistent with a nitrogen interstitial in the tetrahedral site but do not rule out the possibility of a relaxed configuration. Theoretical calculations have, however, found that the migration energy of the nitrogen interstitial is sufficiently low that even at room temperature they would migrate and be trapped at other defects.²⁴ Kiflawi et al have provided evidence that the H1a optical centre seen in irradiated annealed diamonds is due to bond centred nitrogen interstitials.²⁵

The possibility that the broad EPR line in the blue diamonds is due to a nitrogen interstitial is therefore fairly small and the most likely model is a nickel defect in an $S=3/2$ state interacting with neighbouring nitrogens. The $g=2.0319$ defect in synthetic diamond has been shown to be $S=3/2$ and is believed to be due to a Ni^- ion on a substitutional site.⁸ The defect observed in this study could therefore be substitutional Ni^- with a neighbouring nitrogen. This would be consistent with the presence of the NE2 centre in these diamonds which is also believed to involve both nickel and nitrogen.¹⁰

Without the complete angular dependence of the ENDOR spectrum it is not possible to obtain enough parameters of the spin Hamiltonian to determine the exact structure of the defect. The order of magnitude of the quadrupole and shf interactions can, however, be used to give some information about the possible structures. For this we assume that the defect is Ni_s^- , to give the $S=3/2$ spin state, and that the shf interaction is from a neighbouring N^+ . Three approximations are made to obtain estimates of the shf and quadrupole parameters for various positions of the N^+ . Firstly we take the quadrupole interaction and consider the point charge contribution.¹⁸

$$P_{//} = 280.36 \frac{Q(1-\gamma_{\infty})}{4I(2I-1)R^3} \quad [5.10]$$

$P_{//}$ is the element of the quadrupole interaction in MHz, Q is the electric quadrupole moment in units of 10^{-24} cm^2 and is equal to 0.0193 for ^{14}N , I is the nuclear spin, γ_{∞} is the Sternheimer antishielding factor and is expected to be of the order of -3 for N^+ and R is the separation between the Ni_s^- and the N^+ in Angstroms. We base our estimate of γ_{∞} for N^+ on previous estimates of γ_{∞} for B^- which is isoelectronic with N^+ . In SiC $\gamma_{\infty}(B^-)$ was estimated to be -5²⁶ and for $\text{Si}(\text{Fe}^{3+}-B^-)$ pairs it was estimated to be -3.²⁷ We take the value of -3 as a more conservative estimate for our approximations.

The second approximation is to consider only the classic point dipole-dipole contribution to the anisotropic shf interaction.¹⁸

$$b_{dd} = 14.20 \frac{g_n}{R^3} \quad [5.11]$$

Here b_{dd} is in units of MHz, g_n is the nuclear g factor which is 0.40376 for ^{14}N . R is the separation between the Ni and the N^+ in Angstroms.

Finally to gain a rough estimate of the isotropic part of the shf interaction we look at the reported ^{13}C shf parameters for the nearest and next nearest neighbours in the Ni_5^- defect.⁹ Using the table in Morton and Preston²⁸ we note that the isotropic hyperfine interaction predicted for 100% localisation of the electron spin in a 2s orbital is 1811 MHz for ^{14}N and 3777 MHz for ^{13}C . If we assume that the electron wavefunction is not changed when a nitrogen substitutes for a carbon and that the same fraction of electron spin density will be on the N as was on the C, then the isotropic shf interaction for N^+ can be approximated by

$$a(^{14}\text{N}) = \frac{1811}{3777} a(^{13}\text{C}) \quad [5.12]$$

We then look at four positions for the nitrogen. Firstly we consider the nearest neighbour (nn) and next nearest neighbour (nnn) positions. The ENDOR spectrum indicates that the defect has a symmetry axis about [100] and it is therefore natural to consider structures that have this symmetry. Figure 5.7 shows the unit cell for diamond. It can be seen that the fourth nearest neighbour positions belong to the 100 class and are one unit cell spacing (3.56 Å) from the Ni_5^- . We also consider the interstitial position which is half a unit cell spacing from the Ni_5^- and is also in a $\langle 100 \rangle$ direction. The estimates for the quadrupole and shf parameters using equations 5.10-5.12 for these positions are presented in Table 5-1.

Table 5-1 Estimates of quadrupole and shf parameters for different positions of nitrogen.

N ⁺ Position	R (Å)	P (MHz)	b _{dd} (MHz)	a (MHz)
nn	1.54	0.74	1.57	9.2
nnn	2.52	0.17	0.36	4.2
4nn - [001]	3.56	0.06	0.13	-
[00½]	1.78	0.48	1.02	-

When we compare these estimates with the experimental values $P_{||} = 0.092 \pm 0.005$ MHz, $b < 1$ MHz and $a \sim 1$ MHz we conclude that the nitrogen is more distant than the next nearest neighbour position from the Ni. The most probable position is therefore the 4nn position one unit cell spacing in the [100] direction. We also compare our experimental value for the quadrupole parameter with that obtained for the N⁺ in the W7 centre.²⁹ The model for this defect has the N⁺ in a third nearest neighbour (3nn) position relative to the major nitrogen that has the electron spin and has a similar magnitude for the quadrupole interaction ($P_1 = 0.13$, $P_2 = -0.13$, $P_3 = 0.0$ MHz). We therefore propose that the defect structure involves Ni⁺ on a substitutional site and a nitrogen on a 4nn position.

There are several mechanisms that could possibly explain the rather broad line that is observed. These include spin lattice relaxation, dipolar broadening, superhyperfine splittings, and 'strain' broadening due to distributions in g values and/or zero field splitting parameters. These possibilities are each considered in the following paragraphs. In contrast to Ni_s⁺ we do not observe a temperature dependence of the linewidth and hence spin-lattice relaxation does not determine the linewidth. Dipolar broadening from other paramagnetic species does not seem to account for the linewidth as we would expect the other EPR centres to be broadened by the same mechanism which is not observed experimentally.

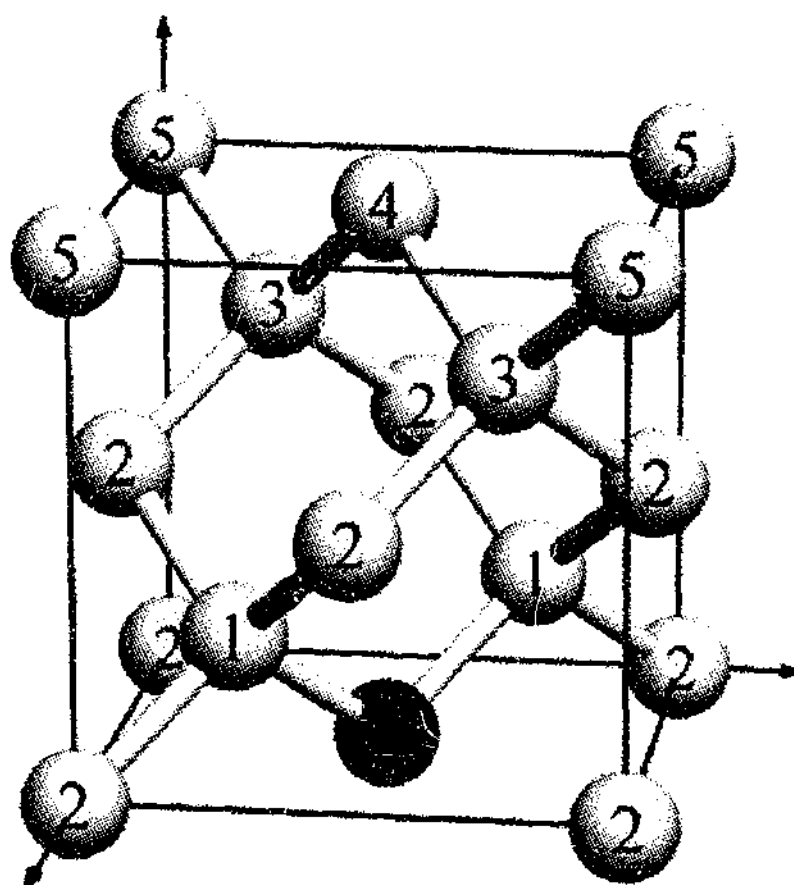


Figure 5.7 Unit cell of the diamond structure. A Ni^{2+} ion is shown on a substitutional position and the first to fifth nearest neighbour carbons are labelled. One of the six fourth nearest neighbour carbons is shown one unit cell spacing from the Ni^{2+} . The interstitial position in the centre of the unit cell can also be seen.

The shf interaction from a single N^+ determined from the ENDOR spectra could only account for at most 0.06 mT of the linewidth. From the ENDOR spectrum we cannot determine the number of nitrogens that are involved. There are six $4nn$ sites and it is therefore possible that up to six nitrogens may be associated with the Ni_s^{2+} . This would produce a Gaussian EPR lineshape. However, an analysis shows that only approximately 0.3 mT of the line width can be accounted for in this way. The high charge state of such a defect would also suggest a high formation energy and a low probability of it forming.

There are two other observations which could indicate the number of nitrogens involved. Firstly, the g factor of the EPR line appears to be isotropic. Secondly, we note that the ENDOR spectrum contains lines from both the $m_s=1/2$ and $m_s=3/2$ manifolds. This implies that the zero field splitting can be no larger than the EPR linewidth and therefore must be less than 40 MHz. This suggests that the Ni_s^{2+} largely retains its local

tetrahedral symmetry. It would be tempting to use a point charge model to estimate the magnitude of the zero field parameters from one or more positive charges at one unit cell spacing in a $\langle 100 \rangle$ direction. However, without accurate values for the Racah and spin orbit coupling parameters for this electronic configuration of nickel it is likely that the point charge approximation will be highly inaccurate. Hence it was not possible to determine whether this value of 40 MHz for the zero field splitting is consistent with the proposed models.

If the defect involved only one nitrogen we would expect some tetragonal distortion of the local environment of the nickel. This would result in anisotropic g values and a zero field splitting. This argument could be used to suggest that the defect has a symmetric structure with all six possible sites for the nitrogen occupied. However, as the nitrogen is proposed to be one unit cell distant from the nickel it is likely that the magnitude of this perturbation is quite small and may not produce noticeable effects.

Other diamonds from the Argyle mine, including the pink and brown coloured stones, are known to have large amounts of random strains resulting from plastic deformation. It is therefore possible that the blue diamonds also contain random strain and it is suggested that this could explain many of the features observed. The random strain would produce a distribution of sites with different zero field splittings and g values which would give rise to a broad isotropic Gaussian line as has been observed.

In a cubic environment the $3d^7 \ ^4F$ ground term is split into two orbital triplets (Γ_4 , Γ_5) and a singlet (Γ_2). In a tetragonally distorted configuration the following g and D values are expected for a Γ_4 ground state.³⁰

$$g_{\parallel} = g_e - 8\lambda / \Delta_0 \quad [5.13]$$

$$g_{\perp} = g_e - 8\lambda / \Delta_1 \quad [5.14]$$

$$D = 8\lambda^2(1/\Delta_1 - 1/\Delta_0) \quad [5.15]$$

λ is the spin orbit coupling parameter, Δ_0 and Δ_1 are the splittings between the $L=0$ and $L=\pm 1$ states of the orbital triplet Γ_5 state and the ground Γ_4 state. This would indicate that in the case of a random perturbation it is the distribution of fine structure splittings that will predominantly give rise to the linewidth. Multi-frequency experiments would have been useful to distinguish between these two cases, however, the only available specimens of the blue Argyle diamonds were too large for Q band measurements.

The relationships in equations 5.13 - 5.15 would tend to argue against the model with only a single nitrogen in the 4nn position. The small observed magnitude of D places limits on the size of tetragonal distortion and it is difficult to account for the difference between the g value of 2.0319 for the Ni_i^- defect and this defect. However, covalency will require the inclusion of a reduction factor for the spin orbit coupling. It is therefore possible that the shift in the g -value from that for the Ni_i^- defect is caused by changes in the electron spin localisation on the carbon atoms surrounding the Ni defect.

A similar distribution of zero field splittings was observed with the Ni_i^- centre.⁹ This would still be consistent with the observation of the $m_s=1/2$ and $m_s=3/2$ manifolds in the ENDOR spectra as a certain fraction of the defects would be unperturbed and have small zero field splittings. The random strains would also produce a distribution in the ENDOR frequencies. This may explain why only weak lines could be resolved on top of a broad baseline in the ENDOR spectra. The model proposed for this defect can therefore account for the features of the EPR and ENDOR spectra.

5.5 Conclusion

The results show that these blue diamonds contain nickel and a high concentration of nitrogen. The diamonds have been subjected to high temperatures over geological time scales. This has led to the formation of nitrogen aggregates and defects containing both nickel and nitrogen. One of these, the NE2 centre, has previously been observed in synthetic and natural diamonds and has been proposed to be Ni^+ in a divacancy position with three neighbouring nitrogens. The second has not been observed previously and occurs exclusively in Argyle blue diamonds. We propose that this defect is Ni_5^- with N^+ in a 4nn position. This defect has not been produced in synthetic diamonds and it appears that annealing over geological time scales is needed. Plastic deformation, which is common in other Argyle diamonds, also appears to play a role in these diamonds. The diamonds also contain high concentrations of hydrogen, which has previously been reported, but it is not clear how this is related to the nickel centres observed or the colour. The new nickel defect we have observed is found only in these blue diamonds and so it is suggested that it may be responsible for the colour.

5.6 Acknowledgments

John Chapman of Argyle diamonds is thanked for the loan of the natural blue diamonds used in this work. Thanks are also given to Dr. Gordon Troup who initiated the research on the Argyle diamonds. Prof. J.M. Spaeth and Dr. T. Pawlik are thanked for their help and hospitality whilst visiting the University of Paderborn in Germany and their continued assistance afterwards. Bayden Wood is also thanked for assisting with the FTIR spectra. Finally, the Queens Trust is thanked for financial assistance to travel overseas to complete aspects of this work.

5.7 References

- ¹ Collins, A.T., *Journal of Gemmology*, **18**, (1982) 37.
- ² Fritsch, E., Scarrat, K., Collins, A.T., in *New Diamond Science and Technology*, *MRS Int. Conf. Proc.*, (1991), 671-676.
- ³ Loubser, J.H.N. and van Ryneveld, W.P., *Nature* **211**, (1966) 517.
- ⁴ Samoilovich, M.I., Bezrukov, G.N. and Butuzov, V.P., *Pis'ma Zh. Eksp. Teor. Fiz.* **14**, (1971) 551 [*JETP Lett.* **14**, (1971) 379].
- ⁵ Collins, A.T., Kanda, H., and Burns, R.C., *Philos.Mag. B* **61**, (1990) 797.
- ⁶ Nazaré, M.H., Neves, A.J., and Davies, G. *Phys Rev B* **43**, (1991) 196.
- ⁷ Paslovsky, L., and Lowther, J.E., *J. Phys. Condens. Matter* **4**, (1992) 775.
- ⁸ Isoya, J., Kanda, H., and Uchida, Y., *Phys. Rev. B* **42**, (1990) 9843.
- ⁹ Isoya, J., Kanda, H., Norris, J.R., Tang, J., and Bowman, M.K., *Phys. Rev. B* **41**, (1990) 3905.
- ¹⁰ Yelisseyev, A., and Nadolinny, V., *Doklady Akademii Nauk* **326**, (1992) 524.
- ¹¹ Nadolinny, V., and Yelisseyev, A., *Diamond and Related Materials* **3**, (1994) 1196-1200.
- ¹² Nadolinny, V.A., Yelisseyev, A.P., Baker, J.M., Newton, M.E., Twitchen, D.J., Lawson, S.C., Yuryeva, O.P., and Feigelson, B.N., *J. Phys.: Condens. Matter*, **11**, (1999), 7357-7376.
- ¹³ Lawson, S.C., and Kanda, H., *J. Appl. Phys.* **73**, (1993) 3967-3973.
- ¹⁴ Mineeva, R.M., Speranskii, A.V., Titkov, S.V., and Bershov, L.V., *Doklady Akademii Nauk* **334**, (1994) 755-758.
- ¹⁵ Lowther, J.E., *Phys. Rev. B* **51**, (1995) 91-96.
- ¹⁶ Ohashi, N., Fukunaga, O., Isoya, J. and Tanaka, J., *Japanese Journal of Applied Physics Part I-Regular Papers Short Notes & Review Papers*. **36**, (1997) 1126-1131.
- ¹⁷ Ludwig, G.W. and Woodbury, H.H., in *Solid State Physics*, edited by Seitz, F. and Turnbull, D., Academic, New York, (1962), Vol. 13, p.223.
- ¹⁸ Spaeth, J.-M., Niklas, J.R. and Bartram, R.H., *Structural Analysis of Point Defects in Solids*, Springer-Verlag, 1992.
- ¹⁹ Woods, G.S., Purser, G.C., Mtimkulu, A.S.S. and Collins, A.T. *J. Phys. Chem. Solids* **51**, (1990) 1191-1197.
- ²⁰ John Chapman, Argyle Diamonds, private communication (1997).
- ²¹ Ammerlaan, C.A.J., *Landolt-Bornstein Numerical Data and Functional Relationships in Science and Technology, New Series III* (Madelung, O., Shulz, M., eds), vol 22b, Berlin, Springer (1990) 117-206.
- ²² Almeida Murphy, T., Pawlik, Th., Weidinger, A., Höhne, M. and Spaeth, J.-M., *Phys. Rev. B* **77**, (1996) 1075.
- ²³ Overhof, H., private communication (1997).
- ²⁴ Mainwood, A., *Phys.Rev. B* **49**, (1994) 7935-7940.
- ²⁵ Kiflawi, I., Mainwood, A., Kanda, H., and Fisher, D, *Phys. Rev. B.*, **54**, (1996) 16719-16725.
- ²⁶ Müller, R., Feege, M., Greulich-Weber, S., Spaeth, J.-M., *Semicond. Sci. Technol.*, **8**, (1993) 1377.
- ²⁷ Spaeth, J.-M., Greulich-Weber, S., Martini, S., *Semiconductor Science and Technology*, submitted
- ²⁸ Morton, J.R., and Preston, K.F., *J. Magn. Reson.*, **30**, (1978) 577-582.
- ²⁹ Newton, M.E., and Baker, J.M., *J. Phys. Condens. Matter*, **3**, (1991) 3591-3603.
- ³⁰ Abragam, and Bleaney, B. *Electron Paramagnetic Resonance of Transition Ions*, Clarendon, (1970).

6. ODMR of Nickel Centres in Synthetic HTHP Diamonds[†]

6.1 Introduction

In the previous chapter EPR and ENDOR spectra of natural blue diamonds were presented. In these diamonds EPR centres involving both nickel and nitrogen were observed. Some of these centres have previously been observed in synthetic diamonds and attempts have been made to correlate these defects with optical absorption spectra. This has been achieved by correlating EPR and optical spectra in diamonds grown with differing amounts of nickel and nitrogen and during differing stages of annealing. However such correlations can be difficult to establish unless a large number of samples are used. In contrast, optically detected magnetic resonance (ODMR) directly correlates optical features with EPR centres.

Only a couple of ODMR studies have been published on these defect centres.^{1,2} These have both recorded ODMR from the broad 2.56 eV luminescence. This band has been related to the $g=2.0319$ EPR defect, Ni_2^- , and substitutional nitrogen. In the current chapter several defects are observed using MCD-ODMR and are correlated directly to optical transitions. This improves on the purely statistical correlation that has been observed in the past between these optical and EPR centres. The ODMR technique is also extremely sensitive and several new defects are reported for the first time.

6.2 Experimental

The synthetic diamonds were grown at the National Institute for Research in Organic Materials in Japan using the temperature gradient method from a pure nickel solvent catalyst at approximately 1500°C and 6GPa. The resulting diamonds contained

[†] Parts of this chapter have been previously published in an article, Pawlik, Th., Noble, C. and Spaeth, J-M., *J. Phys.: Condens. Matter*, 10, (1998) 9833.

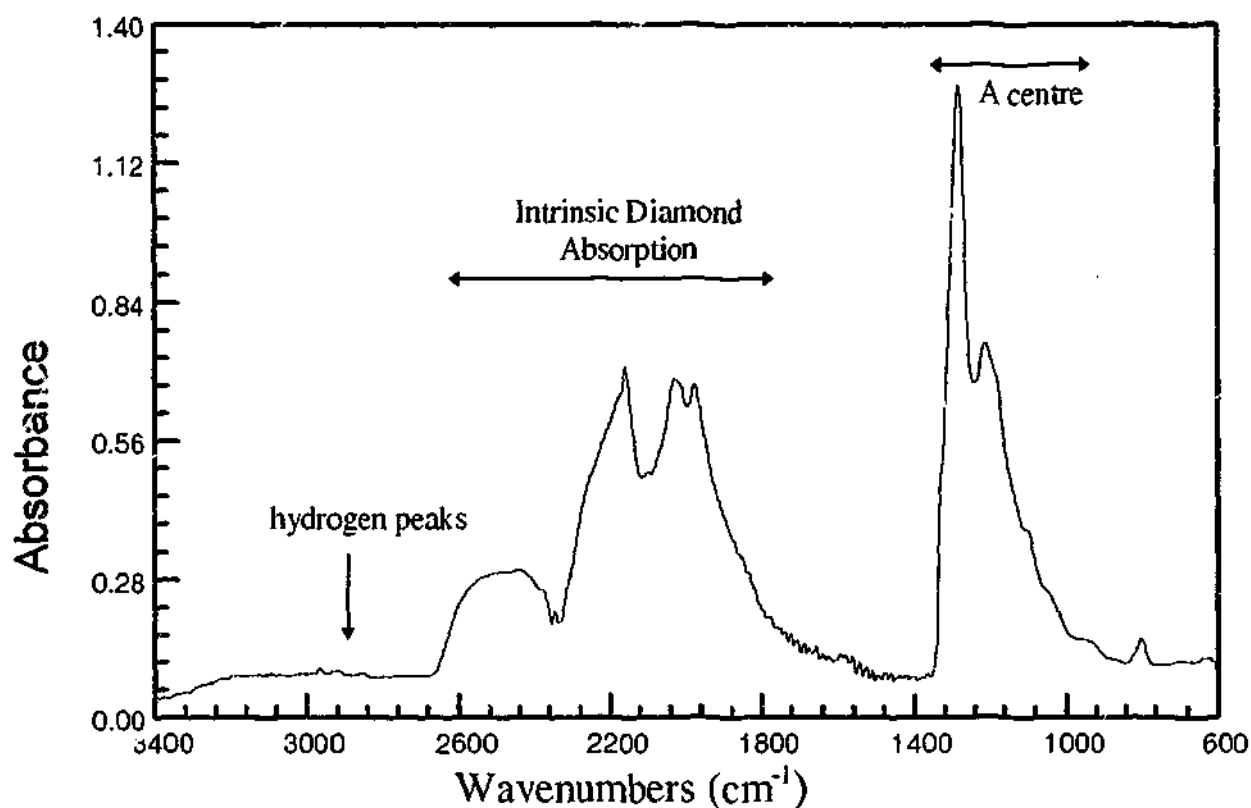


Figure 6.1 FTIR spectrum of the synthetic diamond. The main features are the A centre absorption in the defect induced one phonon region and a set of hydrogen related lines at about 2900 cm^{-1}

substantial concentrations of both nickel and nitrogen. They were subsequently annealed at a temperature of approximately 1700 °C for a period of several hours and at a pressure of between 7 to 9 GPa . The diamonds then had a colour ranging from a golden yellow to brown throughout the crystal indicating some inhomogeneity in the distribution of the defect centres. The diamonds were of a cuboid form with all dimensions less than 2mm. They had been polished with faces approximately in the crystallographic planes (110), (1 $\bar{1}$ 0) and (001) for one diamond and with the other having (111), (11 $\bar{2}$) and (1 $\bar{1}$ 0) faces.

FTIR spectra were obtained in the Department of Chemistry, Monash University, using a Perkin Elmer FTIR microscope attached to a PE 1600 series FTIR spectrometer. The samples were manipulated on the stage of the microscope until sufficient transmission and relatively undistorted spectra were obtained.

The cw EPR was performed on a Bruker ESP380e at Monash University in the Department of Physics. Most of the cw spectra were recorded at room temperature using a standard rectangular cavity. The pulsed EPR and some cw spectra were recorded using a cylindrical dielectric resonator. In this case an Oxford Instruments helium flow cryostat was used and temperatures down to 2 K could be reached. The sample could be rotated in the resonator using a simple one axis-goniometer.

The MCD and ODMR measurements were performed on a home-built MCDA ODMR spectrometer in the physics department at the University of Paderborn in Germany. A helium immersion cryostat was used and temperatures down to 1.5 °K could be achieved with pumping. Split coil superconducting magnets were used for the static field. The magnetic field strength was measured by the current in the coils and hence it was difficult to obtain the absolute field strength without an independent calibration. A photomultiplier was used for detection in the visible range and a cooled germanium detector was used in the red and infra-red region. The sample was in a K band TE₀₁₁ cavity with a klystron microwave source. This source was not used in the experiments due to difficulties coupling to the cavity mode. Instead a 72 GHz source was used. It consisted of a 7.2 GHz varactor tuned transistor oscillator which was frequency multiplied to 72 GHz and amplified to 150 mW. The microwaves were then introduced into the cavity through an optical port. The frequency of the source could be adjusted between 72.2 GHz and 72.55 GHz by adjusting a voltage on the oscillator. The source however had a number of additional modes which gave rise to additional resonances in the ODMR spectra. For more details about the ODMR spectrometer refer to Spaeth et al³.

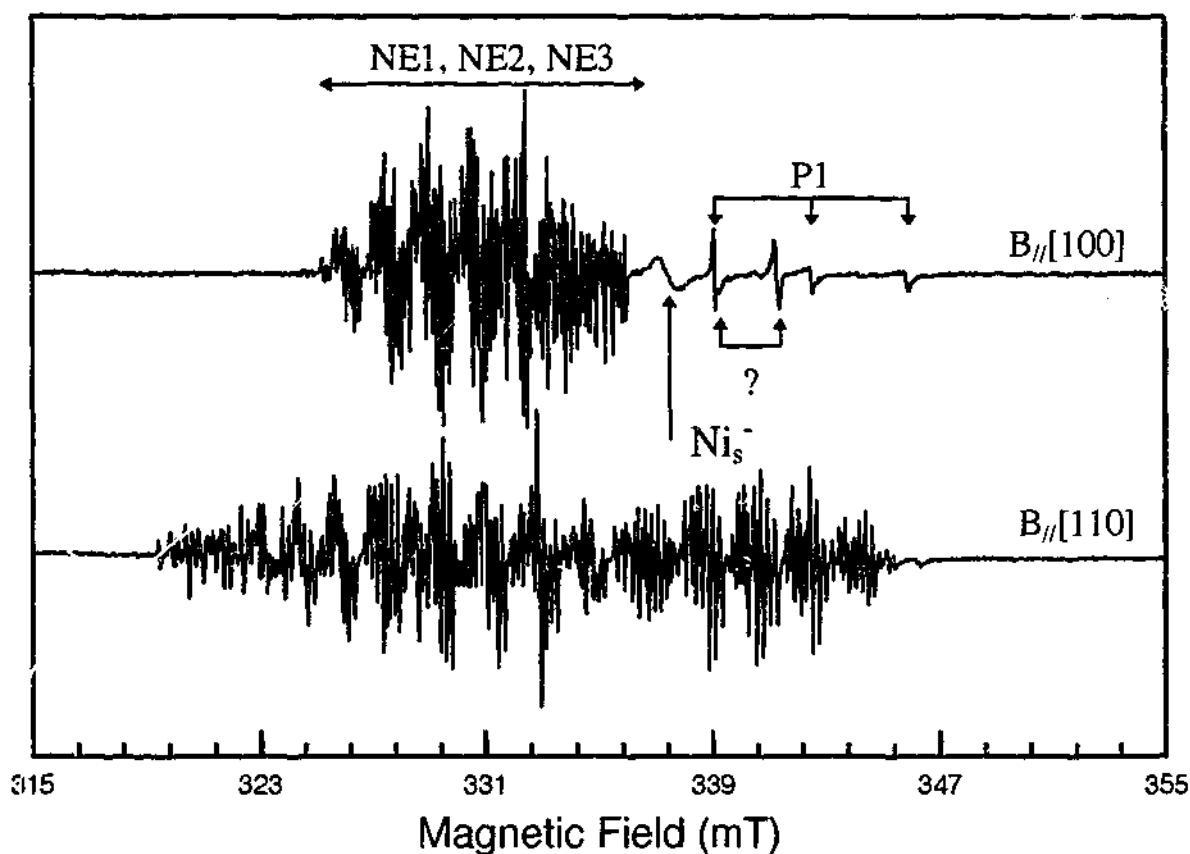


Figure 6.2 EPR spectrum of a synthetic nickel-containing diamond with the applied field parallel to a $\langle 100 \rangle$ axis and a $\langle 110 \rangle$ axis. The P1 centre spectrum is again present in these diamonds as is the NE series of defects that give rise to the complicated set of lines at higher g values. The spectrum is simplest with the field along a $\langle 100 \rangle$ direction.

6.3 Results

The FTIR spectrum of the synthetic diamonds, Figure 6.1, showed a significant concentration of nitrogen in the A form, nearest neighbour pairs. The concentration of nitrogen in the A form is estimated to be 50 atomic ppm using the relation given in Woods et al⁴. This shows that the aggregation of nitrogen from the heat treatment has progressed as far as A centres but not further. Also present are some hydrogen related peaks near 2900 cm^{-1} but peaks at 3107 cm^{-1} and 3235 cm^{-1} seen in the natural blue diamonds are absent in this case.

The EPR spectra of the synthetic diamonds showed strong NE1, NE2 and NE3 resonances, the nickel nitrogen centres described by Yelisseyev and Nadolinny⁵, in addition to the ubiquitous P1 centre and some unidentified centres. As the NE resonances were stronger in these diamonds compared to the natural blue diamonds it

was easier to get well resolved spectra with a higher signal to noise ratio. Figure 6.2 shows the EPR spectra obtained with the magnetic field close to a $\langle 100 \rangle$ axis. A large number of narrow lines are resolved that arise from several superhyperfine splittings and several magnetically inequivalent centres.

A broad line is also seen at approximately $g=2.032$ and is almost definitely Ni_i^2+ . The line appears to broaden when the field is rotated away from the $\langle 100 \rangle$ axis but it is difficult to verify this because the spectra from the NE centres obscures this line when the field is away from the $\langle 100 \rangle$ axis.

The EPR spectra of the NE centres at two orientations of the magnetic field are shown in Figure 6.2. Even in these better resolved spectra it is hard to follow the position of the individual lines as the crystal is rotated and, a complete fitting has not been attempted.

Another set of lines between 338.0 mT and 342.0 mT are also seen when the field is parallel with a $\langle 100 \rangle$ axis, Figure 6.2. This region is expanded in Figure 6.3a. It is only possible to observe the spectrum with the magnetic field within 15° as the NE set of lines overlaps at other orientations. Two sets of lines could be seen that were symmetrical about the $\langle 100 \rangle$ axis, an unresolved line at approximately 341.5 mT and another line showing superhyperfine splitting centred at 343.8 mT. The angular dependence of these lines could be fitted to a $S=1/2$ system with $g_{\parallel}=2.0225 \pm 0.0005$, $g_{\perp}=2.0095 \pm 0.0005$ with the symmetry axis parallel to a $\langle 100 \rangle$ direction.

With the magnetic field parallel to a $\langle 100 \rangle$ axis the high field line is split into five with weightings that suggest a superhyperfine splitting by two equivalent nitrogens with $I=1$. The superhyperfine splitting on the low field line is unresolved and must be less than the linewidth. The estimates for the hyperfine interaction parameters are $A_{\perp} = 1.5 \pm 0.1$

MHz, $|A_{\parallel}| < 0.6$ MHz. The uncertainty in A_{\parallel} leads to a range of values for a and b , the isotropic and anisotropic components of the hyperfine interaction respectively, where $A_{\perp} = a - b$ and $A_{\parallel} = a + 2b$. The two extremes are $A_{\parallel} = +0.6$ MHz, $a = 1.2$ MHz, $b = -0.3$ MHz or $A_{\parallel} = -0.6$ MHz, $a = 0.8$ MHz, $b = -0.7$ MHz. Transition positions calculated with $A_{\parallel} = +0.6$ MHz, $A_{\perp} = 1.5$ MHz are plotted with experimentally observed positions in Figure 6.3b

The large number and complicated pattern of lines due to the NE centres made a complete angular dependence study impossible. Many different centres had transitions in the same magnetic field region and assigning individual transitions was not possible except in a few cases where there was little overlapping. Ideally, samples would be prepared that have different concentrations of the EPR centres, but this was not possible as only two stones were available for study.

Pulsed EPR can in some cases simplify EPR spectra where there are a large number of superhyperfine interactions. The NE centres with several nitrogen superfine interactions therefore present a possibility for the application of pulsed techniques. In contrast to the natural blue diamonds, discussed in the previous chapter, it was possible to observe an echo from the NE centres in these diamonds. These centres have relatively long relaxation times and it was possible to perform 3 pulse ESEEM experiments which are shown in Figure 6.5.

The ESEEM spectra show a number of peaks mostly around 5 and 10 MHz. These correspond to the smaller hyperfine splittings seen in the cw EPR spectra but as these are resolved in the cw spectra little is gained. The ESEEM frequencies change showing that one or more different magnetically inequivalent centres are being sampled at the different field positions. A complete analysis of the ESEEM would therefore

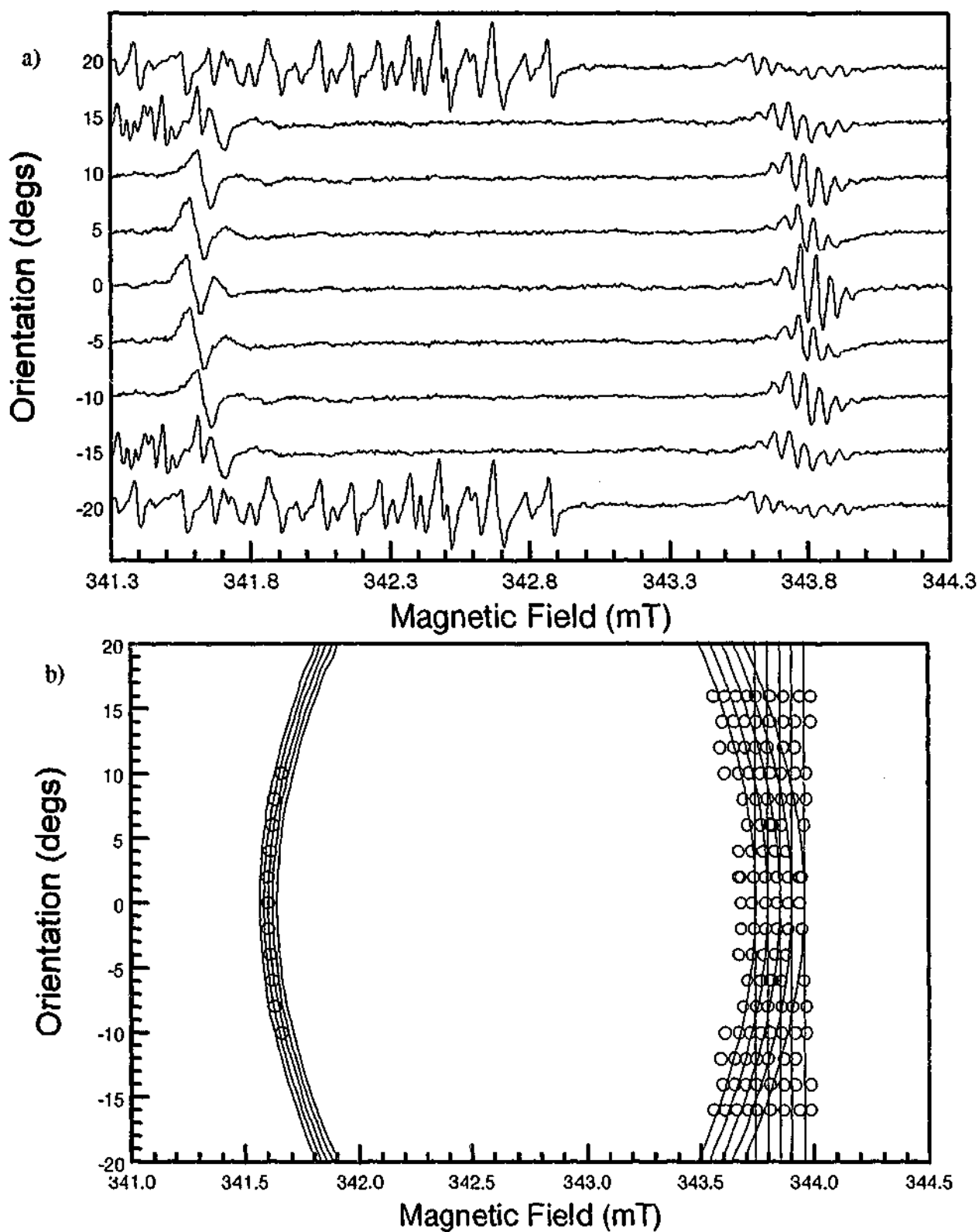


Figure 6.3 An enlarged region of Figure 6.2 showing the angular dependence of the previously unreported centre with $\langle 100 \rangle$ symmetry. The magnetic field is rotated in a $\{100\}$ plane. b) fitting of the experimental line positions with spin Hamiltonian parameters $S=1/2$ and $g_{\parallel}=2.0225$, $g_{\perp}=2.0095$ and two equivalent ^{14}N nuclei with $I=1$ and $A_{\parallel}=0.5$ MHz, $A_{\perp}=1.5$ MHz

require spectra both as a function of orientation and magnitude of the magnetic field. The ESEEM spectra therefore do not significantly simplify the process of obtaining spin Hamiltonian parameters in this case.

The optical absorption spectra of the synthetic diamonds showed a number of

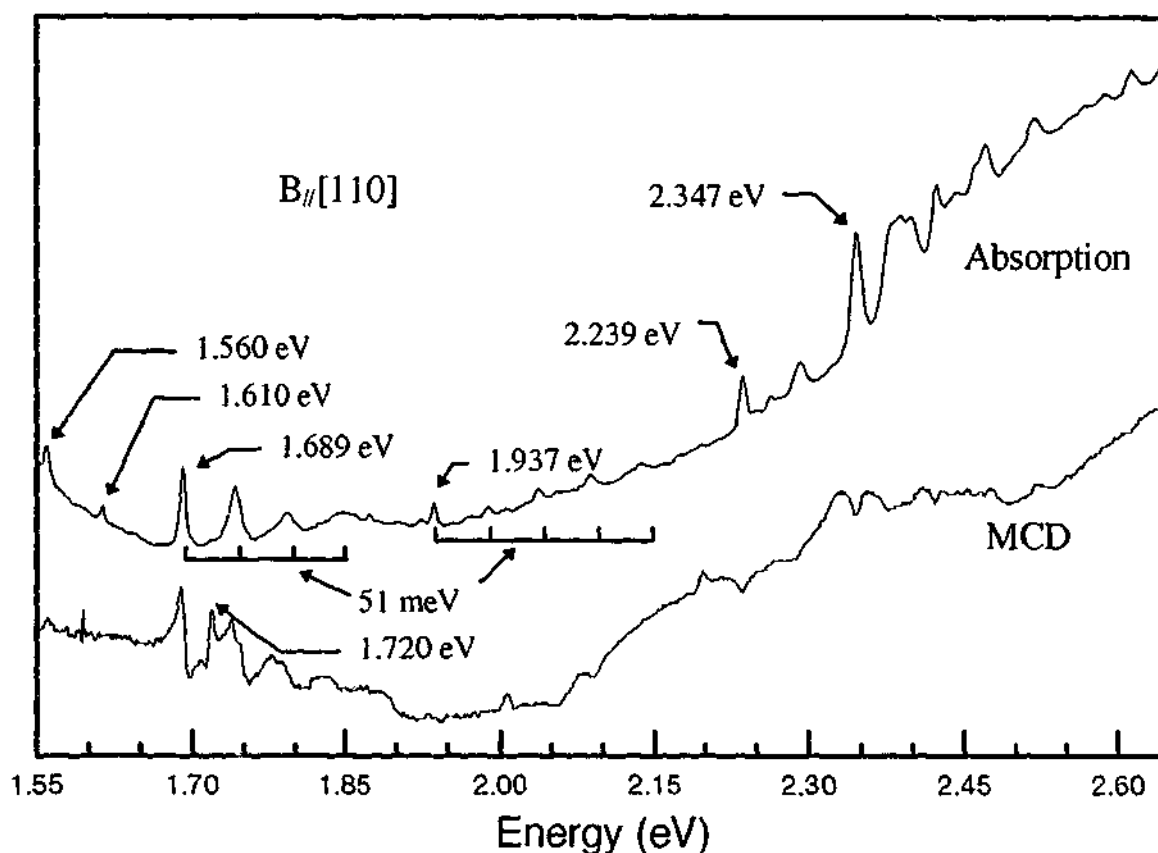


Figure 6.4 Optical absorption spectrum of synthetic diamond recorded at $T = 1.5$ K. Several lines are seen in the absorption spectrum. These lines including ZPLs at 1.689 eV (1.693 eV) and 1.937 eV (1.938 eV) have previously been reported.⁶ Note the dominant 51 meV phonon energy in the phonon assisted band. The MCD spectrum recorded at $B = 2.5$ T, $T = 1.5$ K for the same energy range is shown for comparison. Note that the various lines are present in differing amounts in the two spectra, especially the 1.720 eV line which is visible in the MCD spectrum but are very weak in the absorption spectrum

sharp lines that have previously been reported.⁶ The most notable of these is a well defined vibronic band with a ZPL at 1.693 eV and a dominant 51 meV phonon energy, as well as a set of related lines between 2.2 and 2.6 eV. The MCD spectrum for the same range is shown with the optical absorption spectrum in Figure 6.4. Most of the features in the absorption spectrum are seen in MCD to varying degrees. It is also important to note that some features that are not evident in the absorption spectrum are strong in the MCD spectrum. The best example of this is the line at 1.720 eV which is seen clearly in MCD but not at all in the absorption spectrum. This line has not been reported before in optical studies of these diamonds.

The subsequent MCD and ODMR results are at lower energies due to the better sensitivity obtained in this range using a germanium detector. In this range a number of

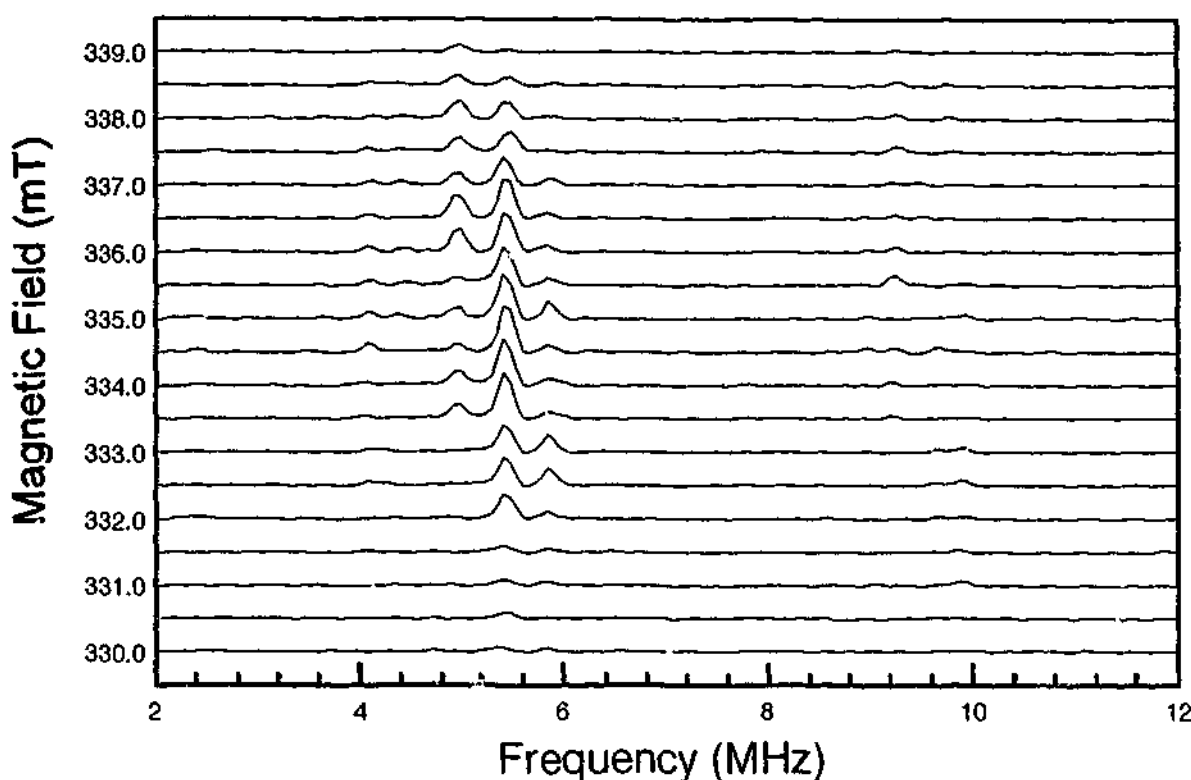


Figure 6.5 Three pulse ESEEM spectra of the synthetic diamond recorded at magnetic field values between 330.0 and 339.0 mT in 0.5 mT steps. The magnetic field is aligned to a $\langle 100 \rangle$ direction. The pulse lengths used in the sequence are 16 ns for the pulses widths, 200 ns for τ and a increment of 32 ns for T with a resolution of 1024 points. The raw data was baseline corrected and Fourier transformed.

lines were seen in MCD. These are shown in Figure 6.7a and include the 1.688 eV and 1.720 eV lines seen in Figure 6.4, the well known line at 1.4 eV and some lines previously unreported at 1.295 eV and 1.059 eV. All of these lines appeared to be due to paramagnetic defects, as their intensity changed with the applied field strength. ODMR was recorded for five different optical energies and these spectra are shown in Figure 6.7b. Of these the spectra recorded at 1.403 eV, 1.277 eV and possibly 1.295 eV appear similar and thus all these optical transitions could arise from the same defect.

It should be noted at this stage that the 72 GHz source used in these ODMR experiments had a number of higher modes some 500 MHz higher than the principal mode. This is evident in the ODMR spectra as additional lines in increments of approximately 20 mT higher in field. The additional modes were several dBs lower in power than the fundamental and the degree to which they were seen in the ODMR

spectra depended on the relaxation behaviour of the defect and the degree of saturation of the EPR transition corresponding to each mode.

The ODMR recorded at 1.688 eV and 1.720 eV were quite distinctive and appeared to be related to different defect centres. This was confirmed by recording MCD spectra with the magnetic field set to two positions marked in Figure 6.6a. These field positions were on-resonance for one of the EPR spectra but off-resonance for the other. The MCD spectrum was also recorded with the field off resonance for both the EPR spectra. The difference between this spectrum and the on resonance spectra then gave EPR tagged MCD spectra for the two EPR spectra.

Figure 6.6b shows the two EPR tagged MCD spectra with field values at 1 and 2. The first EPR spectrum in Figure 6.6a is shown to correlate with a system with a ZPL at 1.720 eV and a dominant phonon energy of 32 meV. The second EPR spectrum in Figure 6.6a is shown to correlate with a system with a ZPL at approximately 1.688 eV and a dominant phonon energy of 52 meV.

The ODMR spectra that was best resolved was that related to the 1.720 eV line and most of the subsequent work focussed on this centre. The angular dependence of the ODMR spectrum of this centre is shown in Figure 6.8a. The rotation was about a $\langle 11\bar{2} \rangle$ direction and again note that additional lines are seen at about 20 mT higher for each resonance due to the extra modes of the source. The transition positions at each orientation were measured and were found to be consistent with an $S=1/2$ defect having $\langle 111 \rangle$ symmetry with $g_{\parallel} = 2.004 \pm 0.005$ and $g_{\perp} = 2.093 \pm 0.005$. The simulation is shown in Figure 6.8b.

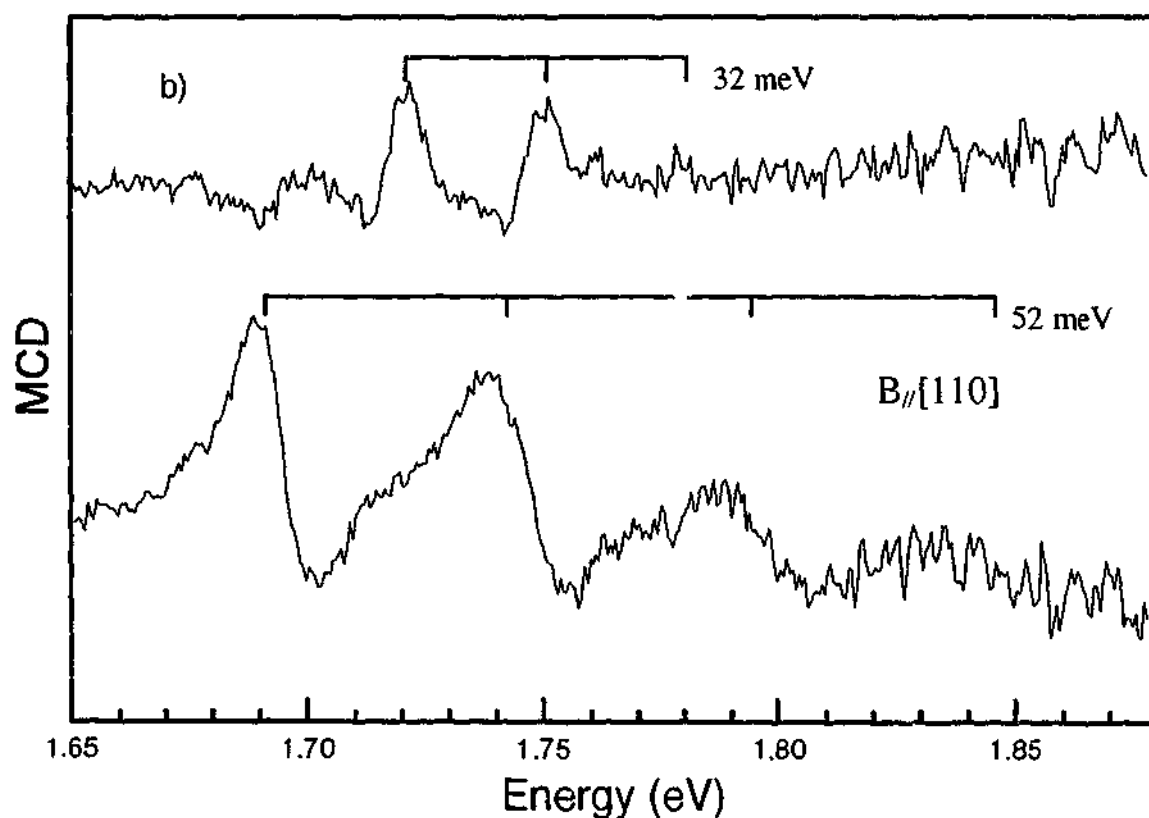
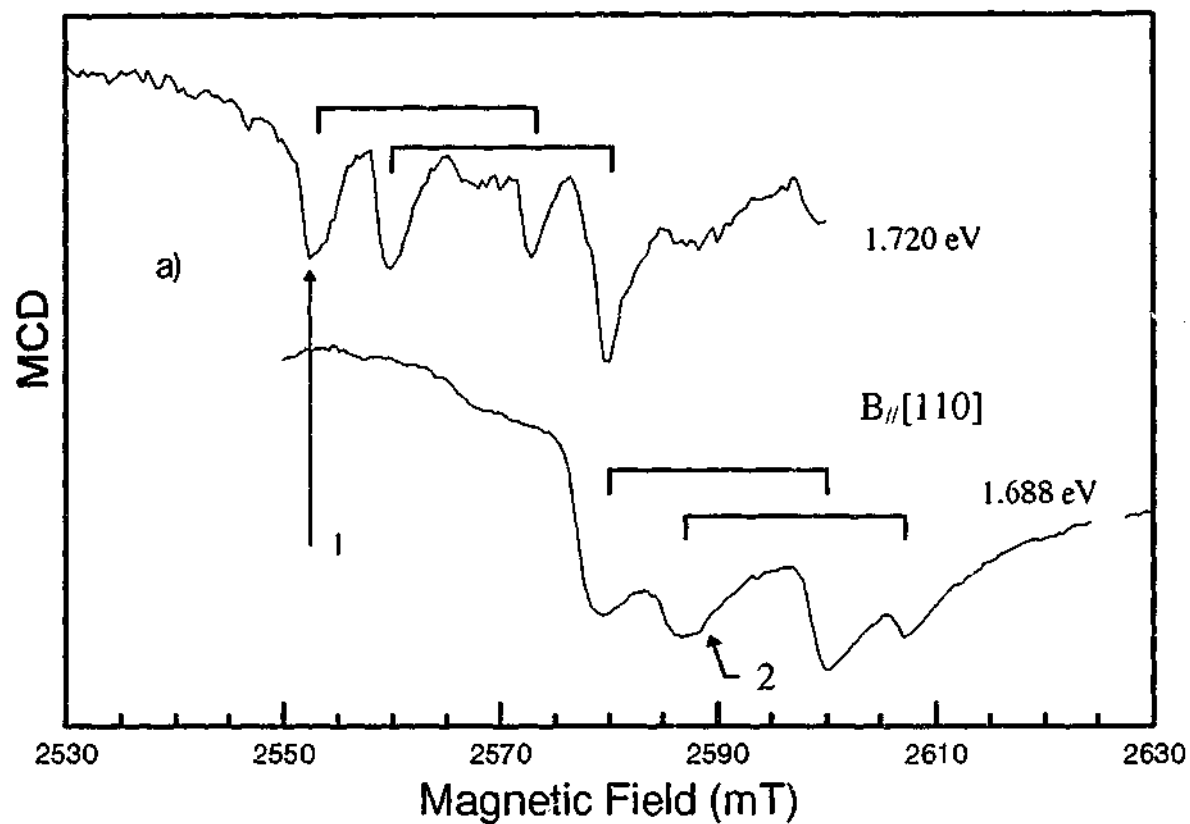


Figure 6.6 a) ODMR spectra of the 1.720 eV and 1.688 eV lines. The field positions marked 1 and 2 are those used in EPR tagged MCD spectra: 1 is on resonance for the 1.720 eV line but off resonance for the 1.688 eV line while 2 is on resonance for the 1.688 eV line but off resonance for the 1.720 eV line b) EPR tagged MCD spectrum for the field positions 1 and 2. The two EPR spectra are shown to correlate with different optical lines. The first EPR spectrum is shown to correlate with a system with a ZPL at 1.720 eV and a dominant phonon energy of 32 meV. The second EPR spectrum is shown to correlate with a system with a ZPL at approximately 1.688 eV and a dominant phonon energy of 52 meV.

It is possible that this centre could be the NE4 centre described by Nadolinny and Yelissev⁷ which has the same symmetry and $g_{\parallel}=2.023$ and $g_{\perp} = 2.098$. The difference in the parameters are larger than the experimental errors in the measurement of the g -values. It therefore appears to be a separate defect centre with a similar structure to the NE4 centre.

In this set of experiments no ODMR was observed for the 1.059 eV line. The centre was however paramagnetic as the MCD signal varied with temperature. By recording the MCD signal at two or more temperatures and two field strengths it is theoretically possible to determine the spin and g value of the defect.³ The MCD signal has two components a diamagnetic contribution, ϵ_d , that is proportional to the magnetic field, and a paramagnetic component, ϵ_p , that is proportional to the electron spin, S , and a Brillouin function, $B_s(x)$.

$$\epsilon_d \propto B_0 \quad [6.1]$$

$$\epsilon_p \propto B_s(x) \quad [6.2]$$

$$x = \frac{g\beta B_0}{kT} \quad [6.3]$$

$$B_s(x) = \frac{1}{S} \left[\left(S + \frac{1}{2} \right) \coth \left(S + \frac{x}{2} \right) - \frac{1}{2} \coth \frac{x}{2} \right] \quad [6.4]$$

As only the paramagnetic component, ϵ_p , is dependent on temperature if measurements at the same field but different temperatures are subtracted then the diamagnetic contribution, ϵ_d , in the experimental spectrum is removed. If the ratio is taken of two of these spectra at different magnetic fields then a number, R , that is dependent only on the Brillouin function, $B_s(x)$, is obtained.

$$R = \frac{\epsilon_p(B_1, T_1) - \epsilon_p(B_1, T_2)}{\epsilon_p(B_2, T_1) - \epsilon_p(B_2, T_2)} \quad [6.5]$$

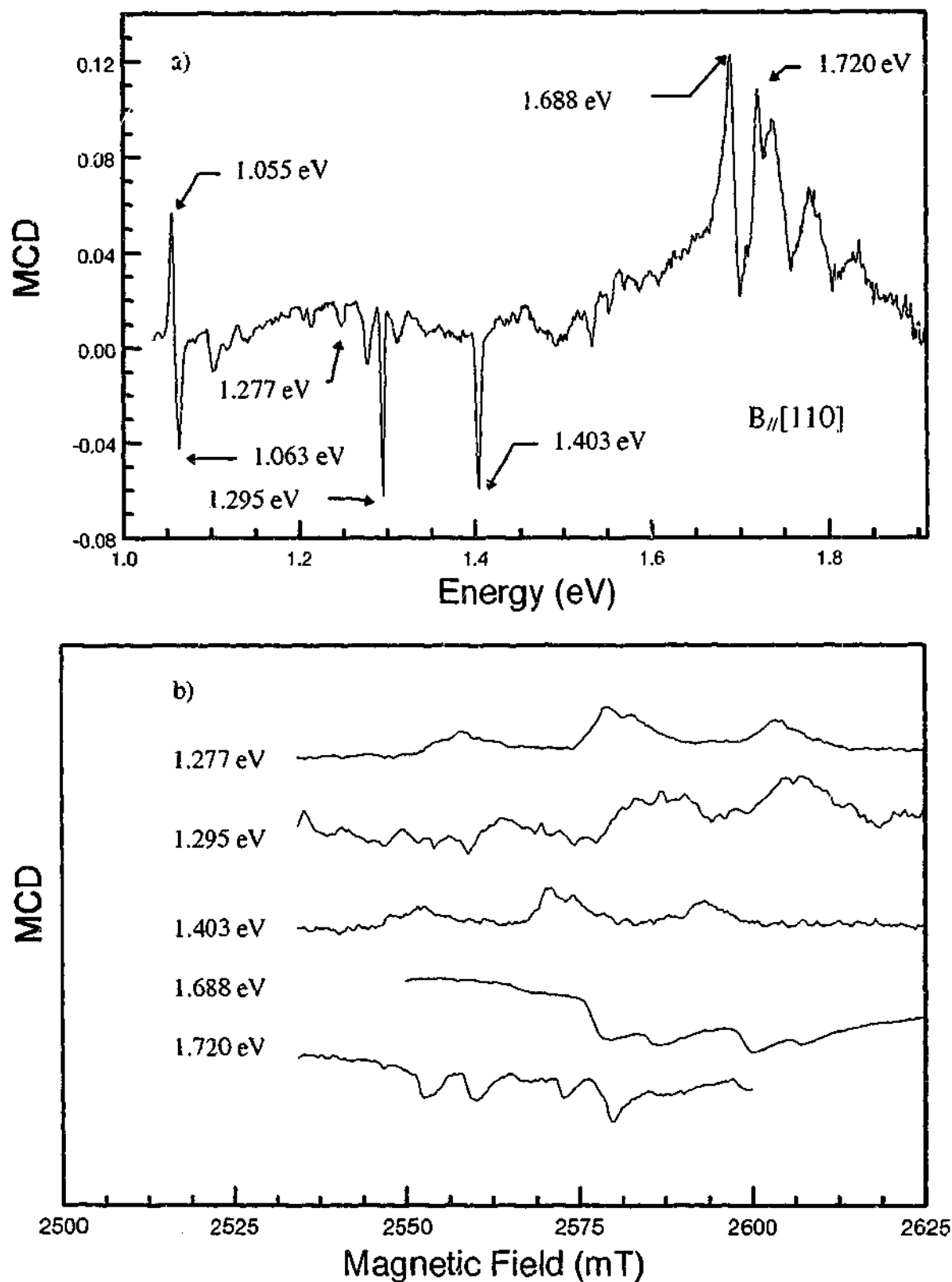


Figure 6.7 MCD spectrum in the low energy range. The 1.4 eV and 1.693 eV lines are seen as well as several unreported lines at 1.720 eV, 1.295 eV and 1.059 eV. b) All of the lines indicated were paramagnetic and the ODMR spectra relating to each of them were recorded. The applied field is aligned approximately along a $\langle 110 \rangle$ direction. Note also that the 72 GHz source used for these spectra had additional modes which gave rise to additional resonance lines in the spectra which are separated by approximately 20 mT

The Brillouin function is determined by the magnetic field and temperature which are experimentally fixed and the electron spin, S , and the electron g factor, g . By substituting values for S and g into equation 6.5 a ratio R can be calculated and

compared to the experimental value. To obtain a unique solution for both S and g at least two of these ratios must be calculated. The MCD was recorded at 1.5 °K and 4.2 °K with field strengths of 750 mT, 1500 mT and 2700 mT and are shown in Figure 6.9. The ratio R for each of the combinations of field and temperature values was fitted well with the parameters $S=1/2$ and $g = 2$.

6.4 Discussion

The synthetic diamonds in contrast to the natural diamonds had polished faces and MCD and ODMR experiments were possible. The research therefore focussed on these experiments and the possibility of relating optical features to EPR centres. Before discussing these results it is worthwhile to summarise the results obtained using other techniques.

The FTIR spectra show a nitrogen content of approximately 50 atomic ppm predominantly in the A form. This shows that the nitrogen in these diamonds is not as aggregated as in the natural blue diamonds. The EPR spectra show the NE1-NE3 centres indicating the presence of nickel-nitrogen defects that have formed by the trapping of nitrogen at the nickel sites during the heat treatment process. It also shows that the nickel defects act as very efficient traps for the nitrogen. A previously unreported EPR centre with $\langle 100 \rangle$ symmetry, $S= 1/2$, and $g_{\parallel}=2.0225\pm 0.0005$, $g_{\perp}=2.0095\pm 0.0005$ and two equivalent ^{14}N nuclei with $I= 1$ and $A_{\perp} = 1.5\pm 0.1$ MHz, $|A_{\parallel}| < 0.6$ MHz. was observed. Another line at approximately $g=2.032$ is also observed and is presumably Ni_s^- . The line appears to broaden when the field is rotated away from the $\langle 100 \rangle$ axis but it is difficult to verify this because the spectra from the NE centres obscures this line when the field is away from the $\langle 100 \rangle$ axis. It is possible that cross relaxation between this

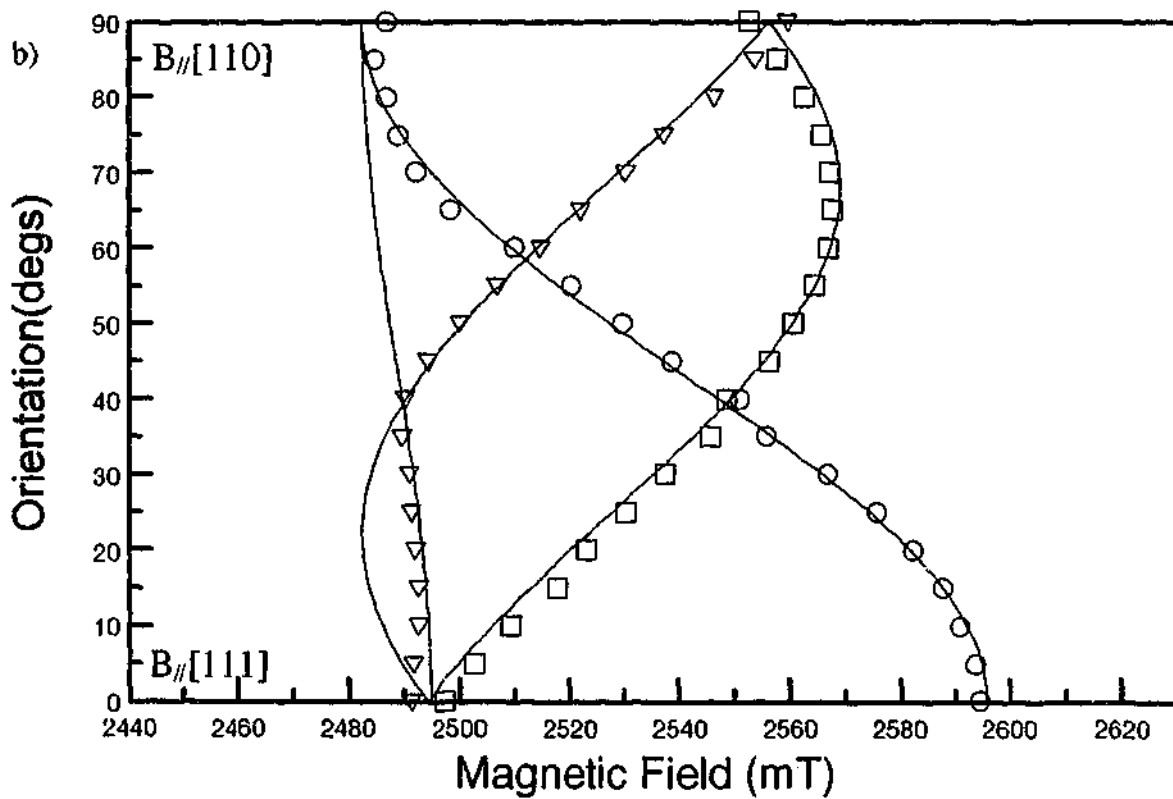
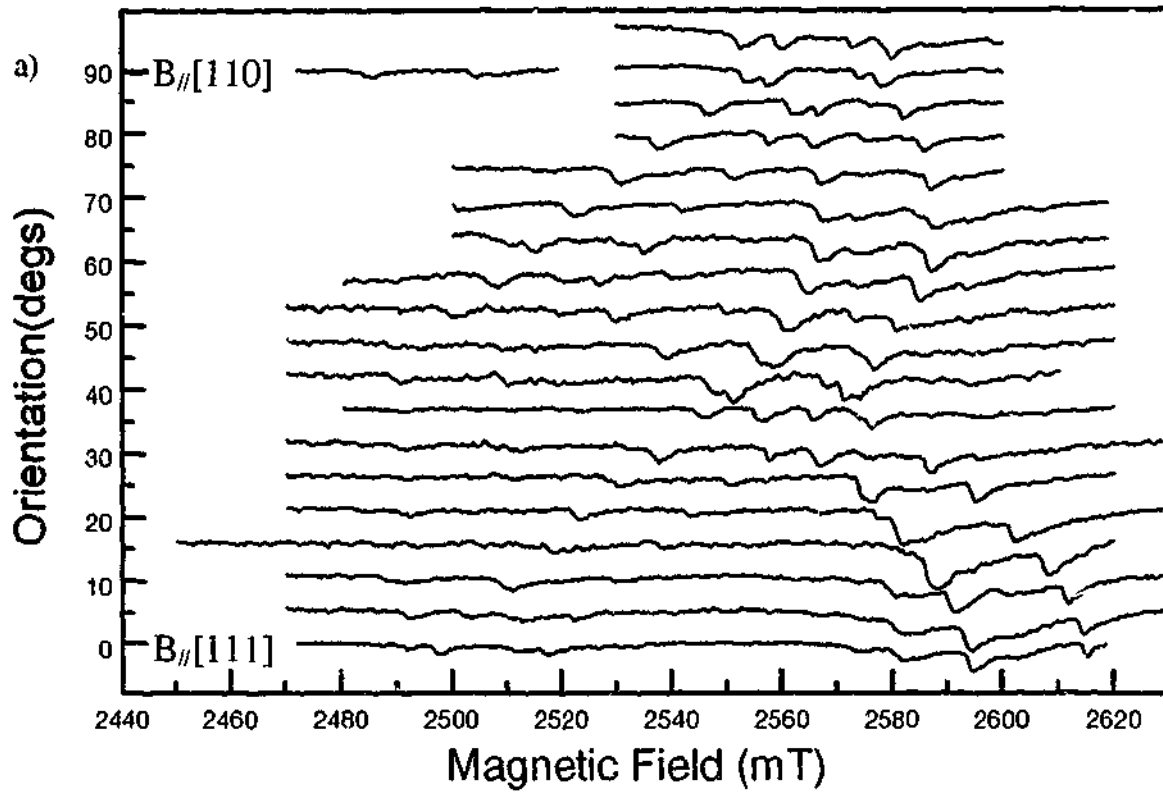


Figure 6.8 a) Angular dependence of the 1.720 eV ODMR. ODMR spectra for the 1.720 eV line were measured as a function of orientation. The sample was rotated about a $\langle 112 \rangle$ axis. b) Calculated transition positions. The EPR centre was found to have $\langle 111 \rangle$ symmetry and was simulated with the g values; $g_{\parallel} = 2.004 \pm 0.005$ and $g_{\perp} = 2.093 \pm 0.005$.

centre and one of the NE centres could take place and this might explain the variation in observed line width.

The optical absorption spectra show the series of sharp lines as observed by Lawson and Kanda.⁶ These ZPLs are related to nickel nitrogen centres but no direct correlation with the NE EPR centres had previously been established. ODMR experiments thus presented an opportunity to correlate features observed in the two spectroscopies and add to the body of knowledge about these defects.

ODMR spectra were recorded while sitting on five different optical transitions. With these results alone it is difficult to determine whether the ODMR recorded are due to different defects. In fact some of the ODMR spectra recorded at different wavelengths looked similar, indicating that the same defect is involved. The uncertainty can be removed by measuring MCD spectra tagged by EPR. This technique looks at the effect on the MCD spectra by being on and off resonance of the EPR transition. The difference between the on and off resonance spectra therefore represents the part of the MCD that is correlated to the particular EPR transition. This was done for the two of the ODMR spectra recorded at 1.688 eV and 1.720 eV. The two EPR spectra are shown to be related to two separate different defects. The defects show distinct vibronic bands one with a ZPL at 1.688 eV (1.693 eV) and 51 meV phonon interaction and the other which was previously unreported at 1.720 eV with 30 meV phonon interaction

The angular dependence of all the ODMR spectra were not recorded due to time constraints. Instead the ODMR spectra that was most resolved, on the 1.720 eV optical transition, was studied further. This defect was found to have $\langle 111 \rangle$ symmetry and $g_{\parallel} = 2.004 \pm 0.005$, $g_{\perp} = 2.093 \pm 0.005$. The similarity between these parameters and those reported for the NE4 defect suggested that it was the NE4 centre but there must be large errors with the frequency or magnetic field measurements to account for the discrepancy

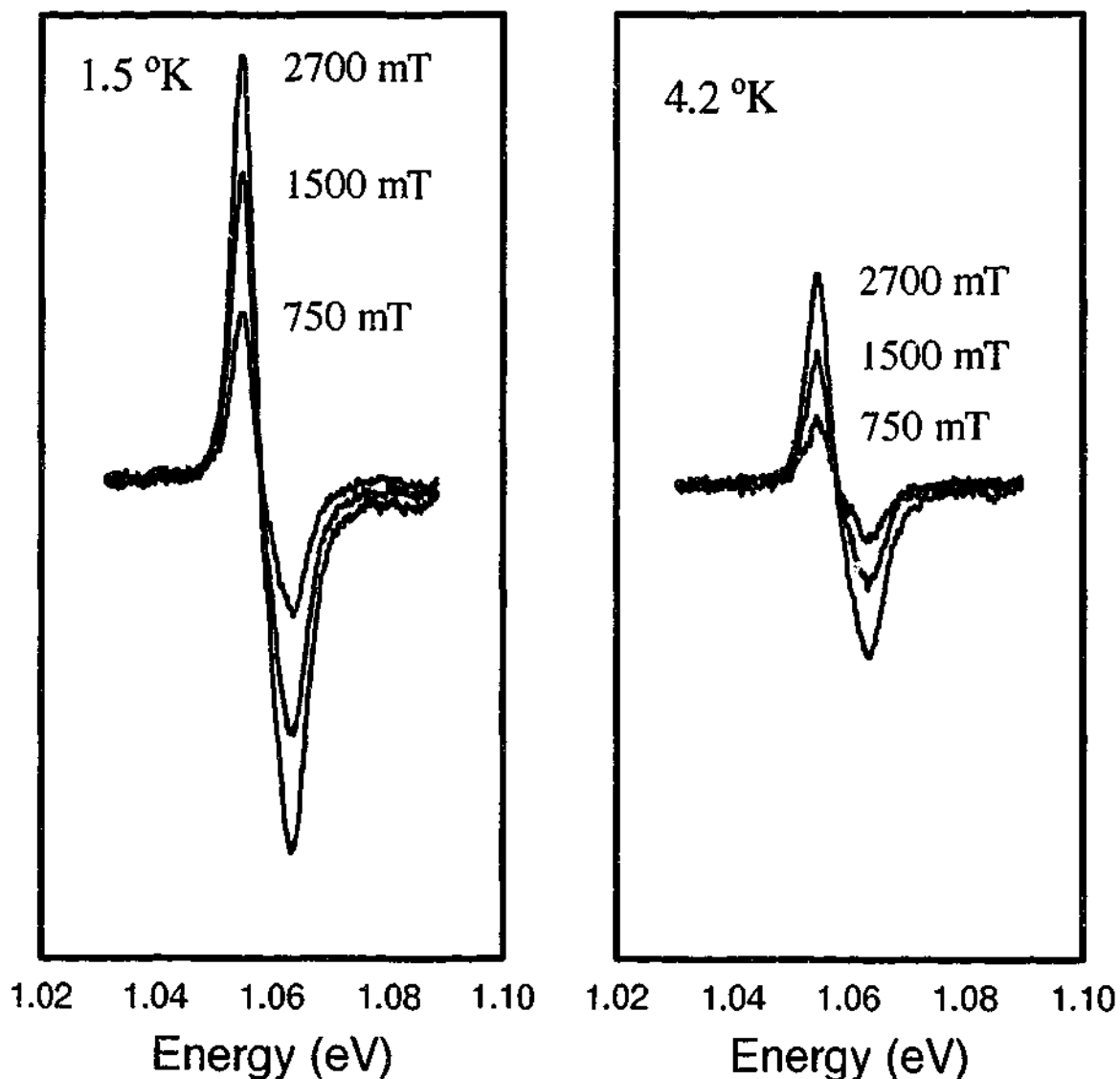


Figure 6.9 Spin determination of the 1.059 eV line. No ODMR was observed for the 1.059 eV line. The centre was however paramagnetic and the spin and g value could be estimated by measuring the MCD at two temperatures and three field values.. A good fit was obtained with $S = 1/2$ and $g = 2$.

in g values. Rather, it is suggested that they are two closely related defects having similar structure.

Despite some effort no ODMR was recorded for the 1.059 eV transition. The defect was known to be paramagnetic as its intensity changed with temperature. There are several reasons for not observing ODMR such as fast relaxation times or looking in the wrong field range. In this case as discussed later it was a combination of both.

The spin and g factor of the defect could however be estimated by measuring the MCD at different temperatures and different applied field strengths and the use of equation 6.5. From these measurements it was estimated that $S = 1/2$ and $g = 2$.

Table 6-1 Nickel centres in diamond that have been reported by various authors. Models for the defects are included where given. Centres that have been observed in this study are marked with an asterisk.

Name	S	Symmetry axes	g values	No. of ^{14}N	Model	Ref.
W8,?	3/2	isotropic	$g = 2.0319$	0	substitutional Ni^-	8
NIRIM1	1/2	isotropic	$g = 2.0112$	0	interstitial Ni^+	8
NIRIM2	1/2	$\langle 111 \rangle$	$g_{\parallel} = 2.3285$ $g_{\perp} \approx 0$	0	interstitial Ni^+ with trigonal perturbation (vacancy ?)	8,10
NE1	1/2	$g_{\parallel} \langle 011 \rangle$ $g_2 \langle 01 \bar{1} \rangle = 14^\circ$	$g_1 = 2.1282$ $g_2 = 2.007$ $g_3 = 2.0908$	2	Ni^+ in double semivacancy and 2 nitrogens	*5
NE2	1/2	$g_1 \langle 011 \rangle = 20^\circ$ $g_1 \langle 01 \bar{1} \rangle = 5^\circ$ $g_2 \langle 01 \bar{1} \rangle = 14^\circ$	$g_1 = 2.1301$ $g_2 = 2.0100$ $g_3 = 2.0931$	3	Ni^+ in double semivacancy and 3 nitrogens	*5
NE3	1/2	$g_{\parallel} \langle 011 \rangle$ $g_2 \langle 01 \bar{1} \rangle = 7^\circ$	$g_1 = 2.0729$ $g_2 = 2.0085$ $g_3 = 2.0476$	3	Ni^+ in double semivacancy and 3 nitrogens	*5
NE4	1/2	$\langle 111 \rangle$	$g_{\parallel} = 2.0227$ $g_{\perp} = 2.0988$	0	Ni^+ in double semivacancy	7
NE5	1/2	$g_{\parallel} \langle 011 \rangle$ $g_2 \langle 01 \bar{1} \rangle = 8^\circ$	$g_1 = 2.0903$ $g_2 = 2.039$ $g_3 = 2.0044$	2	Ni^+ in double semivacancy and 2 nitrogens	7
NE6	1/2	$g_{\parallel} \langle 011 \rangle$ $g_2 \langle 01 \bar{1} \rangle$ $g_3 \langle 100 \rangle$	$g_1 = 1.995$ $g_2 = 2.0207$ $g_3 = 2.0109$	0		7
NE7	1/2	?	> 2	1		7
	1/2	$\langle 100 \rangle$	$g_{\parallel} = 2.0151$ $g_{\perp} = 2.2113$	0	interstitial Ni^+ with tetragonal perturbation (B or Al ?)	11
	3/2 ?	isotropic	$g \approx 2.02$	> 1	Substitutional Ni^- with several nitrogens	9
	1/2	$\langle 100 \rangle$	$g_{\parallel} = 2.0225$ $g_{\perp} = 2.0095$	2	interstitial Ni^+ with tetragonal perturbation	*
	1/2	$\langle 111 \rangle$	$g_{\parallel} = 2.004$ $g_{\perp} = 2.093$	0	interstitial Ni^+ with trigonal perturbation	*10
	1/2	$\langle 111 \rangle$	$g_{\parallel} = 2.25$ $g_{\perp} \approx 0$	0	interstitial Ni^+ with trigonal perturbation	10

Subsequent measurements at the University of Paderborn by Dr Thomas Pawlik recorded at K band found this centre to be a $\langle 111 \rangle$ symmetry defect with $g_{\parallel} = 2.24$ $g_{\perp} \sim 0$.¹⁰ The reason that it was not observed previously was that the centre had fast

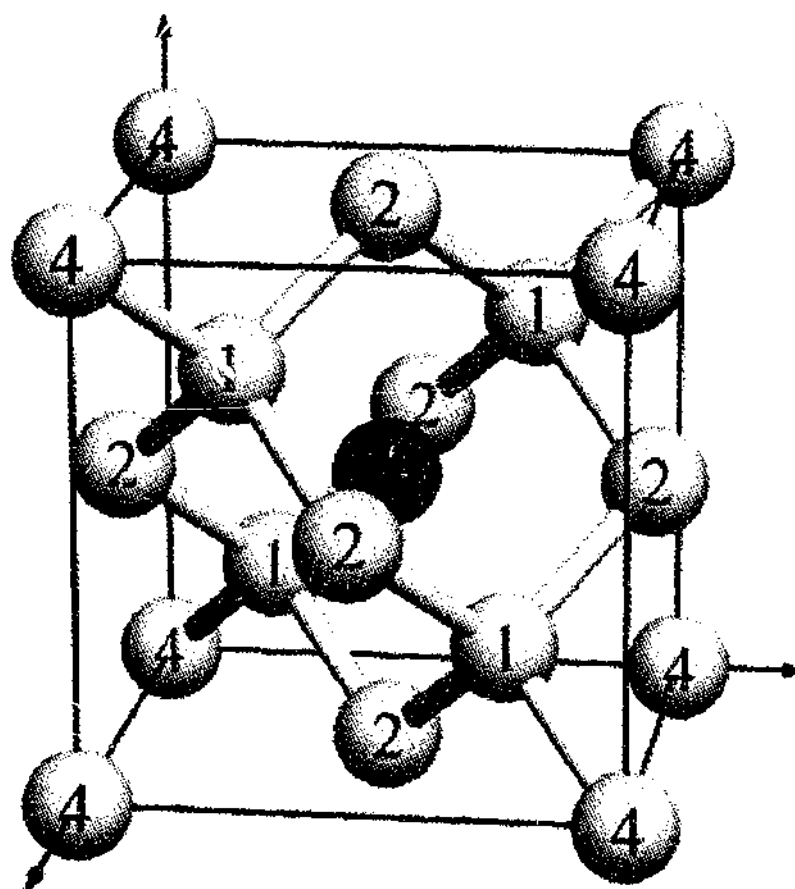


Figure 6.10 Unit cell of diamond structure. A Ni^+ ion is shown in the interstitial position and the first to fourth nearest neighbours are labelled

relaxation and more power was needed to observe it. This was not possible using the 72 GHz source but was possible with the K band klystron. The line also broadens significantly upon rotation of the magnetic field away from the $\langle 111 \rangle$ axis. This makes it difficult to observe the spectrum for orientations away from this axis. The field orientation that was used in the initial work was along a $\langle 110 \rangle$ axis.

The 1.4 eV ZPL was also found by Dr. Pawlik to be due to a $\langle 111 \rangle$ symmetry defect with $g_{\parallel} = 2.32$ and $g_{\perp} \sim 0$.¹⁰ The 1.4 eV centre is therefore the NIRIM2 defect which had previously been suspected but not proven. This is direct correlation of the optical centre and the EPR centre. This means that evidence obtained by both spectroscopies can be used to further characterise the defect structure.

If we look at all the nickel related centres that have been observed so far we can develop a picture of two or three basic defects with the nickel in a substitutional or interstitial position and possibly a double semivacancy position. The variety of EPR

centres that are observed then correspond to perturbations of these basic defects with neighbouring nitrogens, vacancies, interstitials or other point defects. In cases where ^{14}N hyperfine is observed then obviously nitrogen is involved. The NE1, NE2, NE3 and NE5 defect centres have been determined to have two to three nitrogens in the first and second nearest neighbour positions.

In many of the EPR centres there is no observed hyperfine structure. In this case the most likely candidate for the perturbing defect is a vacancy. This has been proposed for the NIRIM2 centre where the vacancy is believed to be on a first or fourth nearest neighbour site to the nickel ion.⁸ This structure would account for the trigonal perturbation which is evident in the EPR spectrum of this defect and the 1.4 eV optical transition at this defect. With only the g values it is not possible to determine the structure of the defect with any certainty but the symmetry of the site provides some clues. The environment of the nickel interstitial is shown in Figure 6.10. The first and fourth nearest neighbours are in a $\langle 111 \rangle$ direction from the interstitial position whilst the second nearest neighbours are in a $\langle 100 \rangle$ direction.

The defects that have been observed in this study for the first time are also likely to be perturbed nickel centres of this kind. The EPR centre with $\langle 111 \rangle$ symmetry and with $g_{\parallel} = 2.24$ $g_{\perp} \sim 0$ is obviously similar to the NIRIM2 centre and its structure is most probably related. It is feasible that the NIRIM2 centre is a nickel interstitial with a vacancy on a first nearest neighbour site while this centre is a nickel interstitial with a vacancy on a fourth nearest neighbour site.

The previously unreported EPR centre with $\langle 100 \rangle$ symmetry, $S = 1/2$, and $g_{\parallel} = 2.0225 \pm 0.0005$, $g_{\perp} = 2.0095 \pm 0.0005$ could also be regarded as a simpler defect with a perturbation. The g values of this centre are similar to that of the centre reported by

Mineeva et al¹¹ with the same symmetry and $g_{\parallel} = 2.0151$ and $g_{\perp} = 2.2113$. It is interesting to note that this defect symmetry is rare in diamond.¹² Mineeva et al proposed that the defect responsible for the spectra they observed was a positively charged interstitial nickel with a charge compensator (B or Al are suggested) nearby. The similarity in the symmetry of the defect reported by Mineeva et al and the defect currently observed suggests that they might be due to similar structures. In this case hyperfine from two nitrogens was observed and could be used to further characterise the centre.

The anisotropic part of the superhyperfine interaction between the Ni ion and the nitrogens was estimated to be between -0.3 and -0.7 MHz. This can be used to gain an estimate of the separation, R , between the Ni ion and the N using the classic point dipole-dipole contribution to the anisotropic shf interaction.³

$$b_{dd} = 14.20 \frac{g_n}{R^3} \quad [6.6]$$

Here b_{dd} is in units of MHz, g_n is the nuclear g factor which is 0.40376 for ¹⁴N and R is in Angstroms. This estimate places the nitrogens between 2.0 and 2.7 Å from the nickel ion. A possible model for this defect would be a Ni⁺ interstitial with two nitrogens in second nearest neighbour shell positions along a <100> axis with some dilation.

Likewise the defect observed by Mineeva et al¹¹ could be a nickel interstitial with a vacancy in the second nearest neighbour position. It would be possible to speculate further but without more information no definite conclusions can be made. Obviously theoretical calculations regarding the stability of these defects would be useful.

6.5 Conclusion

Synthetic diamonds grown by the high temperature method from a nickel solvent were studied by EPR, MCD and ODMR. These diamonds contained both nickel and nitrogen and with heat treatment nickel-nitrogen centres had been formed. These were observed in optical absorption, MCD and ODMR. A new EPR centre, with $S=1/2$ and spin Hamiltonian parameters, $g_{\parallel}=2.0225\pm0.0005$, $g_{\perp}=2.0095\pm0.0005$ and $A_{\perp}=1.5\pm0.1$ MHz. $|A_{\parallel}|<0.6$ MHz from two equivalent ^{14}N nuclei, was observed in the EPR spectra. It is proposed that this centre is a Ni^+ ion on an interstitial site with two nitrogens substituting for carbons in the two nearest neighbour positions along a $\langle 100 \rangle$ axis.

One EPR centre with spin Hamiltonian parameters $g_{\parallel} = 2.004\pm0.005$, $g_{\perp} = 2.093\pm0.005$ was characterised by ODMR and correlated with an optical transition at 1.72 eV. This centre has similar parameters to the NE4 centre and it is proposed that it has a similar structure consisting of a substitutional Ni^+ with a nearby point defect giving a trigonal distortion.

Further work by Dr. Thomas Pawlik characterised two other EPR centres in the same synthetic diamonds using ODMR. One of these centres had not previously been reported but the other was found to be the NIRIM 2 centre. The optical transition correlated with this EPR centre was the 1.4 eV line. Both the 1.4 eV centre and the NIRIM 2 centre had been proposed to be a interstitial Ni^+ but had not been directly correlated.

6.6 Acknowledgments

Dr. Alan Collins and Sarah Sharpe, Kings College, London, are thanked for the kind loan of the synthetic HTHP diamonds. Prof. J.M. Spaeth and Dr. T. Pawlik are thanked for there help and hospitality whilst visiting the University of Paderborn in

Germany and their continued assistance afterwards. Bayden Wood is also thanked for assisting with the FTIR spectra. Finally, the Queens Trust is thanked for financial assistance to travel overseas to complete aspects of this work

6.7 References

- ¹ Pereira, E., Santos, L., Pereira, L., Hofmann, D.M., Christmann, P., Stadler, W., Meyer, B.K., *Diamond & Related Materials* **4**, (1994) 53-58.
- ² Nazaré, M.H., Mason, P.W., Watkins, G.D., and Kanda, H., *Phys Rev B* **51**, (1995) 16741-16745.
- ³ Spaeth, J.-M., Niklas, J.R. and Bartram, R.H., *Structural Analysis of Point Defects in Solids*, Springer-Verlag, 1992.
- ⁴ Woods, G.S., Purser, G.C., Mtimkulu, A.S.S. and Collins, A.T., *J. Phys. Chem. Solids*, **51**, (1990) 1191.
- ⁵ Yelisseyev, A., and Nadolinny, V., *Doklady Akademii Nauk* **326**, (1992) 524.
- ⁶ Lawson, S.C., and Kanda, H., *J. Appl. Phys.* **73**, (1993) 3967-3973.
- ⁷ Nadolinny, V., and Yelisseyev, A., *Diamond and Related Materials* **3**, (1994) 1196-1200.
- ⁸ Isoya, J., Kanda, H., and Uchida, Y., *Phys. Rev. B* **42**, (1990) 9843.
- ⁹ Noble, C.J., Pawlik, Th. and Spaeth, J-M., *J. Phys.: Condens. Matter*, **10**, (1998) 11781.
- ¹⁰ Pawlik, Th., Noble, C. and Spaeth, J-M., *J. Phys.: Condens. Matter*, **10**, (1998) 9833.
- ¹¹ Mineeva, R.M., Speranskii, A.V., Titkov, S.V., and Bershov, L.V., *Doklady Akademii Nauk* **334**, (1994) 755-758
- ¹² Baker, J.M. and Newton, M.E., *Appl. Magn. Reson.*, **8**, (1995) 207.

7. Characterisation of Ion-Implantation Damage in Type IIa Diamond Using EPR

7.1 Introduction

Ion implantation of donor and acceptor impurities into diamond is a promising technique in the attempt to fabricate practical semiconducting diamond materials. Many problems including the low diffusion rate of dopants in diamond could be overcome with this technique. However, one major problem with this technique is the creation of implantation damage that cannot be annealed out. This disordered region can then dominate the electrical properties of the material. In this study the EPR signals associated with the ion implantation damage were studied to obtain data about the nature of these defects.

The creation of these defects has previously been studied extensively by monitoring the electrical properties of ion implanted diamond.¹ It had previously been found that at low doses the electrical resistivity decreased with increasing ion implantation. At higher doses the resistivity briefly increases before it decreases dramatically when a critical dose is reached. The sudden decrease in resistivity was explained by percolation theory as the point where the conducting regions caused by the implantation damage formed a continuous network through the diamond. The temperature dependence of the resistivity indicated that in the low dose range the conductivity was dominated by variable range hopping and in the high dose range it was metallic in nature.

The dose range in which the resistivity increased with increasing dose was however difficult to explain with percolation theory. Interestingly, previous EPR studies showed that both the linewidth and intensity of the EPR line in ion implanted diamond showed similar discontinuities with increasing ion dose.^{2,3} Together with the electrical

measurements, the EPR measurements indicated that the processes during ion implantation were more complicated and that possibly more than one distinct type of defect was being created. It was therefore desirable to attempt a more detailed EPR study in order to determine the nature of the defects created.

Ideally pulsed EPR techniques were to be used to study the implantation damage using methods such as ESEEM, relaxation measurements and by modelling the echo decay function. All of these techniques give some information about the defects and their local environment. The low number of spins in the samples however made pulsed experiments impossible. The main determinant of the spin number was the small volume of the implanted region. The implanted layer was only of the order of 1 μm and although the local spin concentration was high the overall spin number was quite low and was estimated to be of the order of 10^{15} spins.

The study was then restricted to cw techniques. The cw EPR spectrum in ion implanted diamond had previously been well characterised.⁴ The cw EPR spectrum consists of a single isotropic Lorentzian line at $g= 2.0032$ and was assigned to dangling bond defects. The information available from cw EPR therefore appears to be limited to the intensity and linewidth. These parameters, in particular linewidth, were therefore measured as a function of implantation dose and measurement temperature.

The temperature dependence of the EPR linewidth in many amorphous semiconductors has previously been shown to follow a simple relationship with the dc conductivity.⁵ There is a temperature independent component and a term linear with the conductivity.

$$\Delta B_{pp}(T) = \Delta B_{pp}^0 + C\sigma(T) \quad [7.1]$$

The dc conductivity of these materials follows the $T^{-1/4}$ law developed by Mott⁶ indicating variable range hopping (VRH) of localised electrons where a is the localisation length of the wave function, N_F is the density of states at the Fermi level and k is the Boltzmann constant

$$\sigma(T) = \sigma_0 e^{-(T_0/T)^{1/4}} \quad [7.2]$$

$$T_0 \approx \frac{1}{a^3 N_F k} \quad [7.3]$$

The hopping conductivity is related to the linewidth by its influence on the spin-flip probability of the localised electrons on the defects. The probability of a spin flip occurring in a given period is increased by the electron hopping to another site. This relaxation mechanism is then seen in the linewidth of the EPR transition. If the defects in the amorphous regions in ion implanted diamond are similar to other amorphous semiconductors then a similar behaviour is expected.

7.2 Experimental

The samples used were type IIa synthetic diamonds from Drekker company and measured 2x2x0.1 mm. The diamond plates were then irradiated with 300 keV Xenon ions at room temperature with doses from 3×10^{13} to 1×10^{15} ions/cm².

The EPR spectra were recorded on a Bruker ESP380e spectrometer with a standard X-band rectangular Bruker cavity and a quartz nitrogen flow insert for temperature control. Temperatures between 100 and 300 K could then be achieved. The parameters for all spectra are microwave power = 10 mW, modulation amplitude = 0.2 mT, sweep width = 10.0 mT, sweep time = 168 s, time constant = 163.84 ms and resolution = 1024.

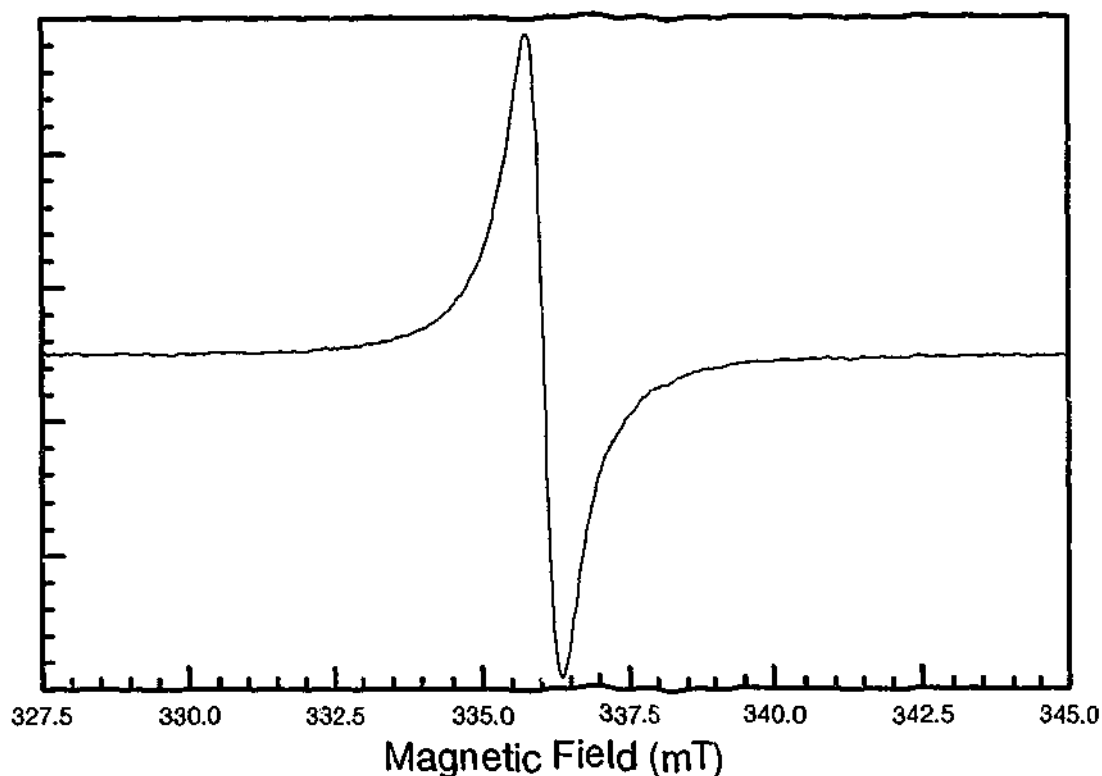


Figure 7.1 Cw EPR spectrum of ion implanted diamond with implantation dose 1×10^{14} ions/cm² recorded at 160 K.

7.3 Results

The EPR spectrum due to the defects created in the ion implantation process consisted of a single isotropic line at $g \sim 2.003$ (Figure 7.1). The lineshape was found to be essentially Lorentzian in character with no observable structure from hyperfine interactions. Attempts were made to use pulsed EPR techniques but no echo could be observed at any temperature and experimental conditions which suggests that either the relaxation times were too short or that the lines were not inhomogeneously broadened..

The peak-peak linewidth of the EPR signals was found to vary both with temperature and implantation dose. The linewidth was found to have two parts; a temperature independent part and a component that increased with increasing temperature. The sample with the lowest dose, 3×10^{13} ions/cm², had the largest temperature independent component and also the largest variation with temperature. With increasing dose the temperature independent component decreased as well as the

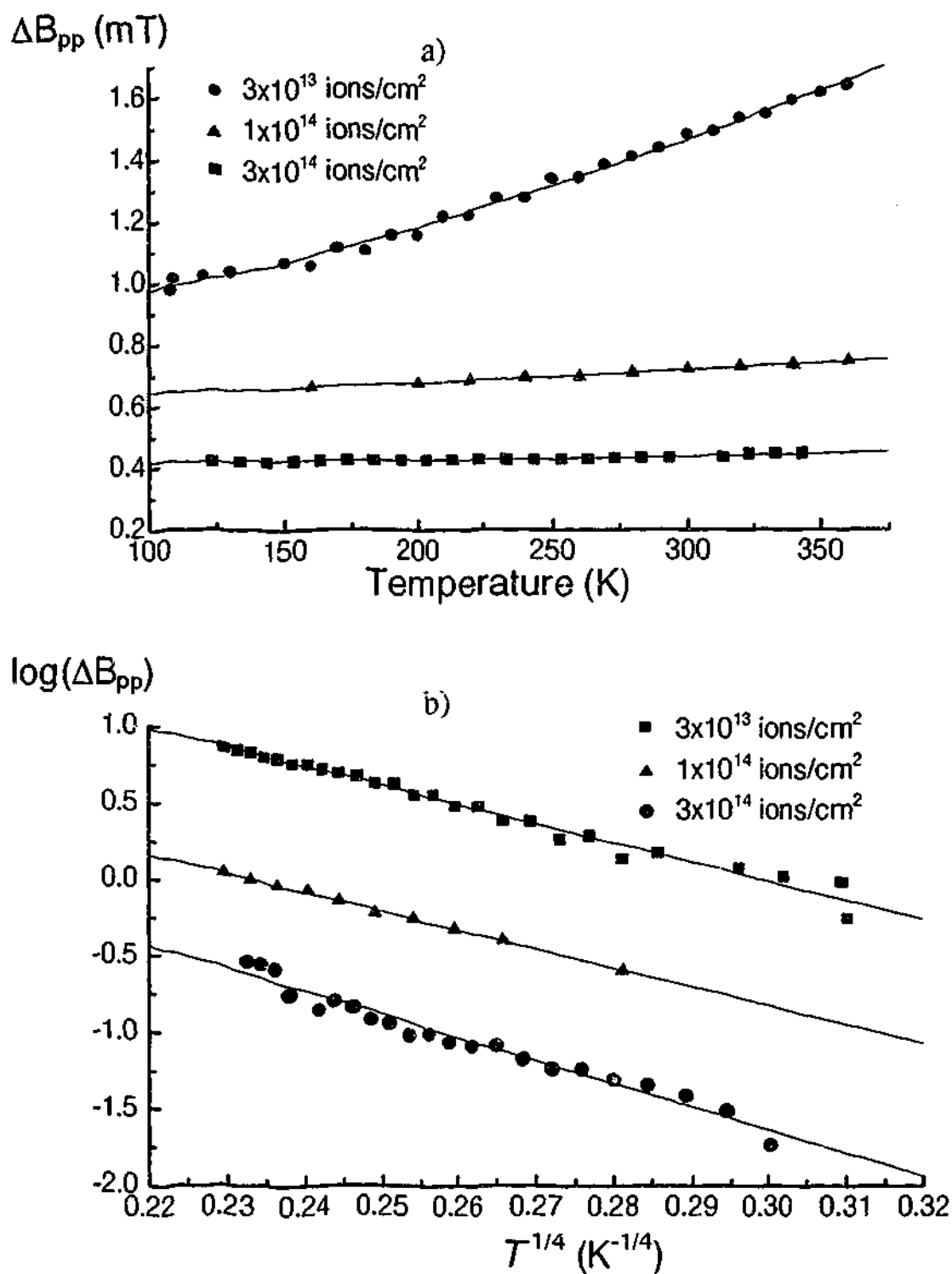


Figure 7.2 a) Temperature dependence of the line width of the EPR signal in ion implanted diamond. Measurements for three ion doses of 3×10^{13} , 1×10^{14} , and 3×10^{14} Xe⁺ ions/cm² are shown. b) the same data plotted on a $T^{-1/4}$ scale showing good agreement with the VRH model.

variation with temperature. The results are plotted in Figure 7.2. The experimental data is fitted well with equation 7.1.

The treatment so far takes into account only the peak-peak linewidth of the EPR signal. While this is a major parameter it does not fully describe the lineshape and

although the lineshape is close to Lorentzian it cannot be fitted exactly by this lineshape.

It was also observed that the lineshape does not remain constant with temperature.

If the theory of defects in amorphous semiconductors is examined more closely it is seen that a simple lineshape is not expected. This is because there exists a distribution of defects that have different local environments. Each of these will have different relaxation times and hence line widths. It is desirable to try to model the experimental lineshapes with physically realistic models in order to obtain information about this distribution of defects.

Two simple models are developed that take into account a random distribution of spin relaxation times. This is compared to simpler fits involving one and two Lorentzians. The lineshape of the EPR signal due to the ion implantation is isotropic and can be fitted well with a signal Lorentzian line. Here ω is the frequency, ω_0 is the centre of the resonance and ν_s is the relaxation rate.

$$S(\omega - \omega_0) = A \frac{\nu_s}{(\omega - \omega_0)^2 + \nu_s^2} \quad [7.4]$$

The fit is not improved using a Gaussian lineshape and in fact the experimental lineshape has more area under the wings than can be fitted with a Lorentzian. The lineshape cannot be modelled by a function between a Lorentzian and a Gaussian. The fit is improved if two Lorentzian components are used each with separate amplitude and relaxation rates. Both the centre of the line and the wings can be fitted well with this function.

$$S(\omega - \omega_0) = A_1 \frac{\nu_1}{(\omega - \omega_0)^2 + \nu_1^2} + A_2 \frac{\nu_2}{(\omega - \omega_0)^2 + \nu_2^2} \quad [7.5]$$

A more physical lineshape model can be developed if we consider the lineshape as resulting from a distribution of individual lines each having a different relaxation rate and

hence linewidth. This reflects the range of relaxation rates expected from a disordered material.

$$S(\omega - \omega_0) = \int_{-\infty}^{\infty} \frac{S(v_s)v_s}{(\omega - \omega_0)^2 + v_s^2} dv_s \quad [7.6]$$

where

$$S(v_s) = e^{\left(\frac{-(v_s - \bar{v}_s)^2}{\Delta v_s}\right)} \quad [7.7]$$

The resulting lineshape is a convolution of Lorentzians with a Gaussian distribution in v_s .

In the variable range hopping model the hopping rate v_s can be given by equations 7.8 and 7.9.⁵

$$v_s = v_s^0 e^{-\xi} \quad [7.8]$$

where i and j are two sites separated by a distance R_{ij} with energies of E_i and E_j and ξ is given by

$$\xi = 2 \frac{R_{ij}}{a} + \frac{E_j - E_i}{kT} \quad [7.9]$$

ξ will have a broad distribution in the material which we can assume for simplicity to be Gaussian

$$S(\xi) = e^{\left(\frac{-(\xi - \bar{\xi})^2}{\Delta \xi}\right)} \quad [7.10]$$

If the spin relaxation time is determined by the hopping rate the theoretical lineshape is then given by

$$S(\omega - \omega_0) = \int_{-\infty}^{\infty} \frac{S(\xi)v_s}{(\omega - \omega_0)^2 + v_s^2} dv_s \quad [7.11]$$

The goodness of fit is improved with the lineshape models that involve a distribution in one of the parameters. The best fit, however, results from a sum of two

Lorentzians. This indicates that the lineshape consists of two components one having a narrow line width and one a broad line width. The addition of a third component with a linewidth intermediate between these two only increased χ^2 , further supporting the contention that two distinct components exist.

Table 7-1 χ^2 values from non-linear least squares fitting of one data set using the Levenberg-Marquart technique.

Lineshape Model	χ^2	no. of parameters
Single Lorentzian	563.9	3
Distribution in ν_s	383.4	4
Distribution in ξ	346.5	4
Two Lorentzians	30.98	5

The EPR signal can therefore be assumed to consist of two distinct components, one broad and one narrow. The variation in the line shape can then be accounted for by the different temperature dependence of the two components. It was observed that ratio of the narrow component to the broad component decreased with increasing temperature. The EPR spectra of the sample with dose 3×10^{13} ions/cm² were fitted with two Lorentzians and the ratio between the narrow and broad components plotted as a function of temperature (Figure 7.3a).

The ratio between the area under the two components was also seen to vary with implantation dose (Figure 7.3b). This indicates that two distinct defect centres are created in the implantation process and their proportion changes with increasing dose.

7.4 Discussion

In the first analysis of the results the line width of the EPR signal in ion implanted diamond was found to vary with temperature in a similar manner to that in other amorphous semiconductors and could be explained by variable range hopping. This result is important because it confirms results obtained from electrical measurements and

provides a direct connection between the electrical conductivity and the defects observed in EPR. This makes further analysis of the EPR signal in ion implanted diamond desirable.

More importantly it also offers the possibility that electrical information can be obtained indirectly from EPR measurements. This method has a number of advantages when the difficulties in making electrical measurements in diamond are considered. The major problem is in achieving Ohmic contacts. If the contacts are non-Ohmic then the measured electrical properties are determined by the contacts rather than the material. In the normal method carbide forming metals, particularly Ti, are used for an initial layer followed by silver and gold. Good contacts are still difficult to achieve particularly for diamonds with low conductivity.

If boron doped semiconducting diamond is used then an Ohmic contact can be made by ion implanting an overdoped boron region on the surface. This method however can only work if the diamond has hole type conduction. In many cases the conduction mechanism is not known and it is the electrical measurements that are to be used to determine this. This obviously presents problems as the contacts can alter the electrical properties that are to be measured. The advantages of a contactless method of obtaining electrical conductivity information are then obvious.

The possibility of using EPR in this way needs to be discussed. The main problem would appear to be that the electrons responsible for the dc conductivity need not be the same that are seen in EPR. This must necessarily be the case as some defects will form isolated groups where electrons may hop between each of them but do not contribute to the overall dc conductivity. In addition other relaxation and exchange mechanisms will affect the line width and shape and cannot be separated from the hopping mechanism. Pulsed EPR measurements can help by providing more direct relaxation time

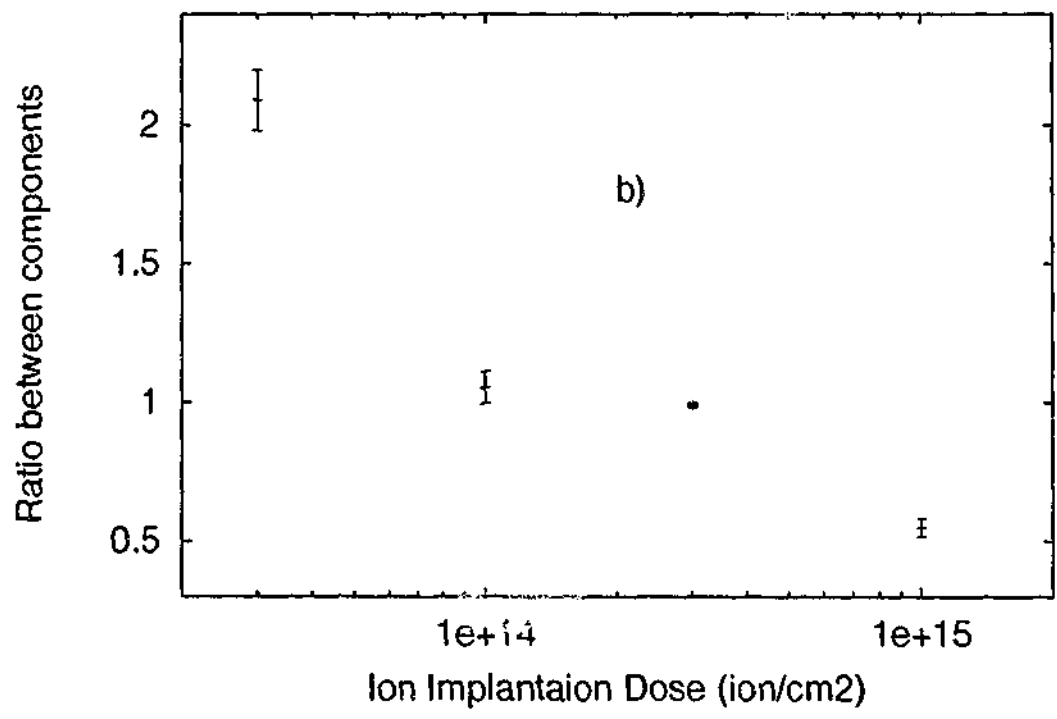
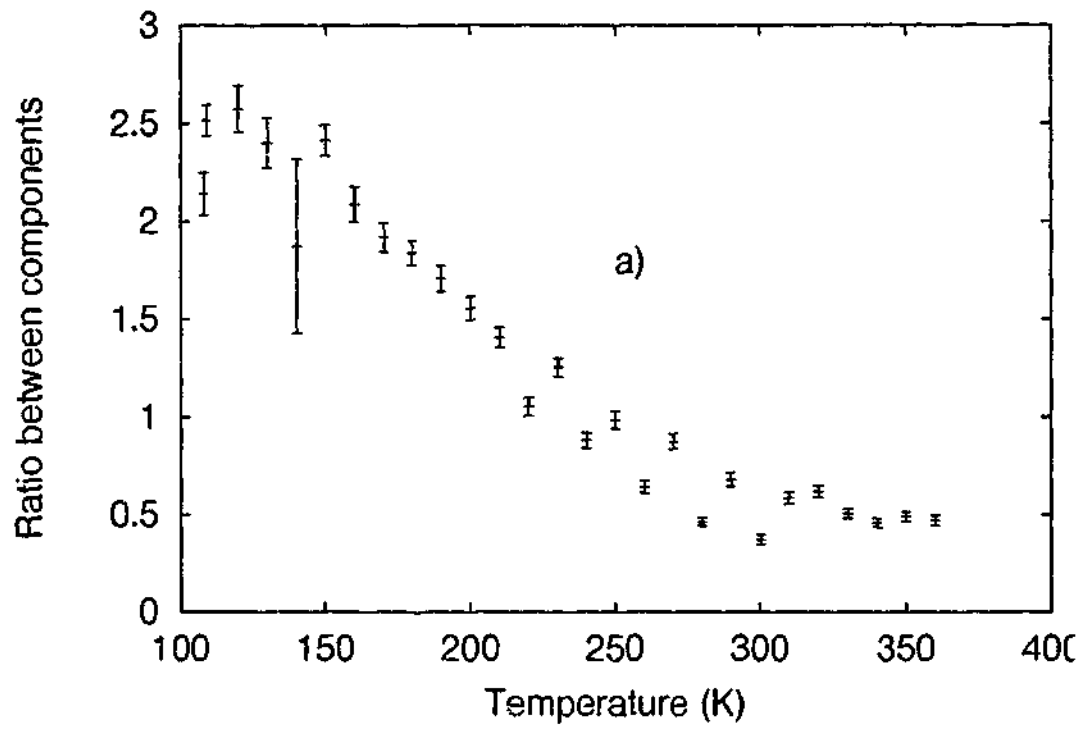


Figure 7.3 a) The ratio between the narrow and broad components obtained by fitting the data for the sample with implantation dose 3×10^{13} as a function of temperature. b) The ratio between the narrow and broad components as a function of implantation dose.

measurement than the line width but as we have seen in this study these are not always possible. In addition the constant C in equation 7.1 cannot be determined and hence no quantitative measurement of conductivity can be made.

Having outlined all the problems with this method it is still seen that some information can be obtained. It would, however, be difficult to use this method in isolation and is best used in combination with other measurements.

In the second part of the analysis an attempt is made to fit the experimental lineshape with a physical model. The models used in the fitting take into account aspects of the variable range hopping that has been shown in the samples. A good fit with one of these models would possibly provide an additional way of characterising the nature of the defects and the type of disorder present. None of the models that involved a single distribution of relaxation times could successfully fit the experimental spectrum. Rather a better fit was obtained if two separate components were used with discrete relaxation times. If there were a distribution in relaxation times it would be bimodal. However to describe such a distribution of relaxation times with two means and two standard deviations would require seven parameters. This would be far too many parameters than could be determined by the experimental data and the fitted values would have large uncertainties.

The results of the fitting showed to some extent the limit of the information that could be obtained from the experimental lineshape. Although treating the lineshape as a single Lorentzian with an intensity, line position and linewidth ignored some of the information present in the experimental data physically realistic models did not significantly improve the fit and any parameters obtained by such fittings were of dubious value. The best fit was obtained using two Lorentzians and little information apart from the existence of two components could be established. The five parameters in the fitting process were not totally independent and hence the reliability of the fitted parameters was quite small. An analysis of the temperature dependence of the linewidth of each of the two components was therefore not attempted.

The origins of the two components could not be established from the data. The available information from the fitting procedure was the line width and relative intensity as a function of temperature. The component with the narrow line width decreased in intensity compared to the broad component as a function of implantation dose. It is therefore proposed that the broad component corresponds to defects in a highly damaged amorphous region and the narrow component corresponds to defects in less damaged diamond. The broad component is seen to grow at the expense of the narrow component as more damage is created at higher doses.

7.5 Conclusion

The temperature dependence of the EPR linewidth of ion implanted diamond was found to follow the $T^{1/4}$ law found previously in some amorphous semiconductors. This dependence matches that found in electrical conductivity measurements and can be explained by a model in which the spin-lattice relaxation rate is directly determined by the variable range hopping conductivity. This result shows that the model also applies in ion implanted diamond and that the EPR signal observed in these samples is directly connected to the conductivity mechanism.

Further analysis of the EPR lineshape showed that the signal was composed of two distinct components. These two components showed different temperature dependence and varied with implantation dose. It is therefore concluded that at least two different types of defects are produced in the implantation process. The two types of defects have different relaxation properties that are evident in their temperature dependence. It is suggested that the defects may correspond to dangling bonds in unperturbed diamond and in amorphous regions. The ratio of the two components in the EPR signal is seen to change with ion dose which is consistent with this model.

7.6 Acknowledgments

I would like to thank Dr Steven Praver and Dr Fun Lai, University of Melbourne, for providing the samples for this study and the collaborative assistance.

7.7 References

-
- ¹ Praver, S., Hoffman, A., and Kalish, R., *Appl. Phys. Lett.* **57**, (1990) 2187.
 - ² Teicher, M., and Beserman, R., *J. Appl. Phys.*, **53**, (182) 1467.
 - ³ Guo-Liang, Z., Hong, Y., and Nmei-Ning, S., *Radiation Effects*, **97**, (1986) 273.
 - ⁴ Brosious, P.R., Corbett, J.W., and Bourgouin, J.C., *Phys. Stat. Sol.*, **21**, (1974) 677.
 - ⁵ Movaghar, B., Schweitzer, L., and Overhof, H., *Phil. Mag. B.* **37**, (1978) 683.
 - ⁶ Mott, N.F. and Davis, E.A., *Electronic Processes in Non-Crystalline Materials*, Clarendon Press, Oxford (1979).

8. Interaction Between Localised And Conduction Electron Spins In The High T_c Superconductor $Gd:EuBa_2Cu_3O_{6+x}$ [†]

8.1 Introduction

The study of the spin-spin interaction between the conduction electrons and localised spins gives significant information about the properties of the conduction electron system.¹ It is important to apply it in the investigation of high T_c superconductors where the conduction electrons play a decisive role in the superconducting properties and the high superconducting transition temperatures.

In this work ESR measurements of small amounts of Gd in $EuBa_2Cu_3O_{6+x}$ ($x \approx 0.85$) are reported. ESR of the localised moments in metals has been very effective in the study of the spin-spin interaction with the conduction electrons. Gadolinium has the advantage over other localised magnetic atoms in that its ground state is an almost pure $S = 7/2$ state and therefore its interaction with the lattice is sufficiently weak enabling one to observe the ESR even above room temperatures. It has also the advantage in the case of $EuBa_2Cu_3O_{6+x}$ that it goes substitutionally in the lattice replacing the europium. Furthermore its effect on the superconducting properties is small as reflected in the small change of T_c even when all the Eu is replaced by Gd.²

The structure of the 123 compounds consist of two sets of double copper oxide sheets in the a-b plane with barium atoms between the sheets (Figure 8.1). The element in the 1 site, such as rare earth elements or Y, are located between these two sets of Cu planes. As the conductivity resides mostly within each of the Cu plane sets their interaction with the elements in site 1 was found to be small. This explains the small effect of most of the magnetic rare earth atoms on T_c .

[†] Parts of this chapter have previously been published in an article, Shaltiel, D., Noble, C., Pilbrow, J., Hutton, D. and Walker, E., *Phys Rev B*, **53**, (1996) 12430.

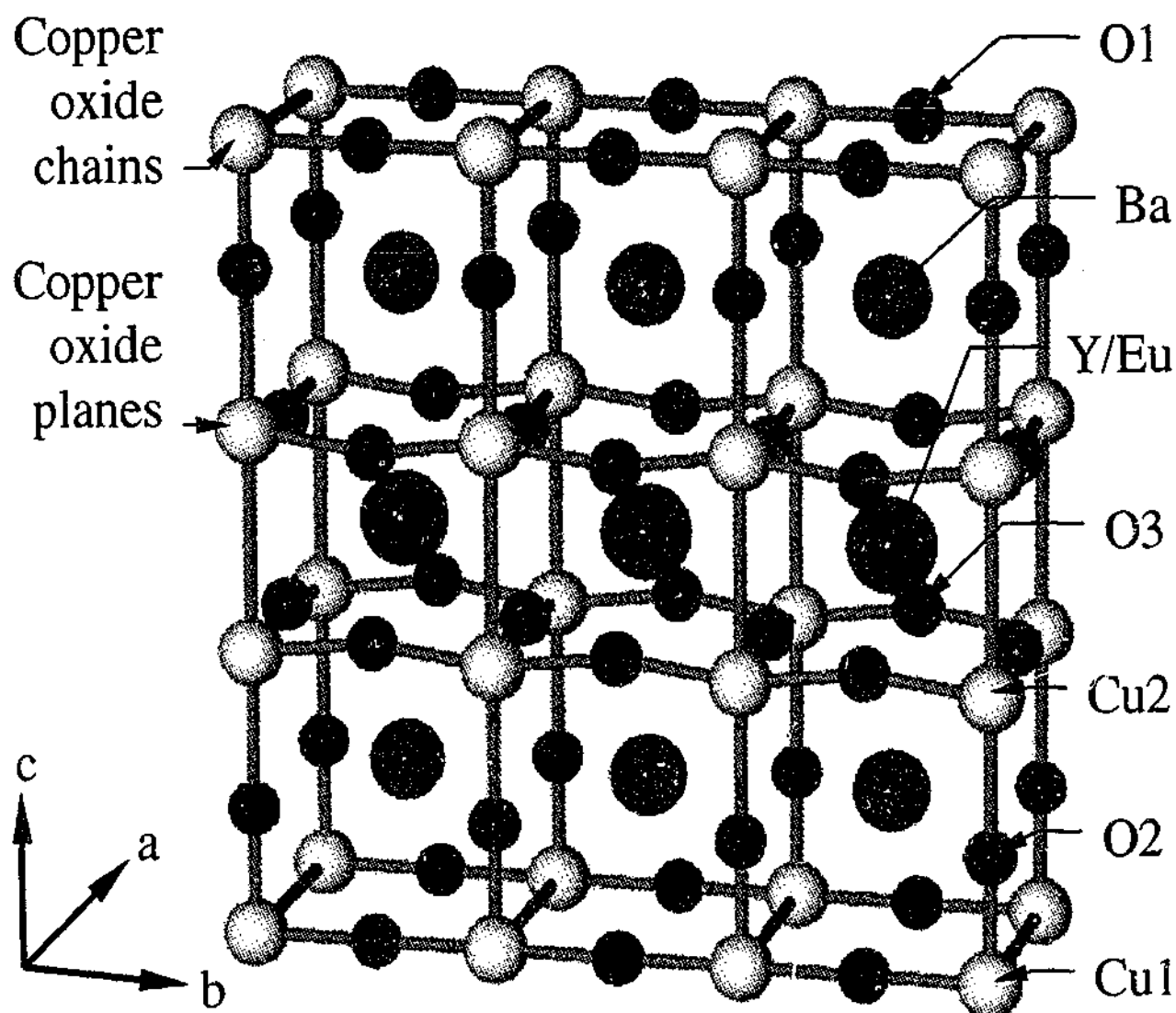


Figure 8.1 Structure of the 123 class of high T_c superconductors indicating the copper oxide layers, the position of the barium ions and that of the rare earth ions.

Interactions between the elements in site 1 and the conduction electrons were investigated mostly by the NMR of $Y^{3,4}$ and also by the ESR of $Gd^{5,6,7}$ partially substituting a non magnetic element such as Y or Eu. The NMR and most of the ESR measurements were carried out either in powders⁵ or in powders aligned along the c axis⁷. Shaltiel et al⁶ have investigated the ESR spectra of Gd in single crystals of $YBa_2Cu_3O_{6+x}$. They reported the observation of a resolved fine structure spectrum at temperatures close to but above T_c and a Korringa relaxation of an exchanged narrowed line. Janossy et al⁸ reported the observation of the ESR spectrum of $Gd:YBa_2Cu_3O_{6+x}$ in oriented powders measured in the c direction. Their results show both the Korringa relaxation and g-shift of the $1/2 \leftrightarrow -1/2$ transition at 245 GHz. NMR of Y in

YBa₂Cu₃O_{6+x} shows a very small Knight shift and small Korringa behaviour^{3,4} that varies with temperature and oxygen concentration.⁴

In this work the Korringa behaviour above T_c of the $7/2 \leftrightarrow 5/2$ transition of a Gd spin probe in a single crystal of a 123 compound is reported. The use of the $7/2 \leftrightarrow 5/2$ transition removes the uncertainty in assigning various contributions to the linewidth that may be present when the central $1/2 \leftrightarrow -1/2$ line is used. This is particularly the case when the Korringa relaxation is fast at high temperatures and when the experiment is performed at X-band. Under these conditions it is unlikely that the spectra will be fully resolved and an additional exchange narrowed component will be present in the same field position as the $1/2 \leftrightarrow -1/2$ transition. Most importantly the $7/2 \leftrightarrow 5/2$ transition will remain resolved at temperatures where the other transitions are obscured by this process.

This method enabled the measurement of linewidths at X-band over a wide temperature range above T_c . These results enabled the determination of the spin-spin exchange interaction J_{Ss} between the local Gd spins and the conduction electrons in a 123 compound. In contrast to NMR so far reported, a deviation from a simple linear broadening with temperature is not observed above 110 K. These results indicate a similar behaviour to that observed in metals indicating an interaction with a Fermi liquid.

The spin Hamiltonian of a Gadolinium ion in an insulator can be described by equations 8.1 and 8.2, where g is an isotropic g -factor and O_n^m , are the spin operators reflecting the symmetry of the Gd ion environment. With cubic symmetry only the operators O_2^0 , O_4^0 and O_4^4 are needed but in the general case more terms are necessary.

$$H = g\beta\mathbf{B}\cdot\mathbf{S} + H_{ZF} \quad [8.1]$$

$$H_{ZF} = \frac{1}{3} \sum_m b_2^m O_2^m + \frac{1}{60} \sum_m b_4^m O_4^m + \frac{1}{1260} \sum_m b_6^m O_6^m \quad [8.2]$$

The temperature and angular behaviour of the spectra indicate that in addition to the electron Zeeman and zero field terms of the spin Hamiltonian of the Gd $S = 7/2$ ground state an exchange narrowing mechanism is present.¹ The origin of the exchange interaction is the interaction with the conduction carriers and can be written as $J_{Sr}(\mathbf{S} \cdot \mathbf{s})$ where J_{Sr} is the exchange interaction between the Gd spins \mathbf{S} and the spin of the conduction carriers \mathbf{s} . The conduction electron spin resonance is not observed due to the fast relaxation of these spins. The total spin Hamiltonian can be written as

$$H = g\beta\mathbf{B} \cdot \mathbf{S} + H_{ZF} + J_{Sr}\mathbf{S} \cdot \mathbf{s} \quad [8.3]$$

The ESR spectra for a system of Gd spins and conduction electrons will depend on the Gd concentration, the conduction electron spin system, the spin relaxation between the two systems and the spin relaxation of each system to the lattice. The behaviour of such a system has been calculated by Hasegawa⁹ for $S = 1/2$. The more complicated system where $S > 1/2$ is given by the Barnes¹⁰-Plefka¹¹ theory. It has been shown that for metals such as Al¹² or Pd¹³ and at "high" temperature, the seven fine structure lines of the Gd spectra collapse into a single line with $g = g_{Gd} + \Delta g$ where $g_{Gd} = 1.993$ is the g value obtained in insulators and

$$\Delta g = J_{Sr}\eta = J_{Sr}\chi_{ce}/g\beta^2 N \quad [8.4]$$

Here η is the density of states per spin at the Fermi surface, χ_{ce} is the spin susceptibility of the conduction electrons per mole, N is Avogadro's number and β is the Bohr magneton.

The line width, ΔB , of this totally collapsed central line will follow the Korringa behaviour

$$\Delta B = \Delta B_K + \Delta B_{res} \quad [8.5]$$

ΔB_{res} is the residual line width and ΔB_K is the Korringa broadening given by:

$$\Delta B_K = \frac{\pi k T}{g \beta} (J_{sc} \chi_{cc} / g \beta^2 N)^2 \quad [8.6]$$

where k is the Boltzmann constant.

The case of complete collapse of the fine structure to a single central line can occur when the Korringa broadening is large compared to the zero field splittings. Under certain conditions, usually when the exchange constant is small, or at "low" temperatures, or when the zero field splittings are large a more complex behaviour can be observed. At high temperatures the spectrum collapse into a single line. However when lowering the temperature the spectra begin to separate. Transitions that occur at magnetic fields where the Korringa interaction between adjacent transitions is small will be the first to become resolved. This is expected of the $\pm 7/2 \leftrightarrow \pm 5/2$ transitions which are isolated from the other transitions when the zero field splitting is large. As the temperature is further decreased a full fine structure spectrum is obtained. This has been demonstrated for Gd in Pd¹³ at low temperatures and Gd in LaSb¹⁴ where it was shown that the value of the exchange constant is small.

In a fully resolved spectrum we expect the temperature dependent broadening of the individual lines for completely resolved spectra to be given by¹⁴

$$\Delta B(M \leftrightarrow M + 1) = \Delta B_K [S(S + 1) - M(M + 1)] \quad [8.7]$$

Thus for the temperature broadening of the individual transitions we expect their line width to be enhanced by a factor of 16, 15, 12 and 7 with respect to the fully exchanged narrowed line width, for the transitions $1/2 \leftrightarrow -1/2$, $\pm 3/2 \leftrightarrow \pm 1/2$, $\pm 5/2 \leftrightarrow \pm 3/2$ and $\pm 7/2 \leftrightarrow \pm 5/2$, respectively. This equation is of course valid only when the applied

magnetic field is parallel to the *c* axis in a highly anisotropic system such as this and therefore the only quantitative use will be restricted to this case.

8.2 Experimental

A few single crystals of $\text{EuBa}_2\text{Cu}_3\text{O}_{6+x}$, $x \approx 0.85$, with a nominal concentration of 5% Gd replacing the Eu atoms were investigated. The crystals were grown in at the University of Geneva using the flux method. Some of these crystals were heat treated in an oxygen atmosphere for 7 days at 400 C to alter the oxygen content. The crystals with a platelet form had the *c* axis perpendicular to the platelet plane. To avoid possible damage due to moisture the crystals were sealed in a 3 mm diameter quartz tube in helium atmosphere with the *c* axis and, either the *a* or the *b* axis perpendicular to the tube axis. The quartz tube axis was perpendicular to the direction of the magnetic field in the ESR experiments. Rotating the quartz tube enabled us to change the magnetic field in the *c*-*a* plane or *c*-*b* plane. We did not determine which of the *a* or *b* direction was in the plane. Magnetisation measurements were made on a Quantum Design MPMS-7 Squid magnetometer.

The Gd ESR was measured at 9.74 GHz with a Bruker ESP380 spectrometer at Monash University, and at 34.011 GHz with a Bruker ESP300 spectrometer at the University of Queensland. A dielectric resonator was used for Q-band and liquid helium temperature X-band measurements while a standard rectangular cavity was used for X-band measurements above 110 K. The dielectric resonator was introduced into a helium flow dewar that enabled variation of the temperature from 4.2 K to room temperature.

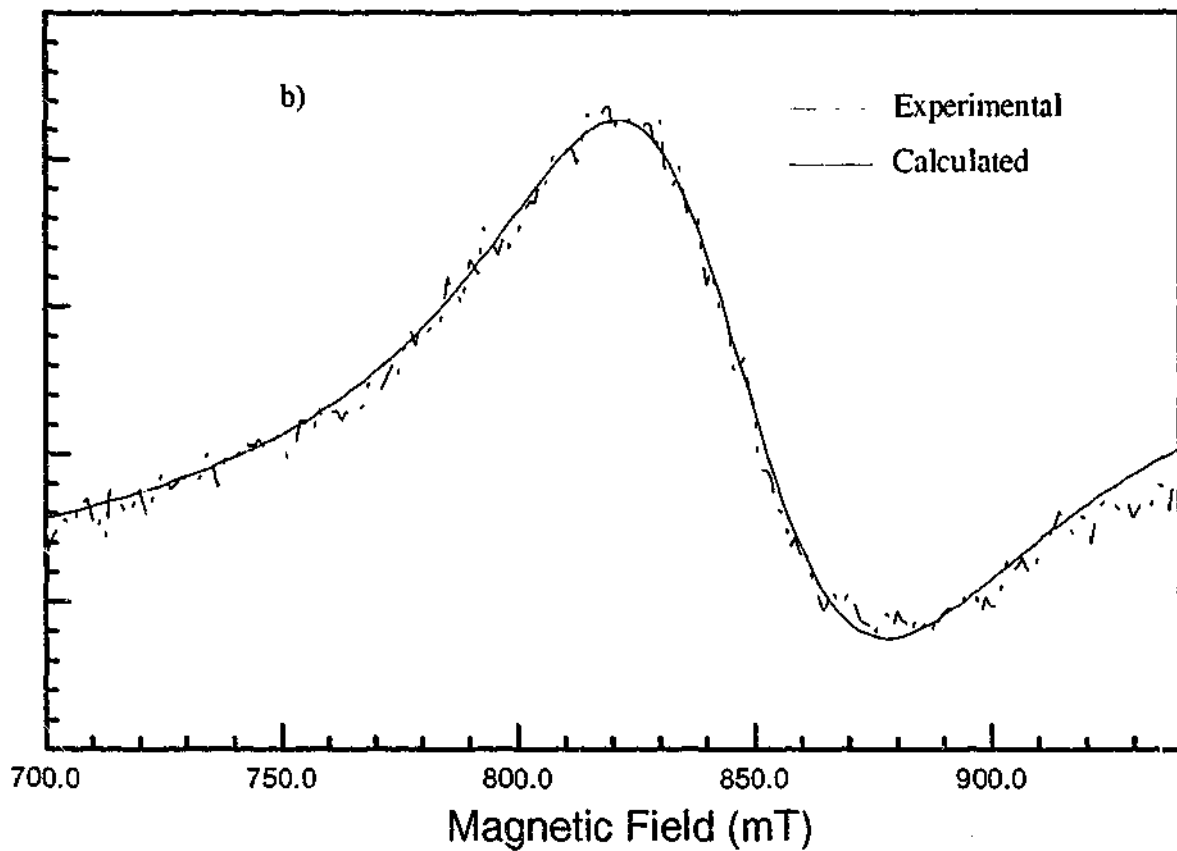
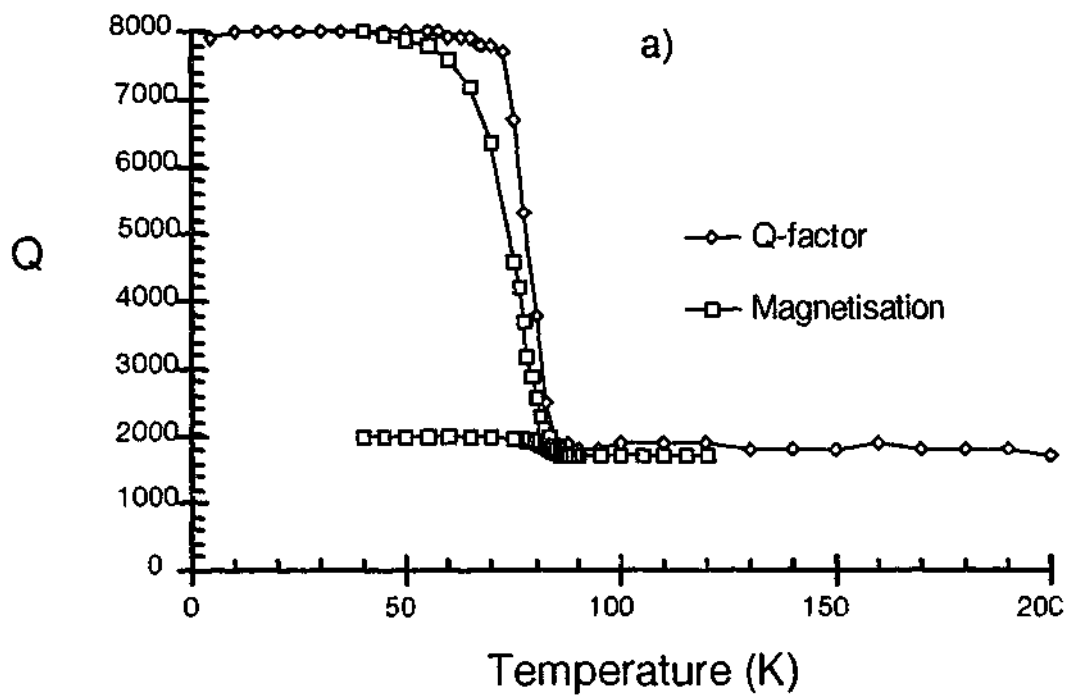


Figure 8.2 a) Q factor of the sapphire resonator as a function of temperature, with the $\text{Gd:EuBa}_2\text{Cu}_3\text{O}_{6+x}$ sample. The magnetisation curve was arbitrarily scaled to compare with the Q factor measurements. b) Fit of the high field ($7/2 \leftrightarrow 5/2$) transition measured at X-band and 120 K with the parameters $d = 0.079$, $B_0 = 843.45$ mT, $\Delta B = 29.47$ mT.

In the rectangular cavity the temperature control system consists of a quartz dewar insert that passes through the cavity and a temperature controlled nitrogen gas system that feeds the nitrogen through the quartz dewar. It allowed the variation of the temperature from 110 K to 330 K and thus a total temperature range of 4.2 K to 330 K

was possible. The monitoring thermocouple was outside the quartz tube, and therefore not in direct contact with the sample. The absolute accuracy of the temperature measurements for the nitrogen flow system was estimated to be ± 2 K from later experiments where the thermocouple was calibrated more accurately. The temperature measurements using the sapphire resonator were less accurate.

The measurement of ESR spectra of paramagnetic ions in HTSCs differs in several different aspects from that in insulators. The foremost of these are the phenomena of nonresonant absorption and vortex noise in the superconducting state. The first refers to a broad absorption at low magnetic fields which gives at best a large baseline error. The second refers to the noise produced with the movement of flux lines through the sample as the magnetic field is modulated¹⁵

The value of T_c was determined by magnetisation measurements using a squid magnetometer but it can also be determined from the ESR spectrum of the sample itself. ESR is a very sensitive technique to determine the onset of superconductivity, from both changes in the Q factor of the cavity and the onset of vortex noise. We used the change in the Q factor of the cavity as a function of the temperature to determine the superconducting transition. This is shown in Figure 8.2a with a sharp transition width of less than 3K evident. This indicates a fairly homogeneous sample. Also shown in Figure 8.2a is the magnetisation of the sample measured in a squid magnetometer. The sample was initially cooled with no applied field. A field of 5 mT (the same field at which the Q factor measurements were performed) was then applied and the magnetisation was then measured as the temperature was raised above T_c and then lowered

In the normal state the conductivity of the sample also leads to a Dysonian like line-shape. This leads to a difficulty in describing the linewidth of a transition. In this case the lineshapes encountered were successfully fitted by considering them to be an

arbitrary mixture of dispersive and absorptive components of Lorentzian shape. This allowed the determination of both the linewidth and line position to a high degree of accuracy. This was particularly important at high temperatures when the lines were several hundred gauss wide and the signal to noise ratio was low. The lines were fitted to the function below using a Levenberg-Marquart nonlinear fitting program.

$$y = A \frac{(d(3-x^2) - (1-d)x)}{(3+x^2)^2} + \text{background} \quad [8.8]$$

$$x = \frac{B - B_0}{\frac{1}{2}\Delta B} \quad [8.9]$$

where A is the amplitude, d is the proportion of dispersion in the signal, B_0 is the centre field, ΔB is the linewidth and the background is assumed to be linear. An example of a fit to an experimental line is shown in Figure 8.2b. At X-band the best fit was obtained using a value of 0.11 for d . At Q-band a higher value of d was used as the skin-depth at this frequency was smaller and hence a higher proportion of dispersion was present. In all cases a Lorentzian line shape gave a better fit than a Gaussian.

8.3 Results

Firstly the angular variation of the ESR spectra were investigated. Figure 8.3a shows the X-band ESR spectra of Gd^{3+} in $\text{EuBa}_2\text{Cu}_3\text{O}_{6+x}$ for different angles θ between the c axis and the magnetic field for a temperature just above T_c . At room temperature only two lines are observed: the $7/2 \leftrightarrow 5/2$ transition and a line around $g = 2.00$. At 81 K in the c direction more transitions are observed and the central line shows a certain amount of structure. Along this direction the highest field line is the $7/2 \leftrightarrow 5/2$ transition followed by the $5/2 \leftrightarrow 3/2$ and the $3/2 \leftrightarrow 1/2$ transitions at lower fields. As can be seen from Figure 8.3a, by rotating the crystal away from the c axis, the $7/2 \leftrightarrow 5/2$ transition shifts to lower fields and after crossing the $5/2 \leftrightarrow 3/2$ transition, the two lines become

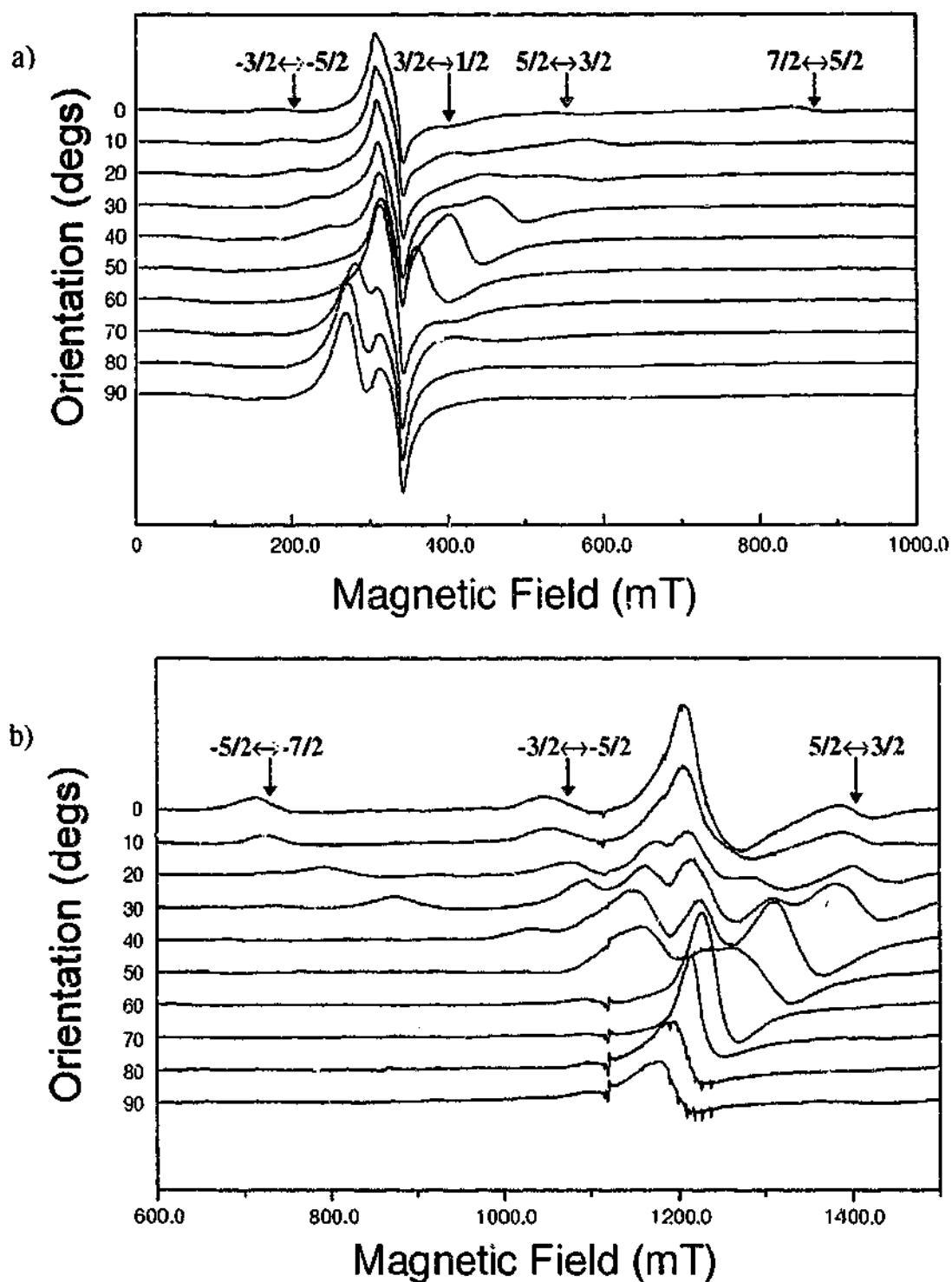


Figure 8.3 ESR spectra of a single crystal of Gd in $\text{EuBa}_2\text{Cu}_3\text{O}_{6+x}$ for orientations between 0 and 90 degrees of the applied magnetic field relative to the c axis in the c-a plane at $T = 81$ K, recorded at a) X-band. b) Q-band.

unresolvable and a single line is then observed. The same is observed when θ is further increased and this line encounters the $3/2 \leftrightarrow 1/2$ transition and only one line remains resolved. This behaviour is an indication of a weak exchange narrowing effect that becomes effective when adjacent transitions begin to interact via the Korringa process.

A similar behaviour is seen in the angular dependence of the Q-band spectra of Gd^{3+} in $EuBa_2Cu_3O_{6+x}$ (Figure 8.3b). In this case at $\theta = 0^\circ$ the high field $7/2 \leftrightarrow 5/2$ transition occurs at a field beyond the range of the magnet. This transition is therefore not seen in these spectra until $\theta = 30^\circ$ where it merges with other transitions. The $-7/2 \leftrightarrow -5/2$, however, is well resolved at $\theta = 0^\circ$ and can be followed to $\theta = 40^\circ$ where it merges with the central line. In all of these cases it is not simply that the width of the transitions obscures the separation between them. When the Korringa broadening becomes comparable to the separation between the transitions an exchanged narrowed line is seen between them which has a width less than spread in field positions of the resolved lines.

The transitions that could be resolved in either the Q-band or X-band spectra were fitted with equations 8.8 and 8.9 to determine the resonant field positions. This procedure was important in determining the field positions particularly in the Q-band spectra where the lineshapes had a large dispersion component. These field positions are tabulated in Table 8-1.

The spin Hamiltonian parameters for equations 8.1 and 8.2 were then determined by numerically diagonalising the spin Hamiltonian calculated at these orientations and magnetic fields. The resonant frequency for each of the observed transitions at the experimentally observed magnetic field value was calculated and compared to the microwave frequency. An error value for a particular set of spin Hamiltonian parameters was calculated by taking the sum of the squares of these differences in energy. The parameters were optimised by minimising this error value. Calculating the error in frequency removed the need to find the resonant magnetic field for each transition and reduced the number of matrix diagonalisations and the calculation time needed. The X-band and Q-band data were fitted simultaneously to the same set of spin Hamiltonian

parameters yielding the parameters; $g = 1.990 \pm 0.002$, $b_2^0 = -1690 \pm 10$ MHz, $b_4^0 = -205 \pm 5$ MHz, $b_4^4 = 500 \pm 200$ MHz, $b_6^0 = -20 \pm 5$ MHz, $b_6^4 = -600 \pm 100$ MHz. The fit was not improved by including an anisotropic g matrix or a non-zero b_6^6 . The transition positions calculated with these parameters are plotted in Figure 8.4 together with the experimentally observed positions.

Table 8-1 Magnetic field positions (mT) of resolved transitions in X-band and Q-band spectra for various orientations of the magnetic field with respect to the c -axis.

θ (degs)	ν (GHz)	$-\frac{1}{2} \leftrightarrow -\frac{1}{2}$	$-\frac{1}{2} \leftrightarrow -\frac{3}{2}$	$-\frac{3}{2} \leftrightarrow -\frac{1}{2}$	$-\frac{1}{2} \leftrightarrow +\frac{1}{2}$	$+\frac{1}{2} \leftrightarrow +\frac{1}{2}$	$+\frac{1}{2} \leftrightarrow +\frac{3}{2}$	$+\frac{3}{2} \leftrightarrow +\frac{1}{2}$
-10	33.852	736.7	1063.6		1210.5		1398.5	
0	33.872	717.1	1053.9		1209.7		1388.7	
10	33.849	729.8	1059.6		1209.7		1393.6	
20	34.027	799.2	1082.7	1177.3	1211.6	1284.4	1404.1	
30	34.027	877.9	1096.7	1163.8	1217.1	1312.1	1383.6	
40	34.025	1035.1		1148.5	1226.1	1311.4	1311.4	
50	34.023				1237.1			
60	34.023				1228.9			
70	34.025				1228.9			
80	34.025				1194.5			
90	34.022				1178.9			
-5	9.7718		195.5			396.5	560.6	842.0
0	9.7797		193.1			391.8	540.6	866.1
5	9.7797		197.0			399.2	563.6	835.9
10	9.7754		202.2			412.4	588.2	753.2
15	9.7756		209.6			442.2	588.4	
20	9.7733		215.2			461.7	567.8	
25	9.7747		226.8					
30	9.7658		234.2					

This exchange narrowing is more obviously seen in the collapsing of the fine structure when the temperature is increased. At $T = 81$ K and $B \perp c$ the central line shows two superimposed lines separated by about 50 mT whilst at room temperature only one line is observed. A similar effect is shown in Figure 8.5a for the evolution of the X-band spectra with increasing temperature. At 81 K with the magnetic field parallel with the c direction the spectrum is well resolved. Increasing the temperature, the semi resolved

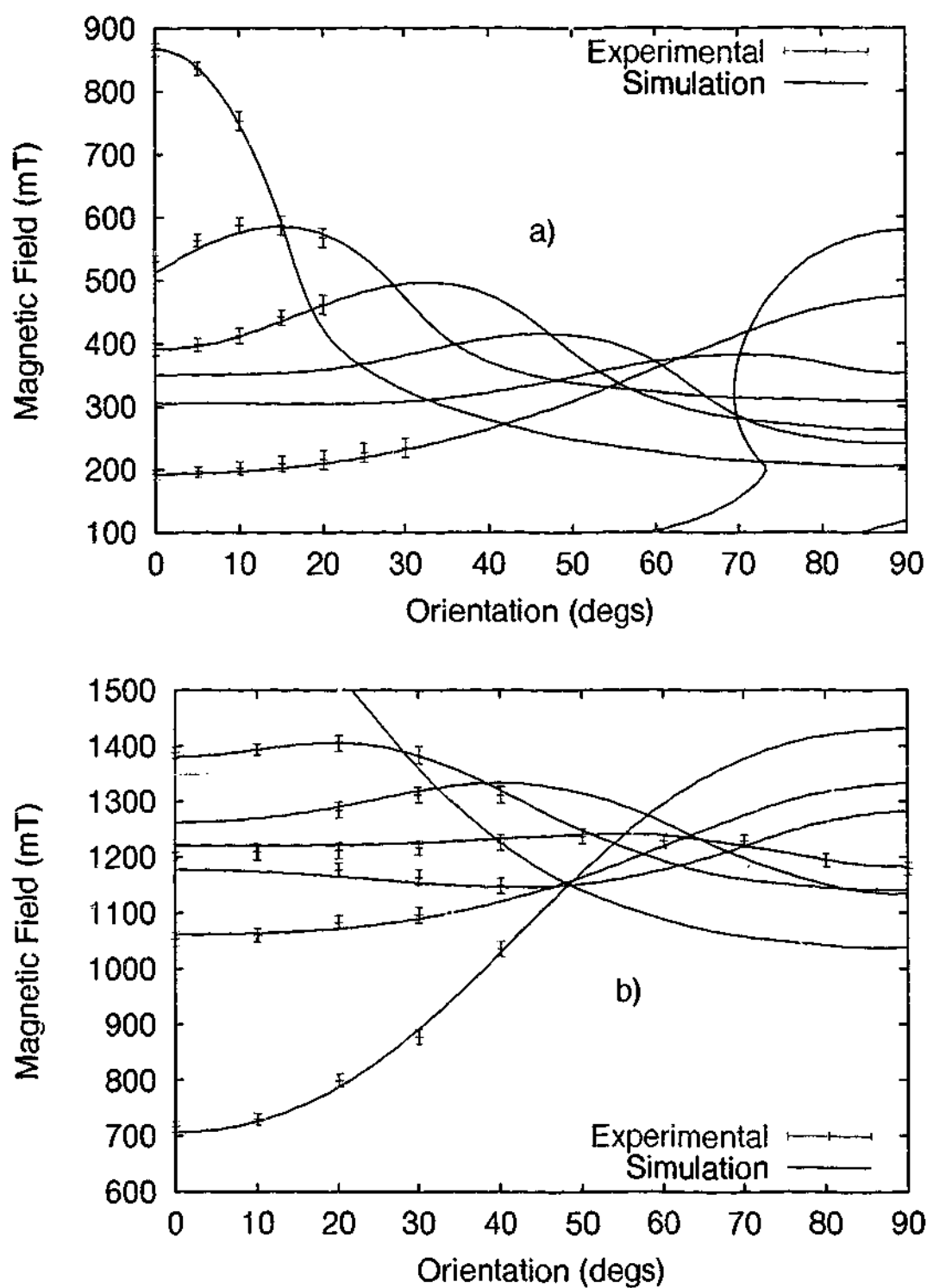


Figure 8.4 Resonant field positions calculated with the spin Hamiltonian parameters; $g = 1.990$, $b_2^0 = -1690$ MHz, $b_4^0 = -205$ MHz, $b_4^4 = 692$ MHz, $b_6^0 = -19$ MHz, $b_6^4 = -559$ MHz, solid lines and experimentally observed values, markers a) X-band. b) Q-band

spectra of the central line coalesces into a single line at 110 K. The peak to peak intensity of most transitions decreases with respect to the central line, as the temperature is increased. At 230 K no transitions could be observed even for the highest amplification of the spectrometer.

The most important result was, that in contrast to the other lines, the $7/2 \leftrightarrow 5/2$ transition did not disappear and could be observed even at 330 K. The position of this transition (within the experimental error introduced by the line width) did not change with temperature.

The linewidth of the $7/2 \leftrightarrow 5/2$ transition was determined by fitting the lineshape with equations 8.8 and 8.9. This automatic fitting procedure overcame the difficulties in measuring linewidths of broad Dysonian lines that often had large baseline effects and poor signal-to-noise. It also removed the possibility of unconsciously influencing the data by judging where the turning points in the derivative spectra are. The linewidths determined in this way are plotted as a function of temperature in Figure 8.5b. The dependence of the linewidth upon temperature can be seen to be linear in the range 80 to 280 K. One set of results, between 90 K and 115 K from a different experimental run, are offset from the line of best fit, presumably due a slight misalignment of the magnetic field with respect to the *c* axis, but they still maintain the same linear dependence on temperature.

The exchange interaction between the Gd spins and the conduction electrons results in the linear increase of the width of the $7/2 \leftrightarrow 5/2$ transition which permits us to obtain quantitative results. From the slope of the line width with temperature of 0.50 ± 0.02 mT/K we calculate the Korringa broadening using equation 8.7 to be 0.071 ± 0.002 mT/K. To calculate J_{Ss} from equation 8.6, χ_{ce} has to be evaluated. The total susceptibility χ_m of $\text{YBa}_2\text{Cu}_3\text{O}_{6+x}$ has been measured by Parkin *et al*¹⁶ and was found to depend on both the temperature and the oxygen concentration. It includes the negative diamagnetic contribution χ_{dia} and the Van Vleck. susceptibility χ_{vv} . Thus $\chi_m = \chi_{ce} + \chi_{dia} + \chi_{vv}$.

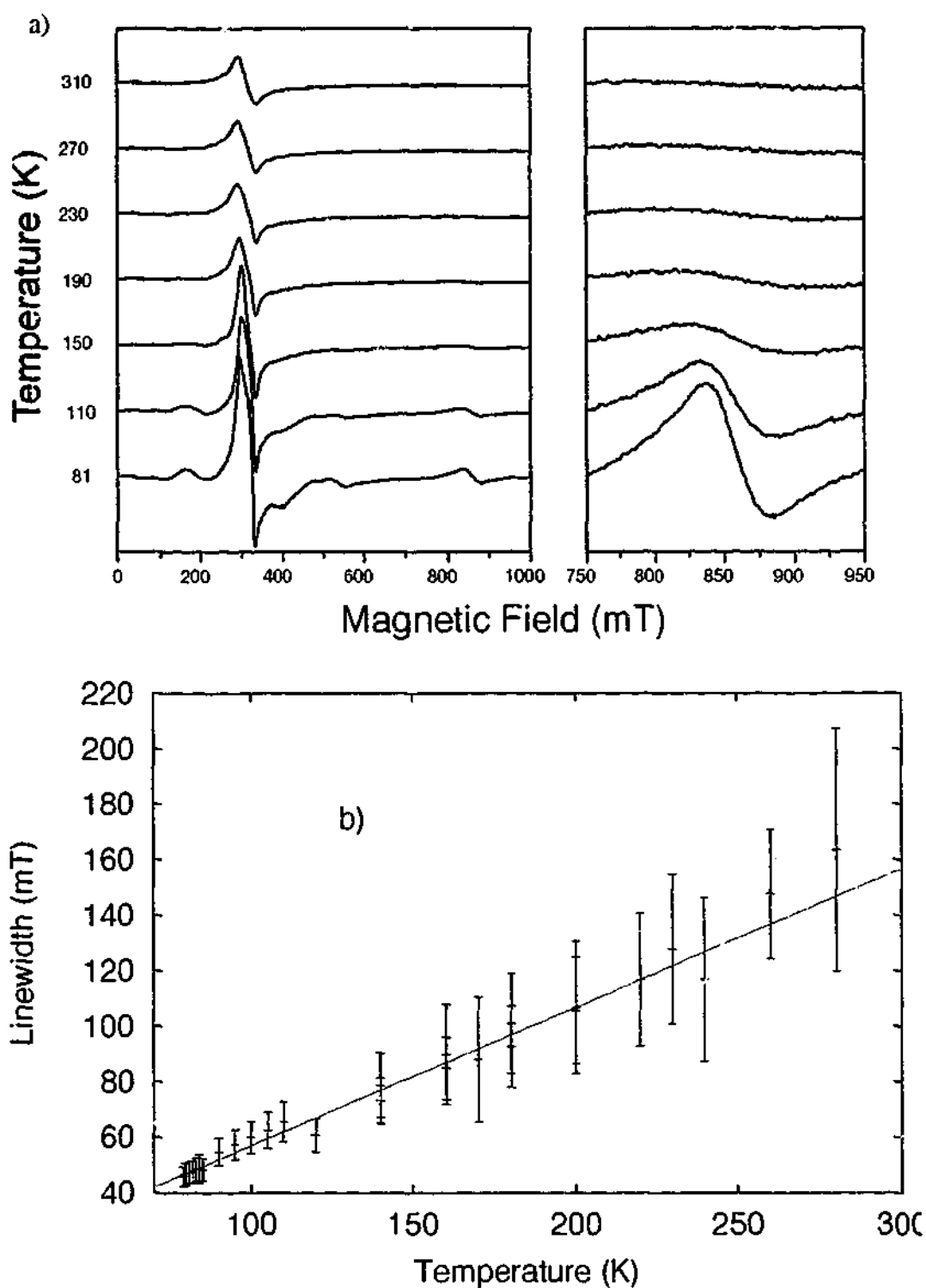


Figure 8.5 a) The X-band ESR spectra of Gd in a single crystal of $\text{EuBa}_2\text{Cu}_3\text{O}_{6+x}$ with the applied field parallel to the c axis in the temperature region 81 K to 310 K. The spectra between 750 and 950 mT is shown enlarged on the right. b) Line width as a function of temperature of the $7/2 \leftrightarrow 5/2$ transition of Gd in single crystal of $\text{EuBa}_2\text{Cu}_3\text{O}_{6+x}$. The full line is a linear best fit to the data with a slope of 0.50 ± 0.02 mT/K and a residual linewidth of 7.2 ± 1.6 mT.

From the T_c of 80 K the stoichiometric ratio of oxygen concentration is estimated to be 6.85^{17} . The magnitude of χ_{dia} and χ_{vv} are approximately equal but of opposite sign and thus cancel each other⁴ therefore $\chi_m \approx \chi_{ce}$. From the results of Parkin *et al*¹⁶

and using an average value for the small variation with temperature we obtain $\chi_m = 2.56 \times 10^{-4}$ emu/mole. Using equation 8.6, we obtain for $J_{S_S} = 0.9 \pm 0.1 \times 10^{-3}$ eV. This value is two orders of magnitude smaller than the corresponding quantity observed in metals¹². It again explains the small effect of the rare earth on T_c in the 123 compounds. From the line width, it is not possible to obtain the sign of the exchange interaction. Using equation 8.4 and the value of J_{S_S} we calculate $|\Delta g| = 0.8 \times 10^{-3}$ with respect to $g = 1.993$ of Gd. This value of Δg lies inside the experimental spread of the g values of Gd in insulators and therefore it will be difficult to obtain the sign of interaction from such a measurements.

8.4 Discussion

The experimental results show behaviour as predicted by the Barnes-Plefka theory. For the lowest temperature where the X-band spectra could be measured just above T_c , and in the c direction, (see Figure 8.3) an almost resolved spectrum is observed. However when the crystal is rotated away of the c axis, so that two or more of the transitions begin to interact via the Korringa process, they merge into a single line. This has been observed in our results when $\theta \geq 25^\circ$. The temperature effect is also seen where spectral components that are resolved at 81 K collapses at 293 K. This is shown in detail for the spectra with the applied field in the c direction. The almost resolved spectrum just above T_c gradually collapses into the centre line when the temperature increases (Figure 8.5a), except for the $7/2 \leftrightarrow 5/2$ transition which remains resolved at high temperatures.

This result by itself is strong evidence for the presence of the exchange narrowing mechanism in this system. Other transitions, most notably the $5/2 \leftrightarrow 3/2$ transition, should be at least a factor of $12/7$ more intense and should be less susceptible to mosaic

broadening than the $7/2 \leftrightarrow 5/2$ transition. Nevertheless these transitions are unresolved when the $7/2 \leftrightarrow 5/2$ transition is still observable. This is however easily understood when it is noted that this transition occurs at a field where the respective energy levels are separated by approximately twice the microwave frequency from all others and hence the exchange narrowing mechanism will have a much smaller effect. The effects of the Korringa process are still seen as its linewidth increases linearly with temperature (Figure 8.5a).

The Q-band spectra also provide evidence for the existence of the Korringa process in these superconductors. The transitions in the Q-band spectra are separated by similar magnetic field values as the X-band spectra but are better resolved. The central collapsed line comprises a much smaller percentage of the spectrum at Q-band than at X-band. This is understandable when it is considered that it is the ratio between the Korringa broadening and the separation between the energy levels that is important in determining whether a collapsed or a resolved spectrum is observed. At the magnetic field values at which Q-band spectra are recorded the separation of the energy levels is approximately 3.5 times that in X-band spectra. It is therefore expected that the Q-band spectra will be more resolved.

The Q-band spectra also enabled a more precise determination of the spin Hamiltonian parameters than those reported in a previous publication.¹⁸ A simultaneous fitting of both the Q-band and X-band spectra gave more accuracy than could be achieved by either sets of spectra alone. The least squares fitting of the line shape with a combination of absorption and dispersion components also gave more reliable values for the transition positions especially where the lines were broad. The same fitting procedure

also gave better estimates of the linewidth even when they were > 100 mT. This enabled a more precise determination of the Korringa constant than previously reported.¹⁸

Many of the papers published on the EPR spectroscopy of these 123 compounds have used aligned powders.^{7,8,19} Powders that are formed by solid state sintering are aligned in a strong magnetic field and then set in an epoxy resin matrix. The alignment of these crystallites is reported to be approximately within 2° and hence the EPR spectra of these samples are regarded as being equivalent to that obtained from single crystals.¹⁹ However, the use of aligned powders resulted from the difficulty in growing single crystals of sufficient size and quality for EPR work. The data presented here is from single crystals and is therefore free of some the problems and uncertainties involved with aligned powders. One drawback of single crystals is that the skin depth at microwave frequencies below T_c is smaller than the dimensions of the crystal. Therefore no EPR spectra can be measured below T_c in such single crystals.

Ideally the relaxation data would be best obtained through pulsed techniques. Inversion recovery experiments directly give the relaxation times without the complications of other factors that contribute to the linewidth. The limiting factor in pulsed experiments is most often relaxation times. If the relaxation times are shorter than the length of the pulse experiment then the magnetisation will have decayed before an echo can be observed. An approximate analysis of the relaxation times determined by the linewidth shows that the relaxation times are too short even at just above T_c .

At 81 K, just above T_c , ΔB_K is measured to be 41.7 mT. If we assume that $T_1^{-1} = g\beta\Delta B_K/h$ then T_1 is estimated to be less than 1 ns. This value of T_1 is much shorter than the minimum time for a two pulse sequence which is about 144 ns and hence no echo will be observed and no pulsed EPR measurements can be made.

The short relaxation times in these high T_c superconductors have been measured more recently using a cw modulation technique.^{20,21} In this method the microwave power is amplitude modulated at a frequency in the MHz range and the signal is amplified and lock-in detected. The T_1 relaxation time is then determined by the ratio of the in-phase and out-of-phase components of the signal. This method can measure the short T_1 relaxation times essentially directly without the assumptions made in analysing the cw linewidths. If these techniques were available then more accurate measurements of T_1 would have been possible, however the main conclusions made in this study are not seriously affected by this fact. The main focus has been on the temperature dependent component of the linewidth. While there are many different contributions to the linewidth it is the T_1 processes that are dependent on temperature.

8.5 Conclusion

X-band and Q-band EPR spectra of a low concentration of Gd substituting the Eu in single crystals of $\text{EuBa}_2\text{Cu}_3\text{O}_{6+x}$ ($x \approx 0.85$) were recorded. The angular dependence of these spectra were analysed to determine the spin Hamiltonian parameters; $g = 1.990 \pm 0.002$, $b_2^0 = -1690 \pm 10$ MHz, $b_4^0 = -205 \pm 5$ MHz, $b_4^4 = 500 \pm 200$ MHz, $b_6^0 = -20 \pm 5$ MHz, $b_6^4 = -600 \pm 100$ MHz. The temperature dependence of the spectra were also analysed. It was found that at low temperatures just above T_c , the X-band ESR spectra is almost resolved and with increasing temperature, exchange effects narrow most of the spectrum into a line close to $g = 2.00$ except the $7/2 \leftrightarrow 5/2$ transition, that remains partially resolved with a linewidth proportional to temperature. The narrowing of the spectra and the linear dependence of the linewidth on temperature indicate an exchange coupling between the conduction electrons and the Gd spin systems, and can be analysed by the Barnes-Plefka theory. From the line width

broadening of the $7/2 \leftrightarrow 5/2$ transition and the Barnes-Plefka theory a Korringa constant $\Delta B_K/T = 0.071 \pm 0.002$ mT/K is obtained. From this value we calculated the exchange interaction J_{Ss} between the Gd spins, S, and the conduction electrons, s, using reported values for conduction electron susceptibility. We obtain $J_{Ss} = 0.9 \pm 1 \times 10^{-3}$ eV, a value that is two to three orders of magnitude smaller than those observed in metals. It explains the small effect of magnetic ions on the T_c in the 123 compounds.

8.6 Acknowledgments

I would like to acknowledge Prof. David Shaltiel for initiating and directing the work presented here and for providing the opportunity to learn from an expert in this field. I would also like to thank B. Moubaraki for performing the magnetisation experiments and Prof. E. Waiker for providing the samples.

8.7 References

- ¹ Barnes, S.E., *Advances in Physics*, **30**, (1981), 801.
- ² Hor, P.H., Meng, R.L., Wang, Y.Q., Gao, L., Huang, Z.J., Bechtold, J., Foster, K., and Chu, C.W., *Phys. Rev. Lett.* **58**, (1987), 1891.
- ³ Market, J.T., Noh, T.W., Russek, S.E., and Cotts, R.M., *Solid State Commun.* **63**, (1987) 847.
- ⁴ Alloul, H., Ohno, T., and Mendels, P., *Phys. Rev. Lett.* **16**, (1989) 1700.
- ⁵ Causa, M.T., Fainstein, C., Nieva, G., Sanchez, R., Steren, L.B., Tovar, M., Zysler, R., Vier, D.C., Schultz, S., Oseroff, S.B., Fisk, Z., and Smith, L.G., *Phys. Rev.* **B38**, (1988) 257.
- ⁶ Shaltiel, D., Barnes, S.E., Bill, H., Francois, M., Hageman, H., Jegondaz, J., Lovy, D., Monod, P., Peter, M., Revcolevschi, A., Sadowski, W., and Walker, E., *Physica C* **161**, (1988) 13.
- ⁷ Rockenbauer, A., Janossy, A. Korecz, L., and Pekker, S., *J. Magn. Reson.*, **97**, (1992) 540.
- ⁸ Janossy, A., Cooper, J.R., Brunel, L.C., and Carrington, A., *Phys. Rev.* **B50**, (1994) 3442.
- ⁹ Hasegawa, H., *J. Phys. Soc. Jpn.* **21**, (1959) 483.
- ¹⁰ Barnes, S.E., *Phys. Rev.* **B9**, (1974) 4789.
- ¹¹ Plefka, T., *Phys. Status Solidi*, **B55**, (1973) 129.
- ¹² Davdov, D., Orbach, R., Rettori, C., Shaltiel, D., and Tao, L.J., *Phys. Rev.* **B5**, (1972) 1171 and references herewith.

-
- ¹³ Moret, J.M., Orbach, R., Peter, M., Shaltiel, D., Suss, J.T., Zingg, W., Devine, R.A.B., and Zimmerman, P.H., *Phys. Rev. B* **11**, (1975) 2002.
- ¹⁴ Urban, P., Davidov, D., Belschner, Plefka, T. and Sperlich, G., *Phys. Rev. B* **12**, (1975) 72.
- ¹⁵ Blazey, K.W., et al. *Phys. Rev. B*, **36**, (1987) 7241.
- ¹⁶ Parkin, S.P., Engler, E.M., Lee, V.Y., and Beyer, R.B., *Phys. Rev. B*, **37**, (1988) 131.
- ¹⁷ Ihara, H., Oyanagi, H., Sugise, R., Ohno, E., Matsubara, T., Ohashi, S., Terada, N., Jo, M., Hirabayashi, M., Murata, K., Negishi, A., Kimura, Y., Akiba, E., Hayakawa, H. and Shin, S., *Physica C* **153-155**, (1988). 948.
- ¹⁸ Shaltiel, D., Noble, C., Pilbrow, J., Hutton, D. and Walker, E., *Phys Rev B*, **53**, (1996) 12430.
- ¹⁹ Janossy, A., Rockenbauer, A., Pekker, S., Oszlanyi, G, Faigel, G. and Korecz, L., *Physica C*, **171**, (1990) 457.
- ²⁰ Atsarkin, V.A., Demidov, V.V. and Vasneva, G.A., *Phys. Rev. B*, **52**, (1995) 1290.
- ²¹ Atsarkin, V.A., Demidov, V.V. and Vasneva, G.A., *Appl. Magn. Reson.* **15**, (1998) 323.

9. Nutation spectroscopy of $\text{Ti}:\text{CsAl}(\text{SO}_4)_2 \cdot 12\text{H}_2\text{O}$.

9.1 Introduction

The EPR spectrum of $\text{Ti}:\text{CsAl}(\text{SO}_4)_2 \cdot 12\text{H}_2\text{O}$ has been the subject of much contention. The $\text{CsM}(\text{SO}_4)_2 \cdot 12\text{H}_2\text{O}$ group of alums are β alums where the trivalent cation, M, occupies four equivalent sites in the unit cell each coordinated by six water molecules in an octahedral arrangement with a trigonal distortion. Ti^{3+} , d^1 , will give a $S=1/2$ spin system and hence, neglecting hyperfine splitting from isotopes with nuclear spin, only one transition for each of the four magnetically inequivalent $\langle 111 \rangle$ sites is expected. The EPR spectrum, however, has been shown to consist of at least seven transitions.¹ Various models have been proposed to explain the experimental spectrum but none have been totally satisfactory.

Two recent papers on caesium titanium alum have shown a possible explanation of this system.^{1,2} In this model a strong cubic field leaves an orbital triplet lowest and the small trigonal field then splits this into a singlet and a doublet. In contrast to other models the trigonal component is assumed to be positive and leave the doublet lowest. A combination of spin-orbit and Jahn-Teller coupling then removes the remaining orbital degeneracy to give three Kramers doublets. The ground state will then have $g_{\parallel}=2(1-k)$ and $g_{\perp}=0$, where k is an orbital reduction factor. It was however shown that a distortion with lower symmetry than trigonal will increase both g_{\parallel} and particularly g_{\perp} . The extra transitions in the experimental spectrum are then explained as a series of discrete distortions caused by strain in the crystal from the Ti substituting for Al.

It has been shown recently that it is possible, using nutation spectroscopy, to accurately measure small g -values that are difficult or impossible to obtain with standard

cw EPR techniques.³ In the case of axial g values and neglecting off-resonance effects the nutation frequency is given by the equation.³

$$\omega_{nut} = 2\pi g_{\perp} \beta B_1 / h \quad [9.1]$$

where

$$g_{\perp} = \sqrt{\left(\frac{g_{\perp} g_{\parallel}}{g}\right)^2 \cos^2 \alpha + g_{\perp}^2 \sin^2 \alpha} \quad [9.2]$$

$$g = \sqrt{g_{\parallel}^2 \cos^2 \theta + g_{\perp}^2 \sin^2 \theta} \quad [9.3]$$

B_1 is the microwave magnetic field, θ is the angle between the static magnetic field and the principal direction of the axial g matrix and α is the orientation of the B_1 field vector in the plane perpendicular to B_0 . If $\theta = 0^\circ$ then we obtain $g_{\perp} = g_{\perp}$ and $g = g_{\parallel}$. The resonant field position gives us g_{\parallel} and the nutation frequency will be proportional to g_{\perp} .

Several echo detected nutation experiments have been proposed. The simplest of this type of experiment consists of a primary echo sequence (Figure 9.1a) where the first pulse is replaced by a high turn angle (HTA) pulse of variable length (HTA- τ - π - τ -echo).⁴ The echo amplitude is then monitored as a function of the HTA pulse length. Alternatively, the turn angle of the first pulse is kept at $\pi/2$ and the second pulse is incremented ($\pi/2$ - τ -HTA- τ -echo).⁵ In another variation both pulses can be incremented so that a ratio of 1:2 is maintained between the length of the two pulses (HTA- τ -HTA- τ -echo).⁶ Alternatively B_1 can be incremented by changing the microwave power⁷

Stoll *et al*⁸ have recently introduced a novel pulse sequence, phase-inverted echo-amplitude detected nutation (PEANUT), which was found to have a number of advantages over the previously described experiments. The PEANUT sequence, $(\pi/2)_x$ - τ -(HTA) $_x$ -(HTA) $_x$ - τ -echo, has two HTA pulses with opposing phases and lengths t and T - t

(Figure 9.1b). The total length of the two HTA pulses remains constant during the experiment as t is incremented. Some of the main advantages of the PEANUT sequence are, the refocussing of B_1 inhomogeneities, the constant length of the pulse sequence which results in nutation spectra that are free from relaxation broadening and the selectivity that can be achieved by adjusting the initial $\pi/2$ pulse.

The pulse sequence used in this study, shown in Figure 9.1c, is another variation of the primary echo experiment. Both pulses are HTA pulses but in contrast to the third example given above the length of the pulses are incremented and decremented, with lengths t and $T-t$, as in the PEANUT experiment. This type of incrementation scheme has also been used for free evolution periods in ESEEM experiments.⁹ The length of the experiment therefore remains constant and the nutation spectra are not broadened by relaxation. The relaxation still limits the length of the pulse sequence. Other features of the PEANUT sequence, such as the refocussing of B_1 inhomogeneities, are not maintained in this pulse sequence.

In the present case the selectivity offered by the initial $\pi/2$ pulse in the PEANUT sequence is actually seen to be a disadvantage. The broad continuous distribution of g -values, and hence nutation frequencies, means that only portions of the spectrum will be selected for a given nominal $\pi/2$ pulse. This will result in a distorted spectrum. We wish to recover information regarding this distribution of g -values and therefore we argue that the pulse sequence used in this study, that does not have pulses with a nominal turn angle, is more appropriate.

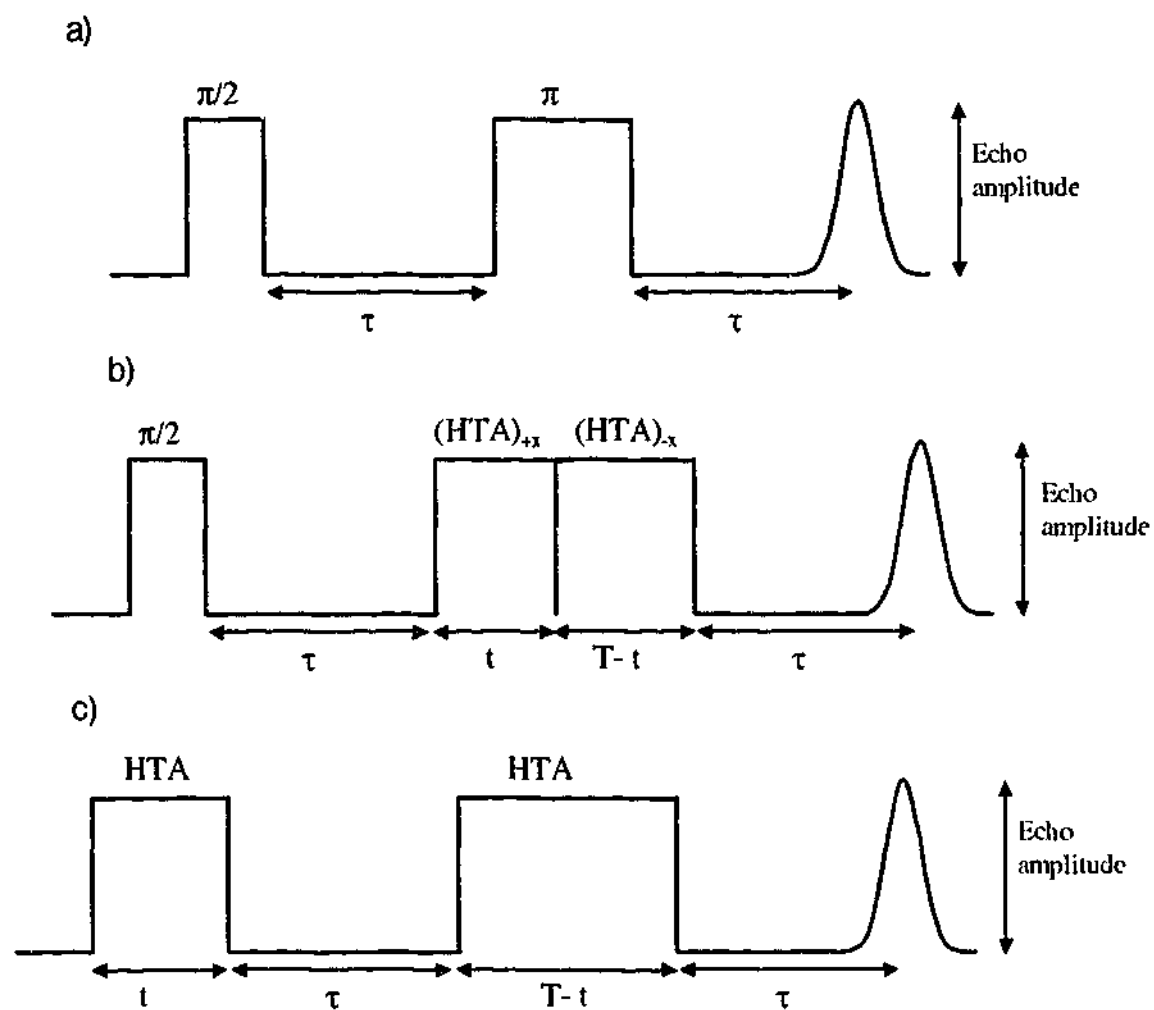


Figure 9.1 Pulse sequences for echo detected nutation experiments. a) Primary two-pulse echo. b) PEANUT sequence. c) Two-pulse echo with HTA pulses.

The sequence used here has one less pulse than the PEANUT sequence. As a large proportion of signal intensity is lost with each additional pulse in a multiple pulse sequence this is extremely important in samples with a low signal-to-noise ratio. More importantly, this sequence does not contain a nominal $\pi/2$ pulse. The $\pi/2$ pulse in the PEANUT sequence assumes that the nutation frequency is known whereas in reality this is the very property we are trying to measure. In the case of $\text{Ti}^{3+}:\text{Al}_2\text{O}_3$ this is not a major consideration as it is easy to adjust the attenuation or pulse length in a two pulse experiment to maximise the echo and thereby achieve a $\pi/2$ pulse. In the Ti alum system this is not as simple because g_{\perp} varies across the spectrum and hence a $\pi/2$ pulse has no real meaning.

The amplitude of the echo is proportional to $\sin(\theta)$, where $\theta = g\beta B_1 t/h$. If the pulse is adjusted to give a turn angle of $\pi/2$ for the part of the spectrum where g_{\perp} is close to zero, then it will be much greater than $\pi/2$ for other parts of the spectrum. This will cause a modulation throughout the spectrum. Conversely if the pulses are set so that $\theta = \pi/2$ for the part of the spectra with the largest g_{\perp} then the part where $g_{\perp} \sim 0$ will have a much lower intensity.

This problem is not seen in the pulse sequence used in this study where no pulses of fixed turn angle exist. All that is needed in this pulse sequence is to adjust the B_1 field so that the experimental nutation frequencies lie within the Nyquist frequency, and if the relaxation times are long enough to extend the length of the nutation pulses. All nutation frequencies that are less than the Nyquist frequency, and large enough to give several nutation periods, are then resolved without significant distortion.

9.2 Experimental

The crystal used in this study was grown by cocrystallisation of $\text{CsAl}(\text{SO}_4)_2 \cdot 12\text{H}_2\text{O}$ and $\text{CsTi}(\text{SO}_4)_2 \cdot 12\text{H}_2\text{O}$ in H_2SO_4 (1 M). The proportion of the two alums was such that titanium represented 2% of the total trivalent cation concentration in solution. Further details of growth are given by Tregenna-Piggot *et al*¹. The crystal had well defined $\{111\}$ faces which allowed it to be mounted on a perspex rod such that the applied field was in a $\{110\}$ plane. All orientations of the magnetic field in this plane could then be achieved by rotation of the sample holder. The sample was sealed in a quartz EPR tube in a helium atmosphere.

The EPR spectra were recorded on a Bruker ESP380e spectrometer. An Oxford Instruments liquid helium cryostat was used for recording low temperature spectra. The spectra were recorded at the lowest temperature, approximately 1.7 K, that could be

achieved while pumping on the helium reservoir. The Bruker dielectric probehead was used for both the cw and pulsed EPR experiments.

The conditions for all cw spectra are microwave power = 0.01 mW, modulation amplitude = 0.8 mT, sweep time = 168 s, time constant = 81.92 ms, resolution = 2048.

The nutation experiment was performed using a two pulse echo sequence with high turning angles. The initial field position was 558.5 mT with 1.2 mT increments and a resolution in the field dimension of 32. The resolution of the time axis was 100 and an increment of 8 ns was used. The time axis was Fourier transformed after using a Gaussian window function and zero filling to give the nutation frequency. The nutation frequency was then converted to a g value scale, assuming that all transitions originate from an S=1/2 system, by calibration with a sample of coal with an isotropic g value of 2.0023. The attenuation on the high power pulse arm was 3 dB where the nutation frequency for the g = 2.0023 standard was approximately 55 MHz.

9.3 Results

The cw EPR spectrum of $\text{Ti}^{3+}:\text{CsAl}(\text{SO}_4)_2 \cdot 12\text{H}_2\text{O}$ with the applied field along a $\langle 111 \rangle$ axis is shown in Figure 9.2a. The spectrum shows one sharp transition at g = 1.168 with resolved titanium hyperfine structure. Several other broader lines are seen with higher g-values. Upon rotation of the magnetic field away from the $\langle 111 \rangle$ axis all transitions move to higher fields and broaden. The angular dependence of each of the transitions was followed upon rotation away from the $\langle 111 \rangle$ axis and could be fitted with an axially symmetric g-matrix (Figure 9.2b).

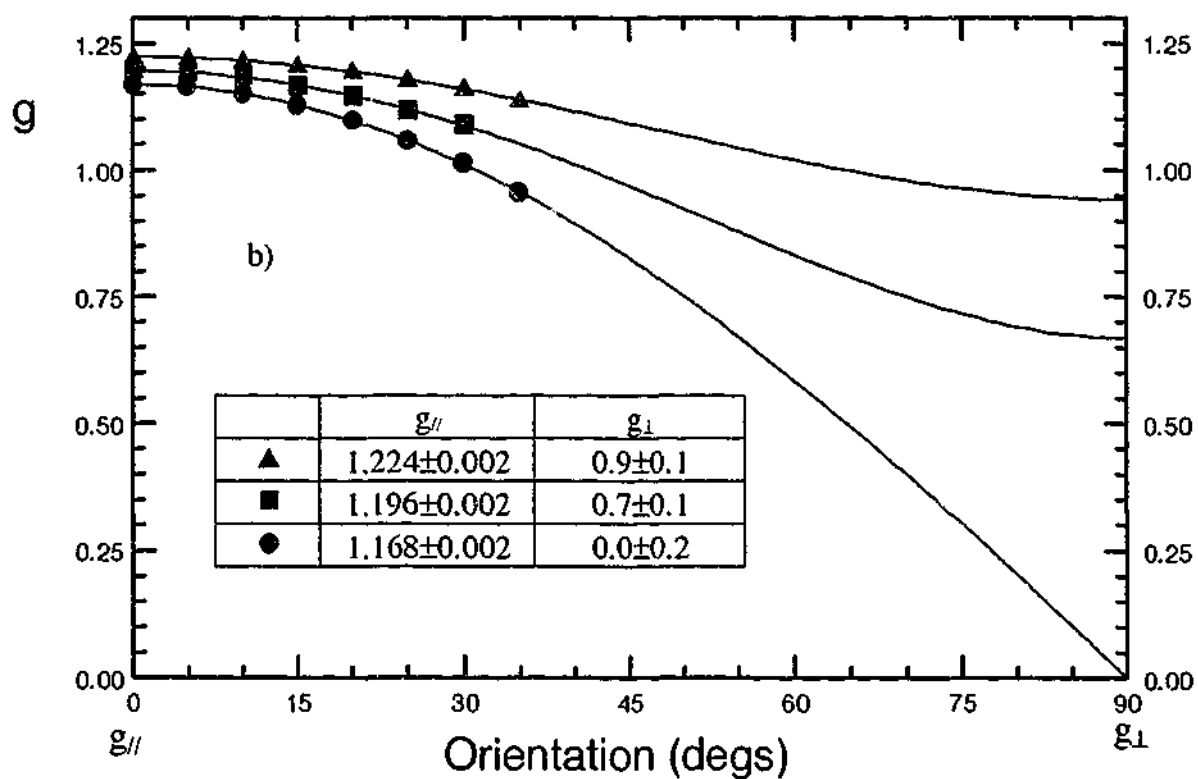
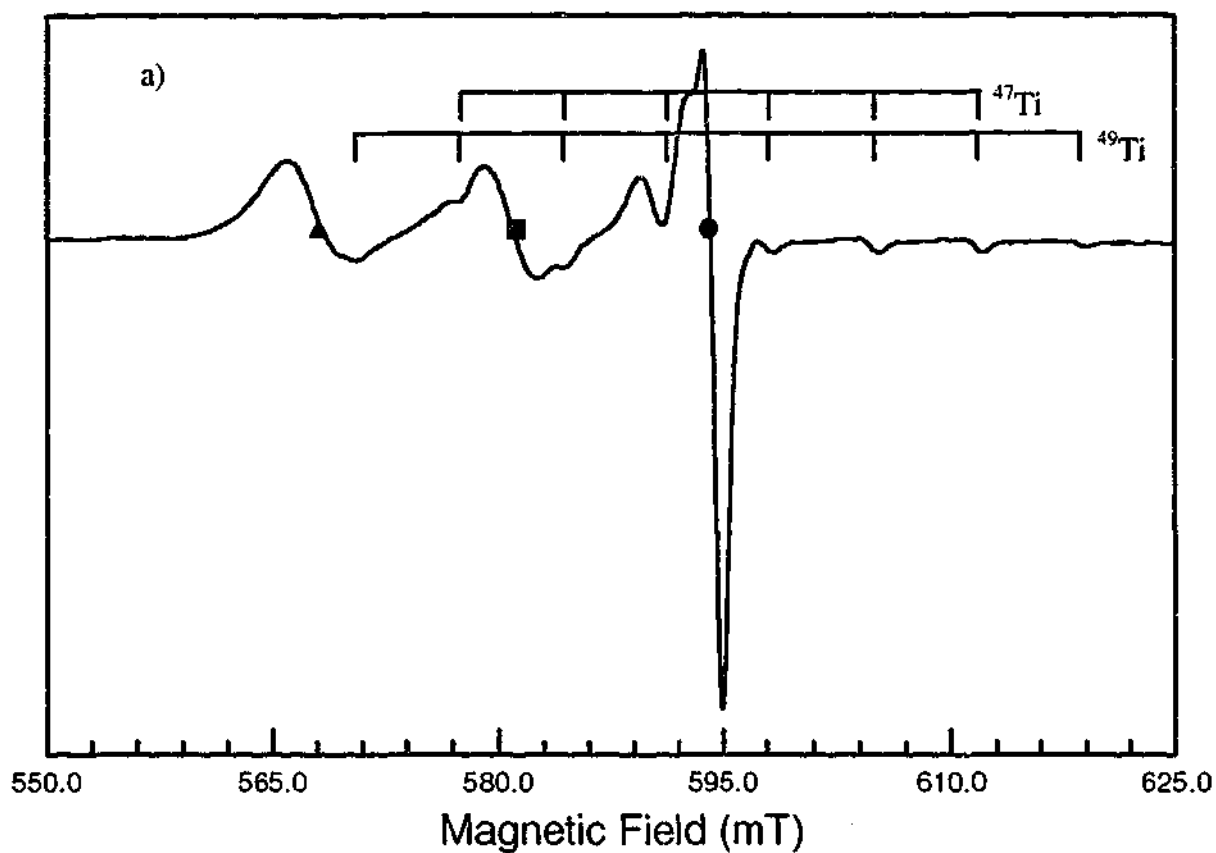


Figure 9.2 a) Cw spectra of Ti:CsAlSH at 1.7 K. The magnetic field is along a $\langle 111 \rangle$ axis. Three well resolved transitions are indicated by the symbols (▲, ■, ●). The sharp transition indicated by ● also shows resolved Ti hyperfine splittings. b) Angular dependence of the three resolved transitions in a. The solid lines show the best fit to $g = \sqrt{g_{//}^2 \cos^2 \theta + g_{\perp}^2 \sin^2 \theta}$

The limitations of the of the cw spectra in determining the g values is evident.

Well resolved spectra were only obtained within 35° of the $\langle 111 \rangle$ axis and one of the

transitions has $g_{\perp} \sim 0$. This transition is beyond the magnetic field range of the spectrometer when the magnetic field is more than 45° from the $\langle 111 \rangle$ axis. Extrapolation must then be used to determine g_{\perp} with subsequent errors. The lines also broaden rapidly with rotation of the magnetic field away from the $\langle 111 \rangle$ axis, which is expected as the linewidth will be proportional to $1/g_{\perp}$.¹⁰ This results in a lower signal to noise and an increased uncertainty in the transition position.

In order to further characterise the spectrum a two dimensional field swept nutation experiment was performed (Figure 9.3). The g_{\perp} values for the main transitions obtained with this method are in general agreement with those obtained by cw methods. The accuracy in this case is limited by the broadening seen in the nutation frequency and the accuracy of the calibration. The broadening in the nutation frequency is due to the low signal to noise ratio, the low number of nutation periods measured in the time interval and to the Gaussian apodisation function used. The ability to resolve low g values is limited by the maximum B_1 value obtainable, approximately 1.2 mT, and various relaxation processes during the nutation experiment. This means that the errors in the measured g value for the transition where $g_{\perp} \sim 0$ may be significant.

In this instance the advantage of the nutation experiment can be seen in the qualitative information that can be gained from the spectrum. It is evident that g_{\perp} varies across each of the lines seen in the cw spectrum. This suggests that the width of these lines results from inhomogeneous broadening in both g_{\parallel} and g_{\perp} . More importantly g_{\parallel} and g_{\perp} are not independent and a relationship between the two is seen across the whole spectrum. It is therefore best to view the spectrum not as consisting of discrete transitions but rather as a distribution of sites with a range of g values. The spectrum highlights the relationship between g_{\parallel} and g_{\perp} and gives important information about the

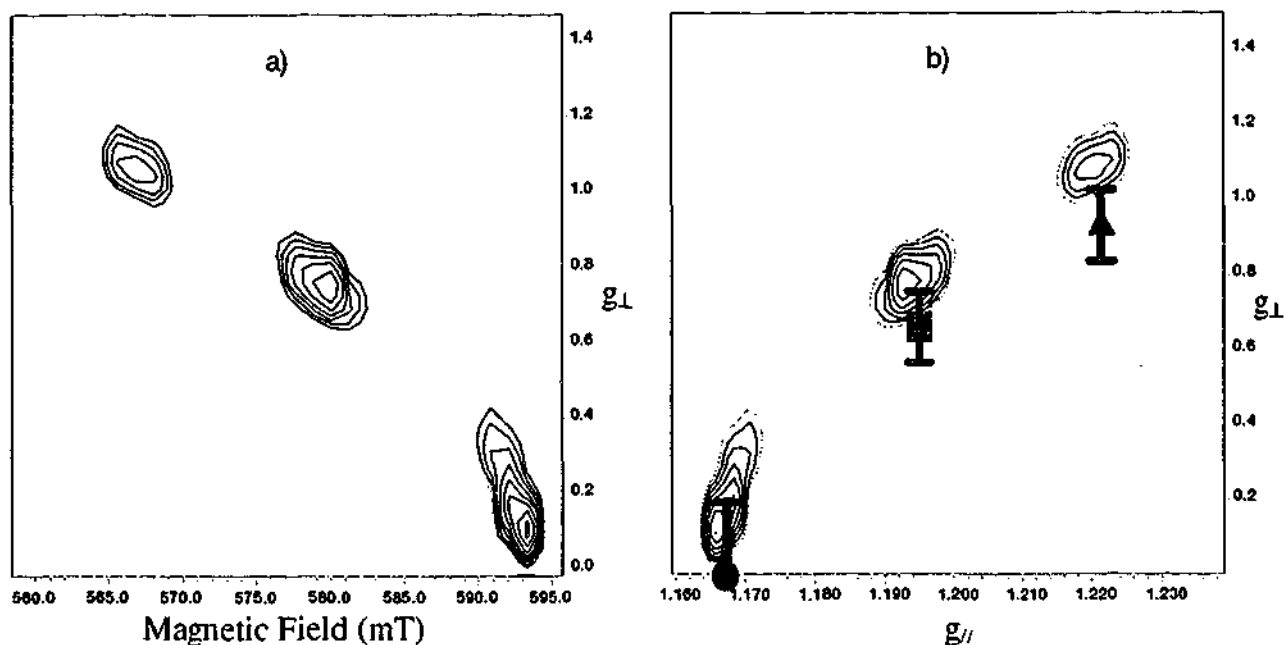


Figure 9.3 a) Two dimensional field swept nutation spectrum of Ti:CsAlSiH at 1.7 K. The static magnetic field is along a $\langle 111 \rangle$ axis. b) The same data with the field scale converted to g-factor using the equation $g = h\nu / \beta B$. The g-values obtained from the fitting of the cw spectra are indicated by (\blacktriangle , \blacksquare , \bullet).

origins of the lines. This can also be seen, but less transparently, in the cw spectra as the lines broaden upon rotation away from the $\langle 111 \rangle$ axis.

9.4 Discussion

The present study demonstrates a novel use of nutation spectroscopy. Nutation spectroscopy has been extensively used in NMR, chiefly in the determination of quadrupole parameters, for example Kentgens et al.¹¹ Similarly it has been used in EPR to determine electron spin in cases where $S > 1/2$ but no fine structure is resolved. An example has previously been given with nickel centres in diamond¹².

More recently, and concurrently with this work, the use of nutation spectroscopy to determine g values has been reported.³ The system studied is Ti^{3+} in Al_2O_3 , again d^1 and $S=1/2$, and a single transition with $g_{\perp}=0.04$ is seen. The utility of the nutation technique in this case is the measurement of such a low g value. Using cw techniques the field required to observe this transition at this orientation with an X-band spectrometer would be 17 Tesla, far in excess of that achievable with normal spectrometers.

In our study the emphasis has been on qualitative rather than quantitative measurements. The ability to resolve small g_{\perp} 's is limited in our case by the maximum B_1 field, about 1.2 mT, the short relaxation times for the various processes that occur during the nutation pulses and the low signal to noise ratio. Also we did not measure the nutation frequency of the standard and the Ti alum simultaneously. This would introduce errors as the Q value and filling factor would be slightly different for the different samples and hence the B_1 field would also differ.

The true value of this particular experiment is seen rather in the two dimensional representation of the experimental data. As in many cases in pulsed EPR a two dimensional spectrum can yield much more information than a one dimensional spectrum. This is mainly because relationships within the data can be seen much more clearly when the data is shown plotted against two appropriate axes. This is evident in various two dimensional ESEEM experiments where the hyperfine interaction from neighbouring nuclei are shown on two axes. In the present case the appropriate axes for representing the strain interaction are g_{\parallel} and g_{\perp} . A two dimensional nutation spectrum with these two axes then graphically depicts the interaction and shows the relationship between g_{\parallel} and g_{\perp} . It is shown that nutation spectroscopy is particularly useful in this instance.

The two dimensional spectrum then gives accurate information about the distribution of g values. Most importantly it gives information about this distribution in both g_{\parallel} and g_{\perp} . This is important in this particular case as it is the relationship between g_{\parallel} and g_{\perp} that gives support for the model put forward by Dubicki and Riley.² It also shows that it is more accurate to think of this distribution as a distribution in two dimensions rather than one as is commonly portrayed.

9.5 Conclusion

The two dimensional nutation spectrum of $\text{Ti}:\text{CsAl}(\text{SO}_4)_2 \cdot 12\text{H}_2\text{O}$ has been recorded at 1.7 K with the magnetic field parallel to a $\langle 111 \rangle$ axis. The resulting spectrum gives the g_{\parallel} and g_{\perp} values for all the lines in the complicated EPR spectrum. These g values are in agreement with those obtained from the angular dependence of the cw spectra. The advantage of the nutation experiment is that instead of g values for each line in the spectrum a complete two dimensional picture is produced. The relationship between g_{\parallel} and g_{\perp} is obvious in this spectrum and supports the model proposed by Dubicki and Riley to account for the complicated spectrum of $\text{Ti}:\text{CsAl}(\text{SO}_4)_2 \cdot 12\text{H}_2\text{O}$.²

The sequence in these experiments is demonstrated to give accurate nutation frequencies which can be used to obtain g values. The sequence is also shown to be able to give g value information where a distribution of g values are present in the spectrum. The two dimensional spectrum obtained is believed to be the first case in which a strain broadening interaction is shown in two dimensions with both g_{\parallel} and g_{\perp} . It can be concluded that this technique will be important in characterising similar systems and will give information that cannot be obtained from other techniques.

9.6 References

- ¹ Tregenna-Piggot, P.L.W., O'Brien, M.C.M., Pilbrow, J.R., Güdel, H.U., Best, S.P. and Noble, C., *J. Chem. Phys.* **107**, 8275 (1997).
- ² Dubicki, L. and Riley, M.J., *J. Chem. Phys.* **106**, 1669 (1997).
- ³ Willer, M. and Schweiger, A., *Chem. Phys. Lett.*, **264**, (1996) 1.
- ⁴ Takui, T., Sao, K., Shiomi, D., Itoh, K., Kaneko, T., Tschchida, E. and Hishide, H., *Mol. Cryst. Liq. Cryst.* **279**, (1996) 155.
- ⁵ Zhong, Y.C. and Pilbrow, J.R., *Chem. Phys. Lett.*, **222**, (1994) 592.
- ⁶ Isoya, J., Kanda, H. and Uchida, Y., *Phys. Rev. B*, **42**, (1990) 9843.
- ⁷ Astashkin, A.V., Mino, H., Kawamori, A., Ono, T-A., *Chem. Phys. Lett.*, **272**, (1997) 506-516.
- ⁸ Stoll, S., Jeschke, G., Willer, M. and Schweiger, A., *J. Magn. Reson.*, **130**, (1998) 86.
- ⁹ Song, R., Zhong, Y.C., Noble, C. J., Pilbrow, J.R. and Hutton, D.R., *Chem. Phys. Lett.* **243**, (1995) 324.

¹⁰ Pilbrow, J.R., *J. Magn. Reson.*, **58**, (1984) 186.

¹¹ Kentgens, A.P.M., Lemmens, J.J.M., Geurts, F.M.M., and Veeman, W.S., *J. Mag. Reson.*, **71**, 62 (1987).

¹² Isoya, J., Kanda, H., Norris, J.R., Tang, J., and Bowman, M.K., *Phys. Rev. B* **41**, (1990) 3905.

10. EPR of Natural Rutile Powder

10.1 Introduction

EPR spectroscopy is a useful tool for the identification and characterisation of transition metal impurities in minerals. Frequently, the hyperfine splitting identifies the transition metal. For example, manganese often has a characteristic six line spectrum from the nuclear spin of $5/2$. The electron spin and zero-field splitting parameters for the defect also can identify the metal ion. For example, Fe^{3+} ions often have a characteristic $S = 5/2$ spectrum. In general, it is necessary to correlate the EPR features with other forms of analysis to identify the metal ion. Once this has been done the characteristic EPR spectrum, or fingerprint, can be used to identify the transition metal ions in other samples where the impurity content is not known.

Previous studies on synthetic rutile have identified several transition metal ion impurities. Cr^{3+} and Fe^{3+} are the most common and earliest studied transition metal ion impurities.^{1,2,3} The single crystal spectra of Cr^{3+} in rutile have been simulated with the spin Hamiltonian parameters $g = 1.97$, $D = -0.68 \text{ cm}^{-1}$, $E = -0.14 \text{ cm}^{-1}$ and the spectra of Fe^{3+} with the parameters $g = 2.00$, $D = 0.67 \text{ cm}^{-1}$, $E = 0.07 \text{ cm}^{-1}$, $a = 0.04 \text{ cm}^{-1}$, $F = 0.02 \text{ cm}^{-1}$.⁴

Manganese has been shown to be introduced into the rutile structure as Mn^{4+} substituting for Ti^{4+} .^{3,5,6,7} It has also been shown that the manganese in rutile can be readily reduced by heating the sample in a reducing atmosphere.⁸ Both Mn^{3+} ⁹ and Mn^{2+} ⁸ have been observed in prepared rutile samples. The hyperfine splitting parameters for these manganese ions are; Mn^{4+} in rutile ($|A_x| = 217 \text{ MHz}$, $|A_y| = 211 \text{ MHz}$, $|A_z| = 218 \text{ MHz}$)⁷, Mn^{2+} in rutile ($|A_x| \approx 237 \text{ MHz}$, $|A_y| = 240 \text{ MHz}$, $|A_z| = 245 \text{ MHz}$)⁸ and Mn^{3+} in rutile ($|A_z| = 159 \text{ MHz}$, $|A_{xy}| = 249 \text{ MHz}$)⁹. Vanadium has also recently been observed in

rutile in a tetravalent state.¹⁰ The reported hyperfine values for V^{4+} in rutile are ($|A_x| = 136$ MHz, $|A_y| = 181$ MHz, $|A_z| = 334$ MHz).

In this study the EPR spectra of natural rutile powder is compared with reported spectra of synthetic rutile in an attempt to determine the identity and chemical state of the paramagnetic centres present in this sample.

10.2 Experimental

The rutile was collected from an abandoned mine near Kragerø in southern Norway. X-ray diffraction showed a very small admixture of feldspar with the rutile. The polycrystalline sample was ground into a fine powder, suitable for Mössbauer and EPR studies, with an agate mortar and pestle. No single crystals of a suitable size for EPR were available.

EPR measurements were performed using an X-band EPR spectrometer, Bruker ESP380, at temperatures between 4K and room temperature. An Oxford CF935 cryostat and ITC4 temperature controller were used when recording liquid helium temperature spectra. The sample was then fired at 1000 °C for 3 hours in air and EPR measurements repeated.

10.3 Results

The room temperature EPR spectrum of the untreated rutile powder is shown in Figure 10.1a. The spectrum is dominated by some two broad features at approximately 50.0 and 140.0 mT which are labelled A and B for convenience. Some partially resolved hyperfine splitting on line A is apparent suggesting that this line might be due to a manganese species. A number of other peaks in the spectrum can be clearly attributed to Fe^{3+} and Cr^{3+} in rutile.^{1,2,3} The simulated EPR spectra of Cr^{3+} and Fe^{3+} in rutile, calculated with the parameters given in Kim *et al*⁴, are shown in Figure 10.1d-e. The

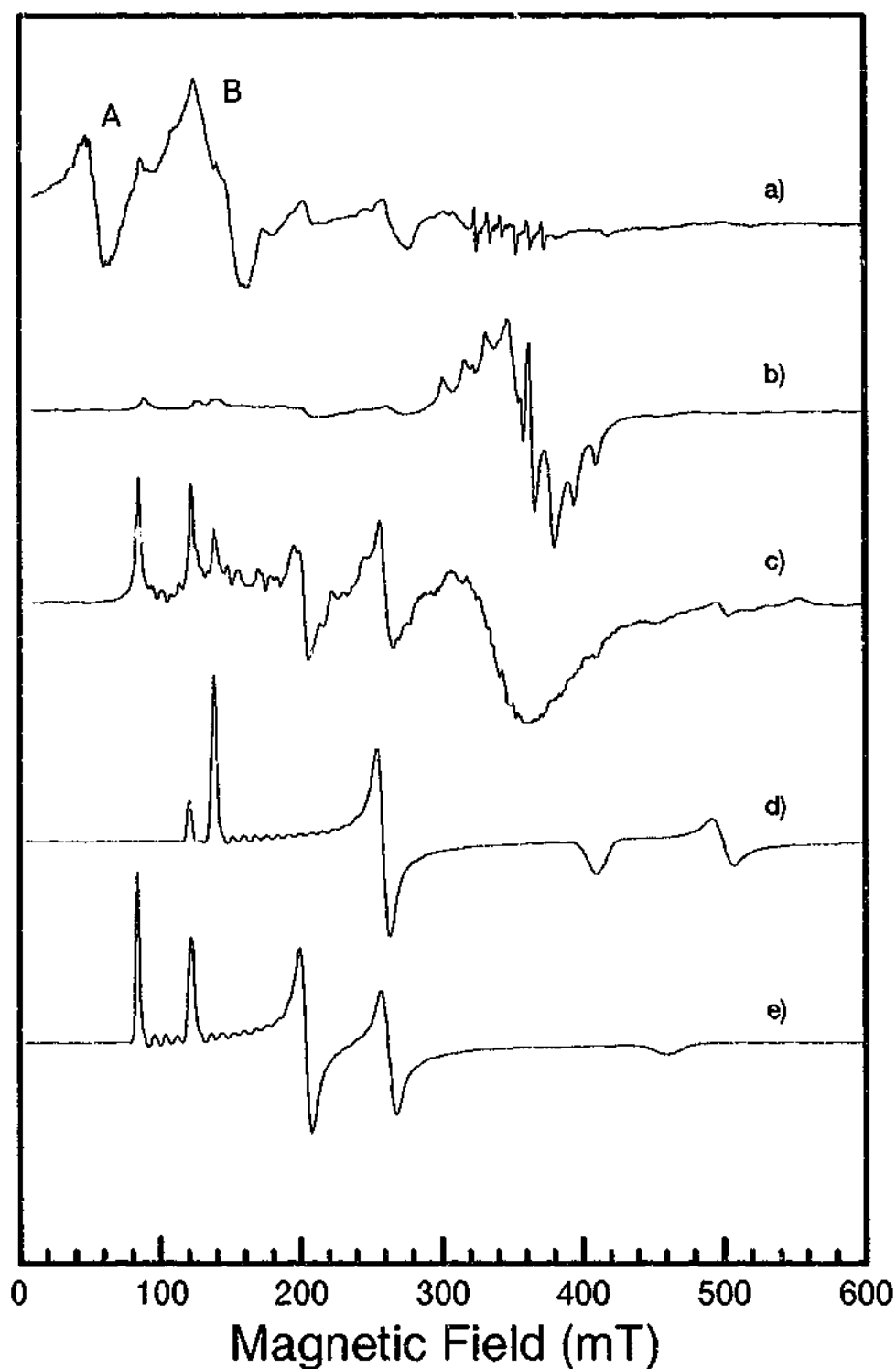


Figure 10.1 EPR spectra of powdered rutile. a) Spectrum recorded at room temperature showing broad features at low field. b) Spectrum recorded at 6 K. c) Room temperature spectrum after heat treatment. d) Simulated spectrum of Cr^{3+} in rutile. e) Simulated spectrum of Fe^{3+} in rutile.

sextet seen at approximately 350.0 mT can also be identified as belonging to manganese ($I=5/2$). However the experimentally determined hyperfine splittings for this set of lines does not match any of reported values for manganese in any charge state. The spectrum most resembles that of a low spin, $S=1/2$, Mn^{2+} , species.

The EPR spectrum of the same sample recorded at liquid helium temperature is shown in Figure 10.1b. The Fe^{3+} and Cr^{3+} components are still present, however the A and B components no longer seen and the spectrum is now dominated by another feature consisting of a series of peaks centred at 350.0 mT. These set of peaks appear to arise from manganese with a hyperfine constant of approximately 435 MHz and g-factor splitting.

The room temperature EPR spectrum of the rutile sample after heating to 1000°C in air for 4 hours is shown in Figure 10.1c. This spectrum differs from the original room temperature spectrum in that the A and B features have been removed and the manganese sextet at $g = 2$ is no longer resolved.

10.4 Discussion

The iron concentration in the rutile sample used in this study has previously been estimated to be 0.41 mol % using neutron activation analysis.¹¹ This earlier study also determined that the iron was predominantly present as Fe^{3+} , with less than 10% Fe^{2+} , using Mössbauer spectroscopy.

De Biasi et al investigated the role of dipole-dipole line broadening in the EPR spectra of Fe^{3+} and Cr^{3+} in rutile and determined a relationship between the iron and chromium concentrations and the EPR linewidths.² Using the estimates from this paper the linewidth of the Fe^{3+} line centred at 202 mT of 8.6 mT, a concentration of approximately 0.5 mol % Fe^{3+} is obtained.

It was not possible to use the relationship given for the concentration of Cr^{3+} as the EPR line used overlaps with a Fe^{3+} line. It is also apparent that these relationships are only valid if no other paramagnetic species are present. The dipole-dipole component of

the linewidth will be determined by the total concentration of paramagnetic species which include Fe^{3+} , Cr^{3+} and possibly others.

Eggleston *et al* showed that strain broadening also has a significant contribution to the EPR linewidths.¹ In the samples that they investigated, with concentrations up to 1000 ppm (~ 0.2 mol %), the linewidths were independent of concentration. Significant variations in linewidth were, however, found between samples with different preparation techniques. Rough calculations also showed that, for the concentrations present in these samples, dipole-dipole line broadening only formed a small proportion of the linewidth.

The applicability to the current sample of the relationship between linewidth and concentration given by de Biasi *et al* is obviously limited. Without a means of separating the different components of the linewidth no reasonable estimates of the concentration can be made. It is possible however to place an upper limit on the paramagnetic concentration of about 0.5 mol %.

The manganese EPR spectra observed in the powdered rutile sample do not match any of the reported spectra for any charge state of manganese. It is possible that the manganese is contained in a phase other than rutile. Even if this phase comprises only a small fraction of the sample a signal from this component may be observed due to the sensitivity of EPR. The possibility of contributions from surface species also exists. This is supported by the observation that they were removed by annealing. Other possibilities include transition metal ion pairs or clusters. The origin of the A and B components of the spectra cannot be easily determined from these results. The A component appears to have some partially resolved hyperfine structure. This structure suggests that it could be

due to manganese in another form. This however cannot be verified with the current polycrystalline sample.

10.5 Conclusions

The EPR results demonstrate that Fe^{3+} and Cr^{3+} are present as substitutional impurities in the rutile in concentrations less than 0.5 mol %. Manganese is also present in the sample. The current results however do not readily determine the form of manganese that is responsible for the EPR signal. Two components of the room temperature EPR spectrum labelled A and B also could not be identified although it is suggested that they could be manganese related. Further experiments with single crystal samples would be necessary to resolve these questions.

10.6 References

- ¹ Eggleston, H.S., Thorp, J.S., *J. Mat. Sci. Letters*, **16**, (1981) 537.
- ² De Biasi, R.S., Fernandes, A.R., and Grillo, M.L.M., *J. Am. Ceram. Soc.*, **76**:1, (1993) 223.
- ³ Cordischi, D., Valigi, M., Gazzoli, D., and Indovina, V., *J. Solid State Chemistry*, **15**, (1975) 82.
- ⁴ Kim, S.S., Jun, S.S. and Park, M.J., *J. Korean Phys. Soc.*, **23**, (1990) 73
- ⁵ Andresen, H.G., *J. Chem. Phys.* **35**, (1961) 1090.
- ⁶ Andresen, H.G., *Phys. Rev.*, **120**, (1960). 1606.
- ⁷ Pechenyi, A.P., Tkachenko, V.D., Frantsevich, I.N., Geifman, I.N., Krygin, I.M., and Lukin, S.N., *Sov. Phys. Solid State*, **21**, (1979). 1642.
- ⁸ Pechenyi, A.P., Blizvyuk, V.N., *Sov. Phys. Solid State*, **22**, (1980) 734.
- ⁹ Gerritsen, H.J., Sabisky, E.S., *Phys. Rev.*, **132**, (1963) 1507.
- ¹⁰ Kubec, F., Šroubek, Z., *J. Chem. Phys.*, **57**, (1972) 1660.
- ¹¹ Murad, E., Cashion, J.D., Noble, C.J. and Pilbrow, J.R., *Mineralogical Magazine*, **59**, (1995) 557.

Appendix: Supporting Publications

Primary or Secondary Author

1. Interaction between localized and conduction electron spins in the high T_c superconductor Gd:EuBa₂Cu₃O_{6+x}. D. Shaltiel, C. Noble, J. Pilbrow, D. Hutton, E. Walker. *Phys. Rev. B*, **53**, (1996) 12430.
2. Optically Detected Electron Paramagnetic Resonance of Ni-Related Defects in Synthetic Diamond Crystals. Th. Pawlik, C.J. Noble, J-M. Spaeth, *J. Phys. Condens. Matter*, **10**, (1998) 9833.
3. Electron Paramagnetic Resonance Investigations of Nickel Defects in Natural Diamonds. C.J. Noble, Th. Pawlik, J-M. Spaeth, *J. Phys. Condens. Matter*, **10**, (1998) 11781.

Other Publications

1. The Chemical State of Fe in Rutile from an Albatite in Norway, E. Murad, J.D. Cashion, C.J. Noble, J.R. Pilbrow. *Mineralogical Magazine*, **59**, (1995) 557.
2. A New Six-Pulse Two-Dimensional Electron Spin Echo Envelope Modulation (ESEEM) Correlation Spectroscopy, R. Song, Y.C. Zhong, C.J. Noble, J.R. Pilbrow, D.R. Hutton, *Chem. Phys. Lett.*, **237**, (1995) 86.
3. A One-Dimensional Mixing-Frequency Electron Spin Echo Envelope Modulation (MIF-ESEEM) Spectroscopy, R. Song, Y.C. Zhong, C.J. Noble, J.R. Pilbrow, D.R. Hutton, *Chem. Phys. Lett.*, **243**, (1995) 324.

4. Separation of Overlapped Lines in Two-Dimensional Electron-Spin-Echo-Envelope-Modulation (ESEEM) Spectroscopy. R. Song, Y.C. Zhong, C.J. Noble, J.R. Pilbrow, D.R. Hutton, *J. Mag. Reson. A*, 117, (1995) 320.
5. Line-Shifting Method in Electron-Spin-Echo-Envelope-Modulation (ESEEM) Spectroscopy. R. Song, Y.C. Zhong, C.J. Noble, J.R. Pilbrow, D.R. Hutton, *Appl. Mag. Reson.*, 11, (1996) 391.
6. Pulsed EPR Investigations of Hyperfine Structure in Gamma-Irradiated Alanine. J.R. Pilbrow, D.R. Hutton, Y.C. Zhong, C.J. Noble, R. Song. *Applied Radiation and Isotopes*, 47, (1996) 1257.
7. Paramagnetism of Caesium Titanium Alum and the Jahn-Teller Interaction. P. L. W. Tregenna-Piggot, M. C. M. O'Brien, J. R. Pilbrow, H. U. Güdel, S. P. Best and C. J. Noble. *J. Chem. Phys.*, 107, (1997) 8275.

Interaction between localized and conduction-electron spins in the high- T_c superconductor Gd:EuBa₂Cu₃O_{6+x}

D. Shaltiel

Racah Institute of Physics, Hebrew University, Jerusalem, Israel
and Department of Physics, Monash University, Clayton, Victoria 3168, Australia

C. Noble, J. Pilbrow, and D. Hutton

Department of Physics, Monash University, Clayton, Victoria 3168, Australia

E. Walker

Department of Physics, University of Geneva, Geneva, Switzerland

(Received 2 March 1995)

This work studies the spin-spin interaction between the conduction electrons and localized spins in high- T_c superconductors. We report the ESR at 9.74 GHz of low concentration of Gd substituting the Eu in single crystals of EuBa₂Cu₃O_{6+x} ($x \approx 0.85$). At low temperatures just above T_c , the Gd ESR spectra in the c axis direction is almost resolved. With increasing temperature, exchange effects narrow most of the spectrum into a line close to $g=2.00$ except the $7/2 \leftrightarrow 5/2$ transition, which remains partially resolved. This transition has a Dysonian line shape and shows a Korringa behavior. The narrowing of the spectra and the Korringa behavior indicate an exchange coupling between the conduction electrons and the Gd spin systems, and can be analyzed by the Barnes-Plefka theory. From the linewidth broadening of the $7/2 \leftrightarrow 5/2$ transition and the Barnes-Plefka theory we obtain a Korringa constant $\Delta H_K/T = 0.5$ G/K. From this value we calculated the exchange interaction J_{Ss} between the Gd spins, S , and the conduction electrons, s , using reported values for conduction electron susceptibility. We obtain $J_{Ss} = 0.5 \pm 0.1 \times 10^{-3}$ eV, a value that is two or three orders of magnitude smaller than those observed in metals. It explains the small effect of magnetic ions on the T_c in the RBa₂Cu₃O_{6+x} compounds ($R =$ rare earth). From the angular dependent spectra of Gd:EuBa₂Cu₃O_{6+x} we obtain zero field terms of $b_2^0 = -1800$ MHz, $b_4^0 = -180$ MHz, and $b_4^4 = +600$ MHz. These values are not significantly different from those obtained for Gd in YBa₂Cu₃O_{6+x}. [S0163-1829(96)00617-1]

INTRODUCTION

The study of the spin-spin interaction between the conduction electrons and localized spins gives significant information about the properties of the conduction-electron system.¹ It is important to apply it in the investigation of high- T_c superconductors where the conduction electrons play a decisive role in the superconducting properties and the high superconducting transition temperatures.

In this work we report the ESR measurements of small amounts of Gd in EuBa₂Cu₃O_{6+x} ($x \approx 0.85$). ESR of the localized moments in metals has been very effective in the study of the spin-spin interaction with the conduction electrons. Gadolinium has the advantage over other localized magnetic atoms in that its ground state is an almost pure $S=7/2$ state and therefore its interaction with the lattice is sufficiently weak enabling one to observe the ESR even above room temperatures. It has also the advantage in the case of EuBa₂Cu₃O_{6+x} that it goes substitutionally in the lattice replacing the europium. Furthermore its effect on the superconducting properties is small as reflected in the small change of T_c even when all the Eu is replaced by Gd.²

The 123 compounds consist of two sets of double Cu planes. The element in the 1 site, such as rare earth elements or Y, are located between these two sets of Cu planes. As the conductivity resides mostly within each of the Cu plane sets

their interaction with the elements in site 1 was found to be small. This explains the small effect of most of the magnetic rare earth atoms on T_c . Interactions between the elements in site 1 and the conduction electrons was investigated mostly by the NMR of Y (Refs. 3 and 4) and also by the ESR of Gd (Refs. 5-7) partially substituting a nonmagnetic element such as Y or Eu. The NMR and most of the ESR measurements were carried out either in powders⁵ or in powders aligned along the c axis.⁷ Shaltiel *et al.*⁶ have investigated the ESR spectra of Gd in single crystals of YBa₂Cu₃O_{6+x}. They reported the observation of a resolved fine spectrum at temperatures close to but above T_c and a Korringa relaxation of an exchanged narrowed line. Janossy *et al.*⁸ reported the observation of the ESR spectrum of Gd:YBa₂Cu₃O_{6+x} in oriented powders measured in the c direction. Their results show both the Korringa relaxation and g shift of the $1/2 \leftrightarrow -1/2$ transition at 245 GHz. NMR of Y in YBa₂Cu₃O_{6+x} shows a very small Knight shift and small Korringa behavior^{3,4} that varies with temperature and oxygen concentration.⁴

In this work we report the Korringa behavior above T_c of the $7/2 \leftrightarrow 5/2$ transition of a Gd spin probe in a single crystal of a 123 compound. The use of the $7/2 \leftrightarrow 5/2$ transition removes the uncertainty in assigning various contributions to the linewidth that may be present when the central $1/2 \leftrightarrow -1/2$ line is used. This is particularly the case when

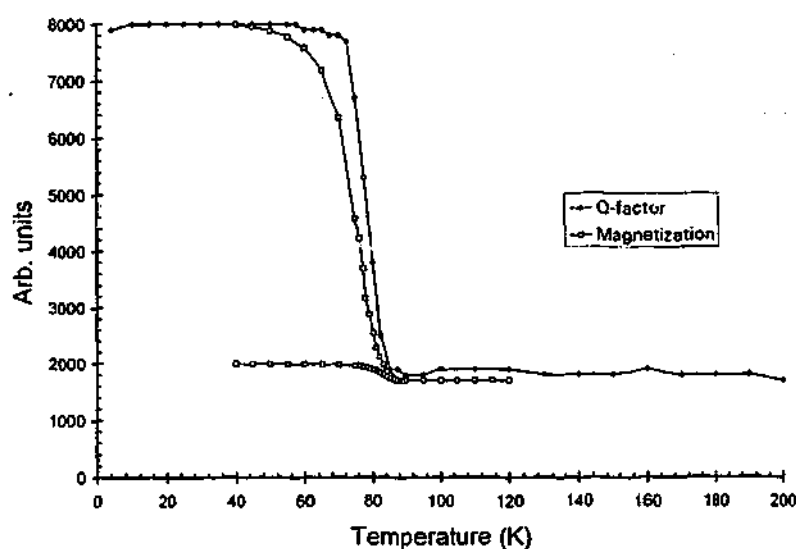


FIG. 1. Q factor of the sapphire resonator as a function of temperature, with the Gd:EuBa₂Cu₃O_{6+x} sample. Also shown is the magnetization of the sample measured in a squid magnetometer. The sample was initially cooled with no applied field. A field of 50 G (the same field at which the Q factor measurements were performed) was then applied and the magnetization was then measured as the temperature was raised above T_c and then lowered. This curve was arbitrarily scaled to compare with the Q factor measurements.

the Korringa relaxation is fast at high temperatures and when the experiment is performed at X band. Under these conditions it is unlikely that the spectra will be fully resolved and an additional exchange narrowed component will be present in the same field position as the $1/2 \leftrightarrow -1/2$ transition. Most importantly the $7/2 \leftrightarrow 5/2$ transition will remain resolved at temperatures where the other transitions are obscured by this process.

This method enabled us to obtain linewidth measurements at X band over a wide temperature range above T_c . These results allowed us to calculate the spin-spin exchange interaction J_{Ss} between the local Gd spins and the conduction electrons in a 123 compound. In contrast to NMR so far reported, we do not observe above 110 K deviation from a simple linear broadening with temperature. Our results indicate similar behavior to that observed in metals indicating an interaction with a Fermi liquid.

EXPERIMENTAL RESULTS

A few single crystals of EuBa₂Cu₃O_{6+x}, $x \approx 0.85$, with a nominal concentration of 5% Gd replacing the Eu atoms were investigated. The crystals were grown in Geneva using the flux method. Some of these crystals were heat treated in an oxygen atmosphere for 7 days at 400 °C to alter the oxygen content. The work reported here however was carried out on a $2 \times 3 \times 0.1$ mm crystal which was not heat treated after being removed from the flux. The value of T_c was determined by magnetization measurements using a squid magnetometer. The Gd ESR was measured with a Bruker ESP380e spectrometer at 9.74 GHz using either a dielectric resonator or a rectangular cavity. The dielectric resonator was introduced into a helium flow dewar that enabled variation of the temperature from 4.2 K to room temperature. In the rectangular cavity the temperature control system consists of a quartz dewar insert that passes through the cavity and a temperature controlled nitrogen gas system that feeds the nitrogen through the quartz dewar. It allowed the variation of the temperature from 110 to 330 K and thus a total temperature range of 4.2 to 330 K was possible.

The crystals with a platelet form had the c axis perpen-

dicular to the platelet plane. To avoid possible damage due to moisture the crystals were sealed in a 3 mm diameter quartz tube in helium atmosphere with the c axis and either the a or the b axis perpendicular to the tube axis. The quartz tube axis was perpendicular to the direction of the magnetic field. Rotating the quartz tube enabled to change the magnetic field in the c - a plane or c - b plane. We did not determine which of the a or b direction was in the plane. As the monitoring thermocouple was outside the quartz tube, and therefore not in direct contact with the sample, the absolute accuracy of the temperature measurements for the nitrogen flow system is estimated to be ± 2 K. In the sapphire resonator the absolute accuracy was even lower. However, differences in temperatures of ± 0.1 K could be measured when desired; this was the case when measuring the ESR spectra just above T_c . Here T_c can be determined by the ESR spectrum of the sample itself. ESR is a very sensitive technique to determine the onset of superconductivity, from both changes in the Q factor of the cavity and the onset of vortex noise. We used the change in the Q factor of the cavity as function of the temperature to determine the superconducting transition. This is shown in Fig. 1 with a sharp transition width of less than 3 K evident. This indicates a fairly homogeneous sample.

Figure 2 shows the ESR spectra for different angles θ between the c axis and the magnetic field for a temperature just above T_c [Fig. 2(a)]. The theoretical field positions that correspond to $\Delta M = \pm 1$ transitions as a function of the angle θ are also shown in Fig. 2(b). At room temperature only two lines are observed: the $7/2 \leftrightarrow 5/2$ transition and a line around $g = 2.00$. At 81 K in the c direction more transitions are observed and the central line shows a certain amount of structure. Along this direction the highest field line is the $7/2 \leftrightarrow 5/2$ transition followed by the $5/2 \leftrightarrow 3/2$ and the $3/2 \leftrightarrow 1/2$ transitions at lower fields. As seen from Fig. 2(a) by rotating the crystal away from the c axis, the $7/2 \leftrightarrow 5/2$ transition shifts to lower fields and after crossing the $5/2 \leftrightarrow 3/2$ transition, the two lines become unresolvable and a single line is then observed. The same is observed when θ is further increased and this line encounters the $3/2 \leftrightarrow 1/2$ tran-

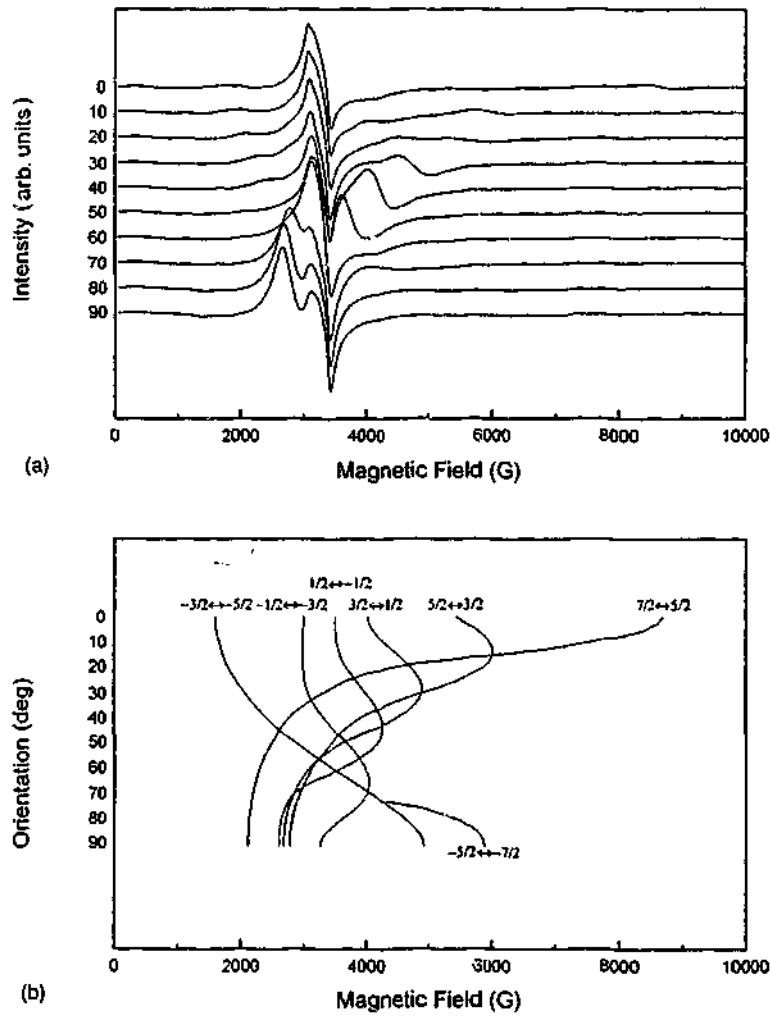


FIG. 2. (a) ESR spectra of a single crystal of Gd in $\text{EuBa}_2\text{Cu}_3\text{O}_{6+x}$ for orientations between 0 and 90° of the applied magnetic field relative to the c axis in the c - a plane at $T=81$ K. (b) Calculated angular dependence of the most strongly allowed transitions of a single crystal of Gd in $\text{EuBa}_2\text{Cu}_3\text{O}_{6+x}$ over the same range of orientations as in part (a). These values were calculated by numerical diagonalization of the Hamiltonian given in Eqs. (1) and (2). The coefficients of the zero-field terms were chosen to best fit the data for the four resolved transitions in the c direction and the two resolved transitions perpendicular to the c axis.

sition and only one line remains resolved. This behavior is an indication of a weak exchange narrowing effect that becomes effective when adjacent transitions begin to interact via the Korringa process.

This exchange narrowing is also evident as a collapsing of

the fine structure when the temperature is increased. At $T=81$ K and $B \perp c$ the central line shows two superimposed lines separated by about 500 G whilst at room temperature only one line is observed. A similar effect is shown in Fig. 3 for the evolution of the spectra in the c direction with in-

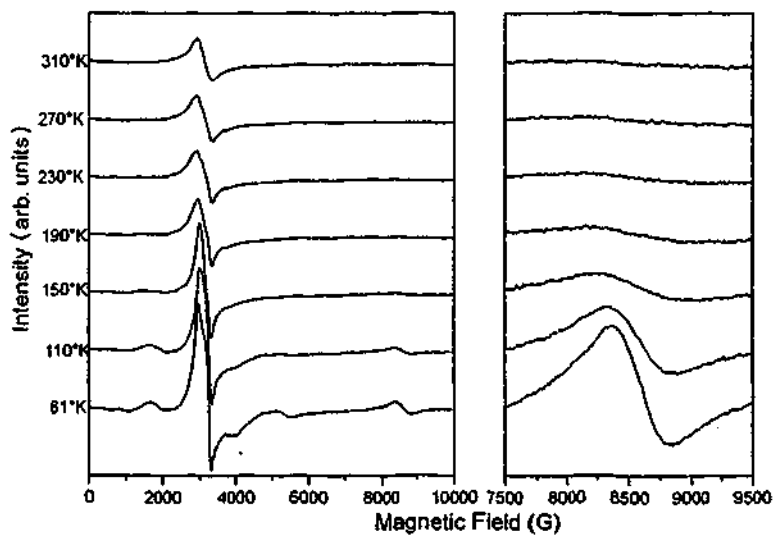


FIG. 3. The ESR spectra of Gd in a single crystal of $\text{EuBa}_2\text{Cu}_3\text{O}_{6+x}$ with the applied field parallel to the c axis in the temperature region 81 to 310 K. The spectra between 7500 and 9500 G to 310 K. The spectra between 7500 and 9500 G to 310 K. The $7/2 \leftrightarrow 5/2$ transition is just discernable at this scale at the highest temperature.

creasing temperature. At 81 K with the magnetic field in the c direction the spectrum is well resolved. Increasing the temperature, the semi resolved spectra of the central line coalesces into a single line at 110 K. The peak to peak intensity of most transitions decreases, with respect to the central line, as the temperature is increased. At 230 K none could be observed even for the highest amplification of the spectrometer.

The most important result was, that in contrast to the other lines, the $7/2 \leftrightarrow 5/2$ transition did not disappear and could be observed even at 330 K. The position of this transition (within the experimental error introduced by the linewidth) did not change with temperature. The linewidth of this transition as a function of temperature shows a linear behavior with a slope of 3.5 G/K (Fig. 4).

THEORETICAL CONSIDERATIONS

The temperature and angular behavior of the spectra indicate that in addition to the zero field splitting of the Gd $S=7/2$ ground state an exchange narrowing mechanism is present.¹ The origin of the exchange interaction is the interaction with the conduction carriers and can be written as $J_{Ss}(S \cdot s)$, where J_{Ss} is the exchange interaction between the Gd spins S and the spin of the conduction carriers s .

The total Hamiltonian is written as

$$\mathcal{H} = g\mu_B \mathbf{B} \cdot \mathbf{S} + \mathcal{H}_{zf} + J_{Ss}(\mathbf{S} \cdot \mathbf{s}), \quad (1)$$

where the zero field Hamiltonian can be approximated by

$$\mathcal{H}_{zf} = b_2^0 O_2^0 + b_4^0 O_4^0 + b_4^4 O_4^4, \quad (2)$$

where O_2^0 , O_4^0 , and O_4^4 are the spin operators reflecting the symmetry of the Gd ion environment. In this approximation we neglect terms higher than fourth order which have little influence on the observed spectra when compared with the uncertainties in the line positions. The parameters b_2^0 , b_4^0 , and b_4^4 are then sufficient to describe the angular dependence of the observed transitions.

The ESR spectra for a system of Gd spins and conduction electrons will depend on the Gd concentration, the conduction-electron spin system, the spin relaxation between the two systems, and the spin relaxation of each system to the lattice. The behavior of such a system has been calculated by Hasegawa⁹ for $S=1/2$. The more complicated system where $S > 1/2$ is given by the Barnes-Plefka^{10,11} theory. It has been shown that for metals such as Al (Ref. 12) or Pd (Ref. 13) and at "high" temperature, the seven fine structure lines of the Gd spectra collapse into a single line with $g = g_{Gd} + \Delta g$, where $g_{Gd} = 1.993$ is the g value obtained in insulators and

$$\Delta g = J_{Ss} \eta = J_{Ss} \chi_{cc} / g \mu_B^2 N. \quad (3)$$

Here η is the density of states per spin at the Fermi surface, χ_{cc} is the spin susceptibility of the conduction electrons per mole, N is Avogadro's number, and μ_B is the Bohr magneton.

The linewidth, ΔH , of this totally collapsed central line will follow the Korringa behavior

$$\Delta H = \Delta H_K + \Delta H_{res}. \quad (4)$$

ΔH_{res} is the residual linewidth and ΔH_K is the Korringa broadening given by

$$\Delta H_K = \frac{\pi k_B T}{g \mu_B} (J_{Ss} \chi_{cc} / g \mu_B^2 N)^2, \quad (5)$$

where k_B is the Boltzmann constant.

The case of complete collapse of the fine structure to a single central line can occur when the Korringa broadening is large compared to the zero field splittings. Under certain conditions, usually when the exchange constant is small, or at "low" temperatures, or when the zero field splittings are large a more complex behavior can be observed. At high temperatures the spectra collapse into a single line. However, when lowering the temperature the spectra begin to separate. Transitions that occur at magnetic fields where the Korringa interaction between adjacent transitions is small will be the first to become resolved. This is expected of the $\pm 7/2 \leftrightarrow \pm 5/2$ transitions which are isolated from the other transitions when the zero field splitting is large. As the temperature is further decreased a full fine structure spectrum is obtained. This has been demonstrated for Gd in Pd (Ref. 13) at low temperatures and Gd in LaSb,¹⁴ where it was shown that the value of the exchange constant is small.

In a fully resolved spectrum we expect the temperature dependent broadening of the individual lines for completely resolved spectra to be given by¹⁴

$$\Delta H_K(M \leftrightarrow M+1) = \Delta H_K [S(S+1) - M(M+1)]. \quad (6)$$

Thus for the temperature broadening of the individual transitions we expect their linewidth to be enhanced by a factor of 16, 15, 12, and 7 with respect to the fully exchanged narrowed linewidth, for the transitions $1/2 \leftrightarrow -1/2$, $\pm 3/2 \leftrightarrow \pm 1/2$, $\pm 5/2 \leftrightarrow \pm 3/2$, and $\pm 7/2 \leftrightarrow \pm 5/2$, respectively. This equation is of course valid only when the applied magnetic field is parallel to the c axis in a highly anisotropic system such as this and therefore the only quantitative use will be restricted to this case.

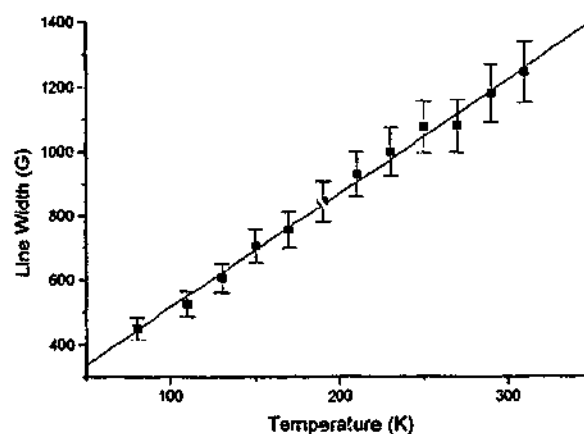


FIG. 4. Linewidth as a function of temperature of the $7/2 \leftrightarrow 5/2$ transition of Gd in single crystal of $\text{EuBa}_2\text{Cu}_3\text{O}_{6+x}$. The full line is a linear best fit to the data with a slope of 3.5 G/K.

ANALYSIS AND DISCUSSION

Our experimental results show behavior as predicted by the Barnes-Plefka theory. For the lowest temperature where the spectra could be measured just above T_c , and in the c direction [see Fig. 2(a)], an almost resolved spectrum is observed. However, when the crystal is rotated away from the c axis, so that two or more of the transitions begin to interact via the Korringa process, they merge into a single line. This has been observed in our results when $\theta \geq 25$ [Fig. 2(a)]. The temperature effect is also seen where spectral components that are resolved at 81 K collapses at 293 K. This is shown in detail for the spectra with the applied field in the c direction. The almost resolved spectrum just above T_c gradually collapses into the center line when the temperature increases (Fig. 3), except for the $7/2 \leftrightarrow 5/2$ transition which remains resolved at high temperatures.

This result by itself is strong evidence for the presence of the exchange narrowing mechanism in this system. Other transitions, most notably the $5/2 \leftrightarrow 3/2$ transition, should be at least a factor of 12/7 more intense and should be less susceptible to mosaic broadening than the $7/2 \leftrightarrow 5/2$ transition. Nevertheless these transitions are unresolved when the $7/2 \leftrightarrow 5/2$ transition is still observable. This is however easily understood when it is noted that this transition occurs at a field where the respective energy levels are separated by approximately twice the microwave frequency from all others and hence the exchange narrowing mechanism will have a much smaller effect. The effects of the Korringa process are still seen as its linewidth increases linearly with temperature (Fig. 4).

In addition to the qualitative results that show the existence of the exchange interaction between the Gd spins and the conduction electrons the linear increase of the width of the $7/2 \leftrightarrow 5/2$ transition permits us to obtain quantitative results. From the slope of the linewidth with temperature of 3.5 G/K we calculate the Korringa broadening using Eq. (4) to be 0.5 G/K. To calculate J_{5s} from Eq. (5), χ_{ce} has to be evaluated. The total susceptibility χ_m of $\text{YBa}_2\text{Cu}_3\text{O}_{6+x}$ has been measured by Parkin *et al.*¹⁵ and was found to depend on both the temperature and the oxygen concentration. It includes the negative diamagnetic contribution χ_{dia} and the Van Vleck susceptibility χ_{VV} . Thus $\chi_m = \chi_{ce} + \chi_{dia} + \chi_{VV}$.

From the T_c of 80 K we estimate the oxygen concentration to be 6.85.¹⁶ The magnitude of χ_{dia} and χ_{VV} are approximately equal but of opposite sign and thus cancel each

other,⁴ therefore $\chi_m \approx \chi_{ce}$. From the results of Parkin *et al.* and using an average value for the small variation with temperature we obtain $\chi_m = 2.56 \times 10^{-4}$ emu/mole. Using Eq. (5) we obtain for $J_{5s} = 0.6 \times 10^{-3}$ eV. This value is two orders of magnitude smaller than the corresponding quantity observed in metals.¹² It again explains the small effect of the rare earth on T_c in the 123 compounds. From the linewidth, it is not possible to obtain the sign of the exchange interaction. Using Eq. (3) and the value of J_{5s} we calculate $|\Delta g| = 0.5 \times 10^{-3}$ with respect to $g = 1.993$ of Gd; this value of Δg lies inside the experimental spread of the g values of Gd in insulators and therefore it will be difficult to obtain the sign of interaction from such a measurement.

Using Eqs. (1) and (2) and the experimental results shown in Fig. 2(a) we calculated the angular dependence of the transitions with $\Delta M = \pm 1$. The parameters used are $b_2^0 = -1800$ MHz, $b_4^0 = -180$ MHz, and $b_4^2 = +600$ MHz. These parameters are close to those of Gd in $\text{YBa}_2\text{Cu}_3\text{O}_{6+x}$ (Ref. 7) and we assume the sign of b_2^0 to be negative to be consistent with their low temperature measurements. A more accurate fit was not possible in the present case due to the difficulties in assigning transition positions in the partially resolved spectra.

In conclusion in this work we were able to obtain the Korringa broadening of the $7/2 \leftrightarrow 5/2$ fine structure transition of a Gd spin probe in a 123 high- T_c compound. This enabled us to use ESR spectra where exchange narrowing is present, to derive the exchange interaction between the localized spins and the conduction electrons, in a straightforward way. This method avoids any ambiguity that one may encounter when obtaining the Korringa slope from the central line in a spectrum where an exchange narrowed component may also be present. The similar zero field parameters of Gd for Eu and Y in the 123 compounds show the distances of the atoms surrounding the Gd atoms in these two compounds are almost the same. Our results indicate similar behavior to that observed in metals indicating an interaction with a Fermi liquid.

ACKNOWLEDGMENTS

Support from ARC Large Grant (No. A69331127) is acknowledged. We would also like to acknowledge B. McBaraki for kindly performing the magnetization experiments.

¹S. E. Barnes, *Adv. Phys.* **30**, 801 (1981).

²P. H. Hor, R. L. Meng, Y. Q. Wang, L. Gao, Z. J. Huang, J. Bechtold, K. Foster, and C. W. Chu, *Phys. Rev. Lett.* **58**, 1891 (1987).

³J. T. Market, T. W. Noh, S. E. Russek, and R. M. Cotts, *Solid State Commun.* **63**, 847 (1987).

⁴H. Alloul, T. Ohno, and P. Mendels, *Phys. Rev. Lett.* **16**, 1700 (1989).

⁵M. T. Causa, C. Fainstein, G. Nieva, R. Sanchez, L. B. Stren, M. Tovar, R. Zysler, D. C. Vier, S. Schultz, S. B. Oseroff, Z. Fisk, and L. G. Smith, *Phys. Rev. B* **38**, 257 (1988).

⁶D. Shaltiel, S. E. Barnes, H. Bill, M. Francois, H. Hageman, J.

Jegondaz, D. Lavy, P. Monod, M. Peter, A. Revcolevschi, W. Sadowski, and E. Walker, *Physica C* **161**, 13 (1988).

⁷A. Rockenbauer, A. Janossy, L. Korecz, and S. Pekker, *J. Magn. Reson.* **97**, 540 (1992).

⁸A. Janossy, J. R. Cooper, L. C. Brunel, and A. Carrington, *Phys. Rev. B* **50**, 3442 (1994).

⁹H. Hasegawa, *J. Phys. Soc. Jpn.* **21**, 483 (1959).

¹⁰S. E. Barnes, *Phys. Rev. B* **9**, 4789 (1974).

¹¹T. Plefka, *Phys. Status Solidi B* **55**, 129 (1973).

¹²D. Davdov, R. Orbach, C. Rettori, D. Shaltiel, and L. J. Tao, *Phys. Rev. B* **5**, 1171 (1972) and references therein.

¹³J. M. Moret, R. Orbach, M. Peter, D. Shaltiel, J. T. Suss, W.

- Zingg, R. A. B. Devine, and P. H. Zimmerman, *Phys. Rev. B* **11**, 2002 (1975).
- ¹⁴P. Urban, D. Davidov, Belschner, T. Plefka, and G. Sperlich, *Phys. Rev. B* **12**, 72 (1975).
- ¹⁵S. S. P. Parkin, E. M. Engler, V. Y. Lee, and R. B. Beyer, *Phys. Rev. B* **37**, 131 (1988).
- ¹⁶H. Ihara, H. Oyanagi, R. Sugise, E. Ohno, T. Matsubara, S. Ohashi, N. Terada, M. Jo, M. Hirabayashi, K. Murata, A. Negishi, Y. Kimura, E. Akiba, H. Hayakawa, and S. Shin, *Physica C* **153-155**, 948 (1988).

Optically detected electron paramagnetic resonance of Ni-related defects in synthetic diamond crystals

Th Pawlik†, C Noble‡ and J-M Spaeth†

† Universität Paderborn, Fachbereich Physik, 33098 Paderborn, Germany

‡ Physics Department, Monash University, Clayton 3168, Australia

Received 15 June 1998, in final form 3 August 1998

Abstract. Synthetic diamond crystals grown using a solvent catalyst that contains Ni were studied by optical detection of electron paramagnetic resonance (ODEPR) using the magnetic circular dichroism of the optical absorption (MCDA). The MCDA spectra in the infrared spectral region consist of a derivative-like line at 1.06 eV, single sharp lines at 1.29 and 1.40 eV, a complex phonon-split band with the zero-phonon line (ZPL) at 1.69 eV and a derivative-like doublet structure superimposed at 1.72 eV. All of these optical absorptions were shown to originate from paramagnetic defects. Using ODEPR it was possible to unambiguously assign the 1.72 eV doublet to the NE4 centre and the 1.40 eV line to the NIRIM-2 centre. The defect responsible for the ZPL at 1.06 eV has the same symmetry as the NIRIM-2 centre with a slightly larger g_{\parallel} -value. The NE4 centre was assigned to substitutional Ni^{+} associated with a carbon vacancy in a nearest-neighbour position whereas the NIRIM-2 centre was assigned to interstitial Ni^{+} with a distortion along a [111] axis.

1. Introduction

Synthetically grown diamond crystals very often contain transition metal impurities. The source of the impurities is the growth environment. The transition metals Ni, Fe, Co are often used as catalysts. Of these, Ni and Co are believed to enter the diamond lattice in the form of dispersed atoms [1, 2].

Diamonds synthesized using a nickel catalyst show optical absorption lines at 1.22, 1.40, 1.883, 2.51 and 3.1 eV [3, 4]. In addition, these diamond crystals show electron paramagnetic resonance (EPR) spectra, which were tentatively assigned to Ni-related defects. By detecting isotope effects it was recently shown that Ni is responsible for the 1.40 eV line [5]. Until now, the correlation of optical spectra and paramagnetic resonance was achieved only indirectly by studying EPR and optical absorption spectra in diamonds grown with different nickel-containing catalysts or at different stages of annealing [6, 7]. In an effort to establish a more direct correlation we used the method of optical detection of electron paramagnetic resonance (ODEPR) via the magnetic circular dichroism of the optical absorption (MCDA). Since the MCDA signal is proportional to the population difference of the ground-state Zeeman levels, a microwave transition induced within these Zeeman levels decreases the MCDA signal (see, e.g., [8]). Thus, the optically detected EPR spectrum can be obtained by monitoring the MCDA over the desired magnetic field range while applying a microwave field of constant frequency. With this method an unambiguous assignment of optical absorptions to specific EPR spectra can be made and thus it is possible to model centres in a safer way than by monitoring simultaneous changes in EPR spectra and optical spectra due to annealing.

2. Experimental procedure

The sample used in the investigation was a Ni-catalysed synthetic diamond, grown at the National Institute for Research in Inorganic Materials (NIRIM), Japan. The sample was grown by the temperature gradient method using a pure nickel solvent catalyst at around 1500 °C and a pressure of 6 GPa. It was then annealed at 1700 °C–1800 °C for several hours at about 7–9 GPa.

The diamond had then a colour ranging from a golden yellow to brown throughout the crystal indicating some inhomogeneity.

The sample was polished into a cube with the cube faces corresponding to $[111]$, $[1\bar{1}0]$ and $[11\bar{2}]$ axes with all dimensions less than 2 mm. The plane of rotation of the magnetic field was a $\{11\bar{2}\}$ plane. B_0 at zero degrees corresponds to $B_0 \parallel [1\bar{1}0]$ and B_0 at 90 degrees corresponds to $B_0 \parallel [111]$.

The ODEPR experiments were carried out in a custom-built spectrometer operating in the K band (24.1 GHz). An Oxford He bath cryostat equipped with a 3.5 T superconducting magnet allowed optical and microwave access to the sample at temperatures $T \geq 1.5$ K. For K-band operation the sample was placed in a cylindrical microwave cavity with optical access. K-band microwaves were provided by a klystron source (900 mW). Operation in a second microwave band (V band, 72 GHz) was possible using a varactor-tuned and frequency-multiplied Gunn oscillator producing 150 mW at 72 GHz. In the latter case the microwave energy was applied to the sample by placing the open end of the V-band waveguide in front of a cryostat window. The lower microwave power in this set-up was not found to be critical for the investigation of the 1.69 eV band and the 1.72 eV doublet due to the long spin–lattice relaxation times of both defects. In addition, the higher magnetic field range provided a higher MCDA signal and a better separation of defects with similar g -matrices.

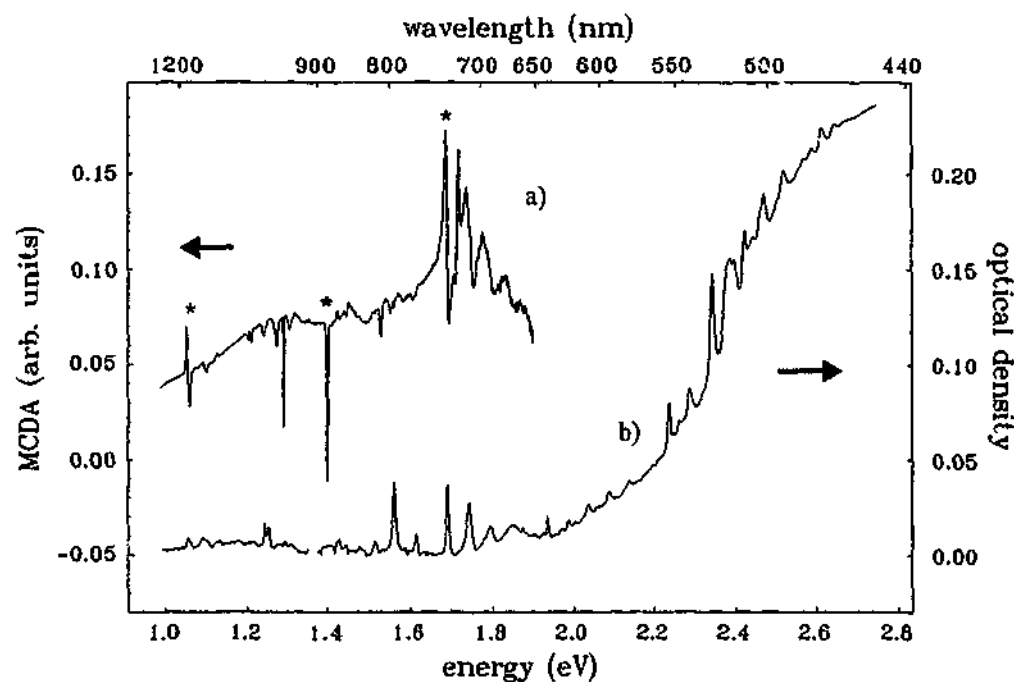


Figure 1. (a) The MCDA spectrum measured at $B = 2.5$ T, $T = 1.5$ K. (b) The optical absorption spectrum measured at $T = 1.5$ K.

In the case of the defects corresponding to the 1.06 and 1.40 eV lines, a much shorter spin-lattice relaxation time made the higher power of the K-band set-up necessary for the ODEPR measurements. The additional components for detecting the MCDA signal are described elsewhere [8]. The measurement temperature was 1.5 K or 4.2 K in all of the experiments.

3. Results and discussion

Figure 1, trace (a), shows an MCDA spectrum of the synthetic diamond measured at 1.5 K with $B = 2.5$ T. The corresponding optical absorption spectrum is shown as trace (b).

The optical absorption spectrum shows a number of sharp lines that have been previously reported [6] for Ni-catalysed diamonds in a similar annealing stage. The MCDA lines are temperature dependent. Their intensity decreases upon raising the temperature. This temperature dependence suggests that all of the bands in the MCDA spectrum originate from paramagnetic defects (see, e.g., [8]). Note that the doublet at 1.25 eV and the single line at 1.57 eV do not appear in the MCDA spectrum. It is therefore probable that these transitions belong to diamagnetic defects.

In a simple model of an atomic $s \rightarrow p$ transition, the appearance of either an absorption-shaped or a derivative-shaped MCDA depends on the magnitude of the spin-orbit splitting in the excited state versus the absorption bandwidth (see, e.g., [8]). For small spin-orbit splittings the MCDA lines are usually derivative whereas for large spin-orbit or crystal-field splittings one may observe separate bands for left- and right-circularly polarized light. The strong MCDA signal of the 1.40 eV and 1.29 eV lines compared to the rather small optical absorption suggests that these lines have a single circular polarization resulting in a strong dichroism of left- and right-circularly polarized light. The MCDA detection method using a modulated circular polarizer and lock-in amplifier leads to a very sensitive detection of the dichroism.

We have limited our ODEPR measurements to the study of the MCDA bands at 1.72 eV,

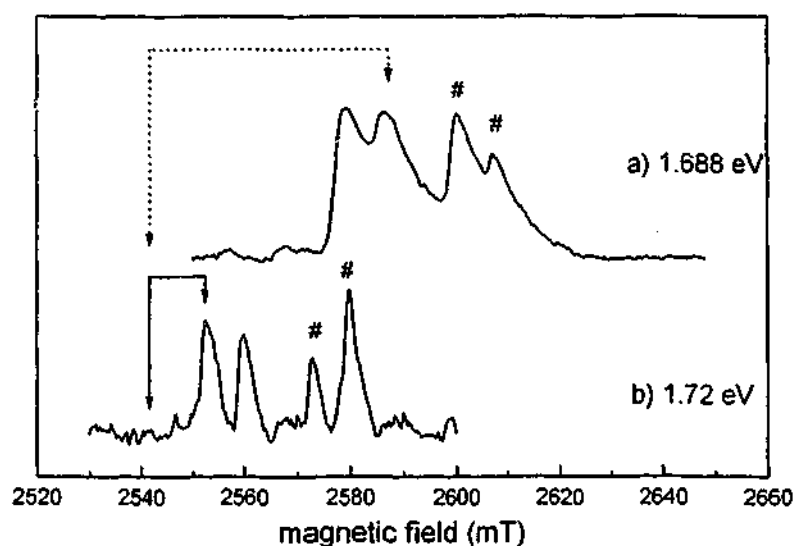


Figure 2. MCDA-detected EPR spectra measured at 1.688 eV (trace (a)) and 1.720 eV (trace (b)). The arrows indicate the magnetic field positions at which the MCDA spectra in figure 3 were measured. The microwave frequencies are 72.76 GHz and 73.32 GHz (see the text).

1.40 eV and 1.06 eV, marked by asterisks in figure 1, on trace (a). The band at 1.40 eV is of particular interest since it is found in the optical absorption spectrum of many synthetic diamonds. Conventional EPR studies [7, 9] have assigned different EPR spectra to this optical absorption band, mainly on the basis of the correlation of the EPR signal intensity and optical absorption spectra in a series of annealing experiments.

3.1. The 1.69 eV band and the 1.72 eV doublet

Figure 2 shows two MCDA-detected EPR spectra for $B \parallel [111]$ measured at 1.688 eV (trace (a)) and 1.720 eV (trace (b)) with the V-band microwave source. Both EPR spectra exhibit four lines grouped into two doublets with a spacing of 20 mT between the two doublets. The appearance of two doublets has to be considered as an experimental artefact. It was found that the V-band microwave source produces, in addition to the fundamental frequency, a sideband which is 0.56 GHz higher in frequency and only 9 dB lower in power (this could be confirmed by measuring the MCDA-detected EPR of the well-studied F centres in KCl). Due to the long EPR spin-lattice relaxation times T_1 , the low microwave power of the sideband is still sufficient to produce a significant change in the ground-state population and therefore an MCDA-detected EPR signal. The lines due to the second frequency at 73.32 GHz are marked by hash signs in figure 2. It will be shown later for the 1.720 eV MCDA that the internal splitting of the doublets is due to a slight misalignment of the crystal. This results in a splitting of the EPR lines corresponding to two orientations of the defect which would be degenerate for $B \parallel [111]$.

From the results in figure 2 it is clear that the MCDA at around 1.7 eV is a superposition of MCDA spectra of at least two defects with different EPR spectra. In order to separate the two MCDA spectra we subtracted the MCDA spectrum with the magnetic field set on an EPR line from the MCDA spectrum measured at a nearby field position off the EPR line. The difference spectrum should only show the MCDA spectrum of the defect responsible for the EPR line. Due to the long spin-lattice relaxation time it was not possible to apply

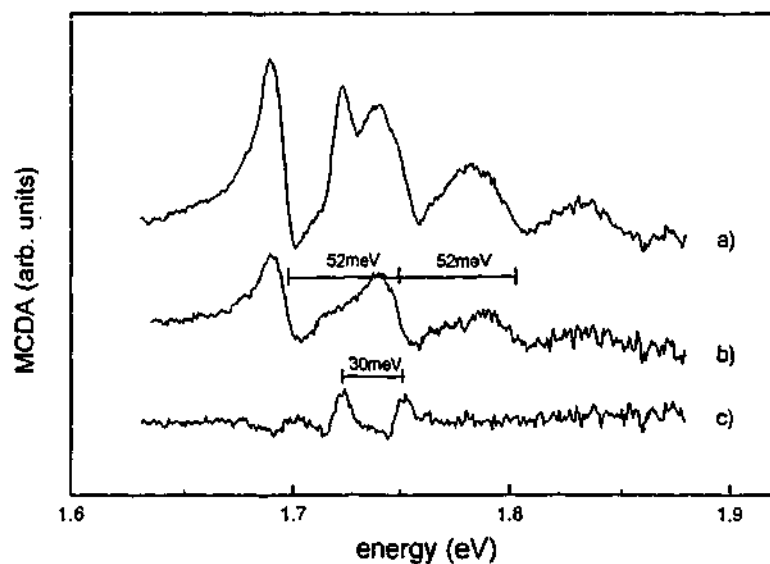


Figure 3. (a) The MCDA spectrum measured at $B = 2543$ mT, $T = 1.5$ K. (b) The difference of the MCDA spectra measured at 2543 mT and 2587 mT with an applied microwave field. (c) The difference of the MCDA spectra measured at 2543 mT and 2553 mT with an applied microwave field.

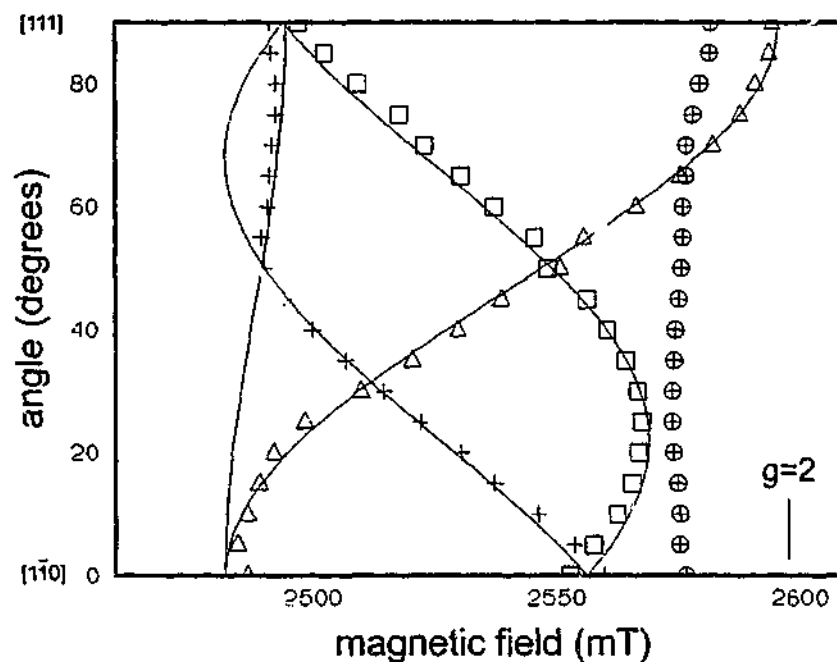


Figure 4. The ODEPR angular dependence of the defect responsible for the MCDA doublet at 1.72 eV and 1.75 eV. Zero degrees corresponds to $B \parallel [1\bar{1}0]$, 90 degrees corresponds to $B \parallel [111]$. The plane of rotation is a $\{11\bar{2}\}$ plane. The symbols represent the experimental EPR line positions. The solid lines are EPR line positions calculated using an axial g -matrix with the parameters $g_{\parallel} = 2.004 \pm 0.005$ and $g_{\perp} = 2.093 \pm 0.005$. The symbols \oplus mark the positions of weak EPR lines from a nearly isotropic centre that was superimposed on the EPR spectrum of the 1.72/1.75 eV centre.

a microwave-modulation technique to measure the MCDA excitation spectrum of the EPR lines (see, e.g., [8]).

Figure 3 shows as trace (a) the MCDA spectrum obtained at $B = 2543$ mT. Trace (b) is the difference of the MCDA spectra measured at 2543 mT and 2587 mT (the two field positions are indicated by dotted arrows in figure 2). Trace (c) is the difference of the MCDA measured at 2543 mT and 2553 mT (marked by solid arrows in figure 2). The difference between traces (b) and (c) is apparent: trace (b) reproduces the phonon-split MCDA band with a ZPL at 1.688 eV and a phonon splitting of 52 meV. Trace (c), the MCDA responsible for the EPR spectrum given as trace (b) of figure 2, shows a doublet structure with a splitting of 30 meV.

The EPR angular dependence measured at 1.72 eV is shown in figure 4. The second resonance position due to the microwave sideband (marked by hash signs in figure 2) is not shown. The angular dependence can be explained well by assuming a defect with axial (111) symmetry and a g -matrix with the parameters $g_{\parallel} = 2.004 \pm 0.005$ and $g_{\perp} = 2.093 \pm 0.005$. These parameters are similar to the ones given in reference [7] for the NE4 centre ($g_{\parallel} = 2.023$ and $g_{\perp} = 2.098$, (111) symmetry). The defect was considered as a substitutional Ni^+ ($3d^9$) defect associated with a C vacancy in a [111] direction. In reference [7], however, the authors assigned the EPR spectrum to the 1.40 eV absorption line. The difference in the values of g_{\parallel} is somewhat larger than the experimental error. This difference could be due to the different measurement temperatures (EPR: 77 K; ODEPR: 1.5 K). However, the possibility that the EPR spectrum that we observed is a new Ni^+ defect with a very similar structure to the NE4 centre cannot be ruled out.

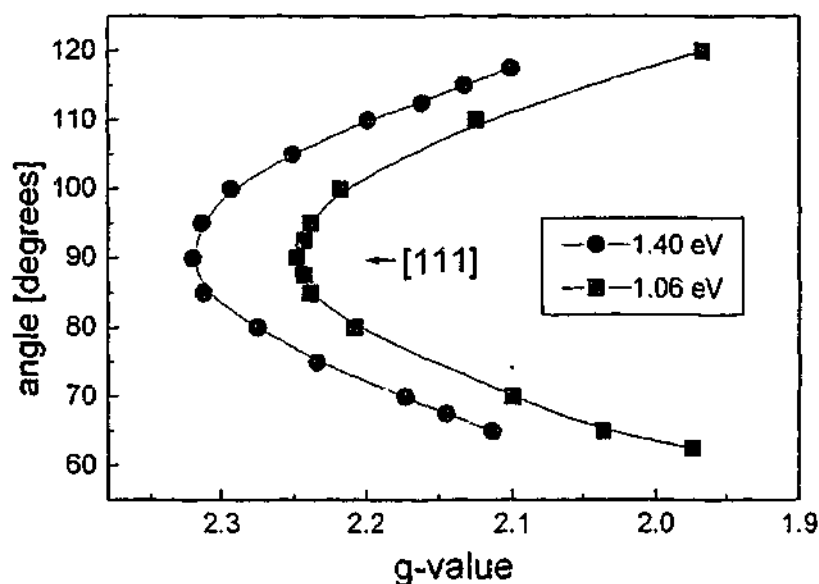


Figure 5. The ODEPR angular dependence of the defects responsible for the MCDA lines at 1.40 eV and 1.06 eV. 90 degrees corresponds to $B \parallel [111]$. The plane of rotation is a $(11\bar{2})$ plane.

3.2. 1.06 eV and 1.40 eV lines

Nazaré *et al* [1] have studied the fine structure of the 1.40 eV ZPL line in detail using high-resolution Zeeman spectroscopy. The authors found that a model of a paramagnetic $S = 1/2$ ground state with trigonal symmetry was able to explain the Zeeman shift within the ZPL fine structure. LCAO cluster calculations for Ni centres in various charge states and lattice positions were performed by Paslovsky and Lowther [10]. Isoya *et al* [9] have assigned the 1.40 eV optical transition to a defect detected in conventional EPR and labelled it NIRIM-2. The NIRIM-2 EPR centre is characterized by an axially symmetric g -matrix with $g_{\parallel} = 2.3285$ and $g_{\perp} \approx 0$ and (111) symmetry. With MCDA-detected EPR at 24.6 GHz, we found EPR signals in the MCDA at 1.40 eV when the crystal orientation was near a $[111]$ direction. Figure 5 shows the angular dependence of the EPR measured in the MCDA at 1.40 eV (circles) and 1.06 eV (squares). The field axis was transformed to display g -values. Due to substantial line broadening, the angular dependence could not be followed for rotations $>20^{\circ}$ from the $[111]$ axis. However, the apparent extrema at $B \parallel [111]$ are consistent with a defect of (111) symmetry. The g -value ($g = 2.32 \pm 0.01$) measured at this angle is very close to the value of $g = 2.3285$ given for g_{\parallel} in [9]. Therefore, the assignment of the 1.40 eV line to the NIRIM-2 EPR centre is very plausible. The angular dependence of the EPR measured in the 1.06 eV MCDA is similar, with the same axis of symmetry and a somewhat smaller g_{\parallel} of 2.25.

Figure 6 shows in analogy to figure 3 the MCDA spectra responsible for the two different EPR centres. Trace (a) is the total MCDA spectrum. The inset shows the two EPR lines measured for $B \parallel [111]$ in the MCDA transitions at 1.40 eV and 1.06 eV, respectively. The difference spectra given as traces (b) and (c) were obtained by subtracting the MCDA measured with microwave radiation at 750 mT and 774 mT from the MCDA measured at the same magnetic fields without microwave radiation. These spectra show that the absorption spectra of the EPR centres with $g_{\parallel} = 2.32$ and $g_{\parallel} = 2.25$ are indeed the 1.40 eV and 1.06 eV optical transitions, respectively.

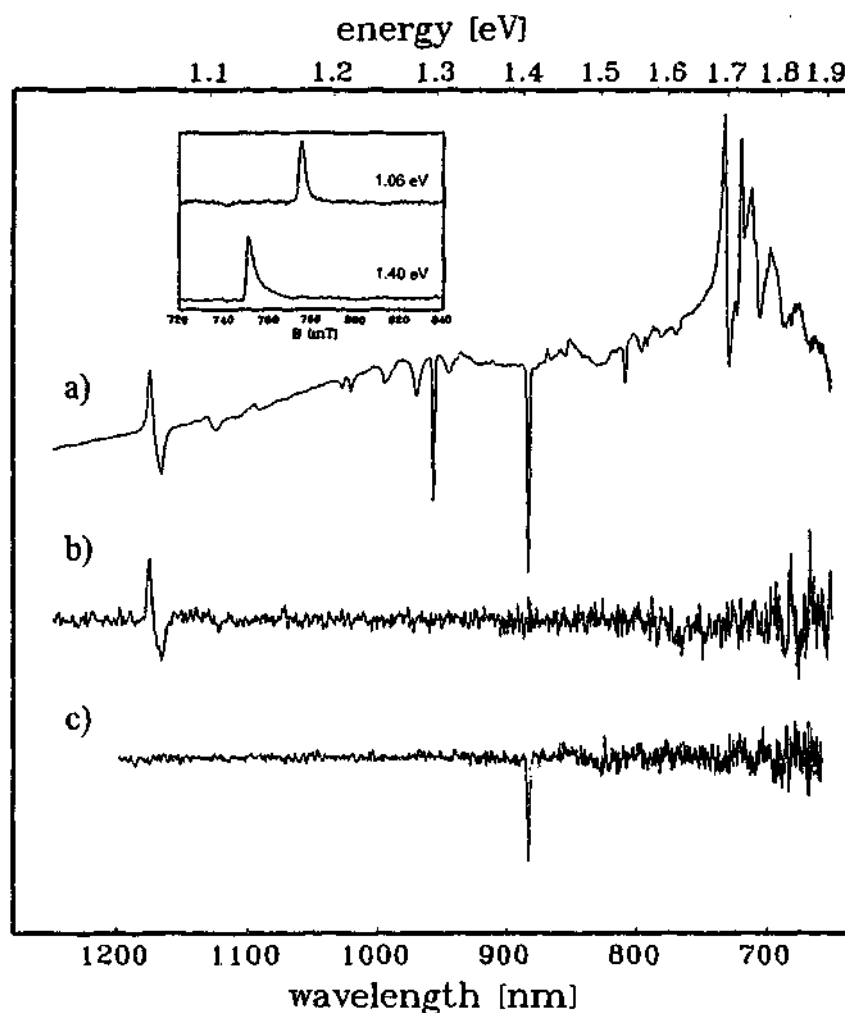


Figure 6. (a) The MCDA spectrum measured at $B = 2.5$ T, $T = 1.5$ K, $B \parallel [111]$. (b) The difference of the MCDA spectra measured at $B = 750$ mT with and without microwaves. (c) The difference of the MCDA spectra measured at $B = 774$ mT with and without microwaves. Inset: MCDA-detected EPR spectra measured at 1.06 eV (upper spectrum) and 1.40 eV (lower spectrum).

4. Conclusions

We have shown that optical detection of electron paramagnetic resonance (ODEPR) via the magnetic circular dichroism of the optical absorption (MCDA) provides a direct correlation of optical absorptions and EPR spectra in diamonds. We have established a connection between the NE4 EPR centre and an absorption band at 1.72 eV as well as between the 1.40 eV line and the NIRIM-2 centre. A new EPR spectrum was detected in the MCDA at 1.06 eV. It has the same symmetry as the NIRIM-2 centre with a somewhat smaller g_{\parallel} -value. Further studies are needed to determine a structural model for this defect.

Acknowledgments

The authors would like to thank S C Lawson and H Kanda for the use of a Ni-catalysed synthetic diamond.

References

- [1] Nazaré M H, Neves A J and Davies G 1991 *Phys. Rev. B* **43** 14 196
- [2] Lawson S C, Kanda H, Watanabe K, Kiflawi I, Sato Y and Collins A T 1996 *J. Appl. Phys.* **79** 4348
- [3] Collins A T, Kanda H and Burns R C 1990 *Phil. Mag.* **B 61** 797
- [4] Lawson S C, Kanda H and Sekita M 1993 *Phil. Mag.* **B 68** 39
- [5] Davies G, Neves A J and Nazaré M H 1989 *Europhys. Lett.* **9** 47
- [6] Lawson S C and Kanda H 1993 *J. Appl. Phys.* **73** 3967
- [7] Nadolinny V A and Yelisseyev A P 1993 *Diamond Relat. Mater.* **3** 1196
- [8] Spaeth J-M, Niklas J R and Bartram R H 1992 *Structural Analysis of Point Defects in Solids: An Introduction to Multiple Magnetic Resonance Spectroscopy (Springer Series in Solid State Sciences 43)* (Berlin: Springer)
- [9] Isoya J, Kanda H and Uchida Y 1990 *Phys. Rev. B* **42** 9843
- [10] Paslovsky L and Lowther J E 1992 *J. Phys.: Condens. Matter* **4** 775

Electron paramagnetic resonance investigations of nickel defects in natural diamonds

C J Noble†, Th Pawlik‡ and J-M Spaeth‡

† Department of Physics, Monash University, Melbourne, Victoria 3168, Australia

‡ Fachbereich Physik, Universität-GH Paderborn, 33095 Paderborn, Germany

Received 25 September 1998

Abstract. Electron paramagnetic resonance (EPR) and electron nuclear double resonance (ENDOR) spectra of natural blue diamonds from the Argyle mine in Western Australia are reported for the first time. These diamonds are shown to contain the NE2 centre which has been observed primarily in synthetic diamonds and has been proposed to be Ni⁺ with three neighbouring nitrogens. A previously unreported EPR centre is observed and is found to have $S = 3/2$, $g = 2.02$ and superhyperfine interaction from one nitrogen. The results are found to be consistent with an Ni⁻ on a substitutional site with an N⁺ on a fourth nearest neighbour site. This defect is found exclusively in Argyle blue diamonds.

1. Introduction

The Argyle mine in Western Australia produces a relatively large number of coloured diamonds. The majority of these are brown but the highly valued pink diamonds are also found to a lesser extent. Both the pink and brown diamonds contain defects which are thought to be produced by plastic deformation. The colour of these diamonds is often believed to be related to these defects. However, it has been reported that also near colourless diamonds from the Argyle production suffer from severe plastic deformation. Another type of diamond which has a greyish blue colour is also found at the Argyle mine. It is extremely rare with only a few found each year and is not related to the semiconducting blue diamonds which contain boron [1].

The greyish-blue diamonds have not previously been extensively investigated. One optical spectroscopy study has been published to date [2]. It was found that these diamonds contain an unusually high concentration of hydrogen. The blue colour of these diamonds was believed to be related to these hydrogen defects.

This paper reports on the first electron paramagnetic resonance (EPR) study of these diamonds. In contrast to other diamonds from the Argyle mine these diamonds were found to contain nickel defects which have previously been observed in synthetic diamonds. More importantly a previously unreported EPR centre was also observed and it is proposed that this defect also contains nickel. This defect is found only in these diamonds.

A number of defects involving isolated nickel and nickel associated with nitrogen have been observed previously in synthetic diamonds. To provide some background to discuss our investigation of nickel defects in natural blue diamonds a brief review of the known centres is presented.

The first observation of a nickel centre in diamond was in a synthetic polycrystalline sample grown at high temperature and pressure from a nickel containing solvent [3]. The

centre gave rise to a single isotropic line at $g = 2.031$. Since it was present only in diamond grown from a nickel containing solvent it was attributed to nickel. It was later confirmed to be a nickel centre from the resolved hyperfine (hf) splitting [4]. This is the only centre where EPR confirmed the involvement of nickel directly. In other EPR investigations [5–8] EPR spectra assigned to nickel centres were only seen in synthetic diamond grown using nickel or a nickel alloy as catalysts. Furthermore, an isotope-related fine structure in the zero-phonon region of the 1.40 eV optical transition has conclusively shown that nickel is responsible for it [9].

A recent study using single crystals refined the g value of the centre showing Ni hf splitting to 2.0319 and, despite the fact that no zero field splitting was observed in the cw EPR spectrum, the electron spin of the centre was determined to be $S = 3/2$ using pulsed EPR techniques [5]. The Ludwig–Woodbury [10] model, which has been used for transition metals in silicon and germanium, was then used to assign this defect to a negatively charged nickel ion on a substitutional site. The Ludwig–Woodbury model predicts the following spin and electronic configurations for the different charge states of the substitutional and interstitial ions: Ni_i^+ , $S = 1/2$, $3d^9$; Ni_i^0 , $S = 0$, $3d^{10}$; Ni_s^+ , $S = 5/2$, $3d^5$; Ni_s^0 , $S = 2$, $3d^6$; Ni_s^- , $S = 3/2$, $3d^7$.

Two of the EPR centres found in synthetic diamonds grown from a nickel catalyst [6] were labelled NIRIM1 and NIRIM2. Both have an electron spin of $S = 1/2$ and, in accordance with the Ludwig–Woodbury model, were determined to be positively charged nickel on an interstitial site. The NIRIM1 centre gave a single line at $g = 2.0112$ although some structure was seen at lower temperatures. The NIRIM2 centre had trigonal symmetry and the following principal g values. $g_{\parallel} = 2.3285$ and $g_{\perp} \cong 0$. It was proposed that the NIRIM2 centre was a nickel interstitial defect with a trigonal perturbation from a nearby vacancy or carbon interstitial whereas the NIRIM1 centre was the unperturbed interstitial defect [6].

Optical transitions have also been found in diamonds grown from a nickel catalyst. These transitions occur at 1.4, 1.883, 2.51, 2.56 and 3.1 eV [11]. The transitions that were seen in any diamond were found to depend not only on the concentration of nickel but also of nitrogen [11]. Diamonds grown with a nitrogen getter, having therefore a low nitrogen content, show a dominant 1.4 eV ZPL [9, 11]. The NIRIM1 and NIRIM2 EPR centres are also seen in these diamonds with low nitrogen content. By contrast, diamonds grown without a nitrogen getter show stronger 1.883 and 2.51 eV lines are also the Ni_s^- EPR centre. It was proposed that the presence of substitutional nitrogen, a deep donor, produced changes in the Fermi level and hence a change in the charge state of the nickel defects [11].

More recently, studies involving the annealing of synthetic diamonds containing nickel have provided evidence that complex defects involving both nickel and nitrogen are formed in this process [7, 8, 12]. Nadolinny and Yelisseyev discovered three EPR centres that formed during the heat treatment at 2100 K and 5.5 GPa in diamonds containing both nickel and nitrogen [8]. These centres were labelled NE1–NE3. All had anisotropic g values with magnitudes between 2.00 and 2.14 and had characteristic superhyperfine (shf) splittings indicating interactions with two, three and three nitrogens respectively for the NE1, NE2 and NE3 centres. The EPR centres were also correlated statistically with optical features labelled as the S2 and S3 bands and a line at 523.2 nm (2.369 eV) but no direct correlation was made.

Further investigation by the same authors uncovered another four EPR centres. One, the NE4 centre, was present in as-grown diamonds and has trigonal symmetry with $g_{\parallel} = 2.0227$, $g_{\perp} = 2.0988$, and showed no shf splittings. The NE5, NE6 and NE7 centres were seen in

the heat treated diamonds but only during optical illumination. They all had anisotropic g values greater than 2 and had interactions with two, zero and one nitrogen, respectively. The centres NE1–NE5 were proposed to be an Ni^+ ($S = 1/2$, $3d^9$) in a di-vacancy position associated with zero to three nitrogens.

A series of optical absorption lines have also been observed in synthetic diamonds after heat treatment [12]. When diamonds, which initially showed the 1.883 and 2.51 eV lines, were annealed these lines decayed in strength and a new series of absorptions appeared. The most prominent of these was a vibronic band with a ZPL at 1.693 eV and a dominant 51 meV phonon energy. Associated with this band was a complicated series of lines between 2.2 and 2.6 eV. The 1.693 eV ZPL annealed out at temperatures over 1700 °C showing that it was a transient species. The maximum in the intensity of the 1.693 eV line was found to correlate well with the initial 1.883 eV line intensity. Some of the lines in the range 2.2 to 2.6 eV annealed out at this temperature and some remained, indicating that several separate defect species were being produced during the annealing. Again, complex defects involving nickel and nitrogen are proposed to account for these features.

These optical and EPR features have all been observed in synthetic diamonds. These defects would appear to be extremely rare in natural diamonds which have quite different origins. The NE1 and NE2 EPR centres have, however, been reported in natural diamonds from the Jakutii and Ural mines [13]. Also reported in [13] is a new EPR centre with $S = 1/2$, tetragonal symmetry, the parameters $g_{\parallel} = 2.0151$, $g_{\perp} = 2.2113$ and no shf structure.

2. Experiment

The diamonds examined in this work were six natural blue diamonds from the Argyle mine in Western Australia. The diamonds were of a grey-blue colour and generally of a rough shape with no discernible crystallographic faces. The largest stone was approximately 8 mm along its longest axis.

The cw EPR was performed on a Bruker ESP380e at room temperature using a standard rectangular cavity. The optical absorption spectra were recorded with a Cary 13 UV-vis spectrophotometer fitted with a diffuse reflectivity attachment. The spectra were recorded in transmission mode, but the diffuse reflectivity attachment was used as it contained an integrating sphere and good spectra could be obtained despite the poor optical quality of the samples. The optical spectra were recorded at room temperature. Fourier transform infrared (FTIR) spectra were obtained in the Department of Chemistry, Monash University, using a Perkin Elmer FTIR microscope attached to a PE 1600 series FTIR spectrometer.

The electron nuclear double resonance (ENDOR) measurements were performed on a home-built X-band spectrometer in the Physics Department at the University of Paderborn in Germany. The microwave source was a 120 mW YIG oscillator and double balanced mixers were used for detection. One mixer provides the absorptive signal while the other provides the dispersive signal which is used for the AFC of the source. The RF is generated with a computer controlled synthesizer and a broad band amplifier. A frequency range of up to 30 MHz could be achieved with this amplifier. The cavity with integrated helium flow cryostat worked in a TE_{011} mode and the RF field was produced by four silver rods in the cavity. For more details about the ENDOR spectrometer refer to Spaeth *et al* [14].

3. Experimental results

The FTIR spectra of the natural blue diamonds, figure 1, show strong absorptions below 1500 cm^{-1} indicating a high nitrogen content. The nitrogen is present predominantly in the form of B aggregates, which contain four nitrogens, and to a lesser degree as A aggregates, which are nitrogen pairs [15]. The concentration of nitrogen in the form of B aggregates is estimated to be 600 atomic ppm using the relation given by Woods *et al* [16]. Also present is a large platelet peak at 1376 cm^{-1} . Platelets are large extended defects that form during the aggregation of nitrogen in diamond [17]. The nature of the platelets is still controversial—they may be composed predominantly of nitrogen or be a precipitate of carbon interstitial atoms [18], perhaps with some nitrogen present. The presence of both the B aggregates and platelets indicates that, at some stage in their history, these diamonds have been subjected to high temperatures for extended periods. Several hydrogen related peaks are also present which have been previously reported by Fritsch *et al* [2]. The most prominent of these are the 3107 cm^{-1} and 3235 cm^{-1} peaks. The concentration of hydrogen in similar diamonds has been estimated to be 500 ppm [2]. Other lines are observed at 1404 cm^{-1} , 1434 cm^{-1} , 1498 cm^{-1} , 1546 cm^{-1} , 2784 cm^{-1} , 2852 cm^{-1} and 2924 cm^{-1} . The peaks in the regions of about 2200 cm^{-1} are two-phonon absorptions and are intrinsic to diamond.

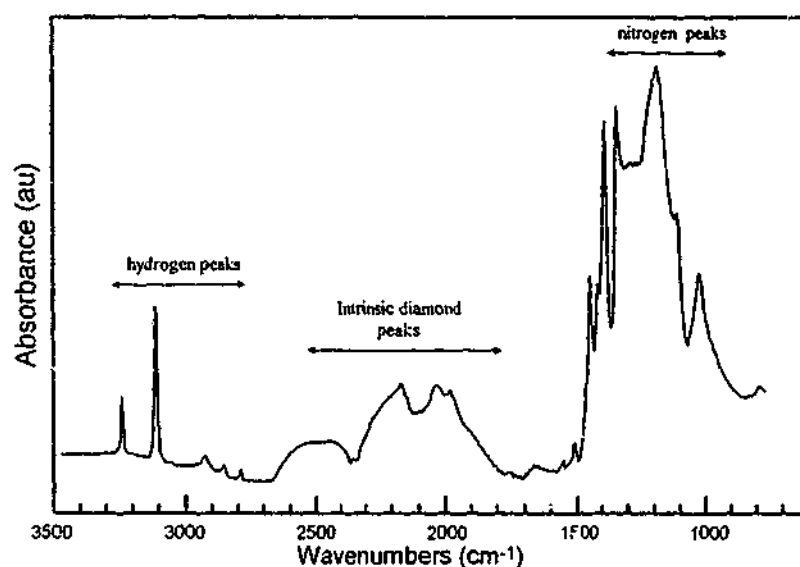


Figure 1. FTIR spectrum of Argyle blue diamond.

The room temperature optical absorption spectra, figure 2, of the natural blue diamonds have two dominant broad absorption bands, one centred at 1.71 eV (725 nm) and another at 2.25 eV (550 nm). It is presumably the peak at 1.71 eV which is responsible for the blue coloration. The peak at 2.25 eV is also of interest because of its similarity to a peak with roughly the same position and line width in optical absorption spectra of pink diamonds from the same mine. It is possible that the same defect is responsible in each case. However, as the absorptions are broad and with no sharp features to indicate zero phonon lines, it is difficult to draw any firm conclusions from optical absorption alone. The smaller features at approximately 2.25 and 1.48 eV are also reproducible, but it is not possible to identify them at this stage.

In the room temperature EPR spectra of the natural blue diamonds, figure 3, several nitrogen related EPR centres with g values close to the free electron value of 2.0023 are

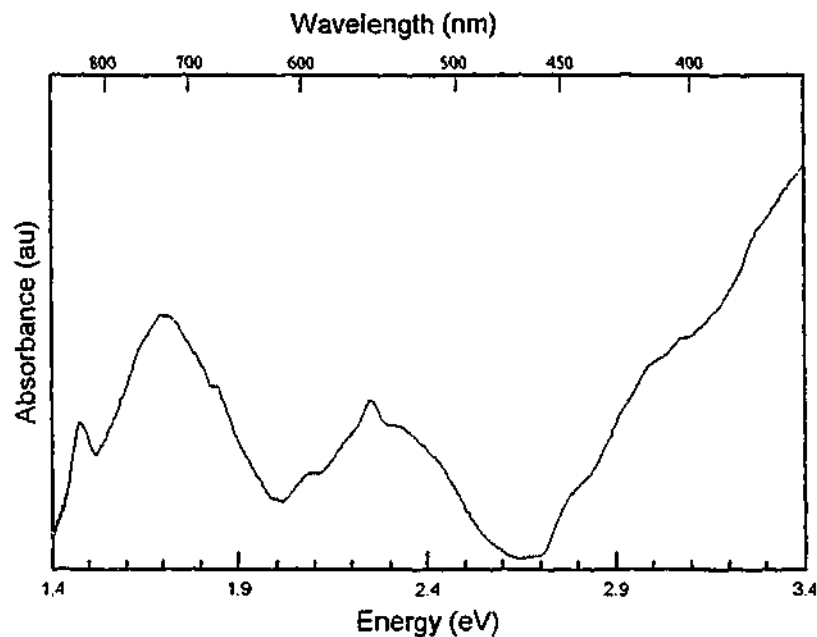


Figure 2. Optical absorption spectrum of Argyle blue diamond.

seen. The P1 centre, substitutional nitrogen, is seen as a well resolved triplet. The P2 centre which contains three nitrogens is also present in these diamonds although in this spectrum it is obscured by other partially resolved systems, possibly due to the OK1 and N2 centres [19]. In addition two other features at higher g values are also present in all of the blue diamonds. These are a broad isotropic line at $g = 2.02$ and a complicated series of lines centred at $g = 2.07$. The complicated spectrum is thought to be the result of shf splittings from at least three nitrogens. A centre involving three nitrogens had previously been described in nickel containing synthetic diamonds [8]. This centre, labelled NE2, was proposed to be Ni^+ in a di-vacancy position with three neighbouring nitrogens. Simulations of the EPR spectrum for the NE2 centre using the literature spin Hamiltonian parameters gave a good fit to the experimental spectrum observed by us. A complete angular dependence of this EPR centre was not recorded as the poor signal to noise ratio prevented a good resolution of the complicated shf splittings. It was only with the field along a [100] axis that a well resolved spectrum could be obtained.

The broad line, seen in figure 3 at $g = 2.02$, has not been previously reported. The line is roughly Gaussian in shape with a peak-to-peak linewidth of 1.4 mT. The linewidth does not appear to vary significantly with temperature or with orientation of the magnetic field and no structure could be resolved. It is difficult to verify this because the NE2 spectrum overlaps with this line and obscures the lineshape at orientations of the applied field away from a [100] axis.

ENDOR spectra recorded on the broad $g = 2.02$ line are shown in figure 4. The spectra were recorded at 55 K with a microwave power of $12 \mu\text{W}$. Long accumulation times were needed to achieve a satisfactory signal-to-noise ratio. The dominant feature in the ENDOR spectra was a peak at the Larmor frequency of ^{13}C indicating an interaction with matrix carbons. With the applied field close to a [100] axis another four lines were observed. These were arranged in two pairs with roughly equal spacing between them centred at 1.711 MHz and 3.020 MHz. These lines decreased dramatically in intensity as the applied field was

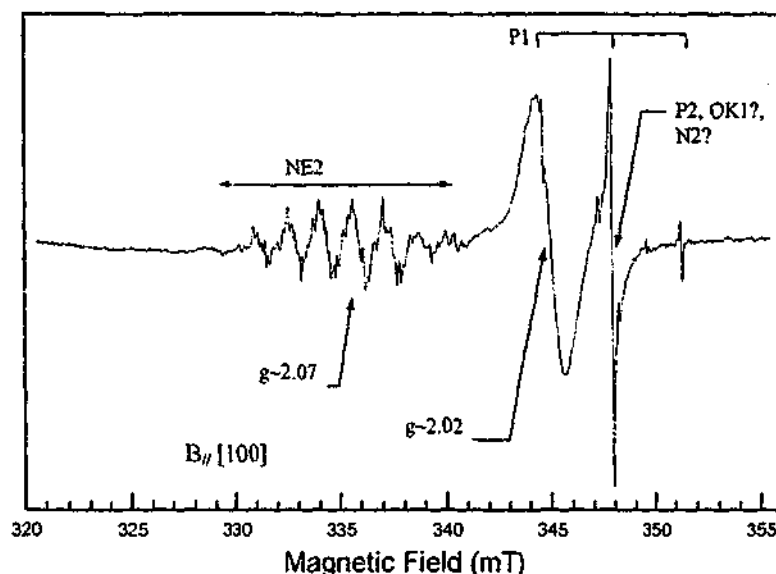


Figure 3. X-band room temperature EPR spectrum of Argyle blue diamond. The applied field is parallel to a [100] axis and the spectrum was recorded under the following conditions: microwave frequency = 9.76 GHz, microwave power = 10 mW, modulation amplitude = 0.1 mT.

rotated away from the [100] axis. There appeared to be some small variation in the line position, of the order of 10 kHz, but as the lines were only observed over a range of a few degrees it was not possible to determine the anisotropic part of the hf interaction with precision.

With these observations it was not possible to unambiguously assign the lines in the spectrum. However, an analysis of equation (1) [14], which shows the ENDOR frequencies to first order, does narrow the possibilities.

$$\nu_{ENDOR} = |m_s A - \nu_L + m_q P| \quad (1)$$

where

$$A = \frac{a + b[3 \cos^2(\theta_A) - 1]}{h} \quad (2)$$

$$\nu_L = \frac{g_n \mu_n B_0}{h} \quad (3)$$

$$P = \frac{3q[3 \cos^2(\theta_Q) - 1]}{h} \quad (4)$$

$$m_q = \frac{m_I + m_{I+1}}{2} \quad (5)$$

Equation (2) describes the shf interaction with a and b the isotropic and anisotropic contributions. These quantities are related to the shf interaction tensor in the principal axis system, in the case of axial symmetry by

$$A_{xx} = A_{yy} = A_{\perp} = a - b \quad (6)$$

$$A_{zz} = A_{\parallel} = a + 2b. \quad (7)$$

θ_A is the angle between the applied field and x direction in this representation and h is the Planck constant. Equation (3) describes the nuclear Zeeman interaction with ν_L the Larmor frequency, g_n the nuclear g factor, μ_n the nuclear magneton and B_0 the applied

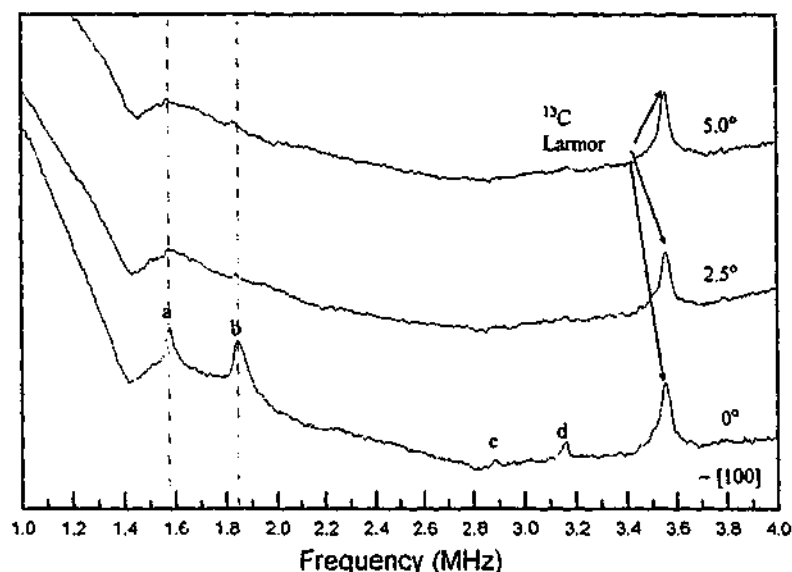


Figure 4. ENDOR spectra of Argyle blue diamond with the static magnetic field set at the broad resonance at $g \approx 2.02$ seen in figure 3. Magnetic field ≈ 332.28 mT, microwave frequency $= 9.3665$ GHz, microwave power $= 12 \mu\text{W}$, temperature ≈ 55 K. For the lower trace the magnetic field was oriented parallel to a [100] axis. The middle and upper traces correspond to crystal rotations of 2.5 degrees and 5.0 degrees away from the [100] axis. A peak at 3.6 MHz, the Larmor frequency of ^{13}C , is seen at all orientations of the magnetic field. It is only with the applied magnetic field close to a [100] axis that a set of lines labelled a-d is observed.

magnetic field. Equation (4) describes the nuclear quadrupole interaction. The quadrupole coupling constant, q , is related to the quadrupole interaction tensor in the principal axis system, in the case of axial symmetry by

$$P_{xx} = P_{yy} = P_{\perp} = -q \quad (8)$$

$$P_{zz} = P_{\parallel} = 2q. \quad (9)$$

θ_Q is the angle between the applied field and z direction in this representation. In these equations m_s and m_I refer to the electron and nuclear spin states respectively and m_q is used to denote the two m_I states involved in the ENDOR transition where the quadrupole interaction is observed.

The most noteworthy feature of the experimental spectrum is the equal spacing between the two pairs labelled a-b and c-d in figure 4. We can see that this splitting could, in principle, be due to any of the terms in equation (1). If we neglect the last term and assume $S = 1/2$, the splitting can be either $2A$ or $2\nu_L$. In the first case each pair would be centred at ν_L . The experimental values do not correspond to the Larmor frequency of any nucleus at this field so we can discount this possibility. Likewise, a nucleus with a Larmor frequency corresponding to the second case with a splitting of $2\nu_L$ cannot be found. We can then assume that the splitting is due to the last term in equation (1) and involves a quadrupole interaction with a nucleus with $I = 1$.

To explain the position of the two pairs, a-b and c-d, we can look at three possibilities. If we assume $S = 1/2$ then the two pairs could correspond either to the $m_s = 1/2$ and $m_s = -1/2$ manifolds or to two different sites with different orientations to the magnetic field. In the first case the separation between the centre of each pair would be equal to $2\nu_L$ and again we find that a nucleus with this Larmor frequency does not exist. If the two pairs

correspond to different sites with their principal axes at different angles to the magnetic field then the quadrupole splitting would not be identical for the two pairs. Therefore, both of these possibilities can be discounted. In the third possibility, $S = 3/2$, and the two pairs correspond to the $m_s = 1/2$ and $m_s = 3/2$ manifolds. In this case the position of the centres of the pairs would occur at $|A/2 + \nu_L|$ and $|3A/2 + \nu_L|$. The Larmor frequency of ^{14}N at this field is 1.0227 MHz and if we assume $A = 1.336$ MHz good agreement is found with the experimental line positions. The calculated positions for the centres of the pairs a-b and c-d are then 1.691 and 3.026 MHz which correspond well with the experimental values of 1.711 and 3.020 MHz.

Using equation (1), for the ENDOR frequencies to first order, we find that the model that best explains the number and position of the peaks in the ENDOR spectrum involves a defect with $S = 3/2$ and $I = 1$. We assume that both the shf and quadrupole interactions have the same principal axis along a [100] direction. The parameters that are calculated from the fitting are then $A_{\parallel} = 1.336$ MHz and $P_{\parallel} = 92$ kHz if we take $\theta_A = \theta_Q = 0^\circ$. As there will be sites with their principal axes along all six of the [100] directions we would expect to see lines corresponding to both A_{\parallel} and A_{\perp} . We therefore assume that the set of the lines corresponding to the perpendicular orientation occur below 1 MHz and are not resolved in the experimental spectra. The situation could, of course, be the reverse with the perpendicular component but not the parallel component. Without evidence to the contrary we will assume the former in the following discussion.

As these peaks in the ENDOR spectrum could only be resolved well with the field parallel to a [100] axis, the anisotropy of the shf interaction could not be determined with precision. The fact that a quadrupole interaction is observed implies that b in equation (2) is non-zero and hence there is some anisotropy in the shf interaction. The ENDOR frequencies for the $m_s = 1/2$ manifold appear to shift by a small amount of the order of 10 kHz within the 5 degrees in which the spectrum could be observed. If we neglect the quadrupole interaction then over 5 degrees we would expect a shift in the ENDOR frequencies of approximately 1% of b . Therefore for a shift of 10 kHz we obtain an upper estimate for b of 1 MHz. If b were significantly larger than 1 MHz, then this would produce a more noticeable angular dependence of the ENDOR frequencies.

4. Discussion

Observations of Argyle blue diamonds show that the colour is caused by a characteristic absorption band at approximately 725 nm (1.71 eV). The absorption spectrum shows no sharp lines or structure indicating vibronic bands and it is not possible to speculate on the defect responsible for the absorption from these spectra. A broad absorption band is also seen at 550 nm (2.25 eV) and it is possible that it is due to the same defect that is present in the Argyle pink diamonds.

A set of hydrogen related lines in the infra-red as observed by Fritsch *et al* [2] is also seen in the blue diamonds. These hydrogen defects had been related to the colour but no direct correlation has been established. The diamonds also contain high concentrations of nitrogen, >500 ppm predominantly in the B form. A statistical correlation between the nitrogen concentration and the hydrogen lines has also been observed [20].

The EPR spectra show P1 and P2 defects and other unresolved defects at $g = 2.00$. Of more interest are other lines at $g > 2.00$ which have also been observed. One of these has been identified as the NE2 centre which is believed to be a complex defect involving Ni^+ in a di-vacancy position with three nitrogens [8]. The other feature, a broad isotropic line at $g \cong 2.02$, has not previously been reported. Out of all these features only the last is observed

exclusively in Argyle blue diamonds. So far all the six Argyle blue diamonds that have been available for study have had this feature. Attempts to determine a direct correlation of the colour and the EPR line with $g = 2.02$ using optical detection of EPR (ODMR) were not successful due to the poor optical quality of the samples. Future experiments with specimens with polished faces might resolve this issue but the rarity of these diamonds presents some problems.

The broad EPR line has no structure even at 4 K and no apparent angular variation. It is therefore impossible to obtain any structural information directly from the EPR spectra. It is possible to make a number of inferences. Firstly the line has a g value greater than 2. This is unusual in diamond where the strong covalent bonding quenches the spin-orbit coupling. Out of all the EPR centres observed, by far the majority have g values close to the free electron value [21]. A g value greater than 2 is indicative of a more than half filled d shell. The centres associated with nickel all have g values greater than 2. The fact that another nickel related centre, the NE2 centre, is found in the blue diamonds also implicates nickel in the new EPR centre.

Synthetic diamonds have been produced that contain nickel in a wide variety of defects but none show this broad line. What then is different in the natural blue diamonds? One feature of the blue diamonds is the high concentration of hydrogen. Neither the EPR nor the ENDOR spectra show an shf splitting characteristic of hydrogen ($I = 1/2$) that would be expected if hydrogen were directly involved in the defect. The involvement of hydrogen could only be indirect such as a distant charge compensator.

The second major difference between the synthetic diamonds and the natural blue diamonds is the concentration and form of nitrogen defects. The natural blue diamonds show a higher concentration of nitrogen, and probably more importantly it is present predominantly in the B form. A large platelet peak was also observed. The nitrogen in the natural blue diamonds is much more aggregated than in the synthetic diamonds where the nitrogen is in the A form. This indicates the extensive annealing that the natural diamonds have experienced over geological time scales. It is reasonable to expect that other defects containing nickel and a number of nitrogens may have been produced in this process.

The ENDOR spectrum was consistent with an $S = 3/2$ and $I = 1$ defect where ^{14}N is the nucleus involved. This could be consistent with a nickel in an $S = 3/2$ spin state, Ni_s^- , with shf from a neighbouring ^{14}N nucleus or alternatively the nitrogen itself could be in an $S = 3/2$ spin state. Nitrogen has recently been observed in nitrogen implanted C_{60} in an $S = 3/2$ spin state [22]. No EPR spectrum associated with interstitial nitrogen has so far been observed although it would be expected to be paramagnetic [19] and theoretical calculations predict that a nitrogen interstitial in the tetrahedral site in diamond would give rise to an $S = 3/2$ state with an hf interaction of the same order of magnitude as that observed in our spectra [23]. This defect would be expected to have a g value close to the free electron value in contrast to the experimental value of 2.02 and no quadrupole splitting also in contrast to the experimental results.

The experimental results are therefore not consistent with a nitrogen interstitial in the tetrahedral site but do not rule out the possibility of a relaxed configuration. Theoretical calculations have, however, found that the migration energy of the nitrogen interstitial is sufficiently low that even at room temperature they would migrate and be trapped at other defects [24]. In this case nitrogen interstitials would not be observed.

The possibility that the broad EPR line in the blue diamonds is due to a nitrogen interstitial is therefore fairly small and the most likely model is a nickel defect in an $S = 3/2$ state interacting with neighbouring nitrogens. The $g = 2.0319$ defect in synthetic diamond has been shown to be $S = 3/2$ and is believed to be due to an Ni^- ion on a

substitutional site [6]. The defect observed in this study could therefore be substitutional Ni^- with a neighbouring nitrogen. This would be consistent with the presence of the NE2 centre in these diamonds which is also believed to involve both nickel and nitrogen [8].

Without the complete angular dependence of the ENDOR spectrum it is not possible to obtain enough parameters of the spin Hamiltonian to determine the exact structure of the defect. The order of magnitude of the quadrupole and shf interactions can, however, be used to give some information about the possible structures. For this we assume that the defect is Ni_s^- to give the $S = 3/2$ spin state and that the shf interaction is from a neighbouring N^+ .

The quadrupole interaction is thought to be caused by the point charge of Ni_s^- experienced by N^+ . It can be estimated by [14]

$$P_{\parallel} = 280.36 \frac{Q(1 - \gamma_{\infty})}{4I(2I - 1)R^3} \quad (10)$$

P_{\parallel} is the element of the quadrupole interaction in MHz, Q is the electric quadrupole moment in units of $[e] \times 10^{-24} \text{ cm}^2$ and is equal to 0.0193 for ^{14}N , I is the nuclear spin, γ_{∞} is the Sternheimer antishielding factor and R is the separation between the Ni_s^- and the N^+ in ångströms. Neglecting the Sternheimer antishielding, values of P_{\parallel} for N^+ represent a lower limit of the quadrupole interaction. In table 1 this is given for various N^+ sites. According to this N^+ cannot be nearest neighbour (nn) because the experimental value of P_{\parallel} (0.09 MHz) is too small for that. Since γ_{∞} is not known for N^+ , we could only speculate on it. However, had we included Sternheimer antishielding, for the isoelectronic B^- ($\gamma_{\infty} \approx -3$), we would arrive at a position of N^+ beyond next nearest neighbours. Similarly, an estimation of the anisotropic shf interaction by the classical point dipole-dipole interaction suggests that N^+ cannot be nearest neighbour, for which the anisotropic shf constant would be significantly above the upper limit of 1 MHz, which was estimated from the experiment.

Table 1. Estimates of quadrupole parameters for different positions of nitrogen.

N^+ position	R (Å)	P_{\parallel} (MHz)
nn	1.54	0.2
nnn	2.52	0.05
4nn-[001]	3.56	0.01
$\{00\frac{1}{2}\}$	1.78	0.1

The ENDOR spectrum indicates that the defect has a symmetry axis about [100] and it is therefore natural to consider structures that have this symmetry. Figure 5 shows the unit cell for diamond. It can be seen that the fourth nearest neighbour positions belong to the (100) class and are one unit cell spacing (3.56 Å) from the Ni_s^- . We also consider the interstitial position which is half a unit cell spacing from the Ni_s^- and is also in a [100] direction.

Regarding both symmetry and magnitude of the measured interactions, the most probable position is the 4nn position one unit cell spacing in the [100] direction. We also compare our experimental value for the quadrupole parameter with that obtained from the N^+ in the W7 centre [25]. The model for this defect has the N^+ in a third nearest neighbour (3nn) position relative to the major nitrogen that has the electron spin and has a similar magnitude for the quadrupole interaction ($P_1 = 0.13$, $P_2 = -0.13$, $P_3 = 0.0$ MHz). We therefore propose that the defect structure involves Ni^- on a substitutional site and a nitrogen on a 4nn position.

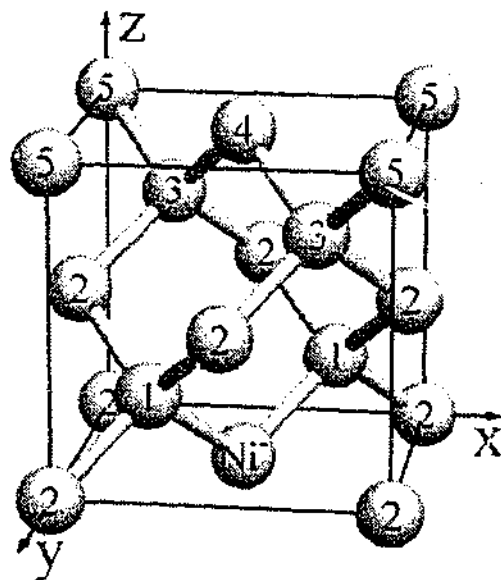


Figure 5. Unit cell of the diamond structure. An Ni^- is shown on a substitutional position and the first to fifth nearest neighbour carbons are labelled. One of the six fourth nearest neighbour carbons is shown one unit cell spacing from the Ni^- . The interstitial position in the centre of the unit cell can also be seen.

We now consider several arguments to account for the rather large linewidth of the EPR line. In contrast to Ni_5^- we do not observe a temperature dependence of the linewidth and hence spin-lattice relaxation does not determine the linewidth. Dipolar broadening from other paramagnetic species does not seem to account for the linewidth as we would expect the other EPR centres to be broadened by the same mechanism which is not observed experimentally.

The shf interaction from a single N^+ determined from the ENDOR spectra could only account for at most 0.06 mT of the linewidth. From the ENDOR spectrum we cannot determine the number of nitrogens that are involved. There are six 4nn sites and it is therefore possible that up to six nitrogens may be associated with the Ni_5^- . This would produce a Gaussian EPR lineshape. However, an analysis shows that only approximately 0.3 mT of the line width can be accounted for in this way. The high charge state of such a defect would also suggest a high formation energy and a low probability of it forming.

There are two other observations which could indicate the number of nitrogens involved. Firstly, the g factor of the EPR line appears to be isotropic. Secondly, we note that the ENDOR spectrum contains lines from both the $m_s = 1/2$ and $m_s = 3/2$ manifolds. This implies that the zero field splitting can be no larger than the EPR linewidth and therefore must be less than 40 MHz. This suggests that the Ni_5^- largely retains its local tetrahedral symmetry. If the defect involved had only one nitrogen we would expect some tetragonal distortion of the local environment of the nickel. This would result in anisotropic g values and a zero field splitting. This argument could be used to suggest that the defect has a symmetric structure with all six possible sites for the nitrogen occupied. However, as the nitrogen is proposed to be one unit cell distant from the nickel it is likely that the magnitude of this perturbation is quite small and may not produce noticeable effects.

Other diamonds from the Argyle mine, including the pink and brown coloured stones, are known to have large amounts of random strains resulting from plastic deformation. It is therefore possible that the blue diamonds also contain random strains and it is suggested

that this could explain many of the features observed. The random strain would produce a distribution of sites with different zero field splittings and g values. It would give rise to a broad isotropic Gaussian line as has been observed. A similar distribution of zero field splittings was observed with the Ni_2^- centre [5]. This would still be consistent with the observation of the $m_s = 1/2$ and $m_s = 3/2$ manifolds in the ENDOR spectra as a certain fraction of the defects would be unperturbed and have small zero field splittings. The random strains would also produce a distribution in the ENDOR frequencies. This may explain why only weak lines could be resolved on top of a broad baseline in the ENDOR spectra. The model proposed for this defect can therefore account for the features of the EPR and ENDOR spectra.

5. Conclusion

The results show that these blue diamonds contain nickel and a high concentration of nitrogen. The diamonds have been subjected to high temperatures over geological time scales. This has led to the formation of nitrogen aggregates and defects containing both nickel and nitrogen. One of these, the NE2 centre, has previously been observed in synthetic and natural diamonds and has been proposed to be Ni^+ in a di-vacancy position with three neighbouring nitrogens. The second has not been observed previously and occurs exclusively in Argyle blue diamonds. We propose that this defect is Ni_2^- with N^+ in a 4nn position. This defect has not been produced in synthetic diamonds and it appears that annealing over geological time scales is needed. Plastic deformation, which is common in other Argyle diamonds, also appears to play a role in these diamonds. The diamonds also contain high concentrations of hydrogen, which has previously been reported, but it is not clear how this is related to the nickel centres observed or the colour.

Acknowledgments

John Chapman of Argyle diamonds is thanked for the loan of the natural blue diamonds used in this work. Thanks are given to Gordon Troup who initiated the research on the Argyle diamonds and to Professor John Pilbrow and Dr Don Hutton for their advice. Bayden Wood is thanked for assisting with the FTIR spectra. Finally, the Queens Trust (Australia) is thanked for financial assistance for one of us, CJN, to travel overseas to complete part of this work.

References

- [1] Nassau K 1983 *The Physics and Chemistry of Color: the Fifteen Causes of Color* (New York: Wiley-Interscience)
- [2] Fritsch E, Scarrat K and Collins A T 1991 *New Diamond Science and Technology, MRS Int. Conf. Proc.* ed R Messier, J T Glass, J E Butler and R Roy (Pittsburgh, PA: Materials Research Society) pp 671-6
- [3] Loubser J H N and van Ryneveld W P 1966 *Nature* **211** 517
- [4] Samoilovich M I, Bezrukov G N and Butuzov V P 1971 *Pis. Zh. Eksp. Teor. Fiz.* **14** 551 (Engl. transl. 1971 *JETP Lett.* **14** 379)
- [5] Isoya J, Kanda H, Norris J R, Tang J and Bowman M K 1990 *Phys. Rev. B* **41** 3905
- [6] Isoya J, Kanda H and Uchida Y 1990 *Phys. Rev. B* **42** 9843
- [7] Yelisseyev A and Nadolinny V 1992 *Dokl. Akad. Nauk* **326** 524
- [8] Nadolinny V and Yelisseyev A 1994 *Diamond Relat. Mater.* **3** 1196-200
- [9] Davies G, Neves A J and Nazare M H 1989 *Europhys. Lett.* **9** 47
- [10] Ludwig G W and Woodbury H H 1962 *Solid State Physics* vol 13, ed F Seitz and D Turnbull (New York: Academic) p 223

- [11] Collins A T, Kanda H and Burns R C 1990 *Phil. Mag.* B 61 797
- [12] Lawson S C and Kanda H 1993 *J. Appl. Phys.* 73 3967
- [13] Mineeva R M, Speranskii A V, Titkov S V and Bershov L V 1994 *Dokl. Akad. Nauk* 334 755
- [14] Spaeth J-M, Niklas J R and Bartram R H 1992 *Structural Analysis of Point Defects in Solids* (Berlin: Springer)
- [15] Clark C D, Collins A T and Woods G S 1992 *The Properties of Natural and Synthetic Diamond* ed J E Field (London: Academic) pp 35-79
- [16] Woods G S, Purser G C, Mtinkulu A S S and Collins A T 1990 *J. Phys. Chem. Solids* 51 1191
- [17] Evans T 1992 *The Properties of Natural and Synthetic Diamond* ed J E Field (London: Academic) pp 181-214
- [18] Woods G S 1989 *Proc. R. Soc. A* 407 219
- [19] Baker J M and Newton M E 1995 *Appl. Magn. Reson.* 8 207
- [20] Chapman J 1997 private communication
- [21] *Landolt-Börnstein New Series* 1990, Group III, vol 22b, ed O Madelung and M Shulz (Berlin: Springer) pp 117-206
- [22] Murphy A T, Pawlik Th, Weidinger A, Höhne M and Spaeth J-M 1996 *Phys. Rev. B* 77 1075
- [23] Overhof H 1997 private communication
- [24] Mainwood A 1994 *Phys. Rev. B* 49 7935
- [25] Newton M E and Baker J M 1991 *J. Phys.: Condens. Matter* 3 3591